



HAL
open science

Advance numerical modelling of the atomization process: application to an aeronautical injection system

Diego Ferrando

► **To cite this version:**

Diego Ferrando. Advance numerical modelling of the atomization process: application to an aeronautical injection system. Fluid mechanics [physics.class-ph]. Normandie Université, 2022. English. NNT : 2022NORMR054 . tel-03922399

HAL Id: tel-03922399

<https://theses.hal.science/tel-03922399>

Submitted on 4 Jan 2023

HAL is a multi-disciplinary open access archive for the deposit and dissemination of scientific research documents, whether they are published or not. The documents may come from teaching and research institutions in France or abroad, or from public or private research centers.

L'archive ouverte pluridisciplinaire **HAL**, est destinée au dépôt et à la diffusion de documents scientifiques de niveau recherche, publiés ou non, émanant des établissements d'enseignement et de recherche français ou étrangers, des laboratoires publics ou privés.



Normandie Université

THÈSE

Pour obtenir le diplôme de doctorat

Spécialité **MECANIQUE DES FLUIDES, ENERGETIQUE, THERMIQUE, COMBUSTION,
ACOUSTIQUE**

Préparée au sein de l'Université de Rouen Normandie

**Modélisation numérique avancée du processus d'atomisation :
application à un système d'injection aéronautique**

Présentée et soutenue par
DIEGO FERRANDO

**Thèse soutenue le 26/04/2022
devant le jury composé de**

M. DOMINIQUE LEGENDRE	PROFESSEUR DES UNIVERSITES, ENSEEIH de Toulouse	Rapporteur du jury
M. FEDERICO PISCAGLIA	PROFESSEUR DES UNIVERSITES, Institut Polytech. de Milan (ITALIE)	Rapporteur du jury
M. ANTONIO ANDREINI	PROFESSEUR DES UNIVERSITES, Université de Florence (ITALIE)	Membre du jury
M. MARCOS CARRERES TALENS	PROFESSEUR DES UNIVERSITES, Université Polytech. de Valence (ESP)	Membre du jury
M. BENJAMIN DURET	MAITRE DE CONFERENCES, Université de Rouen Normandie	Membre du jury
MME KONSTANTINA VOGIATZAKI	PROFESSEUR DES UNIVERSITES, King's College ,LONDRES (R-U)	Membre du jury
M. RENO BRUNO	PROFESSEUR DES UNIVERSITES, INSA DE ROUEN NORMANDIE	Président du jury
M. FRANÇOIS-XAVIER DEMOULIN	PROFESSEUR DES UNIVERSITES, Université de Rouen Normandie	Directeur de thèse

**Thèse dirigée par FRANÇOIS-XAVIER DEMOULIN (COMPLEXE DE RECHERCHE
INTERPROFESSIONNEL EN AEROTHERMOCHIMIE),**



Advance numerical modelling of the atomization process: application to an aeronautical injection system

Thesis submitted for the degree of Doctor of Philosophy of the University of Rouen

Normandie

Diego Ferrando Martínez

diego.ferrando@coria.fr

Jury:

François-Xavier Demoulin	CORIA, Université de Rouen Normandie	Supervisor
Benjamin Duret	CORIA, Université de Rouen Normandie	Co-supervisor
Bruno Renou	INSA, Université de Rouen Normandie	Jury president
Federico Piscaglia	DAER, Politecnico di Milano	Reviewer
Dominique Legendre	IMFT Toulouse	Reviewer
Marcos Carreres Talens	CMT, Universitat Politècnica de València	Examiner
Antonio Andreini	DIEF, Università degli Studi di Firenze	Examiner
Konstantina Vogiatzaki	EPSRC-UKRI, King's College London	Examiner

PhD, University of Rouen and CORIA - France

This research was done under the supervision of François-Xavier Demoulin and Benjamin Duret with the financial support of the European Commission within a total of 3 years, from 2019 to 2022.

Edition date *March 15, 2022*

*I have learned all kinds of things from my many mistakes.
The one thing I never learn is to stop making them.*

Joe Abercrombie, *Last Argument of Kings*

Acknowledgements

When I arrived to Rouen three years ago I could not speak the language and it was the first time I went to live abroad. Before finishing my first year of PhD the world as we know it changed incredibly, we had to stay at home for two months and we had to work for home most of the time. Nevertheless, these three years have passed very quickly and I enjoyed them a lot due to some people I want to acknowledge.

First of all, I want to thank my supervisors, **François-Xavier Demoulin** and **Benjamin Duret**. **FX** has given me a lot of ideas to develop my thesis and he has always tried to let me feel comfortable here. Every time I went to his office for what I thought was a small doubt of 10 minutes talk, it finished on a more than an hour discussion about research topics and other including life. When I had any problem with any of the french bureaucracy (which is a lot) or I needed some correction on my English writings, I could always count on **Benjamin**. Finally, despite he is not officially one of my supervisors, I also want to thanks **Julien Reveillon** because since the first day, he was here to help me to integrating here in France and on the lab.

Since the beginning of my thesis I have been enrolled on the CHAiRLIFT project with amazing people. Despite the global situation of these years we could have some in person meetings and, of course, I will always remember the dinners at Italy and Germany. I would like to thank all the CHAiRLIFT group: **Antonio Andreini, Leonardo Langone, Rainer Koch, Sven Hoffmann, Stefan Harth, Mohamed Shamma, Maria Grazia de Giogi** and also all the people that I have met for the industry that came to our meetings.

I have the pleasure to work with **Marcos Carreres** for these three years. He came 3 months to Rouen when I started and he has always been a great support to me, a fantastic researcher and a friend. During this time I also work with two of his PhD students, **Mario Belmar** who I met at ILASS 2019 at Paris and it was a pity he could not come here, and **David Cervelló**. I want to thank the three of them because it has been really easy to work with.

I have done great friends at the lab with whom I have spent great times and never-ending coffee breaks. **Niccolò Tonicello, Cléante Langrée, Alberto Remigi, Victor Cheron, Hakim Hamdani, Hassan Tofaili, Lorenzo Palanti**. I miss those conversations about non important matters, to be silenced at the CORIA cafeteria and more. Thank you very much. I also want to thank all the people from CORIA and for my research group.

There are people at Spain that have been supporting me all the time. I want to begin thanking my two best friends **Alejandro Laya** and **Israel Gutierrez** because despite the fact that we have not seen each other during long periods it is always as if we see each other every day. My friend **Alejandro Noguero** who helped me a lot when I arrived France and he had talked about the opportunities of this country to me. Of course, to **Yolanda Estepa, Abel Blanco** and **Alodia Buil** because despite we do not talk to much and we do not see each other very often, when we do, it is like coming back to the university times. To my family that have had the oddest time of their life knowing that I was happy and everything was

going well but I was far away. And to the two person that are not longer with me, my mother **Mercedes** and my grandfather **Juan**, that wherever they are, I know they take care of me.

The last, but of course, no the least, I really want to thank my wife **Sabina** to be always with me, to support me and to give me force on the worst moments. I really love you. I do not want to leave out another two really important beings of my life, my cats **Albus** and **Caliope** that with a simple purr they can transform a bad moment into happiness.

Abstract

The combustion inside of aircraft gas turbines is highly affected by fuel injection and atomization. Reaching smaller droplets leads into a cleaner and faster combustion since the evaporation takes place earlier, hence, promoting a good mixing. Thus, study the performance of aeronautical atomizer is of high importance to understand the physical phenomena that drive spray characteristics. On experimental campaigns, measurements such as the drop size distribution and mean velocity of the droplets can be performed. However, due to the complex geometries of atomizers and limitations of the current experimental techniques, early stage of the atomization process is difficult to characterise. Numerical modelling play a role at this level to enforce our description of such multiphase flows. On the last years, numerical studies of aeronautical injectors have been carried out to model the flow inside the atomizer with the goal to recover experimental measurements. Nevertheless, other difficulties are found on numerical modelling such as the computational time and resources required.

On this work, a methodology applicable for numerical modelling of an aircraft atomizer is proposed. In particular, an airblast prefilming atomizer, representative of gas-turbine injection systems, is studied. Since performing one single simulation able to recover the whole injection system is not possible due to the high amount of computational resources, a workflow has been proposed that considers a succession of complementary simulation. This multi-simulation, multi-scale approach allows eventually to study the essential features of the injection system. The atomizer studied belongs to the in the CHAIRLIFT project within the Clean Sky 2 project. Within this project, the aim of this work is to characterize the spray calculating the drop size distribution and the velocity of the droplets that can be used for further combustion characterization. Since the atomization simulation are limited to the early stage of injection, a recently proposed analysis is applied and developed further to give a more complete definition of the spray. This analysis is based on the surface interface density Σ and the curvature κ to predict the joint number distribution of droplets at a given diameter and velocity.

In addition, since the CHAIRLIFT injection system require a swirl injector to initiate the internal liquid film and also because swirl injection are commonly used in gas-turbine systems, this work includes also a simplex swirl injector. A injector applied on an academic project dedicated to gas turbine spray flame is studied. The internal geometry of this Danfos swirl injector is unknown. Thus, the internal geometry has been measured by several measurement techniques and the computational geometry has been reconstructed. Modelling this kind of injectors is not straightforward due to the large range of scale to be considered, hence, a two simulation coupling has been proposed to overcome the difficulties of this simulation. Results have been validated with comparison with previous experimental campaigns. Finally the new analysis has been also applied to determine the spray size distribution at the early stage of the atomization process and compare to experimental measurement obtained further downstream.

Table of Contents

	Page
1 Introduction	1
1.1 CHAIRLIFT	2
1.2 Thesis outline	4
2 Numerical methods for spray atomization	7
2.1 Multiphase spray atomization modelling	9
2.1.1 Dense region: DNS-ICM approach	10
2.1.2 Transition region: LES approach	12
2.1.3 Dilute region	14
2.2 A Volume of Fluid based LES approach	16
2.2.1 The interFoam solver	16
2.2.2 LES turbulence modelling	18
2.3 Numerical simulation set up	19
2.3.1 Discretization schemes	19
2.3.2 Boundary Conditions	20
2.4 CHAIRLIFT configuration modelling	21
3 CRSB Simplex Swirl Atomizer	23
3.1 Literature review of simplex swirl atomization	24
3.1.1 Flow inside of the injector	25
3.1.2 Outer flow and atomization process	32
3.2 CRSB simplex swirl injector description	34
3.2.1 Experimental campaigns	34
3.3 Experimental geometry measurements	35
3.3.1 Computed Tomography Scan	36
3.3.2 Optical microscope visualization	36
3.3.3 Scanning electron microscope visualization	38
3.3.4 Measurement results	39
3.4 Modelling the flow inside of the injector	39
3.4.1 Computational hybrid mesh	40
3.4.2 Numerical set up	43
3.4.3 Mesh converge study	45
3.4.4 Discretization schemes	50

3.4.5	Temperature variation	50
3.4.6	Outputs recovery data	54
3.5	External flow modelling: Spray atomization	55
3.5.1	Computational grid	55
3.5.2	Coupling between numerical simulations	58
3.5.3	Outer domain results	59
3.6	Conclusions	66
4	CHAiRLIFT atomizer	69
4.1	Prefilming airblast atomization	70
4.1.1	Film thickness	70
4.1.2	Sauter Mean Diameter	72
4.1.3	Droplet mean velocity	74
4.2	KIT-ITS atomizer	74
4.2.1	Operating Conditions	75
4.3	Air flow modelling	75
4.3.1	Computational grid	76
4.3.2	Numerical set-up	76
4.3.3	Results	77
4.4	Estimation of the liquid film thickness	78
4.4.1	Numerical domain	79
4.4.2	Computational mesh	79
4.4.3	Numerical set-up	80
4.4.4	Results	80
4.5	Airblast prefilming modelling	81
4.5.1	Numerical domain and computational grid	81
4.5.2	Numerical set-up	82
4.5.3	Results	83
4.6	Conclusions	85
5	Spray Characterization	87
5.1	Drop sizing methods	88
5.1.1	Experimental techniques	88
5.1.2	Numerical methods	89
5.2	Surface interface and curvature analysis	89
5.2.1	Surface interface density	90
5.2.2	Estimation of the curvature	92
5.3	Sauter mean diameter (SMD)	93
5.4	Surface curvature distribution (SCD)	95
5.5	Drop size distribution (DSD)	98
5.6	Velocity joint distribution	101
5.7	Comparison with experiments	103

5.8	Drop size distribution on CRSB injector	105
5.8.1	Ambient temperature case	105
5.8.2	High temperature case	108
6	Conclusions and perspectives	111
A	CHAIRLIFT airblast atomizer: Test rig operating conditions	129
A.1	Air flow modelling	130
A.2	Estimation of the liquid film thickness	130
A.2.1	3D film thickness modelling	130
A.3	Prefilmer simulation	132
A.3.1	Steady fuel film thickness	133
A.3.2	Unsteady fuel film thickness	133
A.4	Spray post-processing	134
A.4.1	Steady fuel film thickness	134
A.4.2	Unsteady fuel film thickness	134
B	Data measurement utility	137
B.1	Implementation	137
B.2	Utility performance	139
C	Publications	141

List of Tables

Table	Page
3.1	Experimental operating condition on the CRSB simplex swirl atomizer 35
3.2	Experimental measurements of the CRSB simplex swirl atomizer 40
3.3	Inner simulation meshes characteristics. 43
3.4	Fluid characteristics for different temperatures 43
3.5	CRSB internal flow boundary conditions. 44
3.6	Computational time step and resources needed 49
3.7	Spray angle measurements from experiments and simulations. 53
3.8	2D grid convergence study: mesh information. 56
3.9	Boundary conditions on the sectorial outer CRSB domain 57
3.10	Computational resources needed for the 3D outer simulation 60
4.1	Sedlmaier test case operating conditions 75
4.2	Fluid properties for the Sedlmaier test case. 75
4.3	Single-phase in detail simulation of the nozzle: Boundary conditions. 77
4.4	Multiphase simulation to estimate the liquid film thickness: boundary conditions . 80
4.5	Prefilmer simulation: Mesh information 82
4.6	Prefilmer multiphase simulation: Boundary conditions 83
5.1	Corrected radius and surfaces of several droplet simulations with different mesh resolution. The recovered surface is computed from Equation 5.3. 92
5.2	Mean velocity by the mass weighted method and the surface-curvature method. . 102
A.1	CHAiRLIFT test rig ambient operating conditions 129
A.2	Fluid properties for the CHAiRLIFT test rig case. 130
A.3	3D channel boundary conditions 131

List of Figures

Figure	Page
1.1	Number of flights through the years from 2004 to 2021 [Mazareanu, 2021]. 1
1.2	CO_2 emissions due to aviation from 1940 to 2018 [Ritchie, 2020] 2
1.3	Schematic comparison conventional and SHC combustor by [Ariatabar et al., 2016] 3
1.4	Summary of the CHAIRLIFT project 3
2.1	Picture of the spray expelled from the CRSB injector by [Verdier, 2017]. The dense, transition and dilute zones and the primary and secondary break-up are plotted. 8
2.2	Atomization zones by dynamic modelling approach [Añez, 2019]. 9
2.3	Front tracking method example [Scardovelli and Zaleski, 1999]. 10
2.4	Level-set method representation. On blue: iso-contour for $\phi = 0$ representing the interface [Canu, 2019]. 11
2.5	Volume of fluid method representation. 12
2.6	Interface among fluid and gas. On the left the minimum interface Σ_{min} is represented meanwhile on the right the real interface Σ is shown. The difference of surface is Σ' 14
2.7	Dilute, dispersed, and dense flow conditions based on various interphase coupling [Crowe, 2005] 15
2.8	Detail of SIMPLE and PISO algorithms [Mughal, 2016]. 18
2.9	5 steps workflow followed to model the CHAIRLIFT airblast atomizer. 22
3.1	Sketch of main pieces of a simplex swirl atomizer. 24
3.2	Atomization process of a simplex swirl atomizer [Lefebvre and McDonell, 1988]. 25
3.3	Main dimensions of a simplex swirl atomizer[Rizk and Lefebvre, 1985a]. D_s represents the diameter of the swirl chamber. L_s represents the depth of the swirl chamber. D_p represents the diameter of the fuel feed port. L_p represents de length of the feed port. d_o represents the diameter of the orifice outlet. l_o represents the length of the orifice throat. 2θ represents the double of the spray angle. 26
3.4	Flow path in simplex swirl atomizers [Lefebvre and McDonell, 1988] 27
3.5	Spray development in a simplex swirl atomizer [Lefebvre and McDonell, 1988] . . 32
3.6	Danfoss OD-H oil nozzle. Cut view[Danfoss, 2020] 34
3.7	Detail of the injection system [Verdier, 2017] 35
3.8	On the left: Computed tomography scan of the assembled simplex swirl atomizer. On the right: Zoom view on the orifice profile 36
3.9	Optical microscope picture of disassembled metallic pieces. On the left: Orifice disk from above. On the right: Tangential ports distributor from above 37

3.10	Optical microscope picture of silicone molds. On the left: upper piece. On the right: lower piece	37
3.11	Scanning electron microscope picture of disassembled metallic pieces. On the left: Orifice disk from below. On the right: Orifice disk from above	38
3.12	Scanning electron microscope picture of silicone molds. On the left: Silicone mold lower part. On the right: Silicone mold upper part.	38
3.13	Sketch of the inner geometry of the injector	39
3.14	Computational grid sketch. Hybrid mesh made of hexahedral and tetrahedral elements.	41
3.15	Tangential ports profile mesh. On the left: Inlet mesh. On the middle: Intersection with swirl chamber. On the right: Transition between hexahedral and tetrahedral elements.	41
3.16	Slice around the swirl and spin chamber showing the mesh.	42
3.17	Slice of the outer domain.	42
3.18	Boundary conditions patches of the CRSB internal flow simulation.	44
3.19	Hollow cone evolution	46
3.20	CRSB mesh convergence study: Liquid volume fraction. At the left of each picture the time averaged values is plotted meanwhile at the right an instantaneous values is plotted.	46
3.21	Air core experiments. On the left: [Sumer et al., 2012]. On the right: [Maly et al., 2018]	47
3.22	Liquid volume fraction iso-surface: $\alpha = 0.5$	47
3.23	Sample experimental pictures by [Verdier, 2017] for three different instants.	47
3.24	Liquid volume fraction α plot along the radial axis on the nozzle. On blue: coarse mesh case. On green: fine mesh case. On black: empirical equation.	48
3.25	Eddy viscosity	49
3.26	Central slice of the velocity. From top to bottom: coarse, medium and fine meshes.	50
3.27	Liquid volume fraction α contour at the atomizer outlet cross-section. Top: three snapshots using the <i>upwind</i> scheme for the spatial divergence. Bottom: three snapshots using the <i>limitedLinear</i> scheme for the spatial divergence. The time step between pictures is $\Delta t = 5\mu s$	51
3.28	Liquid volume fraction iso-surface: $\alpha = 0.5$	51
3.29	Experimental pictures of the CRSB injector spray. On the left: ambient temperature condition by [Verdier, 2017]. On the right: high temperature condition by [Marrero, 2018].	52
3.30	Liquid volume fraction. On the left the time averaged value is plotted and on the right the instantaneous value is plotted.	52
3.31	Liquid volume fraction α plot along the radial axis on the nozzle. On blue: ambient temperature. On red: high temperature. Solid lines: simulation data. Dashed lines: empirical equation.	53
3.32	Injection pressure for several fuel mass flow rates. On a blue star, the pressure drop obtained from the simulations is plotted.	54
3.33	Grid convergence study. Liquid volume fraction for cases of cell size from left to right: $2\mu m$, $1\mu m$, $0.5\mu m$	56
3.34	Geometry domain and boundary condition of the external flow simulation. 1: Inlet. 2: Wall. 3: Cyclic patches. 4: Outlet.	57
3.35	External simulation mesh	57
3.36	Swirl number along the axial axis	58
3.37	Turbulent kinetic energy. On the left: resolved scales. On the right: sub-grid energy.	59

3.38	Liquid volume fraction on the inlet patch. On the top: constant thickness. On the bottom: fluctuating fuel sheet.	60
3.39	On the left: Comparison among the iso-surface ($\alpha = 0.5$) from the constant fuel sheet thickness and the experimental picture by [Miglierina, 2021]. On the right: Comparison among the iso-surface ($\alpha = 0.5$) from the varying fuel sheet thickness and the experimental picture by [Miglierina, 2021]	61
3.40	Liquid volume fraction middle slice. On the left is represented the time averaged value. On the right is represented the instantaneous value.	61
3.41	Velocity magnitude. On the left of each picture: time averaged value. On the right of each picture: instantaneous value	62
3.42	Axial velocity. On the left of each picture: time averaged value. On the right of each picture: instantaneous value	62
3.44	Tangential velocity. On the left of each picture: time averaged value. On the right of each picture: instantaneous value	62
3.43	Radial velocity. On the left of each picture: time averaged value. On the right of each picture: instantaneous value	63
3.45	360° iso-surface ($\alpha = 0.5$) rendering of the ambient temperature case.	63
3.46	Ambient temperature iso-surfaces for several values of α . In the middle the iso-surface $\alpha = 0.5$ and a contour of the liquid volume fraction are represented as a reference.	64
3.47	Qualitative validation of the ambient temperature case compared with experimental pictures by [Verdier, 2017]	65
3.48	Qualitative validation of the ambient temperature case compared with experimental pictures by [Miglierina, 2021]	65
3.49	360° iso-surface ($\alpha = 0.5$) rendering of the high temperature case.	65
3.50	Qualitative validation of the high temperature case compared with experimental pictures by [Marrero, 2018]	66
4.1	Prefilming airblast atomizer sketch [Lefebvre and McDonell, 1988]	71
4.2	Nozzle used on the CHAiRLIFT project [Kasabov et al., 2013].	74
4.3	Simplex swirl nozzle utilized on the CHAiRLIFT project.	75
4.4	Axial velocity contours from the numerical study by [Langone, 2022] compared to the experimental study by [Sedlmaier, 2016]. On the left: 4 million elements mesh. On the middle: 16 million elements mesh. On the right: Experiment data.	76
4.5	In detail single phase simulation domain.	76
4.6	Air flow single phase mesh.	77
4.7	Contours of the velocity at a middle plane. Left side: Instantaneous value. Right side: Mean value	77
4.8	Magnitude velocity contour on a transverse plane with the inlet outline from the prefilmer simulation overimposed.	78
4.9	2D film thickness estimation: Domain and boundary conditions.	79
4.10	Geometric representation on how to fix l on the 2D simulation to estimate the liquid film thickness	79
4.11	Liquid volume fraction contour to obtain the prefilmer film thickness. Test case operating conditions.	80
4.12	Numerical domain. On the left: geometrical domain on black solid lines with a slice of the mesh. On the right: detail of the numerical mesh.	81
4.13	Liquid volume iso-surfaces $\alpha = 0.5$ for three different time steps.	83

4.14	On the left: Time averaged liquid volume fraction $\bar{\alpha}$ on a middle plane. On the right: Time averaged surface interface density $\bar{\Sigma}$. Colour bars are on logarithmic scale. Spray angle is drew on black solid line.	84
4.15	Velocity magnitude contour. On the left: time averaged value. On the right: instantaneous value.	85
4.16	Axial component of the velocity. On the left: time averaged value. On the right: instantaneous value.	85
4.18	Tangential component of the velocity. On the left: time averaged value. On the right: instantaneous value.	85
4.17	Radial component of the velocity. On the left: time averaged value. On the right: instantaneous value.	86
5.1	Surface interface density normalized by cell size and plotted over the liquid volume fraction α iso-surface. From top to bottom: $\alpha = 0.1, 0.25, 0.5, 0.75, 0.9$. From left to right: mesh resolution $dx = 2.5\mu m, 1.25\mu m, 0.625\mu m$	91
5.2	Mean curvature κ plotted over the iso-surface $\alpha = 0.5$. From left to right: mesh resolution $dx = 2.5\mu m, 1.25\mu m, 0.625\mu m$	93
5.3	Mean curvature κ distribution on the iso-surface $\alpha = 0.5$. From left to right: mesh resolution $dx = 2.5\mu m, 1.25\mu m, 0.625\mu m$	93
5.4	Measurements planes inside of the numerical domain	94
5.5	Equivalent Sauter Mean Diameter streamwise evolution.	95
5.6	Link between the DSD and the SCD for a known cloud of spherical droplets [Canu et al., 2018].	96
5.7	Zone were the measurement probes are set up.	96
5.8	Surface Curvature Distribution at 1.2 mm	97
5.9	Curvature plotted over a spray iso-surface ($\alpha = 0.5$).	98
5.10	Drop size distribution calculated from the surface curvature distribution on Figure 5.8.	98
5.11	Drop size distribution rearranged to match $D_{32}^{DSD} = D_{32}^{flux}$	99
5.12	Surface interface kept. From left to right: SCD, DSD and $\alpha = 0.5$ iso-surface with the curvature plotted on it. From top to bottom: all liquid structures, liquid structures with positive curvature $\kappa > 0$ and liquid structures which curvature is less than $\kappa < 4/D_{max}$	100
5.13	Drop size distribution convergence study: $D_{32}(t)$	100
5.14	Drop size distribution convergence study: $D_{10}(t)$	101
5.15	Drop size distribution convergence study: $\sigma(t)$	101
5.16	Velocity joint distribution. From left to right: Axial, tangential and radial component of the velocity	102
5.17	Velocity joint distribution for a droplet of diameter $D = 8.5\mu m$. From left to right: Axial, tangential and radial component of the velocity	102
5.18	Velocity joint distribution for a droplet of diameter $35.0 < D \leq 36.0\mu m$. From left to right: Axial, tangential and radial component of the velocity	103
5.19	Velocity joint distribution for a droplet of diameter $65.0 < D \leq 66.0\mu m$. From left to right: Axial, tangential and radial component of the velocity	103
5.20	Mean velocity by droplet diameter. From left to right: Axial, tangential and radial component of the velocity.	103
5.21	Drop size distribution on mass terms	104

5.22	Qualitatively validation of the CHAiRLIFT airblast modelling. From left to right MIE-scattering by [Sedlmaier et al., 2014], $\bar{\Sigma}$ and $\bar{\alpha}$ contour for the constant velocity and constant distribution, random particles and global velocity joint distribution and constant distribution, random particles and velocity joint distribution by droplet diameter	105
5.23	Equivalent Sauter Mean Diameter l_{32} in function of the axial coordinate.	105
5.24	On the left: experimental drop size distribution by [Verdier, 2017]. On the right: measurement point: blue and yellow starts corresponds to the Verdier measurement points meanwhile the black start is the measurement point of this work.	106
5.25	Drop Size Distribution for the ambient temperature case. On black: post-processed DSD from the simulation. On blue and yellow lines: experimental DSD by [Verdier, 2017].	107
5.26	Drop Size Distribution for the ambient temperature case. On the left: Measurements taken on the angle $\theta_{exp} = 40^\circ \pm 5^\circ$; On black: post-processed DSD from the simulation, on yellow line: experimental DSD by [Verdier, 2017]. On the right: Measurements taken on the angle outside of $\theta_{exp} = 40^\circ \pm 5^\circ$; On black: post-processed DSD from the simulation, on blue line: experimental DSD by [Verdier, 2017].	107
5.27	Equivalent Sauter Mean Diameter l_{32} in function of the axial coordinate.	108
5.28	Drop Size Distribution for the high temperature case. On black: post-processed DSD from the simulation. On yellow : experimental DSD by [Marrero, 2018]	109
A.1	Liquid volume fraction contour to obtain the prefilmer film thickness. CHAiRLIFT test rig operating conditions.	130
A.2	Geometrical domain and two slices representing the numerical grid	131
A.3	Instantaneous snapshot showing the liquid volume fraction iso-surface ($\alpha = 0.5$) and some slices of the velocity magnitude	132
A.4	Planes stored on run time to map the prefilmer simulation. On the top: liquid volume fraction α . On the bottom: velocity magnitude $ \mathbf{u} $	132
A.5	Instantaneous iso-surfaces ($\alpha = 0.5$) for the steady fuel film thickness, airblast case.	133
A.6	Instantaneous iso-surfaces ($\alpha = 0.5$) for the unsteady fuel film thickness, airblast case.	133
A.7	Drop size distribution of the steady fuel film thickness case.	134
A.8	Drop size distribution of the unsteady fuel film thickness case.	135
B.1	On the right: description of the one computational cell. On the left: behaviour of the default probes utility . c_i is the cell i on the computational grid, c_p is the center of the cell, f_i is the i face of the cell, p_i is the probe i , Δx_{f_i} is the distance among the face center and the cell center and Δx_{c_p} is the distance among the cell center and the probe.	137
B.2	139
B.3	Normalized time step by number of probes	139
B.4	Probes file size by number of probes	140

1 | Introduction

The aircraft industry has been growing up since its creation, becoming one major source of pollutant emission such as CO₂ and NO_x emissions. To reduce its impact several initiatives have been performed over the years and, regarding this work, the European CHAIRLIFT project (Clean Sky 2) has the aim to study new technologies for aircraft gas turbines. This chapter shows the goals of the project and presents an outline of the current thesis.

Contents

1.1	CHAIRLIFT	2
1.2	Thesis outline	4

The number of flights performed globally by the airline industry increased steadily since the early 2000s and reached 38.9 million in 2019 with an estimation of 40 million in 2020. However, due to the coronavirus pandemic, the number of flights dropped finally to 16.9 million in 2020. Anyhow, in 2021 the number of flights grew up to 19.3 million and the previsions for 2022 are set on 25.8 million flights despite the COVID pandemic [Mazareanu, 2021].

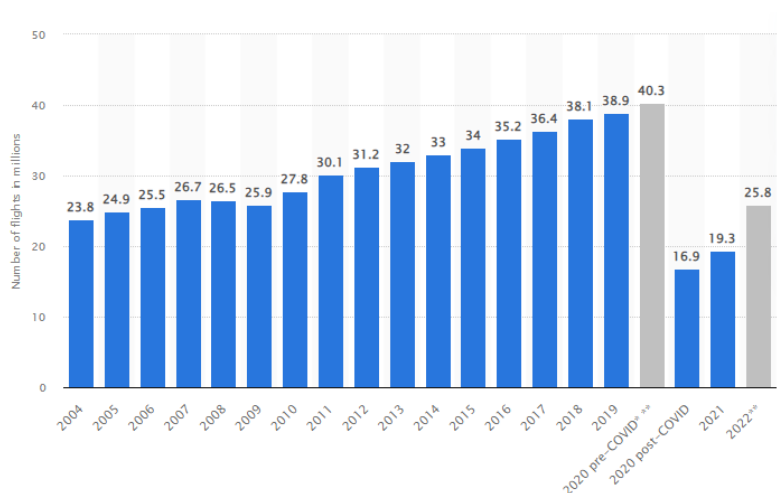


Figure 1.1 – Number of flights through the years from 2004 to 2021 [Mazareanu, 2021].

The more number of flights the more emissions they produce. Nowadays, more than 1 billion tons of CO_2 come from the aviation [Lee et al., 2021] representing the 2.5% of the total CO_2 emission in 2018. On Figure 1.2 we can observe a rise of the emission in 4 – 5% per year. Obviously, this data does not take into account the COVID19 global health crisis where the emission of CO_2 has gone down. Anyway, as it has been shown on Figure 1.1, aviation will reach the pre-pandemic number of flights in a few years and so the emission will.

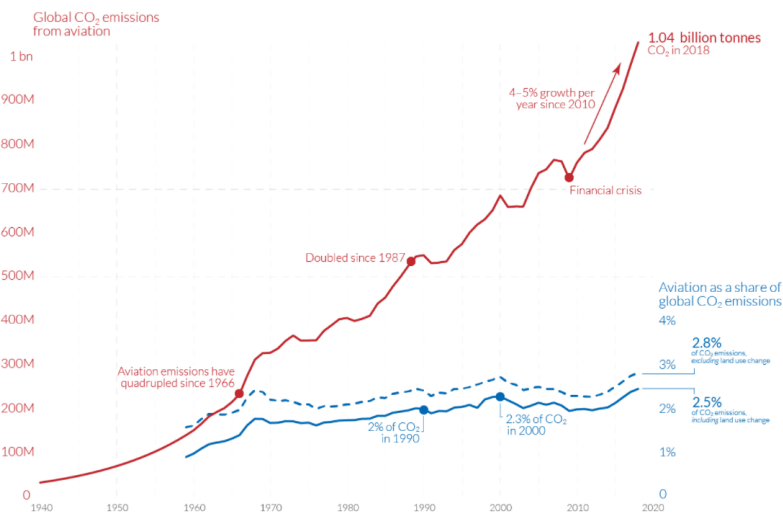


Figure 1.2 – CO_2 emissions due to aviation from 1940 to 2018 [Ritchie, 2020]

Taking into account the non- CO_2 emissions, the aviation industry emits 3.5% of the total. Therefore, through the last decades, efforts on reducing the emissions emitted from the aircraft gas turbines have increased.

The Clean Sky 2 program (currently followed by the Clean Aviation program) was launched on 2014 following the Clean Sky program (2007-2014). Its goal is to develop disruptive new aircraft technologies to support the European Green Deal, and climate neutrality by 2050. These technologies will deliver net greenhouse gas (GHG) reductions of no less than 30% and reducing the CO_2 emission by 90% [CleanAviation, 2022].

This thesis has been founded by one of the projects inside of the Clean Sky 2 program, the CHAIRLIFT (Compact Helical Arranged combustors with lean LIFTed flames) project.

1.1 CHAIRLIFT

The project has the aim to study the combination of two different well-known technologies: the short helical combustor and the lifted flames. Each of these two technologies allow to reduce the NO_x emission by themselves, hence, the goal is to study experimentally and numerically those two technologies together.

The Short Helical Combustor (SHC) concept was introduced by [Ariatabar et al., 2016]. The major feature of SHC concepts is that the primary axes of all burners are tilted in circumferential direction relative to the rotational axis of the gas turbine. A comparison among a conventional combustor and a SHC design is shown on Figure 1.3. The advantages of SHC is to increase the flow residence time thanks to the helical flow pattern in the chamber. The combustor weight can be reduced due to the shortening of the turbine shaft length leading to a more rigid core. Another substantial advantage is to enhance transverse exchange of heat and combustion products between the adjacent flames via advection and radiation which produces a reduction of pollutant and noise emissions.

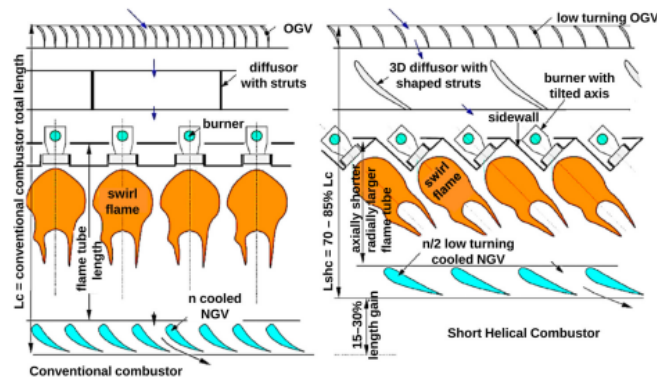


Figure 1.3 – Schematic comparison conventional and SHC combustor by [Ariatabar et al., 2016]

Further information of the SHC concept can be found in [Ariatabar et al., 2017, Ariatabar et al., 2018].

Lifted flames are a hybrid between diffusion and premixed flames. They are partially premixed flame offering some of the benefits of the premixed combustion, but limiting some their disadvantages. They are highly valued for their NO_x reduction potential and for their low susceptibility to flash-back and thermo-acoustic instabilities [Fokaides et al., 2007, Kasabov et al., 2013].

Experimental and numerical studies have been carried out within the CHAIRLIFT project on several research groups. Figure 1.4 shows an overview of every study performed and which research group has performed it. In this project the following groups has been participated: *Università degli Studi di Firenze (UNIFI)*, *Karlsruher Institut für Technologie (KIT)* groups *Engler-Bunte-Institut (EBI)* and *Institut für Thermische Strömungsmaschinen (ITS)*, *Università degli Studi di Salerno (UNILE)* and *Université de Rouen Normandie (URN)*.

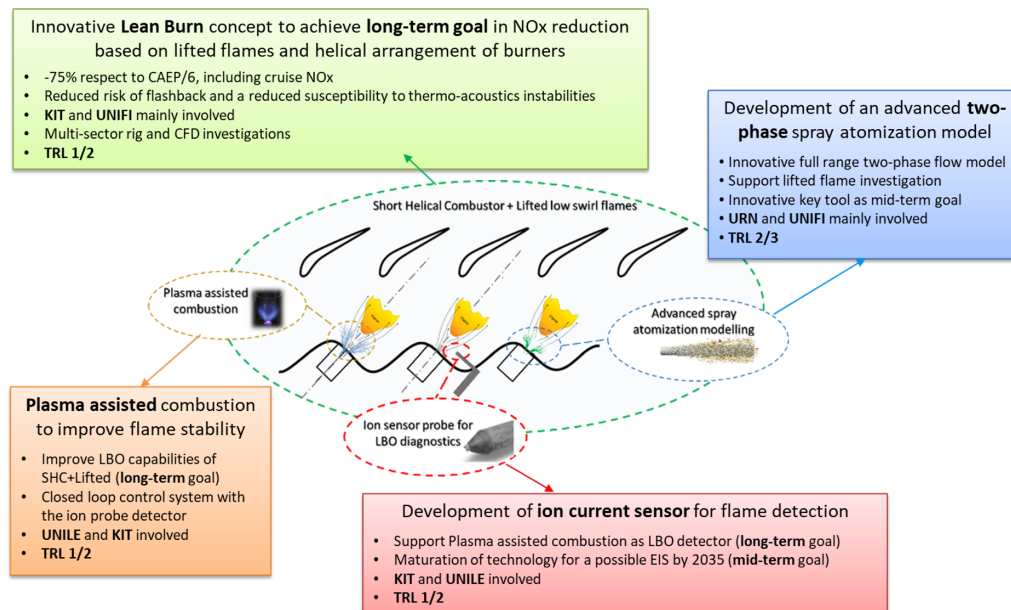


Figure 1.4 – Summary of the CHAIRLIFT project

The studies has been divided into four main groups: SHC conceptual design, numerical

investigations of lifted spray flames, experimental investigations and an implementation to a real scale combustor.

The SHC conceptual design has been studied by KIT/ITS group. They have performed a parametric numerical study to develop a baseline configuration. Afterwards, further optimization of this preliminary design was performed [Hoffmann et al., 2021, Shamma et al., 2021]. Experimental investigations have been performed by KIT/EBI and UNILE on a multi-sector rig simplifying a real SHC [Shamma et al., 2021] where the burner is based on the work by [Kasabov, 2014]. Moreover, preliminary investigations of enhanced flame stabilization were carried out by [De-Giorgi et al., 2021]. The numerical investigation of lifted flames has been carried out by UNIFI; on a first place a fundamental study of the combustion modelling in a single sector [Langone et al., 2022] was carried out based on the work by [Sedlmaier, 2016]. It was followed by the numerical study of the multi-sector rig [Shamma et al., 2021]. Both studies need the spray characteristics to set up the case. Thus, on this part done at URN (University of Rouen Normandy, the multiphase modelling of the spray atomization has been performed [Ferrando et al., 2021c, Ferrando et al., 2021a] to provide the characteristics of the spray to the reactive flame simulation.

1.2 Thesis outline

The aim of this work is to study numerically the atomizer used on the CHAiRLIFT burner to characterize the spray. Afterwards, the extracted data have to be treated to generate proper spray boundary conditions for further reactive flame simulation.

Since this work has been done in parallel to the experimental campaign on the multi-sector rig, the results shown are performed mostly on the single-sector test case by [Sedlmaier et al., 2014] to validate the modelling. The multiphase numerical approaches to model the spray atomization are presented on chapter 2 as well as the physical model selected for this study. Additional numerical methods such as the discretization schemes and the boundary conditions imposed on the simulations are also explained. Finally, a methodology to handle the modelling of this airblast atomizer is proposed.

The first step on this workflow is the numerical study of a simplex swirl atomizer shown on chapter 3. Since numerical modelling has been done in parallel with the experimental campaign, no data were available to validate this first part on the CHAiRLIFT swirl injector, hence, the atomizer used to develop atomization modelling comes from previous studies PhD thesis of [Verdier, 2017, Marrero, 2018]. In spite of the CHAiRLIFT simplex swirl injector is not the main atomizer, this kind of injectors can work standalone on aircraft gas turbines [Remigi, 2021]. Thus, a workflow to model this kind of injector is still of interest for gas turbine. This study include the experimental measurements of the internal geometry performed in collaboration with *Universitat Politècnica de València* (UPV) [Ferrando et al., 2021a] to construct a 3D computational geometry. In addition, the numerical study of the internal flow inside of the atomizer is shown. These first result constitute data that is coupled to another simulation to compute the atomization process on the external domain. This study has been validated with the experiments performed by [Verdier, 2017, Marrero, 2018] at CORIA.

Performing a single simulation of an airblast atomizer remains in general too complex and too expensive (computationally speaking) process. Therefore on chapter 4 a solution is proposed. Due to the large range of length scales involved on this kind of atomizers and the numerous physical phenomena implied, a hierarchy of complementary and coupled simulation has been proposed to study each of them separately. The chapter begins with a literature review of the airblast atomizers in general and the main correlations to calculate the mean

diameter of the droplets and their mean velocity. Following with the 3 steps simulation coupled to simulate a portion of the full atomizer.

Finally, the novel interface-curvature analysis proposed by [Palanti et al., 2022] is explained and further developed to incorporate velocity distribution on chapter 5. It is applied to both, the CHAiRLIFT airblast atomizer and the academic simplex swirl atomizer and compare with available experimental measurement.

2 | Numerical methods for spray atomization

Several numerical approaches can be used to model the spray atomization process. Regarding the spray phase zone and the kind of atomizer under study one or another method can be more suitable. On this chapter the main multiphase approaches are reported emphasizing the context and then methods applied on this work. Finally, the methodology which is developed in this work to address the complex aeronautic injectors is explained.

Contents

2.1	Multiphase spray atomization modelling	9
2.1.1	Dense region: DNS-ICM approach	10
2.1.2	Transition region: LES approach	12
2.1.3	Dilute region	14
2.2	A Volume of Fluid based LES approach	16
2.2.1	The interFoam solver	16
2.2.2	LES turbulence modelling	18
2.3	Numerical simulation set up	19
2.3.1	Discretization schemes	19
2.3.2	Boundary Conditions	20
2.4	CHaIRLIFT configuration modelling	21

The atomization phenomena has been studied both, experimentally and numerically during the last decades. Nowadays, many models have been proposed, but nevertheless, studies such as [Mirjalili et al., 2017, Saurel and Pantano, 2018] collects modelling techniques used as a generic multi-phase models.

The atomization process takes place when two immiscible phases, one liquid and another one gaseous, which are part of the same fluid system, are interacting at different velocities to eventually form a spray. The flow field has been classically divided into three main regions [Lefebvre and McDonell, 1988]. The dense phase zone where primary breakup forms the first coherent liquid structures; at the opposite the dilute phase zone where polydisperse spray

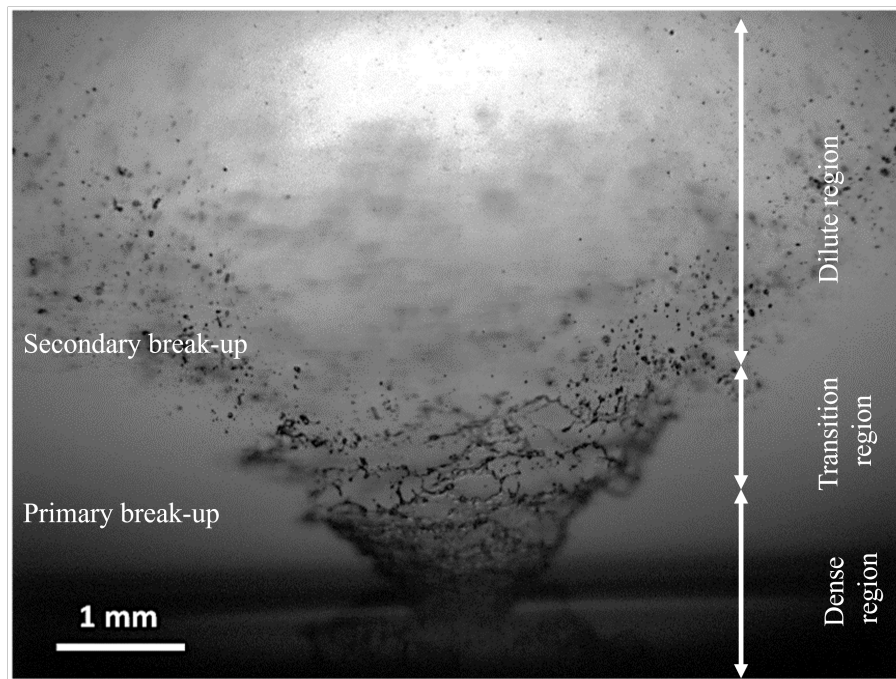


Figure 2.1 – Picture of the spray expelled from the CRSB injector by [Verdier, 2017]. The dense, transition and dilute zones and the primary and secondary break-up are plotted.

is finally found and in between, there is a third phase zone, the transition zone where the break-up of most liquid structures takes place. The three zones are shown on Figure 2.1.

There are two main break-up processes. The first one known as primary break-up transforms the continuous liquid flow into structures such as ligaments or even big droplets. Depending on the fluid properties and the velocity of the gaseous and liquid flow, a second break-up can take place: for instance, when the drag forces over the liquid structures are much higher than the surface tension forces ligaments or big droplets are broken-up into smaller liquid structures until surface tension stabilised droplets and viscosity dissipate liquid structure agitation.

The atomization process is a hard problem to resolve mathematically speaking due to the numerous physical phenomena involved and the wide range of liquid structures. Thus, some models have been developed to address one problem in particular not solving the others. Therefore, choosing the perfect model is not clear and/or straightforward. The complete and direct description is mostly based on the Navier-Stokes (N-S) equations, extended to liquid gas flows. On this chapter the main models are presented and the one used on this work is explained on detail. Since the aim of this work is to study the atomization process on industrial atomizers the main effort has not been to develop new numerical approach. Accordingly, state of the art approaches have been chosen to established a trade off between precision, complexity and the level of detail available. Last chapter, base on these choices will develop an adapted analysis to reconstruct final spray characteristics.

The second part of this chapter is focused on the numerical methods directly applied to the simulations. The OpenFOAM v6 toolbox has been used on every numerical simulation carried out on this thesis. The chosen solver, the discretization schemes as well as the boundary conditions applied are reported.

2.1 Multiphase spray atomization modelling

In principle, solving directly the N-S equation would allow for the complete description of the atomization and injection processes. However, the large range of length and time scales makes this approach practically intractable. Thus, the adopted approach depends on the region to study. A sketch of the atomization phenomena linked to the dynamic approach chosen is shown on Figure 2.2. From left to right we can observe that we go from a DNS (Direct numerical simulation) approach, where all dynamic scales are resolved and the liquid jet has not broken-up jet. This first steps of the atomization process (primary break-up) are capture with the so-called, interface capturing methods (ICM). Beyond this point, liquid-gas interface length scale are reaching the level of mesh refinement, thus to capture the interface is not feasible. Thus, a kind of LES (Large Eddy Simulation) formalism is used to model the dynamic sub-grid scales. The interface between liquid and gas has to be modelled at sub-grid level. Finally, once the spray is fully developed and the droplets are dispersed Lagrangian or Eulerian, two-fluid models and stochastic systems, based on the well-known Williams-Boltzmann equation (WBE) are more suitable [Pope, 1985, Simonin et al., 1993].

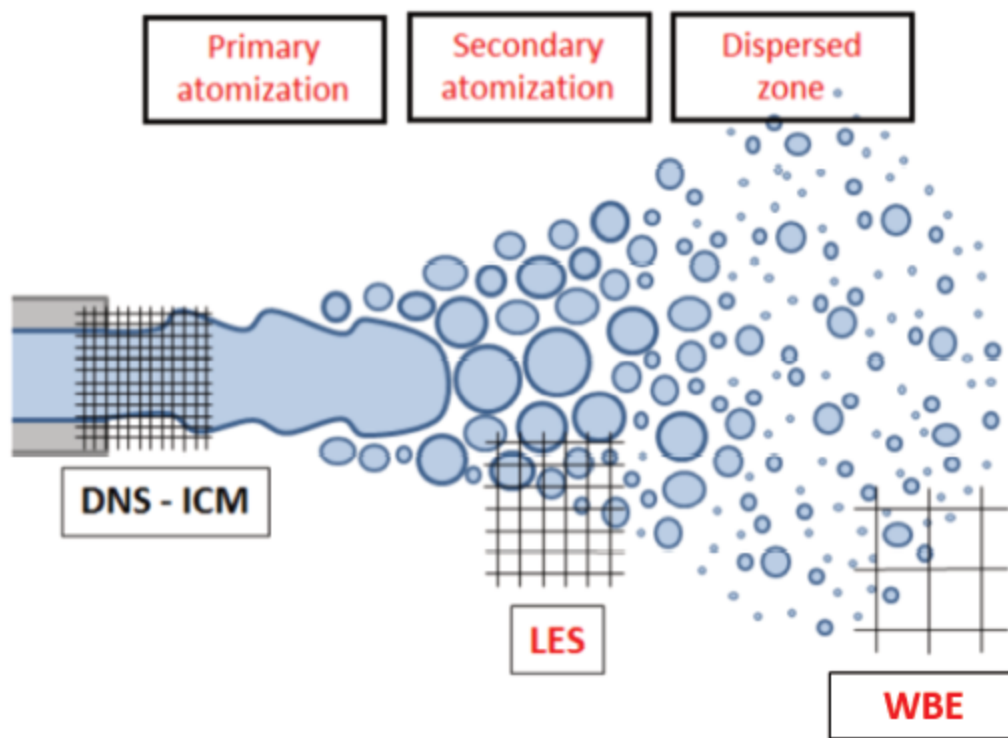


Figure 2.2 – Atomization zones by dynamic modelling approach [Añez, 2019].

The aim of this thesis is to predict spray characteristics issued of complex Gas Turbine (GT) injectors to initiate combustion studies. With respect of the Diesel or Gasoline injection where the liquid dispersion and the density of liquid-gas surface are mostly sufficient to determine evaporation and thus combustion [Lebas et al., 2005], it is expected that GT injection system will be more sensitive to the detail of spray distribution. At the present time there is no proposal for atomization modelling of such detail at sub-grid level, thus ICM approach are necessary. Accordingly, it is expected to model the transition zone where the primary break-up takes place up to a point where spray characteristic can be inferred. Starting from a DNS point of view where a ICM is used, it is necessary to carry on, modelling the

break-up process keeping the capturing of the droplet interface as far as possible up to the LES zone. To complete this effort a dedicated analysis based on the liquid-gas interface and curvature is proposed (see chapter 5) to extract the statistical information of the spray that could be used to set up a stochastic system based on WBE.

2.1.1 Dense region: DNS-ICM approach

These methods are characterized for being able to reconstruct the surface interface between the gaseous and liquid phases. The aim is to capture the spray primary break-up to study the generation of smaller liquid structures such as ligaments or droplets. Among other, there are three main interface capturing approaches: Front Tracking methods [Unverdi and Tryggvason, 1992], Level Set methods [Sussman et al., 1994] and Volume of Fluid methods [Gueyffier et al., 1999].

Front Tracking methods

Inside of a eulerian-lagrangian framework, [Unverdi and Tryggvason, 1992] propose to use Lagrangian particles as markers that are connected along the interface. Those markers will represent the interface between liquid and gas and they will be carried by the flow (see Figure 2.3). The liquid gas flow itself is resolved on a fixed mesh where any interaction at the interface used surface markers. For instance, the surface tension is solved at the interface level with Lagrangian markers and later transfer to Eulerian phase.

This method has been used to model incompressible viscous flows [Unverdi and Tryggvason, 1992], multiphase flows [Tryggvason et al., 2001] and phase change flows [Juric and Tryggvason, 1998, Tryggvason and Lu, 2015].

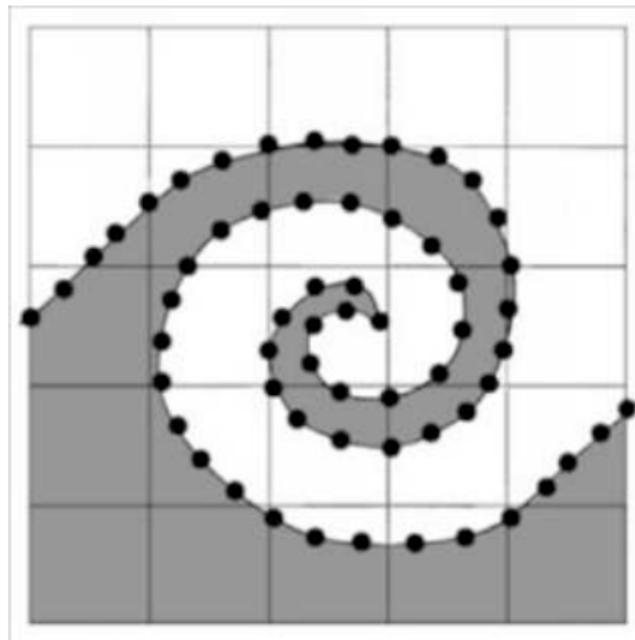


Figure 2.3 – Front tracking method example [Scardovelli and Zaleski, 1999].

The great advantage of this kind of methods is the direct reconstruction of the interface from the position of the markers. However, markers have to be distributed homogeneously and their position has to be adapted at each time step accounting also for connection/disconnection related to coalescence and breakup. Geometrical properties such as the normal or the curvature of the liquid structure are not straightforward to compute [Lin et al., 2019].

Level-set (LS) method

The level-set method [Osher and Sethian, 1988, Sussman et al., 1994, Sethian, 1999] is a method for implicit description of moving fronts. The basic idea is that the front location is given as the zero level set of an auxiliary field defined over the domain of interest. The distance function ϕ is a common choice, it is solve trough a convection function:

$$\frac{\partial \phi}{\partial t} + \mathbf{u} \nabla \cdot \phi = 0 \quad (2.1)$$

The interface is found for $\phi = 0$. Positive values of ϕ correspond to the distance from the interface inside on the liquid. On the contrary, negative values of ϕ represent the distance from the interface on the gas (see Figure 2.4).

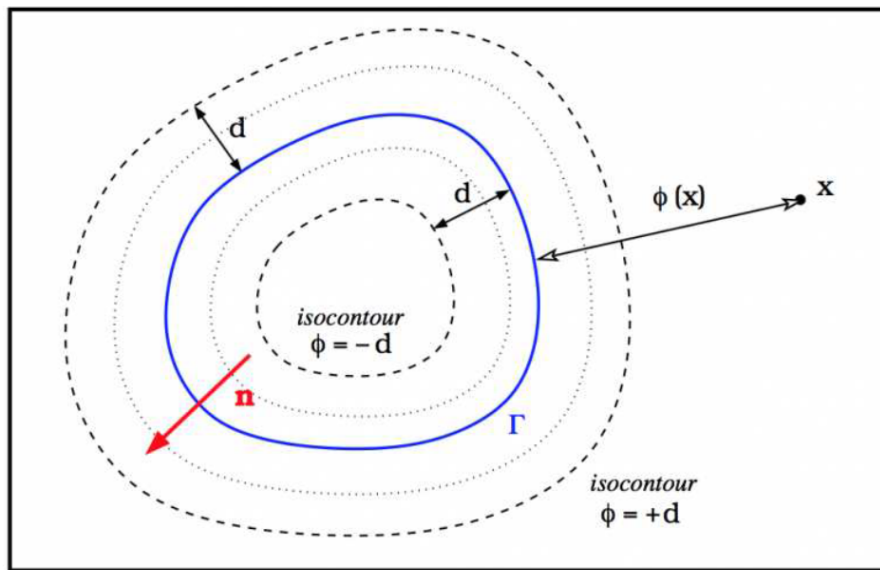


Figure 2.4 – Level-set method representation. On blue: iso-contour for $\phi = 0$ representing the interface [Canu, 2019].

Solving Equation 2.1 does not preserve the distance property of ϕ . Thus, a re-distancing algorithm should be applied in order to return to a mathematically valid distance function [Sussman et al., 1994]. This approach reconstruct accurately the interface and allows to compute its properties such as the normal and the two main curvatures κ_1, κ_2 . Nevertheless, the re-distancing process causes liquid mass losses.

Volume of fluid (VOF) method

The volume of fluid method [Hirt and Nichols, 1981] introduces the liquid volume fraction α concept. This variable measures the volume of liquid inside of a computational cell. Therefore, if $\alpha = 1$ the cell is fulfilled with liquid, and on the other hand, for $\alpha = 0$ the cell corresponds to the gaseous phase (see Figure 2.5). It is describe by a convection equation for the liquid volume fraction:

$$\frac{\partial \alpha}{\partial t} + \nabla \cdot (\mathbf{u} \alpha) = 0 \quad (2.2)$$

This method allows for using finite volume method to enforce the conservation of the liquid mass. In the context of separated phases approach, it is necessary to apply the jump conditions on an actual discontinuity located at the interface, this holds in particular for the liquid volume flux. To capture the interface, it requires to reconstruct it. There are

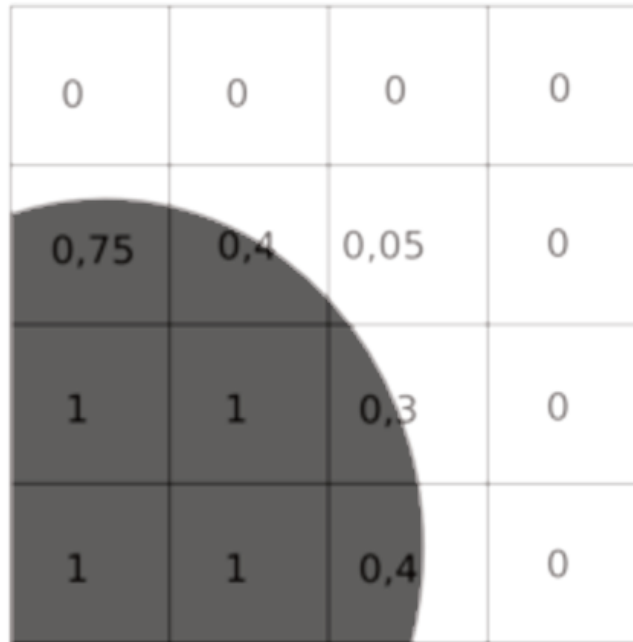


Figure 2.5 – Volume of fluid method representation.

several methods such as geometric reconstruction. The simplest one is the Simple Linear Interface Calculation (SLIC) [Noh and Woodward, 1976, Noh and Woodward, 2005] that fits the interface with a 1st order function, keeping the interface parallel to one of the coordinate of the numerical domain. There are more accurate geometry reconstruction such as Piecewise Linear Interface Calculation (PLIC) which in a similar way than SLIC, it represent the surface interface by lines but oriented according to the interface normal [DeBar, 1974, Youngs, 1984, Skarysz et al., 2018].

Coupled Level-Set Volume of Fluid method (CLSVOF)

To overcome the weaknesses of LS and VoF methods, a coupled level-set volume of fluid (CLSVOF) method was introduced by [Skarysz et al., 2000] and later improved by [Ménard et al., 2007]. It has been used in many studies [Mukundan et al., 2019, Guo et al., 2014]. The advection equation of α is solved together with the level-set equation. By connecting these two approaches, a mass conservative model with an accurate definition of the interface is achieved.

2.1.2 Transition region: LES approach

As the atomization process takes place, smaller and smaller length scale are generated. For complex injection system, eventually performing DNS computations is not longer a possibility due to the computational resources requirement. Therefore, a coarse mesh definition has to be applied with respect to the length scale of the flow, and hence, a LES formalism to model the unresolved scales is required. Pioneering work in the direction of modelling the flow dynamic of multiphase flow including interface and accounting for density jump problems have been done in Reynolds Average Navier-Stokes (RANS) [Vallet and Borghi, 1999, Burluka and Borghi, 2001, Demoulin et al., 2001]. Then, following the LES approach the incompressible mixed phases conservation equations can be filtered alongside with the liquid volume fraction transport equation. The description of the filtered equation will follow previous works by [Chesnel et al., 2011, Puggelli, 2018]:

- Mass transport equation:

$$\nabla \cdot (\bar{\mathbf{u}}) = 0 \quad (2.3)$$

- Momentum transport equation:

$$\frac{\partial \bar{\rho} \bar{\mathbf{u}} + \tau_{\rho u}}{\partial t} + \nabla \cdot (\bar{\rho} \bar{\mathbf{u}} \times \bar{\mathbf{u}} + \tau_{\rho uu}) = -\nabla \bar{p} + \bar{\mu} \nabla \cdot (\nabla \bar{\mathbf{u}} + \tau_S) + \bar{\rho} \mathbf{g} - \tau_\sigma \quad (2.4)$$

- Liquid volume fraction transport equation:

$$\frac{\partial \bar{\alpha}}{\partial t} + \nabla \cdot (\bar{\mathbf{u}} \bar{\alpha} + \mathbf{R}_\alpha) = 0 \quad (2.5)$$

where the unclosed terms can be defined as: $\tau_{\rho u} = \bar{\rho} \bar{\mathbf{u}} - \bar{\rho} \bar{\mathbf{u}}$ represents the sub-grid contribution to the temporal term in the momentum equation [Tavares et al., 2015, Vincent et al., 2018]. $\tau_{\rho uu} = \overline{\rho \mathbf{u} \times \mathbf{u}} - \bar{\rho} \bar{\mathbf{u}} \times \bar{\mathbf{u}}$ which is similar to the sub-grid stress term on single phase flow. It is expected to have a particular behaviour due to the high density variation. $\tau_S = \overline{\mu \nabla \mathbf{u}} - \bar{\mu} \nabla \bar{\mathbf{u}}$ is the sub-grid term of laminar viscous forces. $\tau_\sigma = \overline{\sigma \kappa \mathbf{n} \delta_S}$ is related to the surface tension force. $\mathbf{R}_\alpha = \overline{\mathbf{u} \alpha} - \bar{\mathbf{u}} \bar{\alpha}$ represents the contribution of the under liquid motion that is approximated certain approach (ELSA) by a sub-grid liquid dispersion.

All these terms requires model in order to close the transport equations. Practical closure are still missing for multi-phase flows, so many one-fluid formalism closures have been tested by several authors [Christensen and Deigaard, 2001, Lubin et al., 2006, Añez, 2019, Ahmed, 2019] among others. We have decoupled the description of flow dynamic to the surface representation. This is often the case in many applications in the literature: once an approach has been designed with a liquid-gas surface representation, it is attracting to complete the approach with classical modelling for the flow dynamic based mostly on single phase turbulence models. There are two main reasons. Firstly, the turbulence in liquid-gas flows is very complex and not fully elucidated yet. Secondly, there are many cases where such separation gives good results. However, the coupling between the dynamic of the flow and of the interface is most probably a reality as suggested by the analysis of the unclosed terms. From the work of [Vallet and Borghi, 1999] it is possible to represent certain surface phenomena such as the liquid dispersion and the turbulent liquid flux which would lead into the Eulerian-Lagrangian Spray Atomization (ELSA) model.

Eulerian-Lagrangian Spray Atomization (ELSA) model

This approach was introduced by [Vallet and Borghi, 1999] and is based on the mixed phases formulation supplemented by the liquid volume fraction equation to represent the liquid and gas phase behaviour. This approach has been mostly used for iso-thermal flow, where the energy equation is not considered, but it is possible to include energy also [Lebas et al., 2009].

Another transport equation for a new variable is added, namely the interface area density Σ . This variable considers the portion of interface area in a certain volume. The interface area density transport equation by [Anez et al., 2019] is:

$$\frac{\partial \bar{\Sigma}}{\partial t} + \nabla \cdot \bar{\mathbf{u}} \bar{\Sigma} + \nabla \cdot \mathbf{R}_\Sigma + S_\Sigma = 0 \quad (2.6)$$

where $\mathbf{R}_\Sigma = \overline{\Sigma \mathbf{u}} - \bar{\Sigma} \bar{\mathbf{u}}$ and the source term is modelled following the restoration of equilibrium among the liquid and the gas subjected to turbulence motion as $S_\Sigma = \frac{\bar{\Sigma}}{\tau_{eq}} \left(1 - \frac{\bar{\Sigma}}{\Sigma_{eq}} \right)$ where τ_{eq} .

To solve spray atomization process near to the nozzle and including the droplet dispersion, a coupling between the interface capturing methods and the ELSA approach was developed by [Anez et al., 2019].

ICM-ELSA approach

In order to extend the range of application of the ELSA approach and to capture the early stage of the atomization process through interface capturing methods and the later dispersion of the droplets on a sub-grid framework, a coupling between VoF (with ICM) and ELSA is presented. The main idea is to switch from one approach to another depending on the spray region. The concept of Interface Resolution Quality (IRQ) was introduced by [Anez et al., 2019] and they measure if the computational mesh resolution is sufficient to compute some characteristics by the ICM approach.

The IRQ_{Σ} relies on the interface area resolved and it is defined as the ratio of the minimum interface area resolved (Σ_{min}) given a certain amount of liquid volume fraction to the actual interface area (Σ):

$$IRQ_{\Sigma} = \frac{\Sigma_{min}}{\Sigma_{min} + \Sigma'} = \frac{\Sigma_{min}}{\Sigma} \quad (2.7)$$

We can define a threshold corresponding to the proportion of interface resolved. This IRQ is close to unity where most of the interface is described at the mesh resolution (Σ_{min}) and goes to zero when most of the interface area is at the sub-grid level (Σ') (see Figure 2.6).

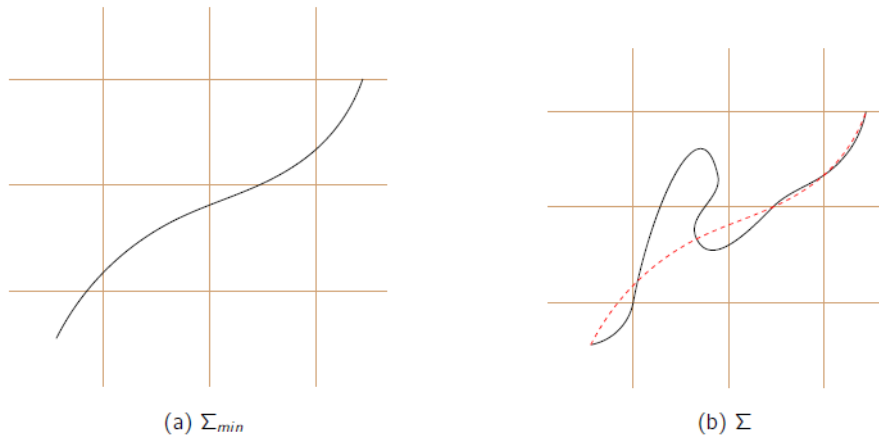


Figure 2.6 – Interface among fluid and gas. On the left the minimum interface Σ_{min} is represented meanwhile on the right the real interface Σ is shown. The difference of surface is Σ'

The IRQ_{κ} It is based on a geometrical property of the interface: the curvature. In [Canu et al., 2019] two possible formulations of the parameter have been proposed:

$$IRQ_{\kappa} = \frac{1}{\Delta X |\kappa_1 + \kappa_2|} \quad (2.8)$$

$$IRQ_{\kappa}^{max} = \frac{1}{2\Delta X \max(|\kappa_1, \kappa_2|)} \quad (2.9)$$

For more detail the reader should read [Canu et al., 2019].

2.1.3 Dilute region

Disperse flows, consist of well defined particles (disperse phase), distributed in a connected volume of continuous phase. The coupling between the particle and its surroundings can be used to classify and choose the appropriate numerical technique. As shown on Figure 2.7,

a multiphase flow can be considered dispersed, if the effects of particle-fluid interactions dominates the overall transport of particles. On the contrary, if particle-particle motion dominates, the flow can be considered to be dense. Dispersed flow, could be classified as:

- One-way coupling: The dispersed-phase motion is affected by the continuous phase but the dispersed-phase does not affect the continuous phase.
- Two-way coupling: The dispersed-phase and the continuous phase affect each other.
- Three-way coupling: Particle wakes and continuous phase disturbances affect the particle motion.
- Four-way coupling: Particle collisions and particle wall interaction dominate the particle motion.

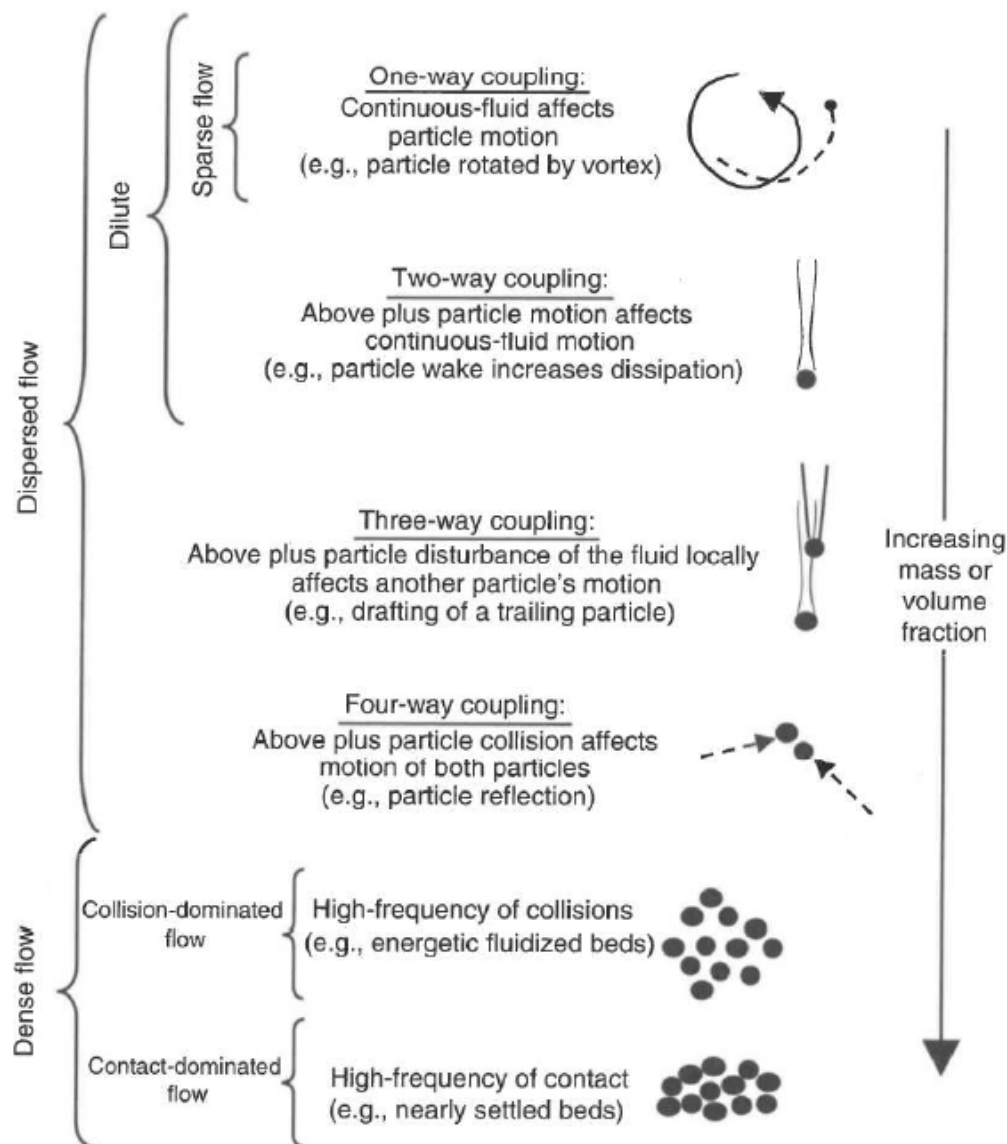


Figure 2.7 – Dilute, dispersed, and dense flow conditions based on various interphase coupling [Crowe, 2005]

From the numerical point of view, there are two modelling approaches prevalent in disperse flows, namely trajectory models and two-fluid models, [Brennen, 2005]. In the former, the motion of the disperse phase is assessed by following either the motion of actual particles,

or larger representative particles. In this case, a discrete method, normally referred to as Lagrange method, is applied on each droplet (or representative droplet), in which droplet properties are update along the path of an individual (or cloud of) droplets. In the latter modelling approach, two-fluid models, the discrete phase is treated as a second continuous phase on which conservation equations (of mass, momentum and energy) are developed for the two-fluid flow. This modelling approach, is also referred as multiphase approach, in which an Eulerian treatment describes the droplet concentration through a droplet volume fraction, which is the fraction of computational cell composed of droplets. Treatment selection is highly dependent on the droplet number density, N_p , see figure 2.2. Normally, Lagrangian treatment is preferred for nondeforming droplets, in which high accuracy of the interface discontinuity is desired, however, the Eulerian treatment is more efficient in terms of droplet breakup or coalescence. There is a third approach, which uses particle distribution functions (PDF approach), to describe the particle flow properties in stochastic systems, based on the well-known Maxwell-Boltzmann equation [Pope, 1985, Simonin et al., 1993]. More information about the Lagrangian, Eulerian, and PDF treatment on droplet field can be found in [Crowe, 2005, Brennen, 2005].

2.2 A Volume of Fluid based LES approach

The main approaches to model the spray atomization process have been reported on the last section. As we have seen, choosing one or another depends on the nature of the flow, the available numerical resolution, the zone of atomization and the expected level of description. On the scope of this work, the first steps of the atomization mechanism wants to be studied. From the nozzle injection through the primary break-up up to the first generation of droplets not reaching the disperse zone. Thus, an approach with an ICM should be used. As we have seen, those approaches are applied, in general, with a DNS approach for dynamic. In this case, since we want to reach the transition zone (see Figure 2.1) and since the computational cost is very important, we have opted for LES description of the dynamics. Nevertheless, the main concept of this study is to have an almost DNS mesh resolution around the liquid structures to be able to capture the interface through the ICM and a coarser mesh farther treating the gaseous phase on those zone with the LES approach.

The ICM-ELSA model could be an option regarding these requirements but this approach does not incorporate yet enough information to determine the characteristic of the spray distribution. Following [Palanti et al., 2022], an ICM approach is used to capture the interface at a level sufficient to get the surface curvature distribution from which an analysis will be develop to determine early the characteristic of the final spray.

This approach to be applied on complex injection system required a robust solver. The open source OpenFOAM toolbox is used, in particular the version 6 [Greenshields, 2019] where its multiphase solvers has been used on plenty of similar works such as [Ahmed, 2019, Remigi, 2021, Piscaglia et al., 2019, Anez et al., 2019].

2.2.1 The interFoam solver

The `interFoam` solver is a incompressible isothermal multiphase pressure based solver for two immiscible phases. It is based on the Volume of Fluid method with an interface capturing method [Deshpande et al., 2012, Greenshields, 2019]. The LES filtered equation solved by `interFoam` are:

- Mass transport equation:

$$\nabla \cdot (\bar{\mathbf{u}}) = 0 \quad (2.10)$$

- Momentum transport equation:

$$\frac{\partial \bar{\rho} \bar{\mathbf{u}}}{\partial t} + \nabla \cdot (\bar{\rho} \bar{\mathbf{u}} \times \bar{\mathbf{u}}) = -\nabla \bar{p} + \bar{\mu} \nabla \cdot (\nabla \bar{\mathbf{u}}) - \nabla \cdot \boldsymbol{\tau}^R + \bar{\rho} \mathbf{g} - \boldsymbol{\tau}_\sigma \quad (2.11)$$

- Liquid volume fraction transport equation:

$$\frac{\partial \bar{\alpha}}{\partial t} + \bar{\mathbf{u}} \nabla \cdot \bar{\alpha} = -\nabla \cdot [\mathbf{u}_c \bar{\alpha} (1 - \bar{\alpha})] \quad (2.12)$$

The $\boldsymbol{\tau}_\sigma$ term on Equation 2.11 models the surface tension forces. Since the interface capturing is resolved, it can be done directly with the curvature and the normal: $\boldsymbol{\tau}_\sigma = \sigma \kappa \nabla \alpha$ where the normal of the interface is $\mathbf{n} = \nabla \alpha / |\nabla \alpha|$ and the mean curvature is $\kappa = -\nabla \cdot \mathbf{n}$ [Brackbill et al., 1992]. The term on the right side of the liquid volume fraction transport equation is a compression term which keeps the interface sharp through the liquid and gas. It creates a counter flux with the velocity \mathbf{u}_c that for definition is $\mathbf{u}_c = C_\alpha |\mathbf{u}| (\nabla \alpha / |\nabla \alpha|)$ [Rusche, 2002]. C_α is then simply a binary coefficient which switches interface sharpening on (1) or off (0). A study of the effect of varying this parameter can be found on [Wardle and Weller, 2013].

PISO algorithm

The velocity-pressure coupling is solved by the PISO (Pressure-Implicit with Splitting of Operators) algorithm. Representative of a low Mach number approach, the solution of the system is found by solving in an iterative manner the equations for velocity and for pressure (see Figure 2.8).

- **Velocity predictor:** Based on the solution of the previous time step, a predicted velocity field is calculated. This step is not mandatory but helps in the convergence process.
- **Compute pseudo-velocity:** With the predicted velocity field or with the previous time step velocity field, the momentum equation is solved not taking into account the pressure gradient. This is the first step of the classical projection methods [Chorin, 1968].
- **Pressure direct solution:** The pressure at the current time step is obtained by solving the Poisson equation obtained by taking the divergence of the correction equation and enforcing the mass conservation, in our case it reduces to ensure a divergence free velocity field.
- **Explicit velocity corrector:** The new pressure has been computed and the velocity can be corrected.
- **Flux corrector:** The flux must be corrected taking into account the pressure computation.

For more detailed information refer to the original work by [Issa et al., 1986] and for the implementation on OpenFOAM to [Holzmann, 2020].

MULES algorithm

The pressure-velocity coupling is solved using the PISO algorithm described previously, while it is necessary to add a method for solving the equation of liquid volume fraction. OpenFOAM uses its implementation of the Multidimensional Universal Limiter for Explicit Solution (MULES) [Boris and Book, 1968, Zalesak, 1979] which is an Flux-Corrected Transport (FCT) algorithm. The purpose of the MULES algorithm is to guarantee the boundedness of the solution of hyperbolic problems.

The principle of FCT is that given a transport equation for a variable ϕ :

$$\frac{\partial \phi}{\partial t} + \nabla \cdot \mathbf{F} = 0 \quad (2.13)$$

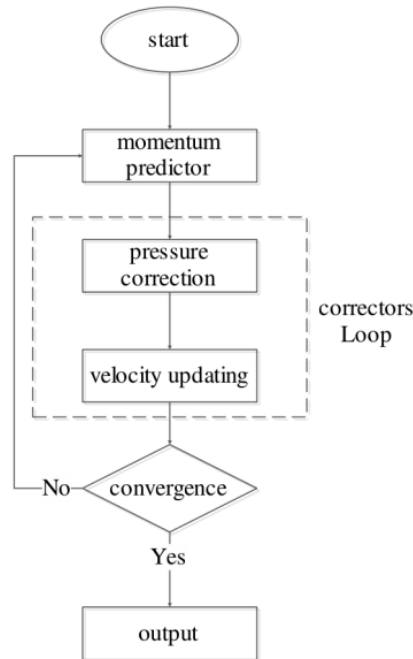


Figure 2.8 – Detail of SIMPLE and PISO algorithms [Mughal, 2016].

Considering a 1D case, given the index i that determines the cell and n the temporal step, Equation 2.13 can be discretized as:

$$\frac{\phi_i^{n+1} - \phi_i^n}{\Delta t} V + \sum_f (\mathbf{F}^n \cdot \mathbf{S})_f = 0 \quad (2.14)$$

Isolating the center of a cell labelled as i , it is possible to write (as for a Godunov first order accurate scheme [LeVeque, 1992]):

$$\phi_i^{n+1} = \phi_i^n - \frac{\Delta t}{V} (F_{i+1/2}^n - F_{i-1/2}^n) \quad (2.15)$$

The boundedness of the temporal solution can be obtained via face value limiting, or limiting face fluxes. A classical Total Variation Diminishing (TVD) scheme algorithm is defined as following:

- Compute F^L , flux computed with a low order scheme.
- Compute F^H , flux computed with an high order scheme.
- Define an anti diffusive flux $A = F^H - F^L$.
- Compute a corrected flux $F^C = F^L + \lambda_i A$, with λ_i defined for each cell and called flux limiter [LeVeque, 2002].
- Solve the equation:

$$\phi_i^{n+1} = \phi_i^n - \frac{\Delta t}{V} (F_{i+1/2}^C - F_{i-1/2}^C) \quad (2.16)$$

2.2.2 LES turbulence modelling

In order to close Equation 2.11 it is necessary to model the Reynolds stress tensor τ^R that represents the effect of sub-grid unresolved flows.

In gas kinetics theory, molecular agitation draws energy from the flow by way of molecular viscosity. So the energy cascade mechanism [Sagaut, 2006] will be modelled by a

term having a mathematical structure similar to that of molecular diffusion, but in which the molecular viscosity is replaced by a sub-grid viscosity ν_{sgs} .

There are several sub-grid scale models, among them, the Smagorisky [Smagorinsky, 1963] and WALE (Wall-Adapting Local Eddy-viscosity) [Nicoud and Ducros, 1999] have been tested on this work. Finally, due to the fact that most of the simulation have been performed with complex geometries where walls play an important role, the WALE model was chosen. Its effectiveness has been also proved for this kind of multiphase flows encountered inside injector in previous works such as [Anez et al., 2019, Ahmed, 2019] among others.

For reasons connected with the near wall behavior of the subgrid-scale model, a new operator based on the traceless symmetric part of the square of the velocity gradient tensor S_i^d is used. Consequently, the sub-grid scale viscosity is modelled as [Nicoud and Ducros, 1999]:

$$\nu_{sgs} = (C_w \Delta)^2 \frac{(S_{ij}^d S_{ij}^d)^{3/2}}{\left((\bar{S}_{ij} \bar{S}_{ij})^{5/2} (S_{ij}^d S_{ij}^d)^{5/4} \right)} \quad (2.17)$$

where C_w is a model constant and \bar{S}_{ij} is the resolved-scale strain rate tensor. As reported in [Ducros et al., 1998] WALE model shows better results in predicting near wall turbulence for wall bounded flows. No wall damping is necessary near wall regions in WALE model. Another study in channel separated flow performed by [Frohlich et al., 2005] shows that best match with DNS can be obtained using WALE model. The main difference between this model with respect to other like Smagorinsky model, is its ability to catch flow instabilities at a given resolution that would require finer mesh resolution with other approaches. Thus, even if this approach has not been developed specifically for multiphase flows, it helps to limit the require mesh resolution for wall flow.

2.3 Numerical simulation set up

On last section the numerical and physical approaches adopted to model ur turbulent liquid gas flows have been resumed. In addition, the transport equations have to be discretized in order to be solved. Moreover, proper boundary conditions are required to solve the later partial differential equations (PDEs). A compilation of the discretization schemes and the boundary conditions used on the different simulation within this thesis are reported below. Later, on chapter 3 and on chapter 4 the specific numerical details dedicated to each application will be given.

2.3.1 Discretization schemes

The discretization schemes play an important role on accuracy and robustness. OpenFoam is an open-source code though for industrial purposes, hence, it includes robust numerical methods up to second order than can be applied on general polyhedral mesh to assure computations on complex geometries. On this section numerical schemes used during this thesis are presented.

Temporal schemes

Three temporal schemes are already implemented on OpenFOAM: Implicit Euler, Crank-Nicolson and 3-step backward.

The implicit Euler [Ferziger and Peric, 1996] is stable and bounded but very diffusive due to its first-order nature. The Crank-Nicolson is a second-order scheme which is implicit and bounded.[Crank and Nicolson, 1947]. It combines Euler first order implicit and explicit

with a blending factor to reach second order. However stability can be an issue and the blending factor can be modified to be closer to the implicit scheme but at the cost to reduce the order of stability. The 3-step backward scheme is second-order accurate but does not ensure boundedness and can not be selected to discretized the time derivative term for variables that must be bounded; on this case, for the α equation. More information about the implementation of such schemes on OpenFOAM is available by [Greenshields, 2019, Monroy and Seng, 2017].

The implicit Euler scheme has been used for initialization. The 3-step backward scheme has been used to discretize the temporal term on the continuity and momentum equations. On the other hand, the Crank-Nicolson scheme has been applied to the liquid volume fraction equation.

Spacial schemes

OpenFoam is based on finite volume approach to benefit of conservative description of fluxes. To take advantage of this properties divergence terms are approximated through fluxes at cell faces thanks to the Gauss-Ostrogradsky theorem. To activate this properties in OpenFOAM the keyword *Gauss* is used on numerical scheme definitions. The convection and divergence terms on the continuity and momentum equations are discretized by the upwind scheme (bounded first order scheme) to initialize the cases and changed to the *limitedLinear* (linear interpolation coupled with a limiter leading to first-second order) scheme once the simulation has reached the operating conditions. This scheme is the linear scheme limited to assure the robustness of the numerical calculation [Greenshields, 2019]. Ideally, the linear scheme should be used but due to the non-isotropic nature of the computational grids it is not possible.

To discretize the spacial terms on the liquid volume fraction equation the Van Leer [van Leer., 1974] scheme is applied.

2.3.2 Boundary Conditions

For each numerical simulation the boundary conditions applied are mostly the same. Thus, a summary of them are collected on this section for the velocity \mathbf{u} , the pressure p and the liquid volume fraction α

To set a boundary patch with a certain value, uniform or non-uniform across the patch, OpenFOAM applies the *fixedValue* boundary condition. It is a Dirichlet boundary condition which fix the value of the variable $\phi_{BC} = v$. Some variation of this conditions are also used.

The *timeVaryingMappedFixedValue* condition maps given values to the boundary patch. It interpolates linear on time and on space the values linked to a certain time in such a way each time step the value of the variable varies $\phi_{BC}(t) = v(t)$.

The *flowRateInletVelocity* computes the value of the velocity normal to the face for a given mass flow rate $\mathbf{u}_{BC} \cdot \mathbf{n} = \dot{m}/(\rho A_{face})$. It is restricted to the velocity.

The *totalPressure* condition sets the static pressure at the patch p_{BC} based on a specification of the total pressure, p_0 .

$$p_p = p_0 - \frac{1}{2}|\mathbf{u}|^2 \quad (2.18)$$

The velocity-pressure coupling requires that when one of the variables is set up with a Dirichlet boundary condition ($\phi = v$) the other one has to be set up as a Neumann boundary condition ($\partial\phi/\partial x = v$) [Ferziger and Peric, 1996]. Thus, each time one of the previous boundary conditions is applied to the velocity or the pressure, the *zeroGradient* conditions is applied to the other. This conditions sets the value of the variable gradient to zero $\partial\phi/\partial x = 0$.

The wall boundary condition is used on solid surfaces. This conditions sets to zero the three components of the velocity $\mathbf{u}_{BC} = 0$ and the gradient of the pressure $\partial p / \partial x = 0$.

The symmetry boundary condition sets to zero the normal component of the velocity to the surface and the gradient of the other components of the velocity and the pressure.

The cyclic conditions is the classical periodic boundary conditions which fixes the values of the faces of one patch to another patch. This boundary conditions has been used when the domain is restricted to a portion of the total geometry, in particular for sectorial simulations.

2.4 CHAiRLIFT configuration modelling

The air-blast atomizers involve a wide range of length scales. The order of magnitude of the diameter of the studied atomizer is four times bigger than the diameter of the smallest droplet expelled from it. This fact enforces difficulties for the multi-phase approach modelling. As is explained on the last section, the volume of fluid method with an interface capturing method, needs a high resolution mesh around the interface between gas and liquid. If the computational domain is big, the number of numerical cells required to mesh it increases hugely since the characteristic length of the smallest cell has to be at least four to eight times smaller than the diameter of the smallest droplet. This leads to several problems such as the requirement of high computational resources, the increase of complexity of the computational domain and the problems of storage for necessary data to post-process the spray characteristics.

The solution adopted is to split the total domain into smaller pieces. Each physical phenomena is treated and analyzed separately to decrease the computational time and reduce the computational resources. On the other hand, with this methodology it is mandatory to perform a good coupling between each part. This methodology was previously adopted to model the experimental planar prefilmer by [Gepperth et al., 2010]. Works such as [Sauer et al., 2014, Warncke et al., 2017, Palanti et al., 2022] proposed a three simulation coupling to carry out the modelling. First, a single phase flow simulation to compute the air flow into the whole experimental set-up. Afterwards, one of the two air channels is simulated using a LES approach with a high refinement grid and from time to time, data of the velocity is stored at a transverse plane location, to later on, map the two phase simulation domain. Finally, the third and last simulation is a two phase flow simulation that models a portion of the total planar prefilmer. The inlet data for the air velocity is mapped from previous simulation. In this work, this multi-scale, multi-simulation procedure is adapted to the real atomizer of CHAiRLIFT project.

Figure 2.9 shows a sketch of the airblast atomizer divided on five smaller parts. The first one is the simplex swirl atomizer. This atomizer injects the fuel into the air-blast system. It atomizes the fuel into a hollow cone shaped spray which spread the fuel into the prefilmer wall. Simulating a swirl injector is a quite complex operation by itself, the present approach is explained on chapter 3 with a similar injector but for which experimental data are available to asses this approach.

The second step is to compute the air velocity on the zone of interest. Therefore, a single phase flow simulation is carried out. To capture the turbulent motion of the flow, a LES simulation with a detailed geometry is performed with a high resolution mesh. The velocity of the air is stored, at run time, on a cross plane and placed behind the prefilmer's lip. This data will be used to set up the premilfing simulation of the atomization.

In parallel, the estimation of the fuel film thickness is done. This characteristic length is strongly linked to the Sauter mean diameter D_{32} (Equation 5.5) being both of the same order of magnitude [Lefebvre and McDonell, 1988]. A two dimensional multiphase simulation

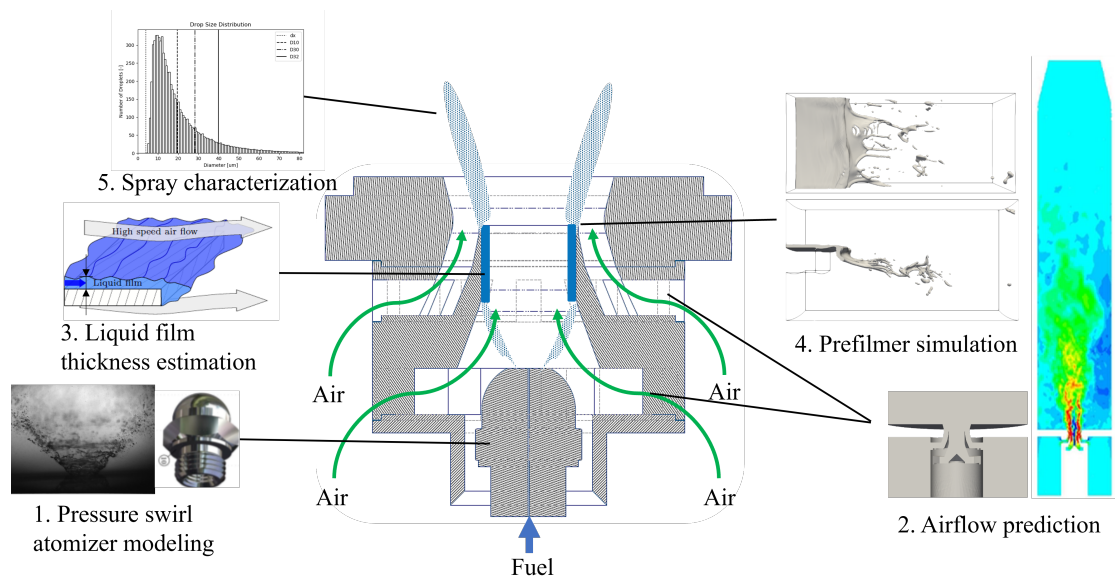


Figure 2.9 – 5 steps workflow followed to model the CHAiRLIFT airblast atomizer.

is proposed to estimate this value. The diameter of the prefilmer is on the order of millimeters meanwhile the liquid film thickness is on the order of tenths of micrometers. This solution achieves a realistic thickness not increasing too much the total computational resources.

The point four is the main simulation of the workflow, the multi-phase prefilming simulation. As it was explained for the planar prefilmer test case, the data recovered from the previous simulations are used to set up the case. The velocity of the air is taken from the point 2 and it is mapped on time and on space to conserve the turbulent motion. The thickness of the liquid boundary is fixed to the value obtained from the point 3. Finally, just a sector of the total circumference is carried out following previous works on air blast atomizers. Points 2, 3 and 4 are explained on chapter 4.

Finally, some data are stored at each time step and are analysed to compute the spray characteristics in particular the joint drop size and the velocity distribution of the spray. Both, the analysis and the results are reported on chapter 5.

3 | CRSB Simplex Swirl Atomizer

On this chapter the numerical modelling of a simplex swirl atomizer is presented. A literature review of the physical processes occurring within simplex atomizers is done at the beginning of the chapter. It is followed by the presentation of the atomizer at study. The atomizer is a commercial atomizer and, therefore, its internal geometry is unknown, hence, the experimental measurements performed to reconstruct the geometry are reported. A first study is performed to simulate the internal flow and to recover some characteristic properties. Nevertheless, this study is not enough to capture the atomization process, thus, a second study focused on the first steps of the atomization process has been carried out.

Contents

3.1	Literature review of simplex swirl atomization	24
3.1.1	Flow inside of the injector	25
3.1.2	Outer flow and atomization process	32
3.2	CRSB simplex swirl injector description	34
3.2.1	Experimental campaigns	34
3.3	Experimental geometry measurements	35
3.3.1	Computed Tomography Scan	36
3.3.2	Optical microscope visualization	36
3.3.3	Scanning electron microscope visualization	38
3.3.4	Measurement results	39
3.4	Modelling the flow inside of the injector	39
3.4.1	Computational hybrid mesh	40
3.4.2	Numerical set up	43
3.4.3	Mesh converge study	45
3.4.4	Discretization schemes	50
3.4.5	Temperature variation	50
3.4.6	Outputs recovery data	54
3.5	External flow modelling: Spray atomization	55
3.5.1	Computational grid	55
3.5.2	Coupling between numerical simulations	58
3.5.3	Outer domain results	59
3.6	Conclusions	66

As reported on chapter 2, the goal of this work is to study the spray atomization performed by the air-blast atomizer used in the CHAIRLIFT burner. The first step of this process is the fuel injection inside of the atomization system by the simplex swirl atomizer. Since no experimental data is available on the CHAIRLIFT simplex atomizer, another similar injector, well-known in the scientific literature, has been studied. The CORIA Rouen Spray Burner (CRSB) injector. The purpose is to define a workflow to model this kind of injectors, to afterwards, being able to repeat the same process with the CHAIRLIFT simplex atomizer.

This chapter reports the numerical study of the CRSB injector carried out in collaboration with the *Universitat Politècnica de València (UPV)*. It begins with a state of the art of the physics and parameters of this kind of injectors. Afterwards, the measurements of the internal geometry of the injector, performed by *UPV* are reported. Following the numerical grid strategy and the modelling of the inner flow. Finally, another numerical study has been performed to capture the atomization process, mapping the data from the internal flow simulation.

At the end of this chapter the results are presented. Mainly qualitative comparison with experiments are shown. Moreover, an analysis of the liquid-gas interface and curvature to reconstruct the drop size distribution is applied to this configuration. The explanation and the results (with experimental comparison [Verdier, 2017, Marrero, 2018]) are reported on chapter 5.

3.1 Literature review of simplex swirl atomization

On simplex swirl atomizers, the orifice outlet of simplex swirl nozzles are preceded by a spin and a swirl chamber as is shown on Figure 3.1. Usually, from two to four feed ports are connected tangentially to the swirl chamber with a certain tilting angle to let the liquid develops swirl motion.

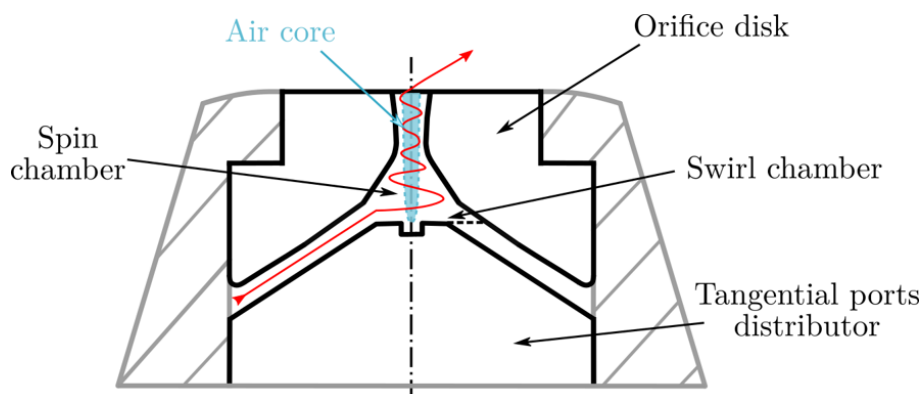


Figure 3.1 – Sketch of main pieces of a simplex swirl atomizer.

The fuel gets into the swirl chamber by the tangential ports where it starts a tangential motion. It is not up to the spin chamber where the fuel develops and increases its swirl motion [Amini, 2016] generating a pressure drop inside of the injector. This pressure drop forces the air to go into the nozzle, creating an air core that, usually, goes from the nozzle orifice up to the bottom of the swirl chamber in function of the Reynolds number Re . Then, the liquid emerges from the discharge orifice as an annular sheet, which spreads radially outward forming a hollow conical spray. The finest atomization occurs at high delivery pressure and wide spray angles [Lefebvre and McDonell, 1988]. Several spray parameters are shown on Figure 3.2 and will be described in the following sections.

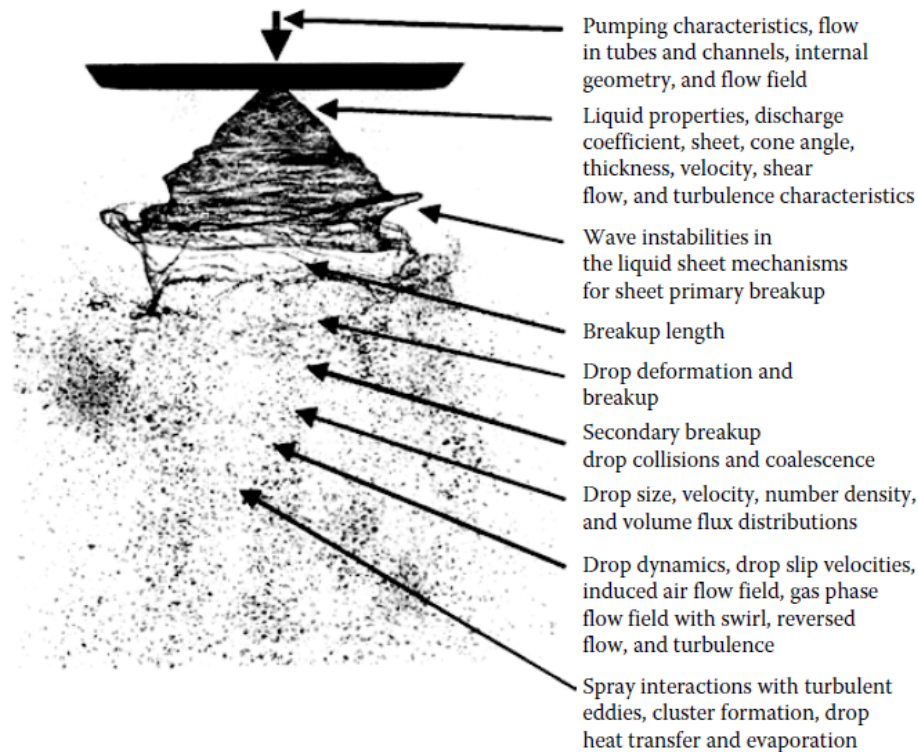


Figure 3.2 – Atomization process of a simplex swirl atomizer [Lefebvre and McDonell, 1988].

3.1.1 Flow inside of the injector

Despite the geometric simplicity of simplex swirl atomizers, the hydrodynamic processes taking place within the nozzle are very complex. Nevertheless, the early theories based on the assumption of frictionless flow led to the formulation of quantitative relationships between the main atomizer dimensions and various flow parameters, such as discharge coefficient, and initial spray cone angle [Taylor, 1948].

In spite of most of the fluid motion can be considered non-rotational, Taylor discovered [Taylor, 1950] that the viscous effects of the boundary layer cannot be neglected. The liquid in contact with the swirl chamber walls cannot rotate at a sufficient rate to hold it in a circular path against the radial pressure gradient, and hence a current directed toward the orifice is set up through the surface layer. For real fluids an outward flow may also occur through a boundary layer around the air core and the surface tension among the liquid and the air core is negligible [Binnie and Harris, 1950].

The following non-dimensional numbers were defined to describe the characteristics of a particular simplex swirl atomizer in 1969 by [Dombrowski and Hasson, 1969] and reviewed by [Chinn, 2009a, Chinn, 2009b]. The characteristic dimensions are described on Figure 3.3.

Flow Number

The flow number (FN) is defined as the effective flow area of a pressure atomizer. The definition is given by:

$$FN = \frac{\dot{m}_{fuel}}{(\Delta P)^{0.5}(\rho_{fuel})^{0.5}} \quad (3.1)$$

where \dot{m}_{fuel} is the fuel mass flow rate, ΔP is the injection pressure drop and ρ_{fuel} is the fuel density.

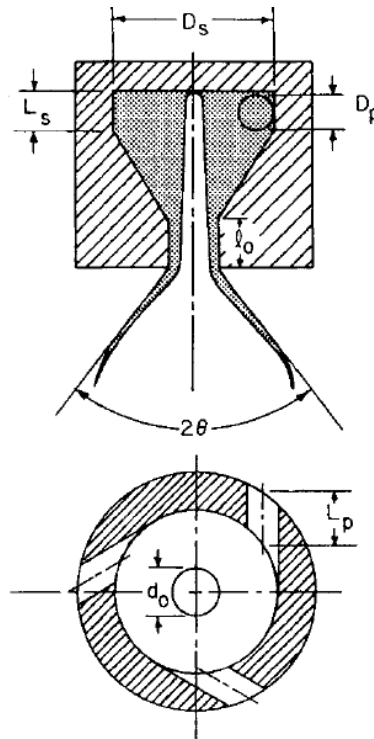


Figure 3.3 – Main dimensions of a simplex swirl atomizer[Rizk and Lefebvre, 1985a]. D_s represents the diameter of the swirl chamber. L_s represents the depth of the swirl chamber. D_p represents the diameter of the fuel feed port. L_p represents the length of the feed port. d_o represents the diameter of the orifice outlet. l_o represents the length of the orifice throat. 2θ represents the double of the spray angle.

The effect of varying main dimensions of the injector was studied by [Kutty et al., 1978]. Enlarging the diameter of the orifice increases the flow number since the flow area is increasing. Meanwhile enlarging the diameter of the swirl chamber reduces the flow number due to the increase of swirl motion that enlarges the air core diameter reducing the effective area.

An empirical formulation was proposed and validated with the experimental study named before:

$$FN = 0.0308 \left(\frac{A_p^{0.5} d_o}{D_s^{0.45}} \right) \quad (3.2)$$

where A_p is the total fuel feed port area. d_o is the diameter of the outlet orifice and D_s is the diameter of the swirl chamber as it is shown on Figure 3.3.

Discharge Coefficient

The discharge coefficient (C_D) is defined as the ratio among the real discharge flow to the maximum discharge flow rate, neglecting the viscous effects. It can be expressed in terms of mass flow rate injected into the injector as follows:

$$C_D = \frac{\dot{m}_{fuel}}{A_o \sqrt{2\rho_{fuel}\Delta P}} \quad (3.3)$$

where, according to Figure 3.3, A_o is the area of the orifice outlet with diameter d_o . ρ_{fuel} is the fuel density and ΔP is the pressure drop injection.

The discharge coefficient in simplex swirl atomizer is in general low. The presence of the air core reduces the effective orifice outlet area blocking off the central zone of the orifice.

In order to find a relationship between the Reynolds number Re and the discharge coefficient, [Radcliffe, 1955] carried out several experiments on a family of injectors based on common design rules, using fluids with a wide range of viscosity and density. At low Reynolds numbers the fuel film is thickened in the final orifice and, hence, the discharge coefficient increases. With nozzles of small flow number, this effect can be significant at low flow rates. However, for high Reynolds numbers, the discharge coefficient is independent of the Reynolds number.

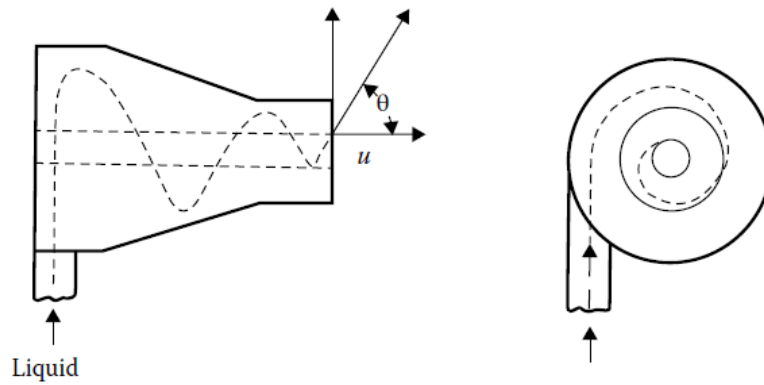


Figure 3.4 – Flow path in simplex swirl atomizers [Lefebvre and McDonell, 1988]

Following the inviscid analysis done by [Giffen and Muraszew, 1953] on a pressure swirl nozzle a derivation of an empirical law bounds the discharge coefficient to the geometry of the simplex swirl injector. In addition, it is useful to derive the empirical law of the liquid film thickness. Using as a reference the simplex atomizer reported on Figure 3.4, it is possible to write the conservation of angular momentum considering non-viscous conditions as follows:

$$u_t r = u_i R_S \quad (3.4)$$

where u_t the tangential velocity and r the radius. Bounding them to the inlet velocity u_i and to one of the main parameters, the swirl chamber radius R_S , it is possible to define the inlet velocity in function of the total cross-sectional area of the inlet ports, A_p , which is in fact the sum of the areas of every inlet ports: $A_p = \sum_i A_i$ being A_i the area of every port.

$$u_i = \frac{\dot{m}_{fuel}}{\rho_{fuel} A_p} \quad (3.5)$$

This equation assumes the existence of an air core. Otherwise, it implies for the case $r = 0$ the tangential velocity u_t would be infinite.

With the assumption that there are not losses within of the atomizer, the total pressure remains constant and equal to the injection pressure P_0 . The total pressure at any point in the liquid flowing inside of the injector is given by the Benourlli's equation as:

$$P_0 = p + 0.5\rho_{fuel}u_a^2 + 0.5\rho_{fuel}u_t^2 = constant \quad (3.6)$$

where p is the static pressure at any point in the fuel and u_a is the axial velocity component in the orifice. In the case we want to study one single vortex there are two statements to consider:

- The axial velocity u is uniform and constant for every value of r in the liquid annulus around the air core in the orifice. Thus, we can say that $p + 0.5\rho_{fuel}u_t^2 = constant$.
- The air core static pressure is the ambient atmospheric pressure, hence, $p = 0$, and so:

$$P_0 = 0.5\rho_{fuel}(u_{a_{ra}}^2 + u_{t_{ra}}^2) = constant \quad (3.7)$$

where the subscript ra means any point where the radius r is equal to the radius of the air core ra . Since the axial velocity remains constant we can rewrite the last equation with $u_{a_{ra}} = u_a$. The axial component of the velocity at the outlet orifice is given by:

$$u_a = \frac{\dot{m}_{fuel}}{\rho_{fuel}(A_o - A_a)} \quad (3.8)$$

where A_o is the orifice area and A_a is the air core area. From equations 3.4 and 3.5 we have:

$$u_{t_{ra}} = \frac{\dot{m}_{fuel}R_s}{\rho_{fuel}A_p r_a} \quad (3.9)$$

Substituting the equations of u_a and $u_{t_{ra}}$ into the simplified total pressure equation gives:

$$P_0 = 0.5\rho_{fuel} \left[\left(\frac{\dot{m}_{fuel}R_s}{\rho_{fuel}A_p r_a} \right)^2 + \left(\frac{\dot{m}_{fuel}}{\rho_{fuel}(A_o - A_a)} \right)^2 \right] \quad (3.10)$$

Now, if we substitute the definition of the discharge coefficient described in Equation 3.3 into the hypothesis we have just described, we obtain:

$$\frac{1}{C_D^2} = \frac{1}{K_1^2 X} + \frac{1}{(1-X)^2} \quad (3.11)$$

where $X = A_a/A_o$ and $K_1 = A_p/\pi r_o R_s$. This equation provides a relationship between the discharge coefficient, the dimensions of the atomizer and the air core diameter. In general is more useful to express this expression in terms of only one parameter. To do so, we establish that for any value of the parameter K_1 , the size of the air core will provide the maximum flow, that is, the value of C_D , expressed as a function of X , is a maximum: $d(1/C_D^2)/dX = 0$. From this assumption we obtain the following relation:

$$C_D = \left[\frac{(1-X)^3}{1+X} \right]^{0.5} \quad (3.12)$$

Modified afterwards by [Giffen and Muraszew, 1953] since the results were too low in comparison with experiments. Therefore, they added a constant value:

$$C_D = 1.17 \left[\frac{(1-X)^3}{1+X} \right]^{0.5} \quad (3.13)$$

In contrast with this equation that links the main geometric parameters of the injector and the discharge coefficient, [Rizk and Lefebvre, 1985a] derived an empirical expression following the non-viscous theory presented in [Giffen and Muraszew, 1953]:

$$C_D = 0.35 \left(\frac{A_p}{D_s d_0} \right)^0 .5 \left(\frac{D_s}{d_0} \right)^{0.5} \quad (3.14)$$

Velocity coefficient

The velocity coefficient (K_v) is the ratio of the actual discharge velocity to the theoretical velocity generated by the injection pressure drop:

$$K_v = \frac{U}{(2\Delta P/\rho_{fuel})^{0.5}} \quad (3.15)$$

where U is the actual discharge velocity, ΔP is the injection pressure drop and ρ_{fuel} is the fuel density. The velocity coefficient can also be calculated using the main geometric parameter of the injector as follows [Rizk and Lefebvre, 1985b]:

$$K_v = \frac{C_D}{(1 - X \cos \theta)} \quad (3.16)$$

where C_D is the discharge coefficient, $X = A_a/A_o$ as defined in the discharge coefficient calculation and θ is the angle of the spray shown on Figure 3.3. The value of the velocity coefficient is highly influenced by the geometry of the injector, the pressure operating condition and the fuel properties. Accurate values of K_v are essential for calculating the true velocity at which the liquid is discharged from the nozzle. This velocity is of prime importance to atomization, since it is the relative velocity between the initial liquid sheet and the surrounding air or gas that largely determines the mean drop size of the spray.

Fuel film thickness

In simplex swirl atomizers, the fuel emerges from the nozzle as a thin conical sheet. The film rapidly is becoming thinner and thinner, spreading radially outwards until it breaks up. The film is disintegrated first into ligaments and afterwards into droplets. Thus, the thickness of the fuel sheet is an important parameter to control in order to achieve a proper atomization process since it influences the mean drop size of the spray [Lefebvre, 1983].

In simplex swirl atomizers the fuel film thickness is directly related to the area of the air core A_a . In [Giffen and Muraszew, 1953] a relationship between the air core and the atomizer dimensions is proposed based on the non-viscous fluid theory.

$$\left(\frac{A_p}{D_s d_o}\right)^2 = \frac{\pi (1 - X)^3}{32 X^2} \quad (3.17)$$

where the parameters are related to the Figure 3.3 and X is the ratio between the area of the air core and the area of the discharge orifice. After calculating X from this equation, the fuel film thickness t can be calculated directly as follows:

$$X = \frac{(d_o - 2t)^2}{d_o^2} \quad (3.18)$$

In equation 3.14 the discharge coefficient is expressed in terms of nozzle dimensions. Combining both equations X and hence t can be calculated from nozzle dimensions as follows:

$$\frac{(1 - X)^3}{1 + X} = 0.09 \left(\frac{A_p}{D_s d_o}\right) \left(\frac{D_s}{d_o}\right)^{0.5} \quad (3.19)$$

In [Simmons and Harding, 1981] another empirical equation is proposed:

$$t = \frac{0.00805 \sqrt{\rho_{fuel}}}{d_o \cos \theta} \quad (3.20)$$

This two equations used to estimate the film thickness followed the idea that the film thickness is independent of liquid viscosity and liquid injection pressure. To overcome this

problem, in [Rizk and Lefebvre, 1985a], a theoretical approach is proposed to investigate the internal flow characteristics of simplex swirl atomizers. Considering a small element of the fuel film thickness flowing in the outlet orifice of length dx , depth dy and a unit width in a direction at right angles to its direction of motion; and assuming only pressure and viscous forces, these forces balance each other, such that:

$$dp \cdot dy = d\tau \cdot dx \quad (3.21)$$

where τ is the shear stress and dp represents the pressure gradient in the x direction. Since:

$$\tau = \mu_{fuel} \frac{du}{dy} \quad (3.22)$$

where μ_{fuel} is the fuel viscosity and u is the velocity of the film. If we consider the pressure gradient constant across the film we have the following equation system:

$$u = \begin{cases} 0 & \text{if } y = 0 \\ U_s & \text{if } y = t \\ \frac{1}{\mu_{fuel}} \left(\frac{dp}{dx} \right) \frac{y^2}{2} + C_1 y + C_2 & \text{otherwise} \end{cases} \quad (3.23)$$

where U_s is the maximum flow velocity attained to at the liquid surface, t is the fuel film thickness, C_1 and C_2 are two constants determined from boundary conditions. Hence, once the system is solved:

$$u = \frac{1}{\mu_{fuel}} \frac{dp}{dx} \left(\frac{y^2}{2} - \frac{ty}{2} \right) + \frac{U_s y}{t} \quad (3.24)$$

The averaged velocity can be described as:

$$\bar{u} = -\frac{1}{\mu_{fuel}} \frac{dp}{dx} \frac{t^2}{12} + \frac{U_s}{2} \quad (3.25)$$

and the maximum velocity is determined by differentiating the general equation of the velocity:

$$U_s = -\frac{1}{\mu_{fuel}} \frac{dp}{dx} \frac{t^2}{2} \quad (3.26)$$

Substituting U_s is possible to obtain the average flow velocity as:

$$\bar{u} = -\frac{1}{\mu_{fuel}} \frac{dp}{dx} \frac{t^2}{3} \quad (3.27)$$

Due to the swirling motion generated at the swirl chamber, the liquid has a flow direction with an angle θ regarding the orifice center line as it is shown in Figure 3.4. Hence, considering $l/\cos\theta$ the length of the flow path and ΔP the pressure drop of this path, we obtain the following expression regarding the average flow velocity:

Substituting U_s is possible to obtain the average flow velocity as:

$$\bar{u} = \frac{\Delta p t^2 \cos \theta}{3\mu_{fuel} l} \quad (3.28)$$

Since there are many types of simplex swirl atomizers, it is difficult to assign a value to l . Nevertheless, every atomizer ends with a circular discharge orifice regardless its internal geometry. Thus, it is convenient to assume l proportional to d_o , for instance $l \approx A d_o$. Also,

assuming the pressure drop Δp along the flow path $l/\cos\theta$ is proportional to the total pressure drop across the nozzle $\Delta p \approx B\Delta P$. We can rewrite the average flow velocity as follows:

$$\bar{u} = \frac{\Delta P t^2 \cos\theta}{3\mu_{fuel} d_o (A/B)} \quad (3.29)$$

The value (A/B) should remain constant since the pressure drop is proportional to the flow length. From the experiments in [Rizk and Lefebvre, 1985a] this value is around $(A/B = 400)$. The angle of the spray at the lip of the injector is the resultant of the axial and tangential components of the velocity. The axial velocity has been defined in Equation 3.8. The angle is defined such that $\cos\theta = u_a/\bar{u}$:

$$\cos^2\theta = \frac{12\dot{m}_{fuel}\mu_{fuel}(A/B)}{\pi\rho_{fuel}d_o\Delta P t^2(1-X)} \quad (3.30)$$

To find a more general equation to obtain the spray angle θ it is necessary to use another parameter of the simplex swirl atomizer such as the discharge coefficient C_D described in Equation 3.12. As this formulation was done in the framework of inviscid fluid, a coefficient K_v is added to correct it:

$$C_D = K_v \left[\frac{(1-X)^3}{1+X} \right]^{0.5} \quad (3.31)$$

The K_v coefficient corresponds to the velocity coefficient described in Equation 3.15. From this equation we can extract the averaged velocity:

$$\bar{u} = K_v \left[\frac{2\Delta P}{\rho_{fuel}} \right] \quad (3.32)$$

The volumetric flow rate Q defined as $Q = \dot{m}_{fuel}/\rho_{fuel}$ is given by:

$$Q = A_o C_D [2\Delta P/\rho_{fuel}]^{0.5} = A_o C_D \bar{u}/K_v \quad (3.33)$$

Now, combining Equation 3.8 and Equation 3.33 we obtain Equation 3.15. And combining Equation 3.15 and Equation 3.31 we obtain:

$$\cos^2\theta = \frac{1-X}{1+X} \quad (3.34)$$

And equalizing this equation to the other one defining $\cos^2\theta$ (Equation 3.30) we arrive firstly to:

$$t^2 = \frac{1560FN\mu_{fuel}}{\rho_{fuel}^{0.5}d_o\Delta P^{0.5}} \frac{1+X}{1-X} \quad (3.35)$$

Finally, substituting the value of $X = A_a/A_o = (d_o - 2t^2)/d_o^2$ we arrive to the final equation for the fuel film thickness t :

$$t = 3.66 \left[\frac{d_o FN \mu_{fuel}}{(\rho_{fuel} \cdot \Delta P)^{0.5}} \right]^{0.25} \quad (3.36)$$

Through experimental and dimensional analysis, the constant was updated in [Suyari and Lefebvre, 1986, Lefebvre and McDonell, 1988]:

$$t = 2.7 \left[\frac{d_o FN \mu_{fuel}}{(\rho_{fuel} \cdot \Delta P)^{0.5}} \right]^{0.25} \quad (3.37)$$

This equation is currently used in the industry to predict the fuel film thickness at the outlet of simplex swirl atomizers.

The liquid sheet thickness can be also estimated from the actual discharge coefficient C_D imposed by the inlet mass flow rate by Equation 3.3. Since the fuel mass flow rate \dot{m}_{fuel} , the injection pressure ΔP and the area of the orifice A_o are known we can calculate the actual C_D . It is also possible to calculate C_D with the correlation by [Giffen and Muraszew, 1953] shown on Equation 3.13 where the ratio of areas X is unknown. Iterative X is calculated from [Giffen and Muraszew, 1953] and after the liquid sheet thickness is computed with Equation 3.18 where we can extract the value of the liquid sheet thickness as follows:

$$t_{fuel} = \frac{d_o(1 - X)^{0.5}}{2} \quad (3.38)$$

This method was proposed by [Sanchez, 2021].

3.1.2 Outer flow and atomization process

A fuel sheet emerging from the nozzle of a simplex swirl atomizer has swirling motion generated inside the spin chamber. The different velocity between the fuel sheet and the surrounding gas generates aerodynamic forces that destabilises the sheet into a wavy flow. The instabilities grow in time and space meanwhile the sheet is becoming thinner to, finally, break-up into liquid ligaments and droplets [Ibrahim and Jog, 2007]. Properties such as the cone angle, sheet instabilities and the break-up length can be defined.

Spray cone angle

When the fuel loses the inner walls of the injector, the centrifugal forces push out the liquid, hence, the tangential velocity is converted completely to radial velocity [Taylor, 1948, Craig et al., 2012]. Consequently, the fuel sheet expands generating a wide angle sheet. The ratio between the axial velocity and the sum of the tangential and radial velocity will define the spray angle. The angle of the spray depends mainly in the internal geometry of the atomizer, but also in the injection pressure, since higher the pressure, higher the mass flow rate and, hence, the Reynolds number Re .

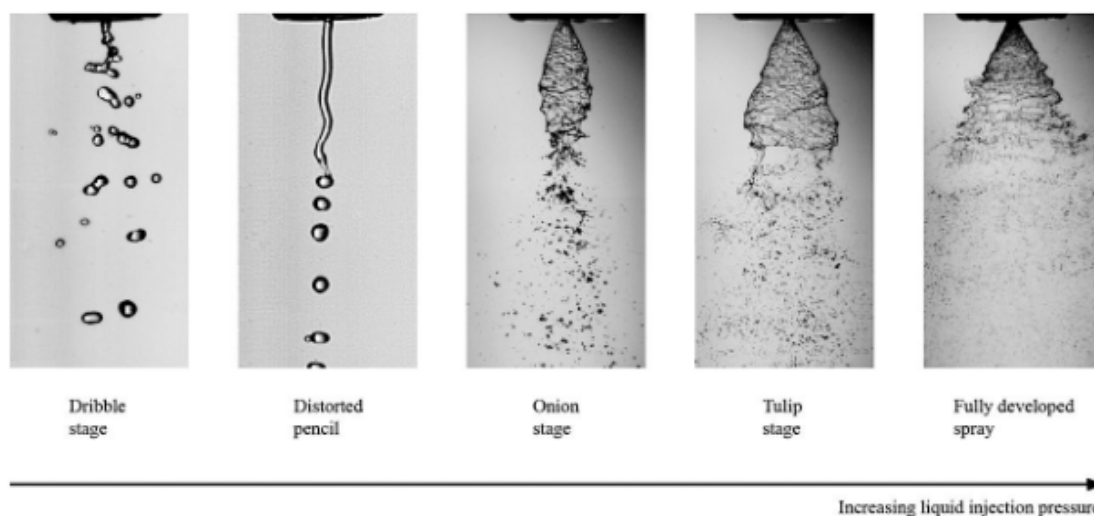


Figure 3.5 – Spray development in a simplex swirl atomizer [Lefebvre and McDonell, 1988]

On Figure 3.5 an evolution of the spray development is shown at different operating pressures. Beginning with the dribble and distorted pencil stages where the injection pressure is low and thus the spray is not developed; through the onion and tulip stages where the spray is beginning to develop and the angle can be measured. Finally, when the spray is fully developed the spray angle is totally straight.

The Taylor's inviscid theory [Taylor, 1948] says that the spray cone angle depends only on the ratio of the inlet ports area to the product of swirl chamber diameter and orifice diameter $A_p/(D_s d_0)$. In [Giffen and Muraszew, 1953] an expression is derived for non-viscous liquids using only nozzle dimensions.

$$\sin \theta = \frac{(\pi/2)C_D}{K(1 + \sqrt{X})} \quad (3.39)$$

where $K = A_p/(D_s d_0)$ and $X = A_a/A_0$.

Substituting Equation 3.12 into Equation 3.39 gives:

$$\sin \theta = \frac{(\pi/2)(1 - X)^{1.5}}{K(1 + \sqrt{X})(1 + X)^{0.5}} \quad (3.40)$$

Base on those equations, Rizk and Lefebvre [Rizk and Lefebvre, 1985b] derived an equation taking into account the liquid properties:

$$2\theta = 6K^{-0.15} \left(\frac{\Delta P d_o^2 \rho_{fuel}}{\mu_{fuel}^2} \right) \quad (3.41)$$

The effect of varying the main liquid parameters are:

- Surface tension: Surface tension should have no effect on spray cone angle and it is confirmed by experiments in [Chen et al., 1992].
- Density: The spray angle widens when the density increases.
- Viscosity: The viscosity is the most important parameter affecting the cone angle since it modifies the flow of the liquid by friction with its containing walls. The cone angle decreases with increase in viscosity.

Liquid sheet thickness

The thickness h of the film can be calculated from the mass flow rate equation [Ashgriz, 2011] as follows:

$$\dot{m}_{fuel} = \rho_{fuel} \bar{u}_a \pi h (2x \tan \theta - h) \quad (3.42)$$

where \bar{u}_a is the averaged axial velocity along the liquid sheet at the stream-wise position x . θ is the semi-angle of the spray. \dot{m} is the fuel mass flow rate and ρ_{fuel} the fuel density.

The equation can be rewritten into:

$$h = x \tan \theta - \sqrt{(x \tan \theta)^2 - \frac{\dot{m}}{\rho_{fuel} \bar{u}_a \pi}} \quad (3.43)$$

This equation is based on the assumption that liquid sheet does not rupture before the breakup length.

Break-up length

The physical phenomena of the liquid sheet produces by the swirl injector it is also a complex process. Properties such as dispersion, penetration and cone angle of the spray can be defined. Those parameters are not only affected by the internal flow but also by the surrounding

gas. The break-up phenomena of the liquid sheet is produced mostly due to instabilities produced from the streamwise shear within the sheet or from a centrifugal instability due to the azimuthal motion within the sheet, or more probably from a combination of both [Billiant et al., 1998]. Those instabilities are called the Kelvin-Helmoltz instability [Thomson, 1871]. Among the spectrum of wavelengths characterising the disturbance, the fastest growing wave is the one that is directly responsible of the liquid sheet break-up [Galbiati et al., 2016].

The break-up length of the liquid sheet is defined as the distance from the nozzle exit to the position where the sheet begins to break. The break-up length can be measured directly from experimental pictures, or in numerical simulation, where the surface interface among liquid and gas is starting to grow up due to the ligaments and droplets generation.

3.2 CRSB simplex swirl injector description

The simplex swirl atomizer studied in this section was used in the *Coria Rouen Spray Burner* (CRSB). It is actually an industrial atomizer by Danfoss [Danfoss, 2020]. This injector is used in oil heating plants, rather than aircraft gas turbines. However, the physical phenomena within it is similar to the simplex swirl atomizer used in aeronautics. Moreover, there are several experimental studies in this Danfoss injector. The aim of this chapter is to study it numerically and compare the results with the experimental campaigns performed at CORIA laboratory.

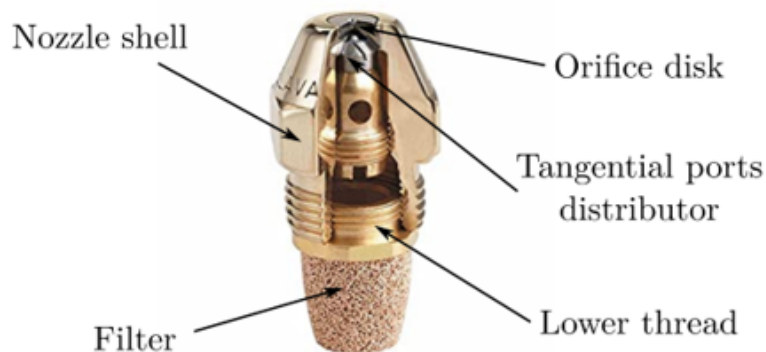


Figure 3.6 – Danfoss OD-H oil nozzle. Cut view [Danfoss, 2020]

Figure 3.6 shows a cut view of the studied injector, the *Danfoss OD-H*. We can compare the cut view with Figure 3.3. The *tangential ports distributor* piece defines the profile of the inlet ports, thus, we can have access to the diameter of the inlet ports d_o . Meanwhile in the *orifice disk* piece is where we can find the swirl chamber and the nozzle orifice defining the swirl chamber diameter D_s and the diameter of the discharge orifice d_o .

3.2.1 Experimental campaigns

Two different experimental campaigns were carried out at CORIA laboratory to study the flame structure and stabilization mechanisms [Verdier, 2017, Marrero, 2018] and the spray behavior. The burner was based on the geometry of the KIAI burner [Cordier et al., 2013] represented on Figure 3.7. The burner is composed of 2 different parts: the plenum with air co-flow and the fuel injection system.

The work by Verdier [Verdier, 2017] was performed at atmospheric operating conditions. Meanwhile the work by Marrero [Marrero, 2018] was performed with the gas at high temperature and the fuel preheated. Both studies were carried out using *N-heptane* as a fuel and with the

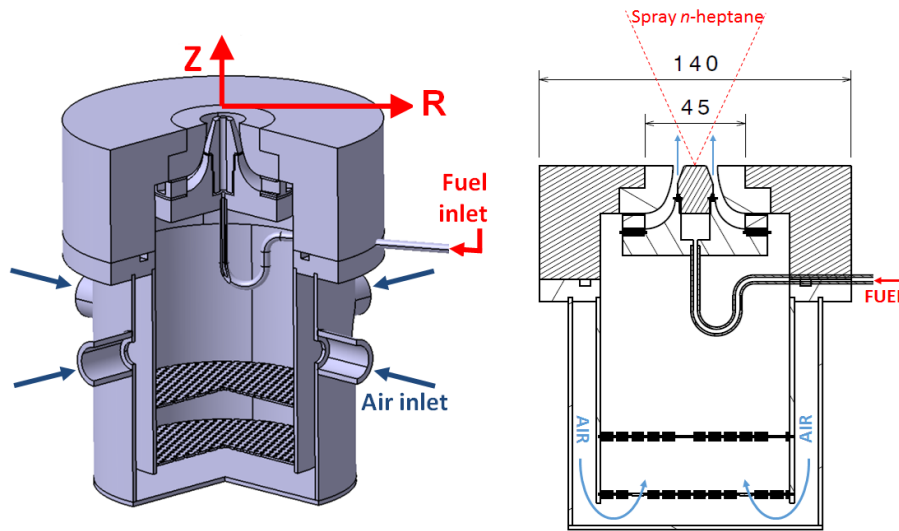


Figure 3.7 – Detail of the injection system [Verdier, 2017]

same fuel mass flow rate. The air co-flow was used to carry on the further droplets to prevent the back-flow of those since they could interfere in the drop measurements. The air co-flow was not influencing at all neither, the early fuel sheet flow nor the sheet break-up process.

	Ambient Temperature		Fuel Pre-heated	
	Fuel	Air	Fuel	Air
$\dot{m}[\text{kg/s}]$	2.8e-4	8.2e-4	2.8e-4	6.0e-4
$T[\text{K}]$	298	298	350	416

Table 3.1 – Experimental operating condition on the CRSB simplex swirl atomizer

From these experimental campaigns, the differences of the spray characteristics can be appreciated. At atmospheric operating conditions the global Sauter mean diameter (SMD) is $SMD \approx 50\mu\text{m}$. In the other hand, at high temperature operating condition we achieve a more refined spray which its Sauter mean diameter is around $SMD \approx 30\mu\text{m}$. The increase of the temperature decreases the viscosity, hence, the Reynolds number Re increases, narrowing the fuel sheet thickness[Lefebvre and McDonell, 1988]. Thus, the fuel sheet breaks up into smaller droplets. Another effect of the film narrowing is the acceleration of the droplets. Since the effective area of the fuel at the orifice ($A_o - A_a$) is reduced, and the mass flow rate remains constant, the axial velocity of the fuel sheet must increase. The average velocity of the droplets at atmospheric operating conditions is $|\bar{u}| \approx 25\text{m/s}$ meanwhile at high temperature operating conditions is around $|\bar{u}| \approx 30\text{m/s}$. Both measurements taken at $z = 20\text{mm}$.

3.3 Experimental geometry measurements

In order to perform numerical simulation, the internal geometry of the injector is required. In this case, the geometry was unknown since it is an industrial injector, therefore, the access to the 3D geometry files or to the lengths of the main dimensions of the atomizers is not open source data. Thus, to measure the internal part of the injector and reconstructing the 3D geometry is mandatory.

At *Universitat Politècnica de València* an experimental campaign of measurements took place to reconstruct the internal geometry of the injector. The measurement experimental

campaign was carried out with the injector used on the works by [Verdier, 2017, Marrero, 2018] of the Danfoss OD-H oil nozzle model. Three methodologies were used:

- Computed tomography scan (CT-Scan).
- Optical microscope visualization.
- Scanning electron microscope (SEM) visualization.

Those measurements techniques were applied directly to the disassembled metallic pieces of the atomizer. In addition, a silicone mold technique was used to extract the inner profiles of the injector [Macian et al., 2003]. This technique was validated for Diesel injector pieces in [Salvador et al., 2018].

3.3.1 Computed Tomography Scan

A tomography scan is a radiologic technique for obtaining clear X-ray images of deep internal structures by focusing on a specific plane within the body. This technique can cover in a single scan external and internal surfaces with a micrometer-level resolution [Ramsey and Villarraga-Gómez, 2017]. It can be applied directly to the assembled injector, which is an advantage regarding the other methods.

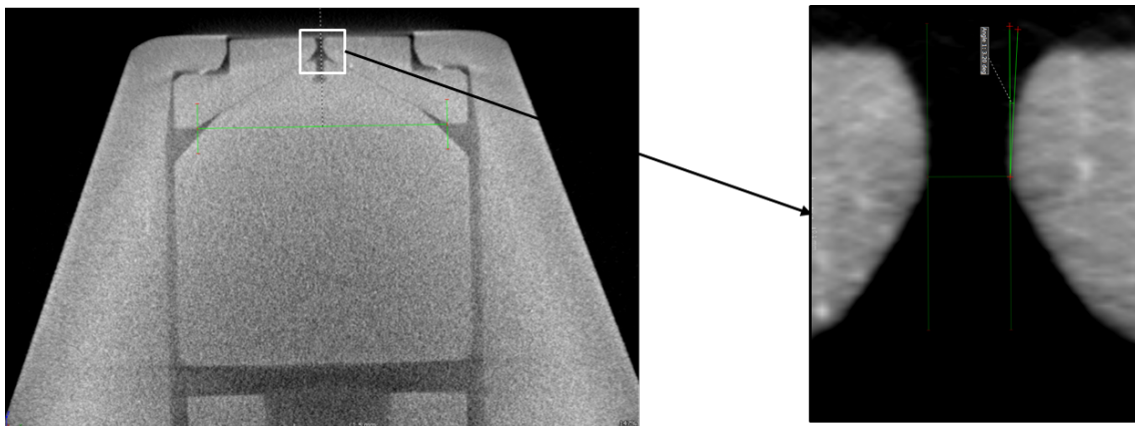


Figure 3.8 – On the left: Computed tomography scan of the assembled simplex swirl atomizer. On the right: Zoom view on the orifice profile

Figure 3.8 shows a picture of a tomography scan of the assembled injector. The nozzle shell, orifice disk and the tangential ports distributor pieces can be identified regarding Figure 3.6. A zoom view on the zone of interest is also shown. The swirl and spin chamber described on Figure 3.1 can be noticed. A convergence/divergence orifice profile is recovered. From this technique some main dimensions of the injector, such as the diameter of the swirl chamber D_s and the diameter of the orifice d_o can be extracted. Another minor dimensions such as the diameter of the spin chamber, the smallest diameter of the throat or the angles defining the nozzle profile can be measured. However, as we can notice in the pictures, the resolution is not high, not due to the technique itself but the differences of size among the metal pieces and the orifice.

3.3.2 Optical microscope visualization

The optical microscope visualization is applied into both, the disassemble pieces of the injector and the silicone molds. This technique has higher resolution than the CT-Scan but, in the other hand, the injector has to be disassembled and, thus, the repeatably of the experiment may be lost.

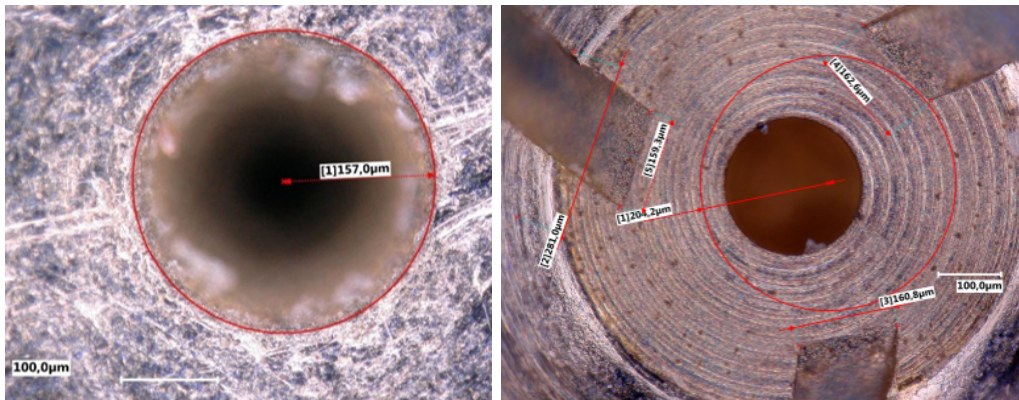


Figure 3.9 – Optical microscope picture of disassembled metallic pieces. On the left: Orifice disk from above. On the right: Tangential ports distributor from above

Figure 3.9 shows two optical microscope pictures from injector metal pieces. The left one corresponds to the orifice disk piece. From this pictures the diameter of the orifice can be measured. The picture on the right corresponds to the tangential ports distributor piece. In this picture the diameter of the swirl chamber D_s can be directly measured. The three tangential ports are represented and the transverse profile of those, where a rectangular profile can be extracted. Finally, a cylindrical hole can be appreciated in the middle of the piece. The depth of this hole can be also measured with the optical microscope.

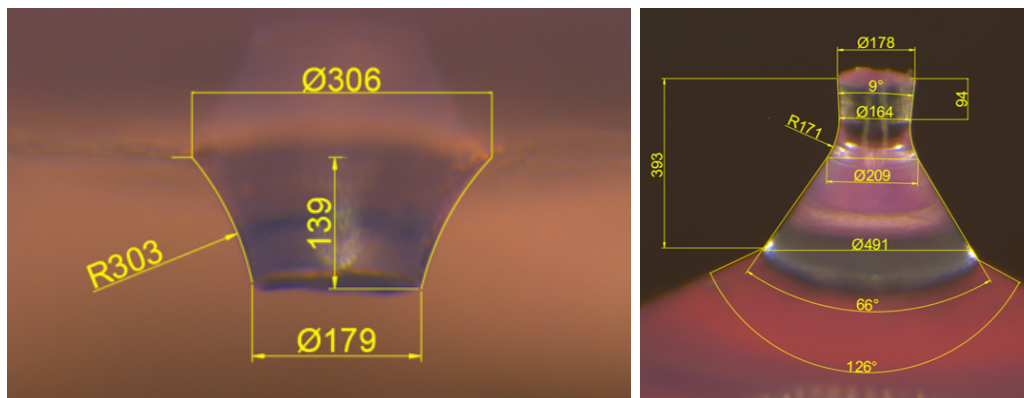


Figure 3.10 – Optical microscope picture of silicone molds. On the left: upper piece. On the right: lower piece

On Figure 3.10 two optical microscope pictures from silicone molds are shown. Both pictures are related to the same silicone mold. When the silicone molding technique is applied into this kind of metal pieces, it is necessary to break up the mold in order to extract it from the piece. Usually, it breaks up in the weaker zone of the mold, in this case, in the throat of the nozzle. In the picture of the left the upper part of the mold is shown. From this picture the diameter of the orifice d_o is recovered. Some differences can be notice in the length of this dimensions compared to the one recovered on Figure 3.9. The variation from one picture to another is $\pm 3\mu m$. This effect is due to the post-process of the pictures. The picture on the right shows the lower part of the mold where the same profile seen on Figure 3.8 can be notice, but in this case the measurement can be done with higher resolution.

3.3.3 Scanning electron microscope visualization

The last method used is the scanning electron microscope visualization. The methodology is similar to the optical microscope visualization but higher resolution can be achieved. This technique produces images of a sample by scanning the surface with a focused beam of electrons, thus, the surfaces have to be metallic.

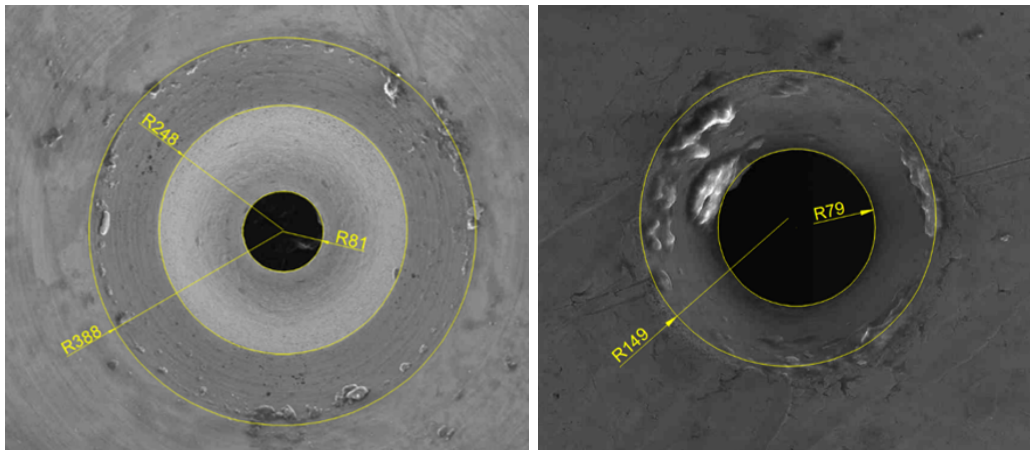


Figure 3.11 – Scanning electron microscope picture of disassembled metallic pieces. On the left: Orifice disk from below. On the right: Orifice disk from above

On Figure 3.11 two pictures from scanning electron microscope visualization of the metallic pieces are shown. Both pictures correspond to the orifice disk disassemble piece; the picture on the left is taken from below, what would correspond within the injector, and the picture on the right is taken from above, therefore, it is the same view represented on Figure 3.9. The dimension measured in with these pictures are the same measured with the optical microscope visualization but with more resolution.

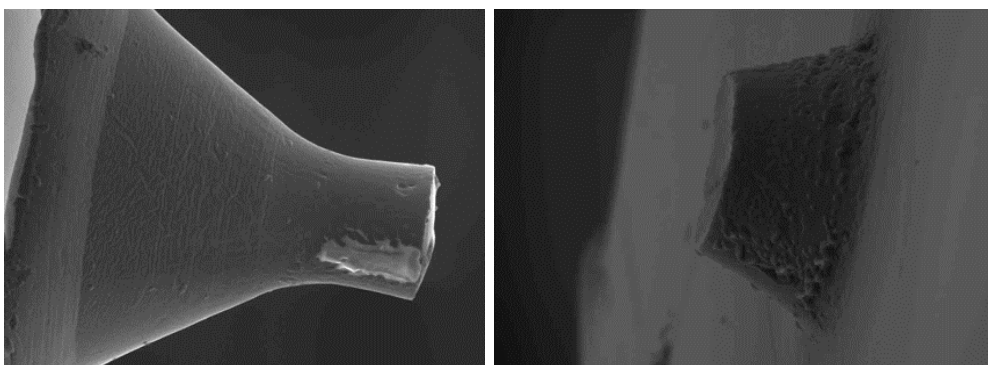


Figure 3.12 – Scanning electron microscope picture of silicone molds. On the left: Silicone mold lower part. On the right: Silicone mold upper part.

Figure 3.11 shows two pictures from the scanning electron microscope visualization of the silicone molds. In order to be able to use this technique in silicone, previously, a gold coating is applied to the molds. Again, the pictures correspond to the same broken mold. The measurements taken are the same that could be taken with the optical microscope visualization with higher resolution.

3.3.4 Measurement results

Once every methodology has been performed for every atomizer the pictures are post-processed. They are measured with *CAD*(Computer-aided design) tools several times and for more than one person. In that manner the measurement errors are attenuated.

Figure 3.13 shows a sketch of the inner geometry of the injector recovered from the experimental measurement campaign. On Table 3.2, the measurements of every parameter may be found. As we can see in the measurement table, some accepted measurements do not correspond whit their actual measurements, because the sketch is over-constrained.

The sketch can be compared with the CT-Scan pictures on Figure 3.8 where we can notice that the profile is well recovered. The sketch has been parametrized to study, in future works, the effect of varying some main parameters of the injector and its effects on the performance of the injector.

To have a deeply knowledge of the measurements process and the different techniques, the reader should read the work presented at ICLASS 2021 in [Ferrando et al., 2021a] and the submitted journal article [Ferrando et al., 2021b] (see Appendix C).

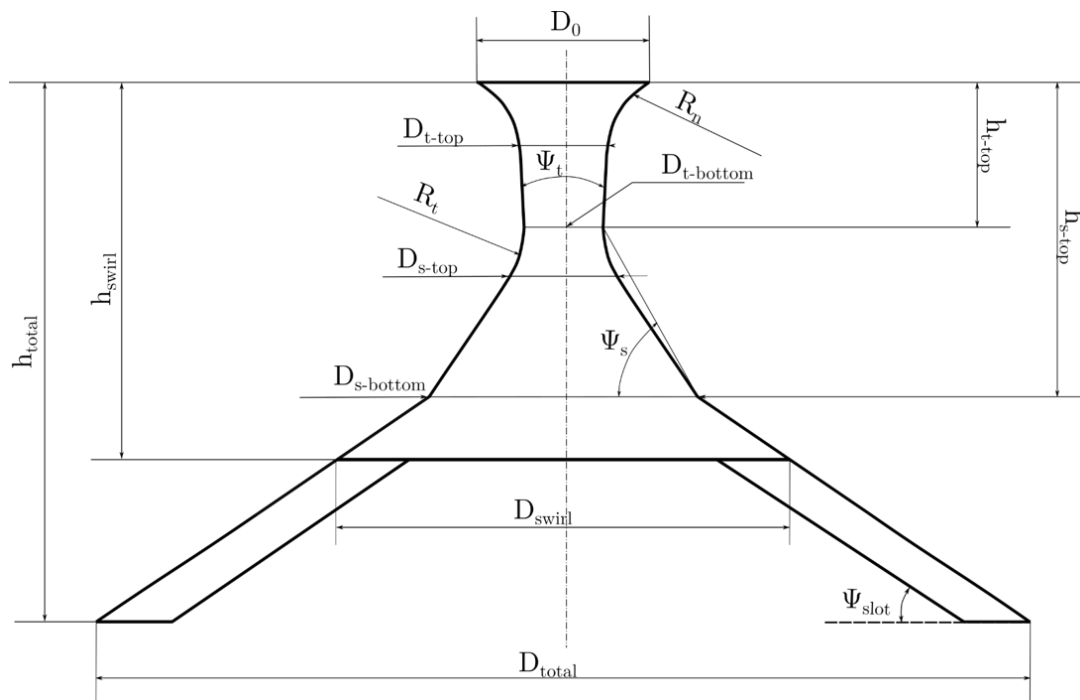


Figure 3.13 – Sketch of the inner geometry of the injector

3.4 Modelling the flow inside of the injector

The modelling of the internal flow of a simplex swirl atomizer has been studied for more than twenty years. In this case, as reported in chapter 2, the *Volume of Fluid (VoF)* method is applied to model the multiphase phenomena. The numerical study is divided in several steps, beginning with the 3D geometry reconstructions explained in the last section. Afterwards, the numerical mesh is generated, the case is set-up and the results are post-processed. Since the physical processes inside and outside the injector are complex and they involve a wide range of length scales, the modelling of the internal flow and the external flow have been divided to simplify the process. From the internal numerical simulation some data are recovered at the injector orifice, treated and used as a boundary conditions for the external domain simulation.

Parameter	Unit	Dimensions				Accepted
		Optical Microscope (Molds)	SEM (Molds)	SEM (Pieces)	CT-Scan	
D_o	μm	313 ± 2	300 ± 2	298 ± 1	301 ± 3	300
D_{t-top}	μm	179 ± 4	180 ± 5	-	-	180
$D_{t-bottom}$	μm	164 ± 2	160 ± 1	160 ± 1	169 ± 3	165
D_{s-top}	μm	209 ± 3	213 ± 2	-	-	210
$D_{s-bottom}$	μm	491 ± 5	480 ± 5	496 ± 2	500 ± 1	500
D_{swirl}	μm	774 ± 6	781 ± 6	776 ± 2	773 ± 4	780
D_{total}	μm	-	-	3492 ± 1	3375 ± 1	3375
h_{t-top}	μm	233 ± 4	238 ± 3	-	-	240
h_{s-top}	μm	532 ± 6	546 ± 3	-	540 ± 2	540
h_{swirl}	μm	600 ± 5	605 ± 4	-	600 ± 2	620
h_{total}	μm	-	-	-	2400 ± 1	2400
R_n	μm	303 ± 5	300 ± 4	-	-	308
R_t	μm	171 ± 6	191 ± 5	-	-	-
Ψ_t	°	6 ± 4	6 ± 2	-	-	6
Ψ_s	°	57 ± 6	58 ± 4	-	-	61
Ψ_{slot}	°	27 ± 6	28 ± 3	-	-	30

Table 3.2 – Experimental measurements of the CRSB simplex swirl atomizer

3.4.1 Computational hybrid mesh

The election of the computational mesh topology is an important step in a multiphase simulation. The minimal resolution has to be enough to be able to capture the interface between the liquid and the gas. A good control of the resolution is required to refine more in the places where the surface interface is supposed to be and let a coarser mesh in the zone where the liquid volume fraction α is either 0 or 1. A special refinement has to be done around the walls to properly model the boundary layer. Therefore, studies such as [Hansen et al., 2002, Sumer et al., 2012] used full hexahedral structured meshes because is straightforward to modify the length of the cells of interest.

Nevertheless, performing a full hexahedral structured mesh turned out into numerical instabilities which triggered divergence on the simulation. High velocities of the liquid were found around the connection between the tangential inlet ports and the swirl chamber, most probably, due to the bad quality of the cells in that part of the mesh. Because of the non-asymmetric nature of the geometry, due to the tangential ports union, quality controls such as skewness, aspect ratio and non-orthogonality were not good enough, and thus, the simulation eventually was diverging.

To overcome this problem a new mesh strategy was tested, a hybrid tetrahedral-hexahedral mesh approach used in works such as [Madsen et al., 2004, Ding et al., 2016]. The main idea of this approach is to keep, as much as possible, the hexahedral elements everywhere but in the conflicting zone. Accordingly, a ring around the axial center, where the tangential ports are intersected to swirl chamber, is performed of tetrahedral elements. Everything else, the three tangential ports, the body of the injector and also the external zone of the domain are hexahedral cells following a structured mesh. With this solution the instabilities were solved, since the quality control were already good, and the refinement control of the cell were kept.

A representation of the mesh strategy is shown in Figure 3.14 where the different cell topologies are represented.

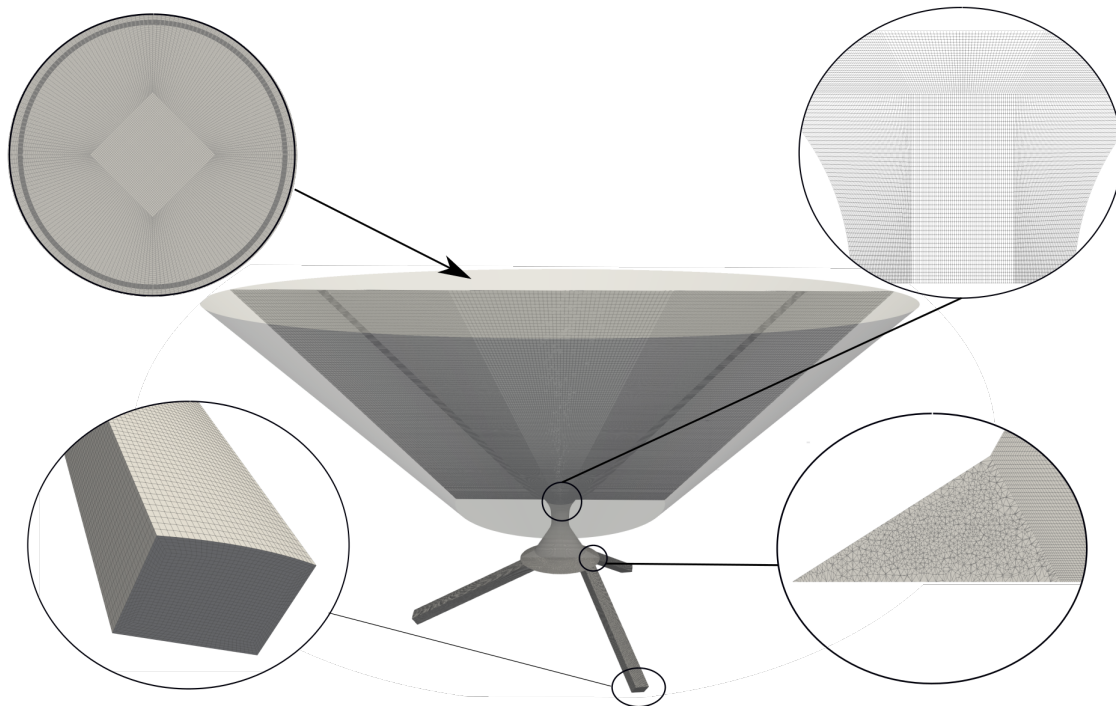


Figure 3.14 – Computational grid sketch. Hybrid mesh made of hexahedral and tetrahedral elements.

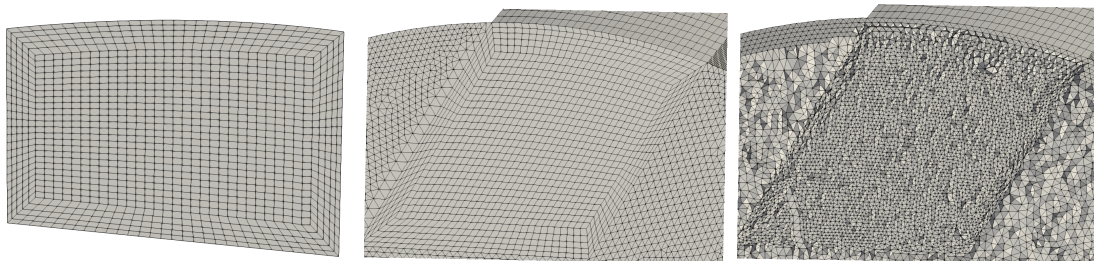


Figure 3.15 – Tangential ports profile mesh. On the left: Inlet mesh. On the middle: Intersection with swirl chamber. On the right: Transition between hexahedral and tetrahedral elements.

On Figure 3.15 a closer view to the tangential ports mesh is shown. It can be noticed the finer refinement performed around the walls to let boundary layer develops. On the left, the inlet mesh of the tangential ports, which is also the numerical domain inlet, is shown. The surface mesh is extruded along the ports up to the swirl chamber where the tetrahedral transition is performed. On the middle and right pictures the merge between the two topologies is shown. To be able to merge hexahedral and tetrahedral elements, pyramidal elements are required. The hexahedral elements at the swirl chamber seems deformed compared to the original surface mesh due to the inclination and contact angle with the swirl chamber. The transition with the tetrahedral elements is straightforward and those elements have good quality control parameters avoiding any numerical instability.

Figure 3.16 shows a zoom in a frontal slice of the mesh at where the swirl and spin chambers can be noticed. The external part of the swirl chamber is full filled with tetrahedral elements, bigger than the hexahedral elements in the inner part. The control over the size of tetrahedral elements is less precise than the control over the hexahedral elements, thus, achieving an equal size of those elements in respect to the hexahedrals ones, means to increase

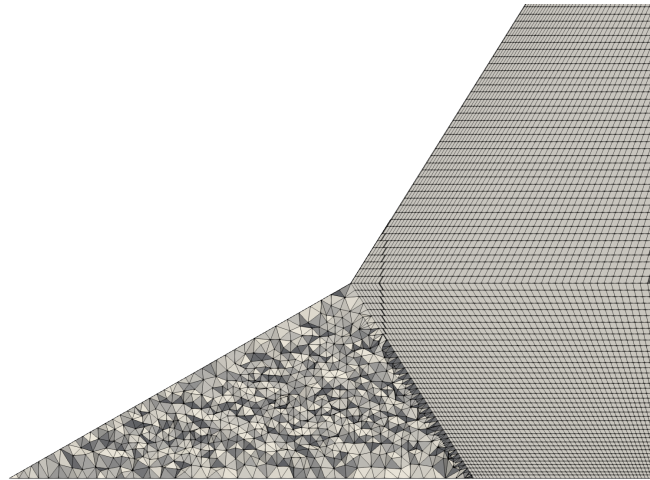


Figure 3.16 – Slice around the swirl and spin chamber showing the mesh.

hugely the number of elements. In the picture can be also noticed a linear refinement in radial direction of the hexahedral elements, achieving finer elements around the walls to capture better the boundary layer development. As is reported in [Amini, 2016], the fuel is injected by the tangential ports into the swirl chamber but is not up to the spin chamber where the swirl flow is developed. Hence, the lower resolution of the mesh around the swirl chamber walls is not affecting the development of the swirl motion due of the lower velocity in this zone.

Regarding the outer part of the computational domain shown on Figure 3.17, a refinement zone is placed in a hollow cone shape where the liquid sheet is expected. The mesh resolution in the outer part is low; not enough to capture the primary break-up and the droplet atomization but enough to capture qualities such as the spray cone angle and the fuel film thickness. The outer domain dimensions are a radius of 2mm and also 2mm high to let the liquid sheet develop and atomizes. The refinement angle and the angle of the domain is set up to 80° accordingly to the spray angle reported in [Verdier, 2017].

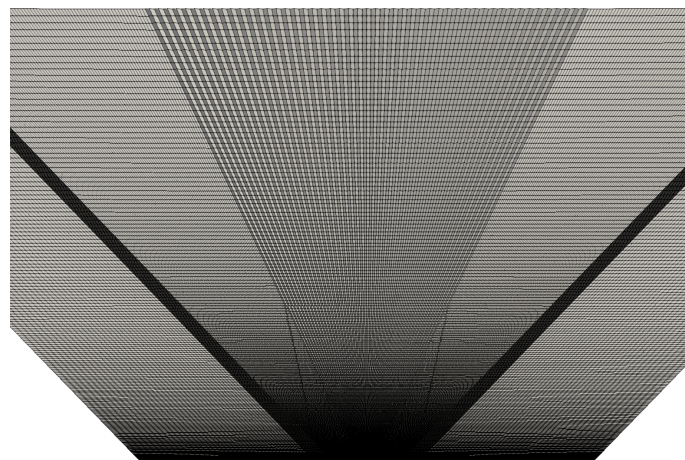


Figure 3.17 – Slice of the outer domain.

Finally, three different resolution meshes were performed. The characteristics of the computational grids are shown on Table 3.3.

	Coarse Mesh		Medium Mesh		Fine Mesh	
Number of elements	2.7e6		13.2e6		32.8e6	
Tetrahedra	0.13e6		1.6e6		3.2e6	
Hexahedra	2.6e6		11.6e6		29.6e6	
Pyramids	4.3e3		11.7e3		24.9e3	
Y ⁺	Max	Avg	Max	Avg	Max	Avg
Full geometry	66.1	12.1	21.8	2.6	3.4	1e-2
Inlet ports	66.1	9.2	21.8	2.8	1.7	0.78
Swirl Chamber	28.5	12.8	11.3	3.7	3.4	0.96
Spin Chamber	13.7	3.2	2.9	1.3	2.7	1.8
Throat	24.6	13.8	3.3	2.4	2.3	1.8
Nozzle	33.4	21.5	3.5	2.6	2.8	2.2

Table 3.3 – Inner simulation meshes characteristics.

3.4.2 Numerical set up

As it was reported in previous sections, two different operating conditions were studied experimentally. In this section, both of them are studied. Since the *interFoam* solver (see chapter 2) is an incompressible isothermal solver, to define the *N-heptane* and the air parameters, the density ρ and the kinematic viscosity ν have to be defined. Also, the surface tension σ among the two fluids. Those parameters change with the temperature, and they can be found on Table 3.4.

	Ambient Temperature		Fuel Pre-heated	
	Fuel	Air	Fuel	Air
$T[K]$	298	298	350	416
$\rho[kg/m^3]$	678.9	1.117	634.3	0.848
$\nu[m^2/s]$	5.67e-07	1.57e-05	3.67e-07	2.70e-05
$\sigma[mN/m^2]$	20.0		14.5	

Table 3.4 – Fluid characteristics for different temperatures

Boundary conditions

Three different zones are defined in the numerical domain regarding the boundary conditions. Figure 3.18 shows the boundary patches; starting from the bottom, the three inlet ports on green (number 1) where the fuel is injected, on grey (number 2) the walls of the injector are represented and, finally, on blue (number 3) the domain outlet.

The fuel mass flow rate $\dot{m}_{fuel} = 0.28g/s$ is divided by three for each tangential port. The velocity boundary condition imposed is called *flowRateInletVelocity*. The pressure is set-up as *zeroGradient* boundary condition fixing the pressure gradient to zero. Finally, a constant value is set-up for the liquid volume fraction $\alpha = 1$.

The walls are set up with usual boundary conditions. Therefore, the *no slip* boundary condition is set-up for the velocity, meaning the three components of the velocity are equal to zero. The pressure and liquid volume fraction are set-up as *zeroGradient* boundary conditions.

Finally, for the *outlet* patch, *zeroGradient* is imposed for the velocity as it is for the liquid volume fraction α . The *totalPressure* boundary condition is used and fixed to atmospheric pressure.

A summary of the boundary conditions is reported on Table 3.5 and are explained deeply on chapter 2.

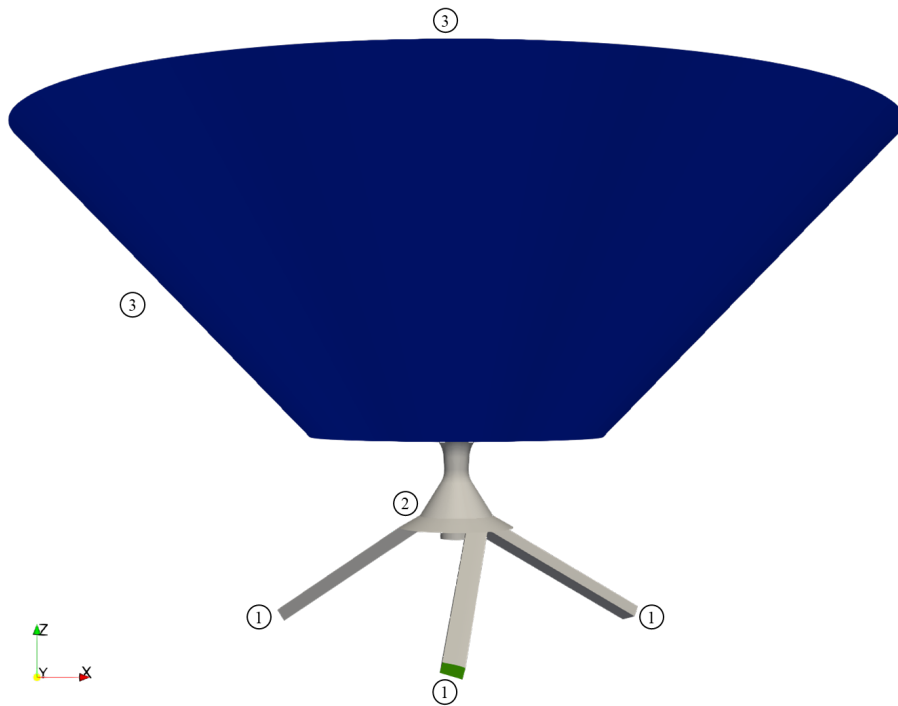


Figure 3.18 – Boundary conditions patches of the CRSB internal flow simulation.

	1. Inlet	2. Wall	3. Outlet
\mathbf{u}	Imposed flux	$\mathbf{u} = 0$	$\nabla \mathbf{u} = 0$
p	$\nabla p = 0$	$\nabla p = 0$	<i>totalPressure</i>
α	$\alpha = 1$	$\nabla \alpha = 0$	$\nabla \alpha = 0$

Table 3.5 – CRSB internal flow boundary conditions.

Numerical methods

In chapter 2 the *interFoam* solver from the *OpenFOAM v6* toolbox was introduced. This solver, is a Volume of Fluid (VoF) method solver that includes a sharpening term in the liquid volume fraction transport equation to capture the interface between the liquid and the gas. This solver uses the PISO algorithm to solve the Navier-Stokes equation and the MULES algorithm for the liquid volume fraction transport equation.

Since the nature of this flow is clearly turbulent ($Re \approx 4200$), and running Direct Numerical Simulation (DNS) simulation is out of the scope of this thesis, the turbulent flow has to be model. To capture better the dynamics of the flow, a LES formalism has been adopted with the sub-grid *WALE* model.

To discretize the equations, numerical schemes have to be imposed. The *OpenFOAM* toolbox includes robust numerical methods up to second order accurate since it is thought as a industrial toolbox to perform CFD simulations not as high efficiency and high accuracy tool. Thus, first and second order schemes have been use in time and in space. In time, the second order scheme *backward* and the hybrid first-second order *Crank Nicholson* are set. The convection schemes are either *limited linear* or *van Leer*. For more information check chapter 2.

3.4.3 Mesh converge study

To carry out a preliminary study of mesh convergence with the three mesh resolutions proposed on Table 3.3 the ambient operating conditions studied by [Verdier, 2017] are set up.

First, the initialization of the case is done. Since the dynamics inside of the injector are complex and the transient state is relatively long, reaching the steady state of the injector requires some computational resources; in order to reduce them, all the initialization process is done with the coarsest mesh. Afterwards, the results from the coarsest mesh case are mapped into the higher resolution meshes.

Initialization: Time evolution of hollow cone generation

Having a clear understanding of liquid flow emanating from orifice section could be important for some engine regimes. Considering the boundary and initial conditions, eventually a certain amount of time is required by the fluid to establish the cone-shaped flow [Razeghi and Özgür Ertunç, 2018].

Figure 3.19 shows the time evolution of the air core generation and the hollow cone shape of the spray. Figure 3.19a represents the initial conditions of the simulation where the fuel fills the whole injector. The states of the initialization of the simplex swirl atomizer simulation can be compared with the spray states on Figure 3.5 as is done by [Chen and Tang, 2020]. From Figure 3.19b to Figure 3.19d the fuel is expelled in a distorted pencil shape.

From Figure 3.19e the jet begins to break-up and is in Figure 3.19h where is comparable with the onion stage shape. From Figure 3.19j the hollow cone spray is fully developed, thus, the cone angle could be measured and also the liquid film thickness. Nevertheless, the air core is not fully developed, hence, it would have necessary $250\mu s$ more to let the air core develops reaching the bottom wall of the injector and widen it. In conclusion, the total time to initialize the simulation, and thus, the transient period of the injector from stop to nominal conditions is in the order of $0.5ms$.

Liquid Volume Fraction

Once the initialisation process is finished, the data from the coarsest mesh simulation is mapped into the more refined meshes using the OpenFOAM tool `mapFields`. This tool reads the field data from one simulation and interpolates it into the new mesh. In this case, to speed up the process, the order of the interpolation was zero, meaning that the values were mapped to the closest cell. A transient time is needed to stabilize the flow into the steady state values.

Figure 3.20 shows a central slice of the domain representing the liquid volume fraction α ; the fuel is represented on blue ($\alpha = 1$) and the air is represented on white ($\alpha = 0$).

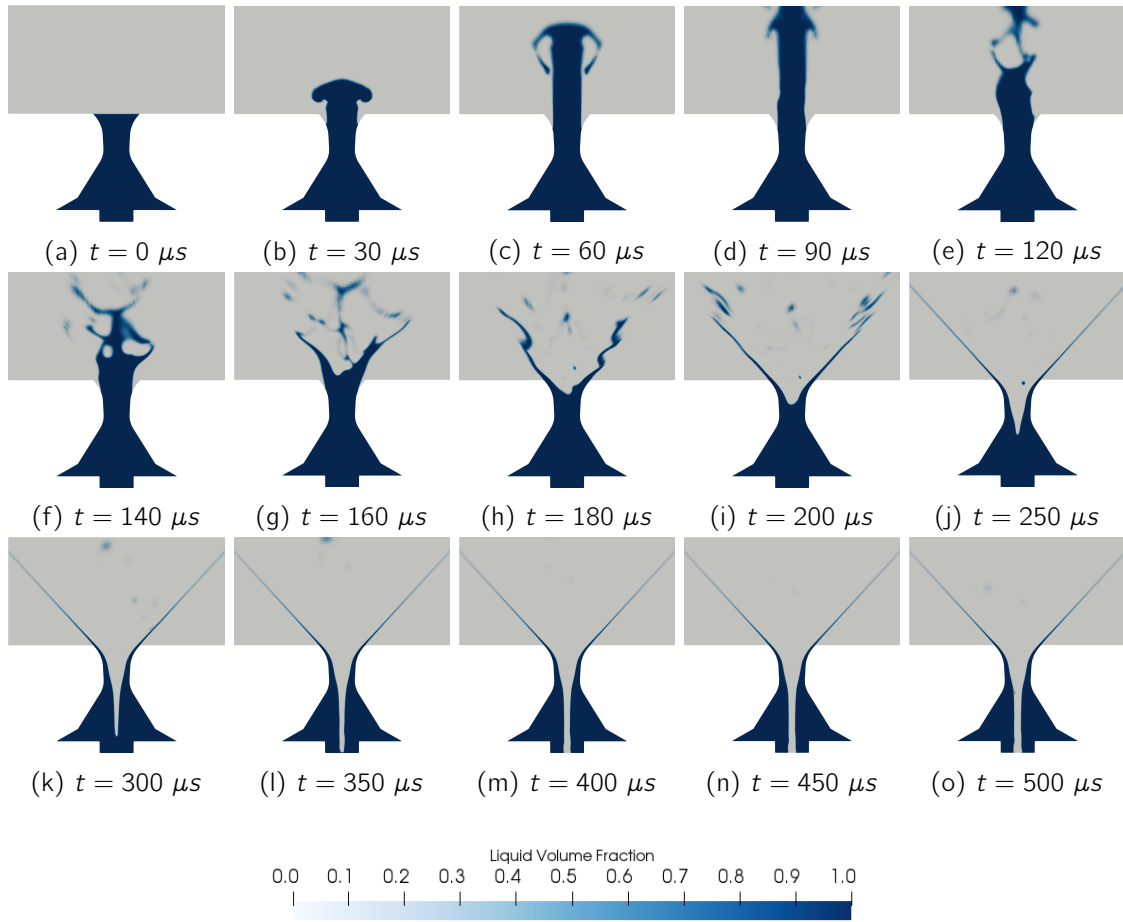


Figure 3.19 – Hollow cone evolution

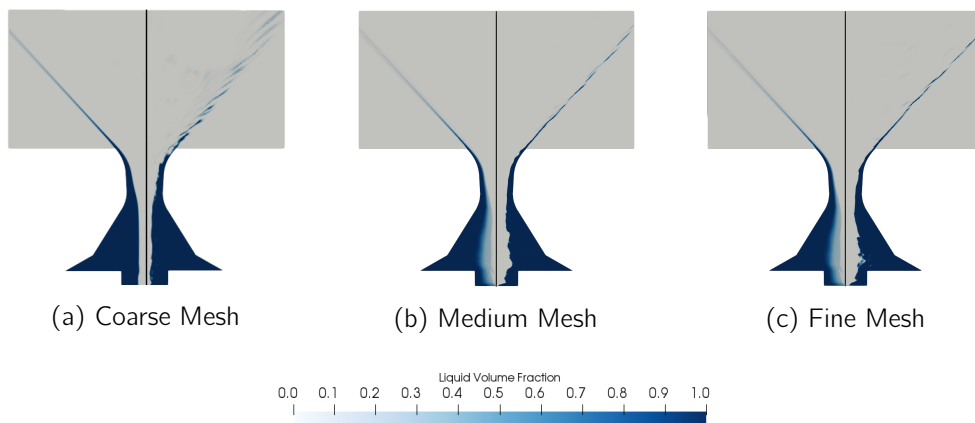


Figure 3.20 – CRSB mesh convergence study: Liquid volume fraction. At the left of each picture the time averaged values is plotted meanwhile at the right an instantaneous values is plotted.

On the coarse mesh case the air core is almost stable, not having big perturbations on the stream-wise direction up to the nozzle. Some instabilities appear near to the orifice. The diameter of the air core is almost constant from the atomizer bottom wall up to the end of the swirl chamber where it enlarges due to the divergent geometry. If we take a look into

the finer mesh cases, instabilities can be captured at the bottom part of the air core. This phenomena has been previously reported in studies such as [Sumer et al., 2012, Maly et al., 2018] where they manufactured a transparent atomizer to perform measurements on the internal flow of a simplex swirl atomizer; this effect can be seen in Figure 3.21.

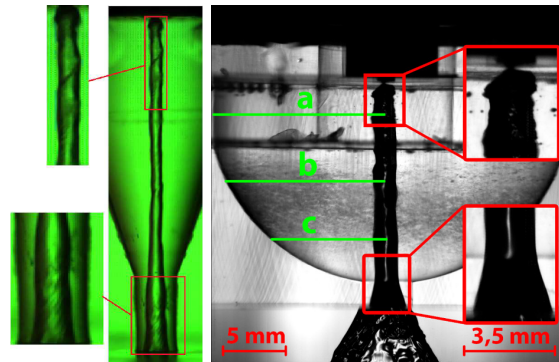


Figure 3.21 – Air core experiments. On the left: [Sumer et al., 2012]. On the right: [Maly et al., 2018]

To have a better comparison of the liquid volume fraction α , on Figure 3.22, a iso-surface for $\alpha = 0.5$ is shown representing the liquid-gas interface.

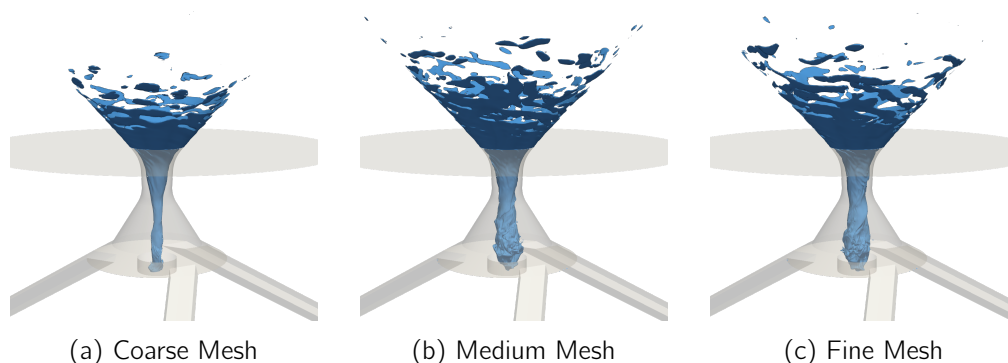


Figure 3.22 – Liquid volume fraction iso-surface: $\alpha = 0.5$.

In spite of the fact that the finer meshes are able to capture instabilities on the air core, the limitation of this computation is visible on the fuel sheet. The more refined meshes are able to capture longer liquid sheets than the coarsest mesh, but still are not comparable with the results obtained from experiments on Figure 3.23. Thus, to be able to model the fuel sheet dynamics, another methodology is proposed later on this chapter.

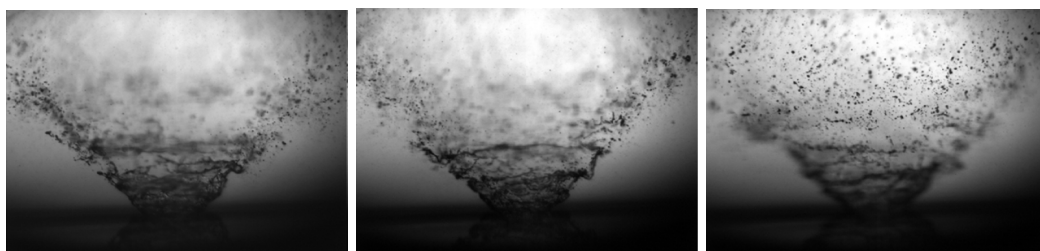


Figure 3.23 – Sample experimental pictures by [Verdier, 2017] for three different instants.

On Figure 3.24 a plot of the time averaged liquid volume fraction $\bar{\alpha}$ over the nozzle is represented for every case. This plot shows the film thickness for the three meshes. It is also plotted the empirical value obtained from Equation 3.37 and the one based on the discharge coefficient C_D . The differences with the empirical equation by [Lefebvre and McDonell, 1988] are remarkable but expected because the equation was done with a geometrically much simpler atomizer (see Figure 3.3). Nevertheless, the value obtained by C_D mach very well the values obtained from both, the medium and fine meshes.

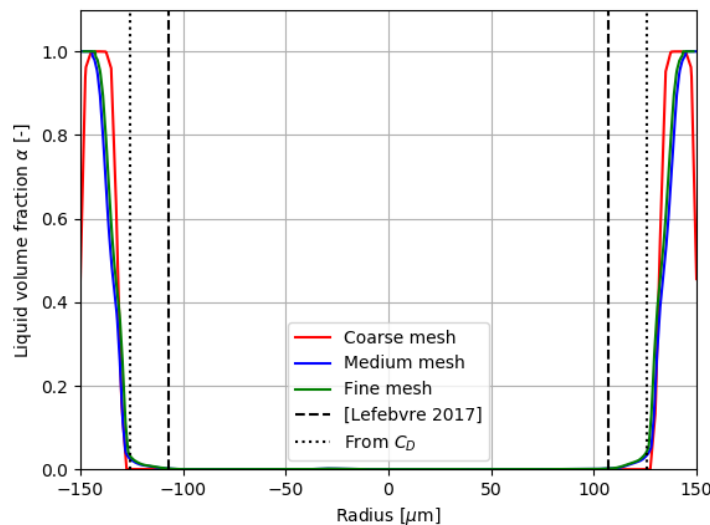


Figure 3.24 – Liquid volume fraction α plot along the radial axis on the nozzle. On blue: coarse mesh case. On green: fine mesh case. On black: empirical equation.

It is also noticed that the coarsest mesh can not capture well the instabilities of the sheet at the nozzle recovering a more constant liquid volume fraction value. On the other hand, the medium and fine meshes are able to capture those instabilities where the maximum value of the sheet thickness is near to the value obtained from Equation 3.37. The film thickness on the coarsest mesh has a value of $t^{coarse} = 24 \pm 4 \mu m$ meanwhile the medium and fine meshes give a value of $t^{fine} = 22 \pm 15 \mu m$

Eddy Viscosity

Another parameter to compare is the effectiveness of the LES turbulence model. Those models filter the sub-grid length scales, those that are smaller than the mesh grid sizes. Thus, as higher the resolution the less turbulence model is needed. In the Figure 3.25 the eddy viscosity over the liquid viscosity ν_t/ν_l is represented. It is an indicator where the LES model is playing a role.

In every case, the eddy viscosity is near zero inside of the injector. That means the LES model is not modelling the turbulence in these zones due to the high level of refinement inside the injector. Nevertheless, it can be notice that in the coarse mesh case, the eddy viscosity is higher than on the finer meshes, and moreover, around the walls. Thus, the medium and fine mesh cases are more accurate since inside the injector is closer to a Direct Numerical Simulation than the coarsest mesh case.

If we take a look to the outer domain, high values of ν_t are shown around the liquid sheet. The outer domain is less refined than the inner one and also, due to the asymmetric geometry and the wide spray cone angle, the further from the nozzle, the worse is the

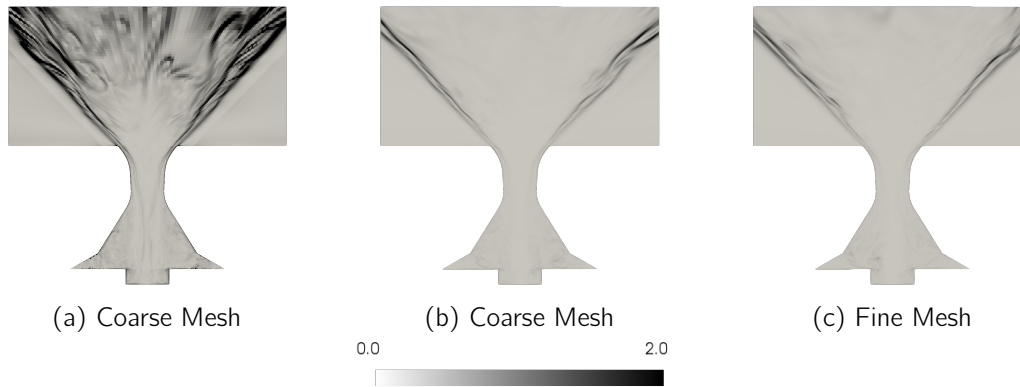


Figure 3.25 – Eddy viscosity

resolution of the mesh. This effect is also playing a role on the interface capturing method as it is reported in the following section.

Velocity field

Finally, the velocity field is represented on Figure 3.26 where the magnitude and the three components of the velocity (axial, radial and tangential) are shown. In spite of the values of the velocity are similar among the three refinement levels, it is straightforward to see that in the finer mesh cases the fluctuations appears more regularly than the coarsest mesh case due to the higher refinement. This effect is taking place more in the swirl and spin chamber where the flow is more turbulent. If we take a look to the liquid film velocity we can see the fluctuations are less frequent. The axial velocity at the nozzle is $U_a(z = 0mm) \approx 40m/s$ being higher than the averaged droplet velocity obtained by [Verdier, 2017] which is somehow expected since the liquid structures will be decelerated due to the friction with the surrounding gas.

Mesh refinement study conclusions

The coarsest mesh is enough to compute properties such as the spray cone angle and the time averaged liquid film thickness but is not capturing all the physical phenomena inside the injector. The shape of the air core is not comparable with the experiments in the scientific literature and the velocity fluctuations are not well captured in comparison with the fine mesh case.

In the other hand, to initialize the simulation is a better choice than the fine mesh since the computation is faster and less costly as it is shown in Table 3.6.

	Coarse Mesh	Medium Mesh	Fine Mesh
$\Delta t_{physical}$	5e-9 s	2.5e-9 s	5e-10
<i>CPUs</i>	112	420	672
Δt_{sim}	0.26 s	0.6 s	2.9 s
<i>CPUh/ms</i>	1.6e3	28e3	1e6

Table 3.6 – Computational time step and resources needed

The equilibrium between accuracy and computational resources has to be found and, hence, the elected mesh to carry out the study is the medium refinement. With this election we can obtain accurate results and capture well the fluctuations of the liquid sheet on the nozzle orifice with a relatively cheap computation.

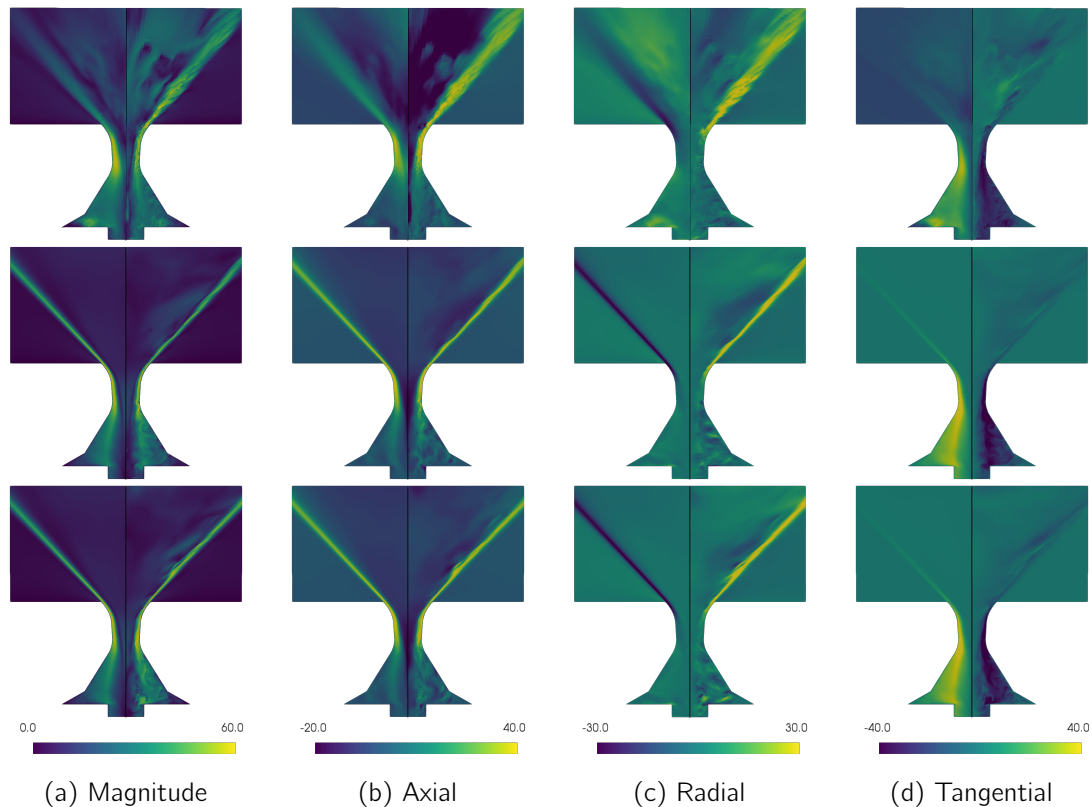


Figure 3.26 – Central slice of the velocity. From top to bottom: coarse, medium and fine meshes.

3.4.4 Discretization schemes

As it has been explained on the last section, once the case is mapped from the coarsest mesh values, the computation is run for a certain time to reach nominal values. This computation is performed with the *upwind* first order scheme reported on chapter 2. Coming from a low resolution computation to a higher resolution computation could lead into numerical instabilities and with the first order schemes we are able to stabilize them losing some accuracy since the *upwind* scheme is too diffusive. Once the simulation is stabilized the spacial schemes are switched to *limitedLinear* which is a second order accurate scheme.

We can notice the difference between these two schemes on the nozzle orifice, in particular if we take a look to the instantaneous liquid volume fraction $\alpha(t)$. Figure 3.27 shows a cross plane on the nozzle orifice $z = 0\mu m$ using the *upwind* and *limitedLinear* schemes. Meanwhile with first order schemes the liquid sheet thickness remains constant through time, setting up second order schemes enables to capture the instabilities inside the nozzle. As it is reported on the following section about the study of the atomization process of the simple swirl injector, this effect plays an important role on the atomization mechanisms.

3.4.5 Temperature variation

The main study of this section is the comparison between the numerical simulation of the CRSB injector with two operating conditions and their validation with experimental results. Both cases are performed with the medium mesh presented in the last subsection.

The higher the temperature, the lower the density is. The Reynolds number of the high temperature $Re^{HighT} = 6000$ condition case is higher than the ambient condition case

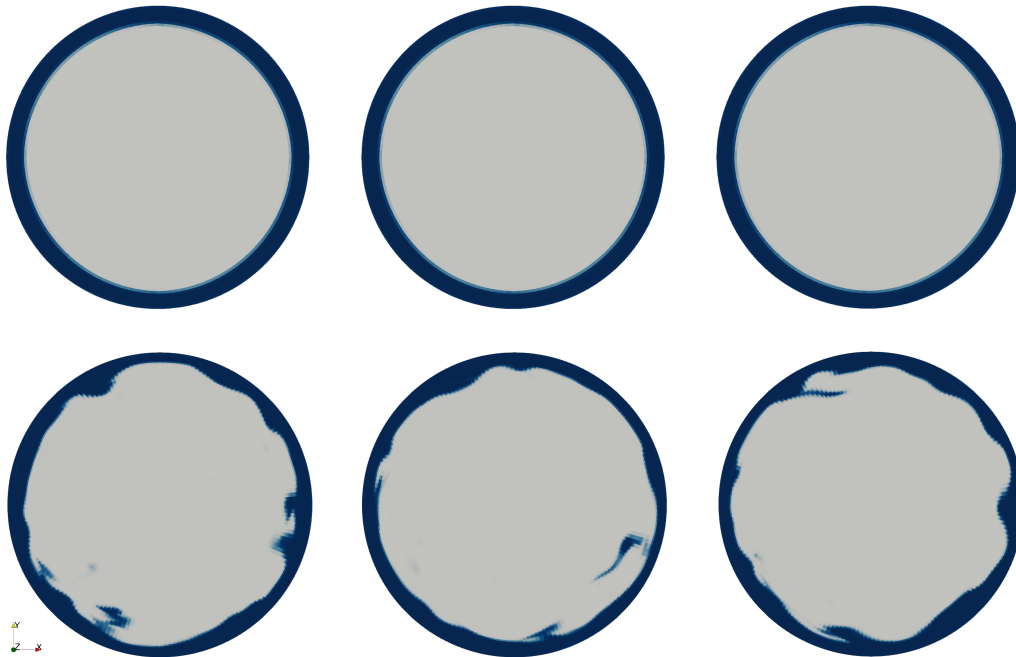


Figure 3.27 – Liquid volume fraction α contour at the atomizer outlet cross-section. Top: three snapshots using the *upwind* scheme for the spatial divergence. Bottom: three snapshots using the *limitedLinear* scheme for the spatial divergence. The time step between pictures is $\Delta t = 5\mu s$

$Re^{AmbT} \approx 4000$. Thus, the flow is expected to be more turbulent and, as is reported in [Lefebvre and McDonell, 1988], the fuel sheet thickness should be thinner, and hence, its velocity should increase to maintain the same mass flow rate.

Liquid Volume Fraction

On Figure 3.28 the iso-surface for $\alpha = 0.5$ of both cases are represented. Comparisons can not be done directly with these pictures. On Figure 3.29 pictures of the experimental spray are shown.

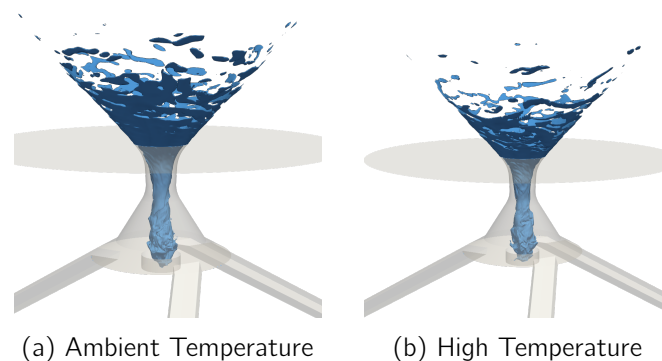


Figure 3.28 – Liquid volume fraction iso-surface: $\alpha = 0.5$.

As we can observe in both pictures, with this level of refinement in the outer zone, qualitative validation with these pictures can not be done. The fuel sheets in both numerical cases is totally flat and they break-up due to lack of grid resolution and not due to the

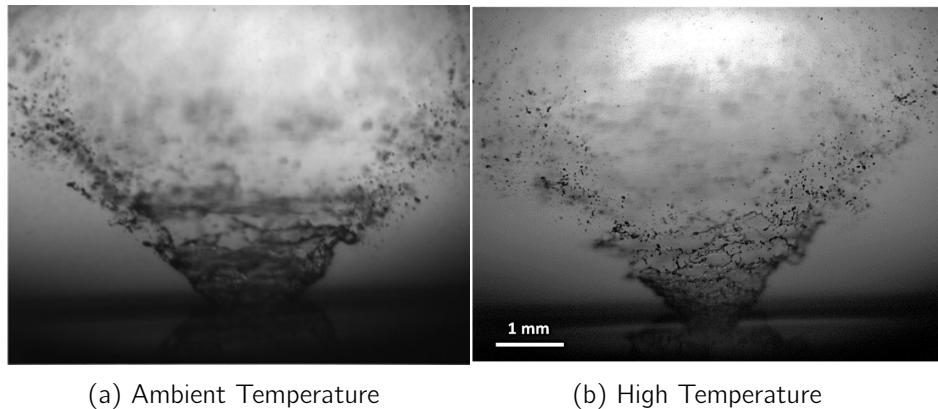


Figure 3.29 – Experimental pictures of the CRSB injector spray. On the left: ambient temperature condition by [Verdier, 2017]. On the right: high temperature condition by [Marrero, 2018].

interaction between the liquid and the gas. Anyhow, the high temperature case is breaking-up earlier than the ambient temperature case which agrees with the experimental results.

Another methodology has been defined to overcome this problem and it is shown in the last section of this chapter. However,, another parameters such as the cone angle and the liquid film thickness can still be validated with the experimental results and the empirical equations.

Liquid film thickness

The liquid sheet thickness of the high temperature case should decrease in comparison with the ambient temperature case since Reynolds number of the flow increase and so does the fuel sheet velocity. Since the fuel mass flow rate remains constant, the film thickness has to be smaller. On Figure 3.30 this effect is not easy to find out.

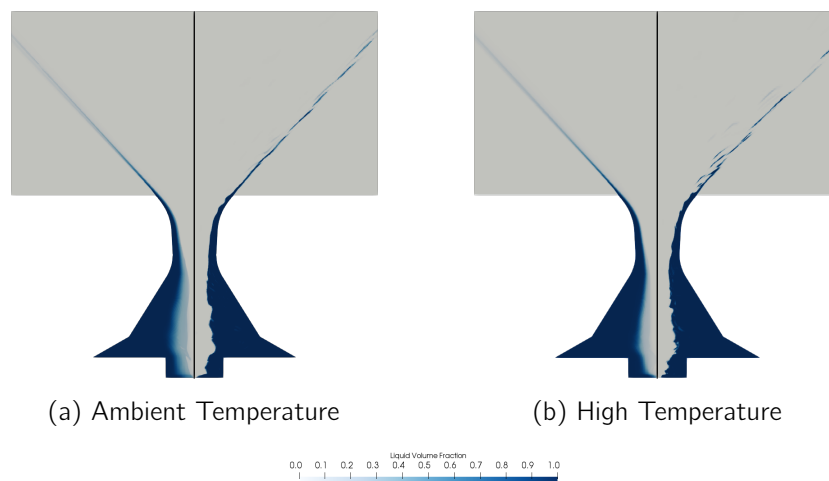


Figure 3.30 – Liquid volume fraction. On the left the time averaged value is plotted and on the right the instantaneous value is plotted.

Thus, Figure 3.31 shows the averaged liquid volume fraction α at the nozzle. Both liquid film thickness are similar being the fluctuation more prominent on the high temperature case due to the higher turbulent flow. In comparison with the empirical correlation by [Lefebvre and McDonnell, 1988], both cases have more than 40% of error. Nevertheless, as it was pointed

before, those formulas were calculated with much simpler injector geometries as they did not take into account non-straight throats.

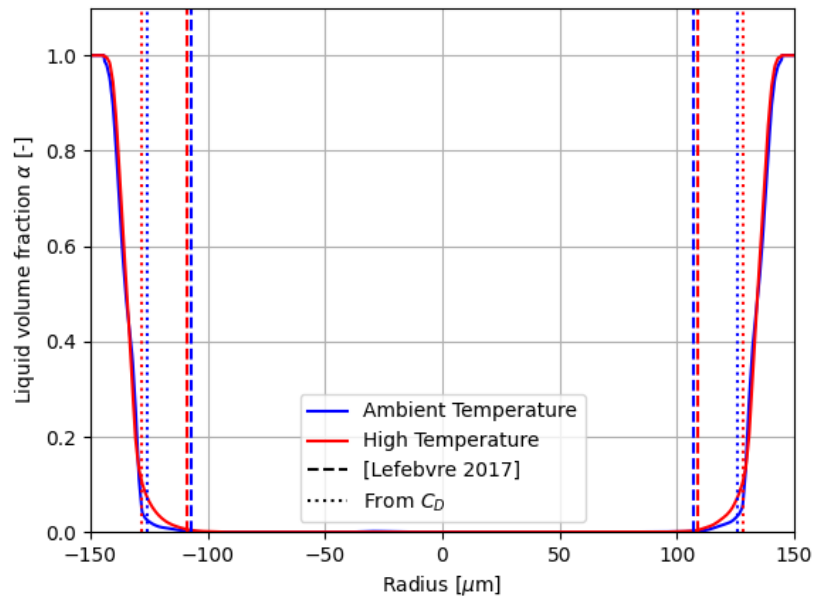


Figure 3.31 – Liquid volume fraction α plot along the radial axis on the nozzle. On blue: ambient temperature. On red: high temperature. Solid lines: simulation data. Dashed lines: empirical equation.

On the other hand, the film thickness calculated with the discharge coefficient C_D is again leading good agreement with the computational results.

Spray cone angle

The spray cone angle 2θ can be directly extracted from the simulations using the liquid volume fraction α slices on Figure 3.30. It is also possible to measure from the experimental pictures on Figure 3.29.

Table 3.7 shows the measurements of the spray cone angle 2θ and the comparison with the numerical study. It can be appreciated that the spray angle widens, slightly, with the temperature in the experiments. This property is properly caught in the numerical simulations despite the small error of 2° among the experiments and the computations.

	Simulation	Experiment	Error
Ambient Temperature	82°	80°	2.5%
High Temperature	84°	82°	2.4%

Table 3.7 – Spray angle measurements from experiments and simulations.

Injection pressure

Finally, to validate the internal flow simulation and the measuring process to obtain the internal geometry of the injector, the pressure drop between the inlet ports and the outlet of the domain is calculated. A comparison of the injection pressure for several mass flow rates was done by [Miglierina, 2021] on Figure 3.32. On blue, the value obtained from the simulation

is plotted. We can notice that the pressure drop recovered by the simulation $\Delta P^{Sim} \approx 7.5\text{bar}$ is near to the experimental values obtained by [Verdier, 2017, Marrero, 2018, Miglierina, 2021] $\Delta P^{Exp} \approx 8\text{bar}$.

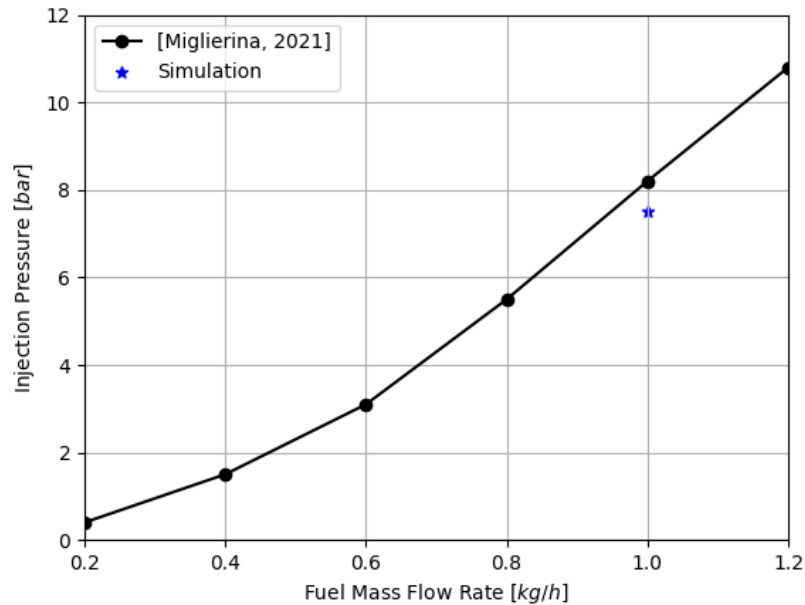


Figure 3.32 – Injection pressure for several fuel mass flow rates. On a blue star, the pressure drop obtained from the simulations is plotted.

The lower pressure drop recovered by the simulation could be for many reason. The internal geometry could not be as accurately described as if it was given by Danfoss. Another option could be that 0.5bar drops on the injector filter of even on non-simulated part of the tangential ports.

Temperature variation conclusions

The measurements of the internal geometry of the injector have been validated recovering a similar spray angle, having good agreement with the liquid sheet thickness in comparison with the theoretical equations and recovering almost the same pressure injection.

Slight differences are noticed on the two operating conditions studied. The earlier break-up of the high temperature case is captured and more turbulent flow is recovered.

The qualitative comparison with experiments can not be done since the atomization process is not properly captured; the resolution and the topology of the outer computational grid is not enough to do such study. However, the computational grid works perfectly to model the inner flow of this kind of injectors. Hence, another methodology is proposed in the next section to overcome this difficulty and to model the atomization process. The objective is to carry out a simulation only on the external zone above the nozzle using as inlet data the one computed in this section.

3.4.6 Outputs recovery data

To set up the outer flow simulation, a cross plane of the velocity field \mathbf{u} and liquid volume fraction field α are stored. The central point is the center of the orifice $(0, 0, 0)$ and the normal

vector \mathbf{n} is the axial direction $(0, 0, 1)$. Each $0.05\mu\text{s}$ the fields are stored, that corresponds to 20 computational time steps.

This procedure has been done for both temperature cases. In the next section, the interpolation on space and on time is explained in details.

3.5 External flow modelling: Spray atomization

In the last section we have seen that the hybrid mesh works good in modelling the inner flow of a simplex swirl atomizer. Nevertheless, once the fuel is ejected from the orifice, the length scales of the sheet and the droplets are much smaller than the grid resolution. To overcome this problem, studies such as [Galbiati et al., 2016, Shao et al., 2017], carried out numerical simulation of the spray generated by a simplex swirl injector. The numerical domain begins in the orifice of the nozzle and it is extended several length magnitudes to be able to catch the suction process generated by the pressure drop performed inside of the injector. As a boundary conditions they use a turbulent inlet velocity and a fixed liquid sheet thickness. On [Galbiati et al., 2016] a preliminar LES simulation is also performed to extract the velocity and liquid volume fraction fields to map it on time and on space on the external simulation. However, this preliminary simulation is not performed with the internal geometry of the injector but with a straight pipe. The qualitative comparison improves with the use of this boundary conditions.

Following these studies, an external simulation is proposed. Instead of a full isotropic, structured mesh, a periodic sector is used with a refinement zone where the spray is expected to be, to reduce the computational resources needed. The data stored from the previous simulation is used as boundary condition to preserve as much as possible the previous work.

3.5.1 Computational grid

Some tryouts were done with the same topology followed in the previous section, structured hexahedral mesh. However, the further from the orifice the worse the resolution of the cell was. This problem comes from the fact that the angle of the spray is highly wide, thus, performing an asymmetric structured mesh brings to well refined cells around the orifice nozzle ($z \sim 0\mu\text{m}$, $r \sim 0 - 300\mu\text{m}$) and large cell with big aspect ratio far from it ($z > 500\mu\text{m}$, $r > 500\mu\text{m}$). This effect avoids the interface capturing method to have sharp interfaces where the break-up process is expected. Hence, a similar topology to the studies cited above was used; an isotropic, almost structured mesh with a refinement zone performed with the open source mesher code `cfMesh`.

2D grid convergence study

Once defined the topology of the mesh, a small grid converge study was performed to find the minimal cell size. To minimize the computational resources and speed up the process, the domain was defined as 2D asymmetric. In this case, the meshes were made with the `blockMesh` utility.

Figure 3.33 shows the liquid volume fraction α on three different cases. From left to right. the cell size is $2\mu\text{m}$, $1\mu\text{m}$ and $0.5\mu\text{m}$; every resolution is able to capture the interface between the liquid and the gas, not only on the liquid sheet but also on the "droplets" that break-up from it. The main differences from the lowest resolution to the highest one is the lack of instabilities of the liquid sheet. Even though the resolution is higher than the one showed on Figure 3.30 at the external zone, $2\mu\text{m}$ are not enough to capture the fluctuations triggered on the liquid sheet by the air motion. Instead, on the case with $1\mu\text{m}$ of cell size, those fluctuations are captured. Moreover, the interface is better captured as it was expected and the shape of the 2D "droplets" are more realistic.

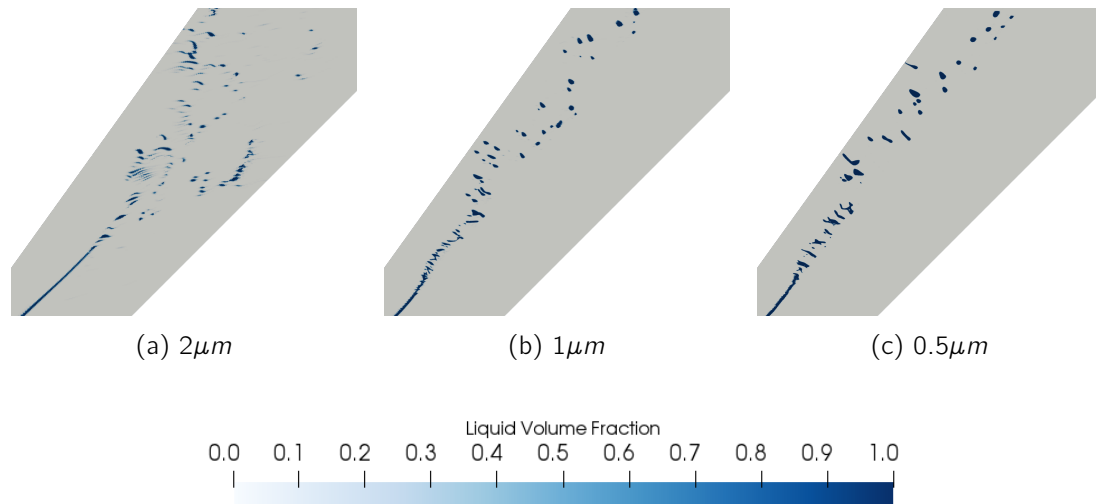


Figure 3.33 – Grid convergence study. Liquid volume fraction for cases of cell size from left to right: $2\mu m$, $1\mu m$, $0.5\mu m$

Finally, the finer resolution improves the interface capturing but it does not increment the instabilities triggered on the sheet.

Table 3.8 reports mesh information for the three different meshes used in the grid convergence study. Since the simulation are 2D the number of cells increased by a factor of two every time the resolution is doubled. Since the Courant number remains the same for the three cases, the physical time step $\Delta t_{physical}$ is reduced by half every refinement and also the time step for each iteration Δt_{sim} is increasing by a factor of two.

	$2\mu m$	$1\mu m$	$0.5\mu m$
Number of elements	0.27e6	1.1e6	4.4e6
Cells at liquid sheet	4	8	16
$\Delta t_{physical}$	1.7e-8 s	0.8e-8 s	0.4e-8s
<i>CPUs</i>	72	72	72
Δt_{sim}	0.92 s	1.8 s	3.7 s
<i>CPUh/ms</i>	≈ 1000	≈ 4500	≈ 18500

Table 3.8 – 2D grid convergence study: mesh information.

Finally, the cell size chosen is $1\mu m$ since the mesh resolution is enough to capture the instabilities of the liquid sheet and also the computational resources needed can be managed in a 3D case. Of course, the $0.5\mu m$ cell size resolution is better on accuracy, but not only the number of elements will increase the computational resources, but the small time step required will increase hugely the time needed to perform the simulation.

3D sector mesh

The outer domain is 45° a sector domain to reduce the computational resources. The geometry and the boundary condition used are shown on Figure 3.34.

The number 1 is the inlet patch of the domain. It is an arc which radius is equal to the orifice radius. The boundary conditions for the velocity \mathbf{u} and the liquid volume fraction α is fixed dynamically on time with the results from the previous inner flow simulation. The pressure p is set as *zeroGradient* boundary condition.

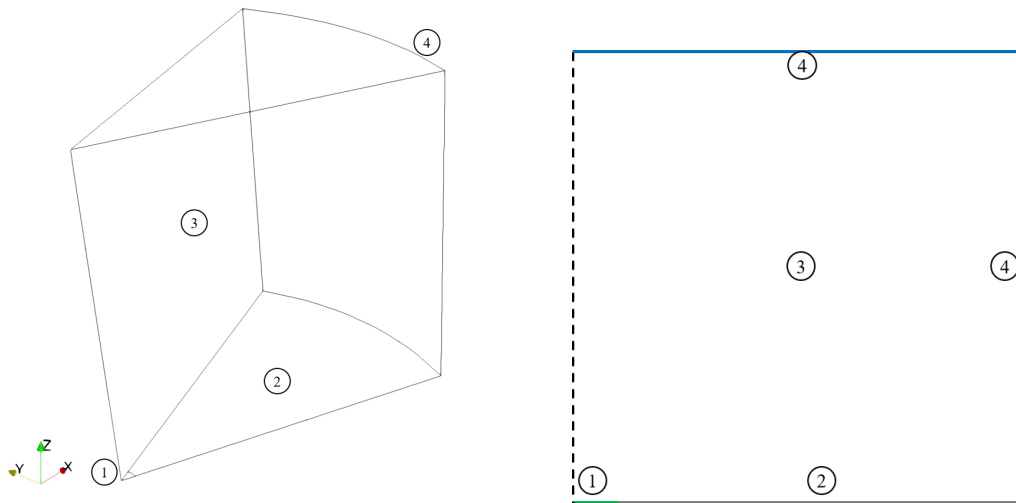


Figure 3.34 – Geometry domain and boundary condition of the external flow simulation. 1: Inlet. 2: Wall. 3: Cyclic patches. 4: Outlet.

The number 2 is set as boundary conditions. The velocity \mathbf{u} is set as *noSlip*. The pressure p and the liquid volume fraction α are set as *zeroGradient*.

The number 3 are two periodic patches. In *OpenFOAM* this boundary conditions are called *cyclic*; specifically, in this case, as the two patches are not equally created, a version of this boundary condition has to be used and it is called *Cyclic Arbitrary Mesh Interface*.

Finally, the number 4 is the outlet of this simulation. As it was set up in the previous simulation, the velocity \mathbf{u} and the liquid volume fraction α are set as *zeroGradient* and the pressure p is set as *totalPressure* already explained on Equation 2.18.

A summary of the boundary conditions is reported in Table 3.5:

	1. Inlet	2. Wall	3. Periodic	4. Outlet
\mathbf{u}	$\mathbf{u} = \mathbf{u}(t, x)$	$\mathbf{u} = 0$	Cyclic	$\nabla \mathbf{u} = 0$
p	$\nabla p = 0$	$\nabla p = 0$	Cyclic	totalPressure
α	$\alpha = \alpha(t, x)$	$\nabla \alpha = 0$	Cyclic	$\nabla \alpha = 0$

Table 3.9 – Boundary conditions on the sectorial outer CRSB domain

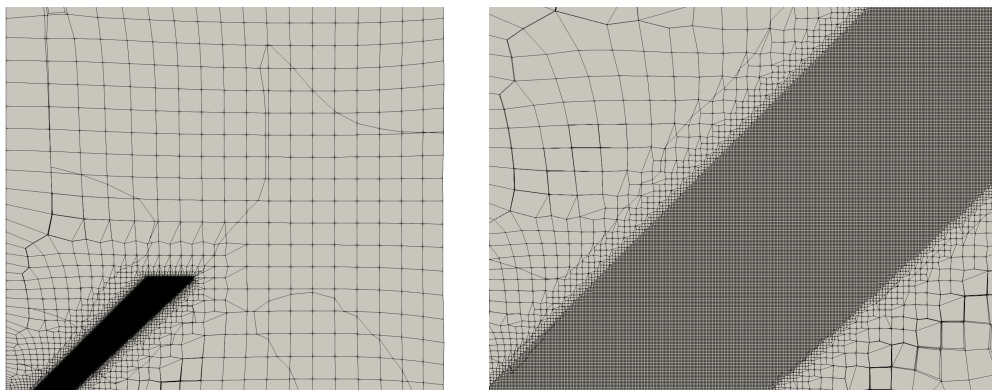


Figure 3.35 – External simulation mesh

To perform the mesh, the open source code *cfMesh* is used since it is possible to make cartesian, isotropic, regular meshes. This software was thought to work with *OpenFOAM*. On Figure 3.35 the mesh of the external flow simulation is shown. It is a mostly hexahedral mesh with few tetrahedral and polyhedral elements. A refinement zone is set with a hollow cone shape to achieve a better resolution to match the $1\mu\text{m}$ cell size of the previous subsection.

The mesh has $88\text{e}6$ elements where most of them are inside of the refinement zone.

3.5.2 Coupling between numerical simulations

The coupling between simulation is done storing the data from the velocity \mathbf{u} and the liquid volume fraction α from the internal flow simulation and setting up the inlet boundary condition of the external flow simulation as *timeVaryingMappedFixedValue* boundary condition already implemented in *OpenFOAM*.

This boundary conditions takes the data from one field and interpolates it linear on the patch. It also interpolates linear on time the data given if it has more than one time step. The data have been stored each $0.05\mu\text{m}$.

To validate the efficiency of the boundary condition, the conservation of the swirl number and the turbulent kinetic energy was checked.

Swirl number

At the first section of this chapter the importance of the swirl motion inside the injector was remarked. The degree of swirl for a swirling flow is usually characterized by the swirl number. It was originally proposed by [Chigier and Beér, 1964] and simplified by [Sheen et al., 1996] as follows:

$$SN = \frac{G_{tg}}{RG_{ax}} = \frac{\int_0^R wur^2 dr}{R \int_0^R u^2 r dr} \quad (3.44)$$

where SN is the swirl number. G_{tg} is the axial flux of the tangential momentum, G_{ax} is the axial flux of the axial momentum, R is the outer radius, w and u are the tangential and axial velocity at corresponding radial position r .

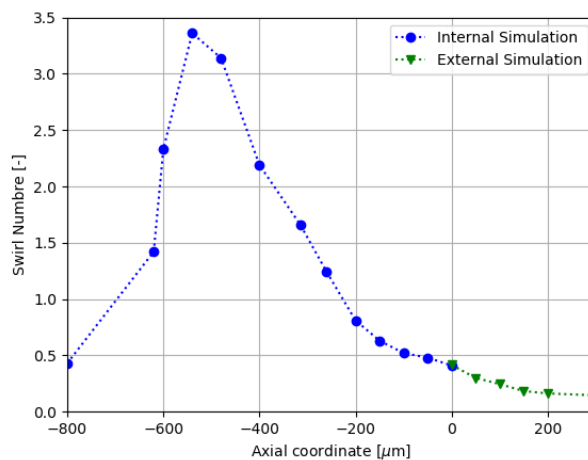


Figure 3.36 – Swirl number along the axial axis

Figure 3.36 shows the swirl number evolution along the axial axis (Z) of the ambient temperature case. In blue is plotted the swirl number of the internal flow and in green the

external flow. The peak of SN is reached inside the spin chamber in agreement with the theory. After this point, the swirl motion is reduced on the injector's throat reaching values below 1.0 near to the nozzle. Once the liquid sheet loses the centripetal force performed by the wall, the tangential momentum is transform into radial momentum, and thus, the SN is becoming zero. It also can be appreciated that the output from the internal flow simulation match the input for the external flow simulation.

Turbulent kinetic energy

The preservation of turbulent kinetic energy (TKE) is fundamental in the mapping process. Since not every time step is stored and mapped into the external flow simulation, some turbulence data can be lost. In addition, the sub-grid turbulence can be lost in the process. To compare the good behaviour of the method, the diagonal of the Reynolds stress tensor are plot on Figure 3.37.

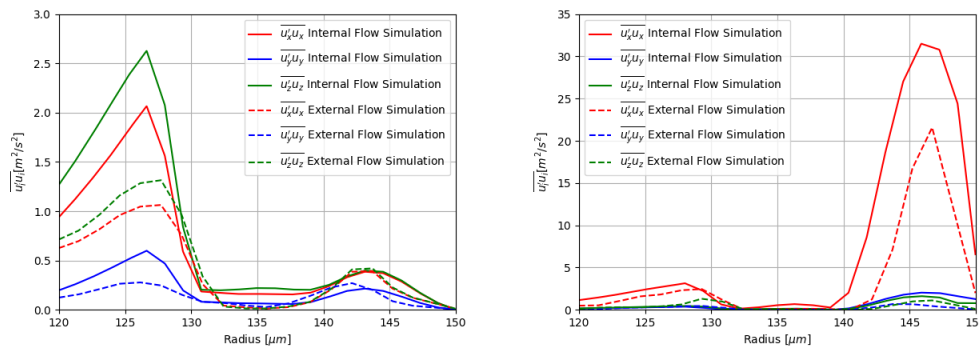


Figure 3.37 – Turbulent kinetic energy. On the left: resolved scales. On the right: sub-grid energy.

It can be observed, that in general, the turbulent kinetic energy is underestimate in the external flow simulation. This effect means that some data of the turbulent flow is miss in the mapping process. Nevertheless, the agreement between the two simulation is good enough to ensure accurate results on the external flow simulation. It is remarkable that, despite of no mapping or injecting sub-grid turbulence to the domain, the sub-grid turbulent kinetic energy computed in the external simulation has good agreement with the internal one.

3.5.3 Outer domain results

The aim of this section is to validate the process, starting from the geometry measurements, going through the two simulation methodology and finishing with a qualitative comparison with experiments.

The simulations has been launch using 1400 CPUs with a total time of 6 days. Table 3.10 shows the computational resources needed to perform $1ms$ of this simulations. The total time simulated within these 8 days is $0.1ms$.

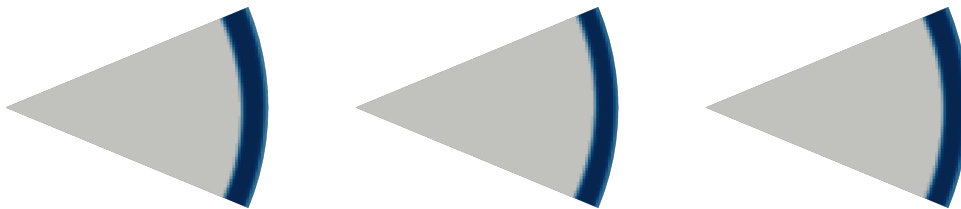
Fuel sheet fluctuation study

On the internal flow modelling section, a remark about the fuel sheet fluctuation has been done. With first order schemes none fluctuation was recovered but with second order schemes the fuel sheet had instabilities. Therefore, to study the differences on the atomization mechanism with and without instabilities on the liquid sheet thickness two simulation have been carried out with the ambient temperature operating conditions. Both simulation have been carried out with second order schemes on space and on time.

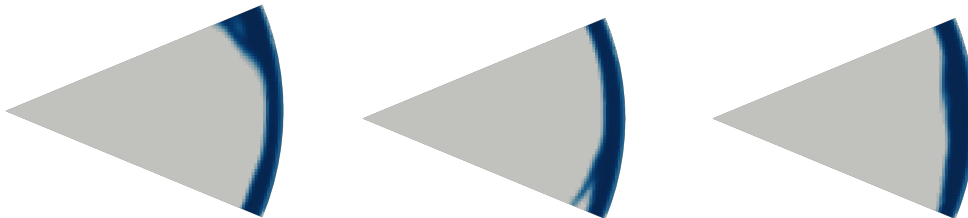
	Ambient Temperature	High Temperature
Number of elements	88e6	88e6
Cells at liquid sheet	16	14
$\Delta t_{physical}$	8.1e-10 s	7.6e-10 s
CPU s	1400	1400
Δt_{sim}	8 s	8 s
CPU h/ms	$\approx 3.8e6$	$\approx 4.1e6$

Table 3.10 – Computational resources needed for the 3D outer simulation

Figure 3.38 shows the liquid volume fraction plotted on the inlet patch of the external sectorial simulation for the data recovered with the *upwind* scheme (on the top) and the *limitedLinear* scheme (on the bottom).



(a) First order upwind scheme. From left to right: $t = 80\mu s$, $t = 85\mu s$, $t = 90\mu s$.



(b) Second order limitedLinear scheme. From left to right: $t = 60\mu s$, $t = 65\mu s$, $t = 70\mu s$.

Figure 3.38 – Liquid volume fraction on the inlet patch. On the top: constant thickness. On the bottom: fluctuating fuel sheet.

On Figure 3.39 the results from the two cases are shown. The iso-surface for $\alpha = 0.5$ is plotted for both cases and compared qualitatively with an experimental picture by [Miglierina, 2021]. It can be observed that on the constant sheet thickness case the liquid sheet remains straight until it breaks-up meanwhile on the experiments there are fluctuation starting on the nozzle orifice. Another difference is the arrangement of the ligaments; on the experiments, the ligaments are arranged on a transversal plane meanwhile on the simulation are formed along the streamwise direction. Finally, the droplet formation seems not fully developed with almost flat liquid structured.

On the other hand, the results from the fluctuating fuel sheet match better the experimental results. In this case, the fluctuation of the liquid sheet start from the beginning of the domain. The ligaments are arranged in the same way than the experimental picture and the droplets seems on the same order than the experimental ones.

In conclusion, the data from the internal flow simulation is essential to carry out an accurate modelling of the atomization process.

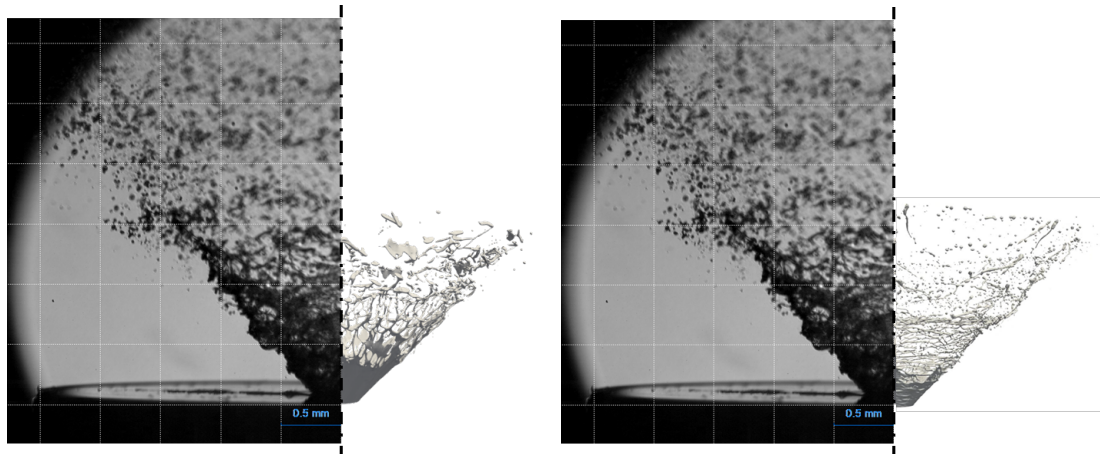


Figure 3.39 – On the left: Comparison among the iso-surface ($\alpha = 0.5$) from the constant fuel sheet thickness and the experimental picture by [Miglierina, 2021]. On the right: Comparison among the iso-surface ($\alpha = 0.5$) from the varying fuel sheet thickness and the experimental picture by [Miglierina, 2021]

Temperature variation study

On Figure 3.40 the liquid volume fraction field is represented for both operating conditions. On the left of every picture the time averaged field is plotted and on the right the instantaneous one. In comparison with Figure 3.30, the outer flow simulation can capture the instabilities of the liquid sheet and also the break-up process is taking place in both simulations.

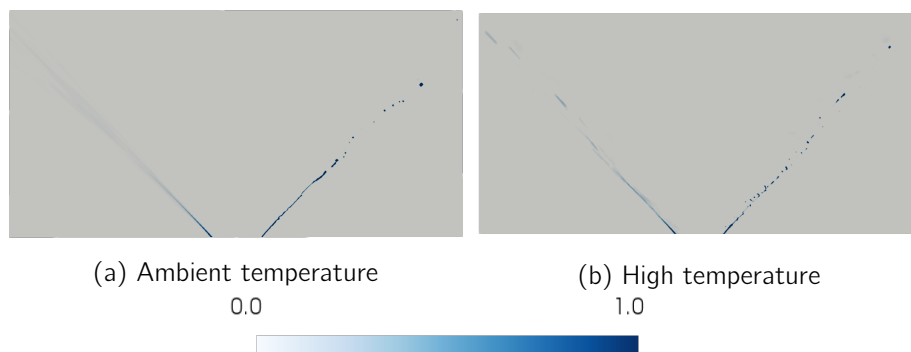


Figure 3.40 – Liquid volume fraction middle slice. On the left is represented the time averaged value. On the right is represented the instantaneous value.

It can be observed that since the liquid sheet thickness is thinner in the high temperature simulation, the break-up also takes place before. This is in agreement with the experiments shown in Figure 3.29.

Figure 3.41 shows the velocity magnitude of both simulations. Overall, it can be noticed that the high temperature simulation reach higher velocities than the ambient temperature simulation. That is in agreement with [Marrero, 2018] and [Verdier, 2017] where the average velocity of the droplets was measured.

On Figure 3.42 the axial velocity is represented. In these pictures, the suction effect, due to the pressure drop inside of the injector can be noticed. Thus, the mapping method is replicating the physics inside the injector. Moreover, a big re-circulation zone of the air is caught at the internal zone of the liquid sheet and near to the axis. This are re-circulation is

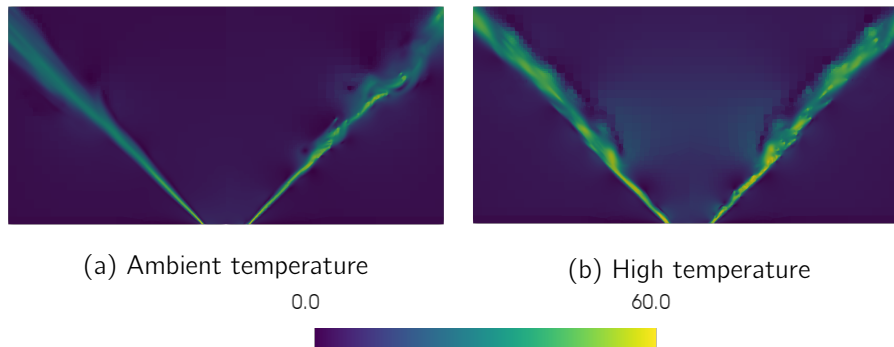


Figure 3.41 – Velocity magnitude. On the left of each picture: time averaged value. On the right of each picture: instantaneous value

the one which triggers the liquid sheet to fluctuate. Compared to the internal flow simulation, in this case, more physical effects are captured.

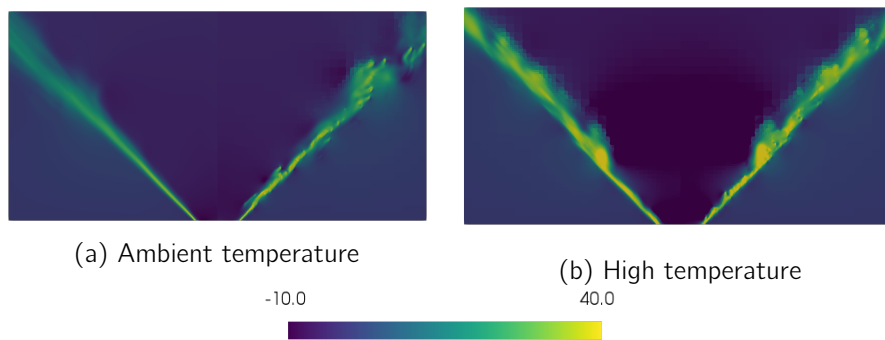


Figure 3.42 – Axial velocity. On the left of each picture: time averaged value. On the right of each picture: instantaneous value

Figure 3.43 and Figure 3.44 represents the radial and tangential velocities respectively. As it happened with the internal flow simulation, when the liquid loses the walls of the injector, the tangential component of the velocity is converted, slowly, into the radial component. It can be appreciated in those pictures where the tangential velocity is attenuated meanwhile the radial velocity is much higher than inside of the injector.

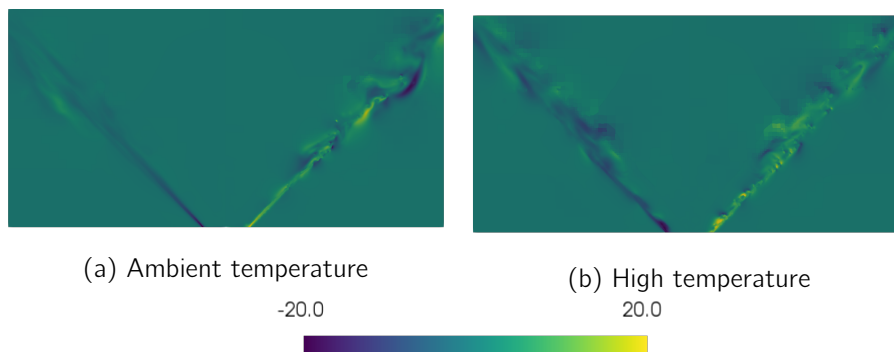


Figure 3.44 – Tangential velocity. On the left of each picture: time averaged value. On the right of each picture: instantaneous value

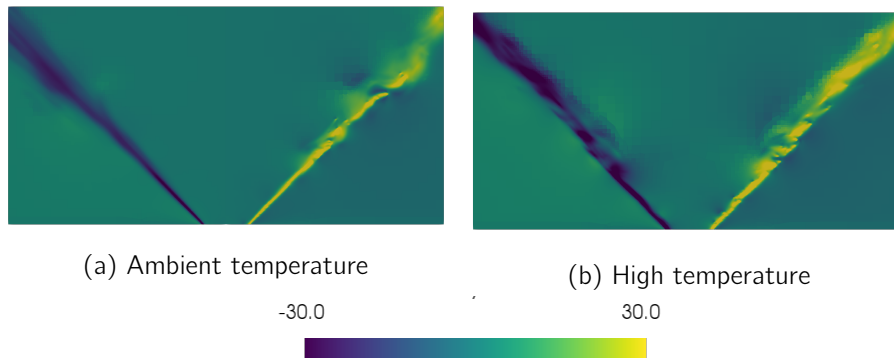


Figure 3.43 – Radial velocity. On the left of each picture: time averaged value. On the right of each picture: instantaneous value

Qualitative comparison

The main problem found in the internal flow simulation was the lack of instabilities that trigger the liquid sheet to break-up. As we have already seen, the external flow simulation is capable of catch those perturbations. Following the same procedure than on the last section, the iso-surface $\alpha = 0.5$ shown on Figure 3.45 is a rendering of the 45° sector simulation to have a clearer view of the spray.

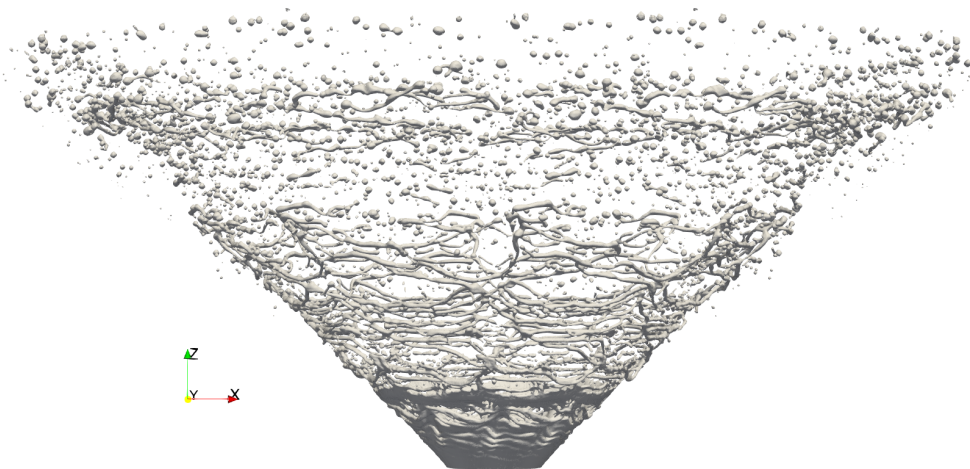


Figure 3.45 – 360° iso-surface ($\alpha = 0.5$) rendering of the ambient temperature case.

Before to compare the iso-surface rendering with the experimental pictures, a comparison among different values of α to create the iso-surface are shown on Figure 3.46. This picture shown the iso-surface rendering for five values of α : 0.1, 0.25, 0.5, 0.75, 0.9. We take the $\alpha = 0.5$ iso-surface as a reference and we can compare also with a liquid volume fraction contour where we can see that the interface thickness is, indeed, recovered by several cell. In spite of the form change among iso-surfaces with different value of α , we can see that the liquid structures remains unchanged. It is not until we check the extremes values ($\alpha = 0.1$ and $\alpha = 0.9$) where we can see some differences. We can say that the resolution is enough to capture the interface, despite the fact that having a finer refinement would lead into a sharper interface. From now to the end of the chapter, every iso-surface is represented for $\alpha = 0.5$

Figure 3.45 shows the results for the ambient temperature case based on the work by

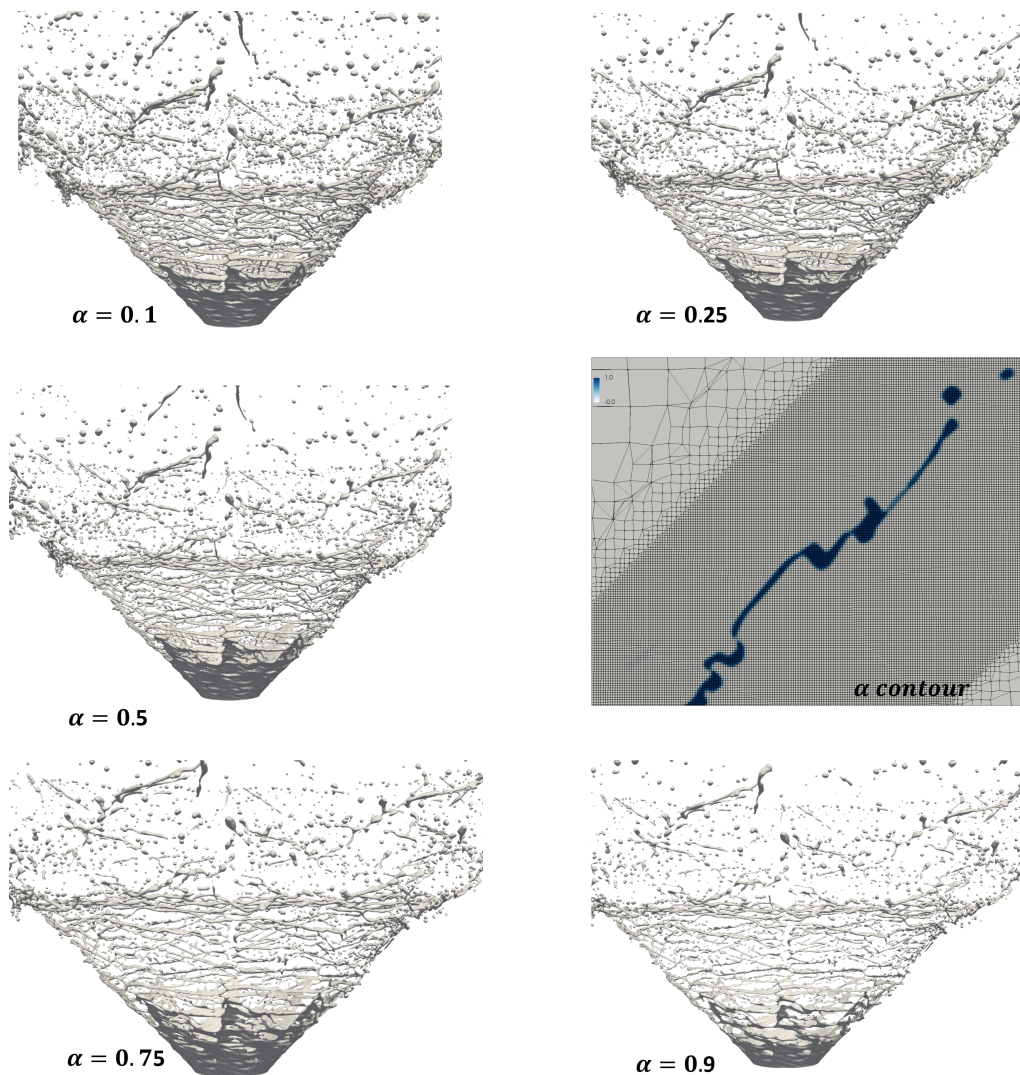


Figure 3.46 – Ambient temperature iso-surfaces for several values of α . In the middle the iso-surface $\alpha = 0.5$ and a contour of the liquid volume fraction are represented as a reference.

[Verdier, 2017, Miglierina, 2021]. It can be seen that the liquid sheet has small waves until it breaks-up ($z = 0.2mm$) into smaller transversal ligaments. Afterwards, the ligaments begin to break-up from $Z = 0.2mm$ up to $Z = 0.4mm$ into smaller droplets. It can be remarked that the liquid sheet and also the ligaments do not fluctuate on stream-wise direction. This effect could be due to the periodicity imposed as boundary condition on the side patches. Some of the break-up mechanisms captured are mostly due to numerical resolution and not due to a physical process. Anyhow, the interface capturing method (counter flux compression explained on chapter 2) keeps the ligaments in a correct shape and that leads to a physical spray atomization into droplets.

Figure 3.47 shows a comparison among the iso-surfaces and the experimental pictures taken by [Verdier, 2017]. The agreement among simulation and experiments in general terms is good. As it has been said, the big fluctuations that are captured on the liquid sheet on experiments are not appearing on the simulations. Nevertheless, on this pictures the correct arrangements of the ligaments can be validated.

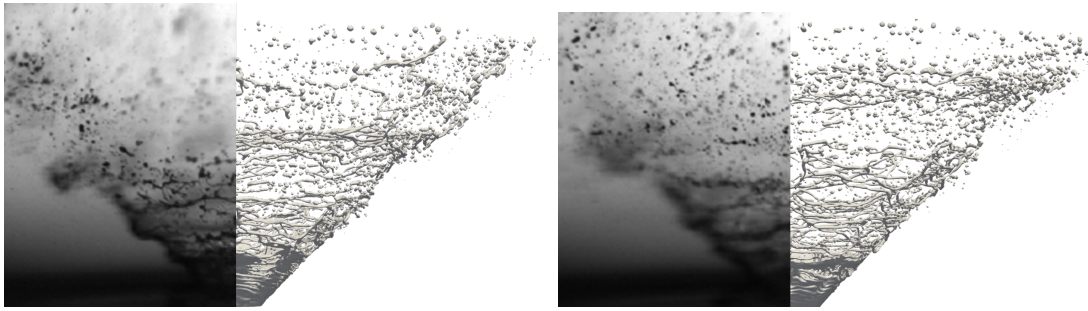


Figure 3.47 – Qualitative validation of the ambient temperature case compared with experimental pictures by [Verdier, 2017]

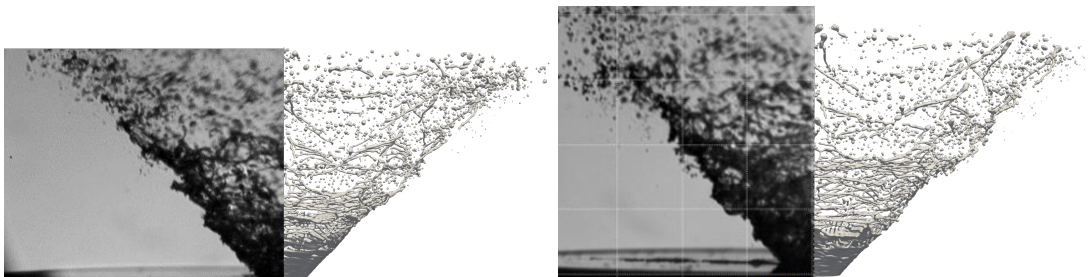


Figure 3.48 – Qualitative validation of the ambient temperature case compared with experimental pictures by [Miglierina, 2021]

A comparison with the work by [Miglierina, 2021] is also done on Figure 3.48. This experimental work is more recent and more focused on the spray atomization. It can be noticed that the picture is more focused on the early stage of the atomization and a manufacturing technique has applied to the nozzle to be able to capture the liquid sheet at the nozzle orifice. On these pictures the small fluctuation of the liquid sheet can be appreciated on experiments and how they replicated on simulations. Some grey and white holes can be found on the experimental picture and it gives us an idea where the liquid sheet begins to break-up and it is well recovered by the simulation.

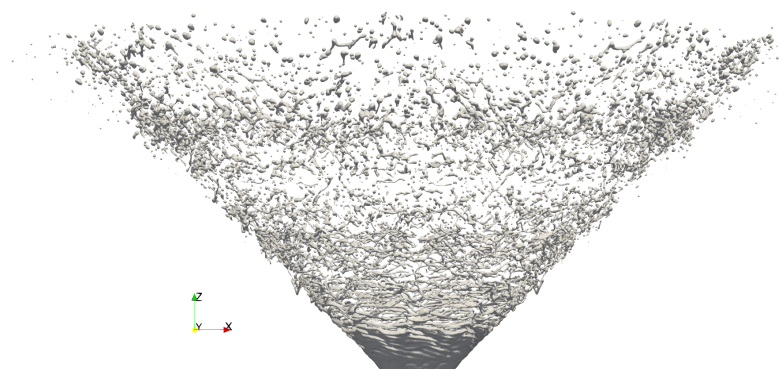


Figure 3.49 – 360° iso-surface ($\alpha = 0.5$) rendering of the high temperature case.

Figure 3.49 shows the iso-surface $\alpha = 0.5$ for the high temperature case based on the work by [Marrero, 2018]. It is similar to the ambient temperature case but the sheet break-up takes place earlier at high temperature which is in agreement with the experiments.

A comparison with experiments has also been done on Figure 3.50. On the same way, there are good agreements between experiments and simulation. The same problems of lack of big fluctuation is found on this high temperature case. The droplet diameter seems on the order of the experimental picture.

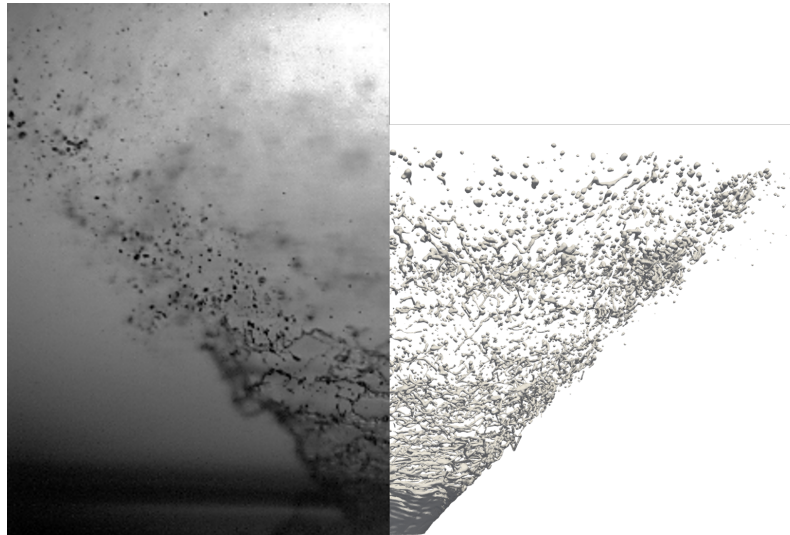


Figure 3.50 – Qualitative validation of the high temperature case compared with experimental pictures by [Marrero, 2018]

3.6 Conclusions

Modelling a commercial simplex swirl atomizer is not a straightforward process. Beginning with the fact that the internal geometry of the injector is unknown and most of the times it can not be requested to the company, going through meshing a complex geometry for a multiphase modelling. And finishing on the fact that the computational resources required for this kind of injectors are high.

On this chapter, a solution for every of those problems has been proposed and validated. The internal geometry of the injector can be recovered using experimental measurement techniques such a computed tomography scan, optical microscope visualization and scanning electron microscope visualization. Due to it is not possible to apply some techniques on the inner zone of some pieces, a silicon molding technique has been applied to afterward measure the molds.

The internal flow of the injector has been modelled using a hybrid numerical grid to avoid numerical instabilities created due of the use of a full structured mesh on a complex geometry. With this computation main parameters of the spray can be computed such as the spray cone angle and also the liquid sheet thickness. Along side with the pressure drop recovered from the simulations, all of those parameter match the experimental results validating not only the modelling but also the experimental measurement of the pieces. A slight variation of the results is also noted changing the operating conditions and in agreement with the experiments.

The atomization process is not an easy task to model on this kind of injectors due to the finer the spray the more resolution is required. The amount of computational resources required is huge to run a single simulation. Thus, a multi-scale, multi-simulation coupling was proposed. Using the data computed and stored from the internal flow simulation, an

outer simulation beginning at the nozzle orifice has been proposed. Moreover, to reduce the computational resources and make the simulation viable a 45° sector domain has been made. It has results on an accurate simulation where it is true that some information is lost but most of it is preserved through simulations. The importance of the coupling is also demonstrated when we compare the outer flow simulation with a liquid sheet with a constant thickness and with a varying thickness.

The proposed workflow could be applied to any simplex swirl atomizer similar to the one described or extrapolated to atomizers with different geometries. The inner flow modelling could be interesting for industrial purposes since the computational requirements are relatively low and parametric studies on the geometry lengths can be performed to see the differences on the internal flow.

4 | CHAiRLIFT atomizer

Performing an unique single simulation to model an airblast atomizer is a complex and costly task. Therefore, a workflow to divide the physical phenomena involved inside of this kind of atomizers is proposed on this chapter. To validate the process the atomizer used on the CHAiRLIFT burner is studied. This chapter follows the workflow proposed on chapter 2 reporting the configuration and the results of the preliminar steps to finish with the airblast simulation. Due to lack of experimental data to validate the process, the results have been validated with empirical equations described at the beginning of the chapter.

Contents

4.1	Prefilming airblast atomization	70
4.1.1	Film thickness	70
4.1.2	Sauter Mean Diameter	72
4.1.3	Droplet mean velocity	74
4.2	KIT-ITS atomizer	74
4.2.1	Operating Conditions	75
4.3	Air flow modelling	75
4.3.1	Computational grid	76
4.3.2	Numerical set-up	76
4.3.3	Results	77
4.4	Estimation of the liquid film thickness	78
4.4.1	Numerical domain	79
4.4.2	Computational mesh	79
4.4.3	Numerical set-up	80
4.4.4	Results	80
4.5	Airblast prefilming modelling	81
4.5.1	Numerical domain and computational grid	81
4.5.2	Numerical set-up	82
4.5.3	Results	83
4.6	Conclusions	85

This chapter addresses the numerical study of the airblast atomizer from the CHAIRLIFT project. It begins with a brief introduction of the prefilming atomization, how it works and its characteristics. Following with methods to calculate the main characteristics of the spray expelled from this kind of atomizers; from the more traditional ways to the newer ones. To finish with the description of the CHAIRLIFT atomizer and the strategy followed to address it.

As it was explained on chapter 1, the spray characterization is needed inside the CHAIRLIFT project to set-up properly the lagrangian spray model used by the University of Florence (UNIFI) to carry out the reactive simulation. The coupling between the multiphase and the reactive simulation is shown on chapter 5 which is not straightforward due to the use of different CFD solvers.

4.1 Prefilming airblast atomization

The main principle behind the airblast atomization is the employment of the kinetic energy of a flowing airstream to shatter the liquid sheet into ligaments and then into smaller droplets. This kind of atomizers are especially suited for combustion systems operating at high pressures. They require low fuel pump pressures and produce a fine spray. In addition, this process ensures a good mixing of air and fuel, and hence, the combustion process is characterized by very low soot formation and a blue flame of low luminosity, resulting in a relatively low flame radiation and a minimum of exhaust smoke [Lefebvre and McDonell, 1988].

Most of the systems in service are of the prefilmer type as it is in this work. In these systems, the liquid is first spread out in a thin continuous sheet and then subjected to the atomizing action of high-velocity air. On Figure 4.1 a general representation of a prefilming airblast atomizer is shown. In this case the fuel is supplied by some tangential ports directly on the prefilmer. Nevertheless, there are many ways to create the liquid sheet such as using pressure swirl atomizers or discrete nozzle to atomize the fuel before developing the fuel sheet.

Prefilming airblast nozzles are suited for atomizing liquid fuels in continuous-flow combustion systems, such as gas turbines (GT), where high velocity air flows are available. In this kind of atomizers, the fuel is first spread out in a thin liquid sheet and then subject to the atomization provoked by the shear stress at the liquid gas surface due to the high-velocity air flows. Prefilming airblast atomizers are widely used in the aeronautic field since they allow an excellent atomization of the liquid fuel. Unlike other kind of atomizers, prefilming airblast atomizers creates smaller droplets which evaporates faster than large droplets. Thus, they preserve well balanced fuel vapor - air mixing before reaching the flame front, allowing for a better controlled combustion [Chaussonnet et al., 2013].

[Lefebvre and Miller, 1966] identified the following key factors to achieve a good atomization:

- The liquid should first be spread into a thin continuous sheet of uniform thickness.
- Finest atomization is obtained by producing a liquid sheet of minimum thickness.
- The annular liquid sheet formed at the atomizing lip should be exposed on both sides to air at the highest possible velocity.

4.1.1 Film thickness

An experimental campaign was carried out by [Rizk and Lefebvre, 1980] to study the development of the fuel film thickness and its relevance with the final drop size distribution. Those experiments could not be performed with the typical airblast atomizer used on gas turbines

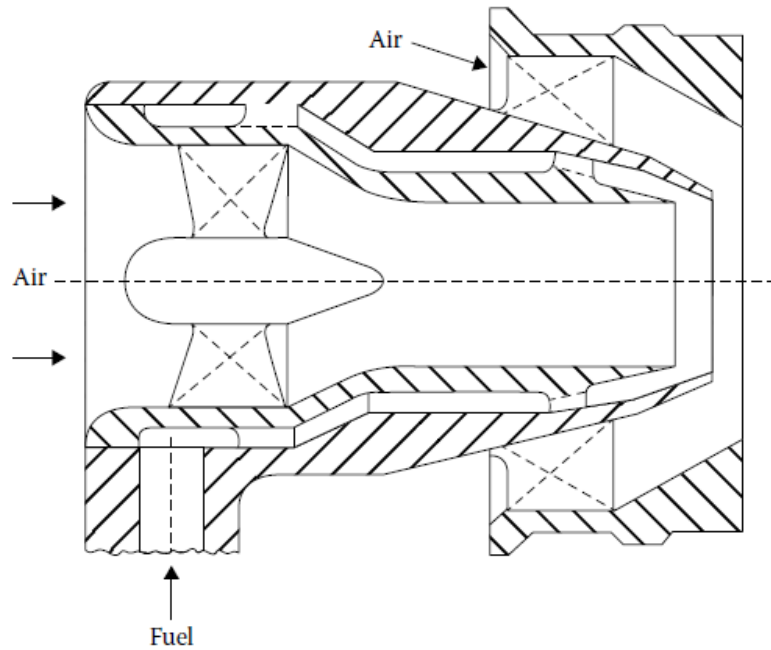


Figure 4.1 – Prefilming airblast atomizer sketch [Lefebvre and McDonell, 1988]

due to its cylindrical shape. Instead of, two planar airblast atomizers were tested. Water and kerosene were used as liquids.

The higher the liquid mass flow rate \dot{m}_l the thicker the film was. This value goes down with the increase of the air velocity. An expression was derived to calculate the liquid film thickness. It assumes that the shear stress in the thin liquid film will be constant and equal to the wall shear stress:

$$\tau = \mu_l U_i / t = 2\mu_l U_l / t \quad (4.1)$$

where U_i is the interfacial liquid velocity approximated to U_l which is the mean velocity of the liquid and t is the thickness of the film and μ_l is the liquid viscosity.

For the simplest case of a thin liquid film flowing along the inner wall of a circular pipe which also contains air flowing in the same direction, we have:

$$\tau = \frac{2\mu_l \dot{m}_l}{t \rho_l A_l} = \frac{2\mu_l \dot{m}_l}{t^2 \rho_l \pi d} \quad (4.2)$$

where \dot{m}_l is the liquid mass flow rate, A_l is the cross-sectional area of the liquid, d is equivalent diameter of the pipe and ρ_l is the liquid density.

The interfacial friction factor is given by:

$$f_i = \frac{\tau}{0.5 \rho_a U_a^2} \quad (4.3)$$

where ρ_a and U_a refer to the density and mean velocity of the air.

Combining these last two equation we achieve:

$$f_i = \frac{4\mu_l \dot{m}_l}{\pi \rho_a \rho_l d t^2 U_a^2} \quad (4.4)$$

The interfacial friction factor is also given, accordingly to [Hewitt and Hall-Taylor, 1970], by:

$$f_i = f_a (1 + 300t/d) \quad (4.5)$$

where f_a is the friction factor for air flowing along a smooth-walled tube in the absence of a liquid film. For turbulent flow f_A is given by the Blasius equation:

$$f_a = 0.79(Re_a)^{-0.25} \quad (4.6)$$

hence, substituting this equation into the previous one we obtain:

$$f_i = 0.79(1 + 300t/d)(Re_a)^{-0.25} \quad (4.7)$$

equating Equation 4.4 and Equation 4.7 leads to the following equation for liquid film thickness, t :

$$t^2(1 + 300t/d) = \frac{16\mu_l\dot{m}_l}{\rho_l\rho_a d U_a^2} \left(\frac{\dot{m}_a d}{A_a \mu_a} \right) \quad (4.8)$$

This equation has to be solved on an iterative way. On the work by [Rizk and Lefebvre, 1980] found the equation provides higher values than the experiments but it is good on predict general trends. The sought an empirical equation based on the main parameters contained on Equation 4.8:

$$t/d = 132(Re_l)^{-0.4}(\dot{m}_l/\dot{m}_a)^{0.8} \quad (4.9)$$

This equation showed a good agreement with the experiments performed.

A more current correlation is given by [Gepperth et al., 2013], based on the correlation on Equation 4.9:

$$t = 7.367d \left(\frac{\mu_l}{\rho_l \bar{u}_g d} \right)^{0.4} (\dot{m}_l/\dot{m}_a)^{0.8} + 6.35 \times 10^{-8} \quad (4.10)$$

4.1.2 Sauter Mean Diameter

The performance of a prefilming airblast atomizer can be measured with the Sauter mean diameter (Equation 5.5) of the cloud of droplets it expels. Therefore, there have been many attempts to model and create correlations to define it. The first attempt to develop a correlation on this topic was [Rizkalla and Lefebvre, 1975]. This correlation consists of two basic terms; the first term is dominated by the air velocity and density and the second term by the liquid viscosity.

$$\frac{D_{32}}{L_c} = A \left(\frac{\sigma}{\rho_g \bar{u}_g^2 D_p} \right)^{0.5} \cdot (1 + \dot{m}_l/\dot{m}_g) + B \left(\frac{\mu_l^2}{\sigma \rho_l D_p} \right) \cdot (1 + \dot{m}_l/\dot{m}_g) \quad (4.11)$$

where A and B are two constants determined experimentally, D_p is the diameter of the prefilmer and L_c represents a linear scale of the prefilmer. The most common choices of L_c are the film thickness as done in the original work by [Rizkalla and Lefebvre, 1975] or doing $L_c = D_p$ as done by [El-Shanawany and Lefebvre, 1980].

Further work by Rizkalla and Lefebvre lead them to the conclusion that for liquids with a low viscosity, the key factors are surface tension, air velocity and air density. The Sauter mean diameter was found to be also dependend on the air-fuel ratio $AFR = \dot{m}_g/\dot{m}_l$. As it has been explainen before, they found that the film thickness plays an important role on the final D_{32} [Rizk and Lefebvre, 1980]. They dimensionally corrected the Equation 4.11 [Rizkalla and Lefebvre, 1975, Lefebvre, 1989, Lefebvre, 1992]:

$$D_{32} = 3.33E-3 \frac{(\sigma \rho_l t)^{0.5}}{\rho_g \bar{u}_g} \cdot (1 + \dot{m}_l/\dot{m}_g) + 13.0E-3 \left(\frac{\mu_l^2}{\sigma \rho_l} \right)^{0.425} \cdot t^{0.575} \cdot (1 + \dot{m}_l/\dot{m}_g) \quad (4.12)$$

where t represents the film thickness.

As it was said, [El-Shanawany and Lefebvre, 1980] investigated the effect of liquid and air properties using L_c as the prefilmer diameter. They concluded that the spray quality is reduced with an increase of the atomizer dimension. They also found the air velocity to be the dominant factor influencing the droplet size. The droplet diameter decreases with increasing air velocity. Based on Equation 4.11 they correct it into:

$$D_{32} = 0.073 \left(\frac{\sigma}{\rho_g \bar{u}_g^2} \right)^{0.6} \cdot \left(\frac{\rho_l}{\rho_g} \right)^{0.1} \cdot D_p^{0.4} \cdot (1 + \dot{m}_l / \dot{m}_g) + 0.015 \left(\frac{\mu_l^2 D_p}{\sigma \rho_l} \right)^{0.5} \cdot t^{0.575} \cdot (1 + \dot{m}_l / \dot{m}_g) \quad (4.13)$$

On the work by [Sattelmayer and Wittig, 1986] concluded that the droplet size is independent of the channel height and liquid flow rate and the air velocity and surface tension were found to be the dominating parameters. In contrast with the previous works, [Sattelmayer and Wittig, 1986] shown that the film thickness is not linked to the final drop size distribution. Finally, they derived the following simple correlation based only on the surface tension σ and the gas velocity:

$$D_{32} = 0.67 \frac{\sigma^{0.67}}{\bar{u}_g^{1.57}} \quad (4.14)$$

Following this last work, [Aigner, 1986] analyzed several cylindrical airblast atomizer at elevated pressure. Aigner also investigated the effect of swirl, air channel height and atomizing edge thickness. According to this study, the effect of the swirl on atomization is difficult to characterize. If the turbulence and shear forces are increased by the swirl, it has a beneficial effect on the spray quality. Whereas, if the swirl induces flow separation at the atomizing edge, it may result into a coarser spray [Aigner and Wittig, 1988]. [Aigner, 1986] derived, based on dimensional analysis the following correlation:

$$D_{32} \propto \sigma^{0.5} \rho_g^{-0.4} \bar{u}_g^{1.05} \delta^{0.3} (\dot{m}_l / \rho_l)^{0.15} \mu_g^{0.15} \quad (4.15)$$

where δ is the thickness of the turbulent boundary layer defined by [White, 1991] as:

$$\delta = 0.16 \frac{L_{surf}}{Re^{1/7}} \quad (4.16)$$

with

$$Re = \frac{\bar{u}_g L_{surf}}{\nu_g} \quad (4.17)$$

where L_{surf} is the distance from the of the surface overflow of the gas flow from the primary swirler outlet to prefilmer's tip [Holz et al., 2016].

[Gepperth et al., 2012] proposed a more current correlation. Based of 300 test cases on a planar prefilmer at atmospheric operating conditions they proposed the following equation:

$$\frac{D_{32}}{\delta_{xedge}} = 4.96 \left(\frac{\rho_g \bar{u}_g \delta_{xedge}}{\mu_g} \right)^{-0.17} \left(\frac{\rho_g \bar{u}_g^2 \delta_{xedge}}{\sigma} \right)^{-0.36} \left(\frac{\rho_l}{\rho_g} \right)^{-0.013} \left(\frac{h}{\delta_{xedge}} \right)^{0.46} \quad (4.18)$$

The correlation from [Chaussonnet et al., 2016] is derived from the idea that the liquid accumulation is accelerated in axial direction, leading to a Rayleigh-Taylor instability and calibrated using the experiment by [Gepperth et al., 2010]:

$$D_{32} = \frac{2.41}{\bar{u}_g} \sqrt{\frac{h_a \sigma}{\rho_l \rho_g}} (\sqrt{\rho_l} + \sqrt{\rho_g}) \quad (4.19)$$

To have a more complete knowledge on this topic, it is recommended to the reader to take a look to [Gepperth et al., 2013, Chaussonnet et al., 2020]. These works compile the state of the art of the correlation for D_{32} on airblast atomizers and compare them with the experiment by [Gepperth et al., 2010].

4.1.3 Droplet mean velocity

To characterize the spray behaviour is also important to know the velocity of the droplets. Thus, [Gepperth et al., 2013] derived a correlation for the volume weighted mean droplet velocity which can be defined as:

$$u_{D,3} = \frac{\sum_{i=1}^N u_i \cdot D_i^3}{\sum_{i=1}^N D_i^3} \quad (4.20)$$

The correlation proposed was:

$$u_{D,3} = 49.49 \bar{u}_g \left(\frac{\rho_g \bar{u}_g \delta_{xedge}}{\mu_g} \right)^{-1.83} \left(\frac{\rho_g \bar{u}_g^2 \delta_{xedge}}{\sigma} \right)^{1.18} \left(\frac{\rho_l}{\rho_g} \right)^{0.52} \left(\frac{h}{\delta_{xedge}} \right)^{-0.8} \quad (4.21)$$

4.2 KIT-ITS atomizer

The nozzles used on the CHAIRLIFT project was proposed and investigated by [Kasabov et al., 2013]. The main goal of that study was to investigate lifted flame in terms of position, shape and characteristics of the liquid fuel spray. The nozzle is based on the airblast concept and comprises two radial swirlers and an axial fuel supply line (Figure 4.2). The combustion air flows through the nozzle vanes of the primary and secondary swirlers.

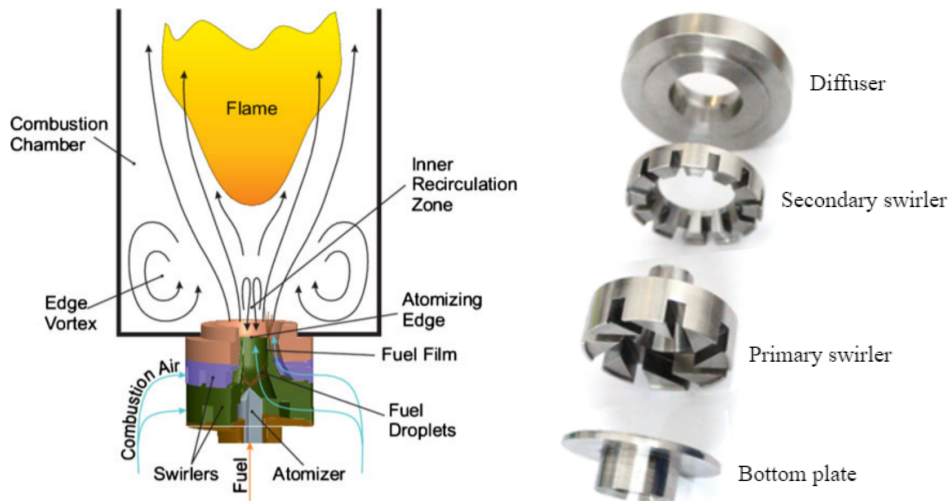


Figure 4.2 – Nozzle used on the CHAIRLIFT project [Kasabov et al., 2013].

Later on, [Sedlmaier et al., 2014] continued the study of lifted flames with the same nozzle design. The experimental and numerical studies carried out inside of the CHAIRLIFT project have been performed using [Sedlmaier et al., 2014] test case as a reference.

The atomizer on Figure 4.2 refers to a simplex swirl atomizer, same kind of nozzle described on chapter 3. The model chosen is the *SCHLICK-Mod.121 V* (Figure 4.3 by Schlick Nozzles [Schlick, 2020]). The diameter of the nozzle orifice is 0.2mm and the spray cone angle at nominal conditions is 60° . The flow number (FN) calculated with Equation 3.1 is equal to $0.83\text{kg/h/bar}^{0.5}$.

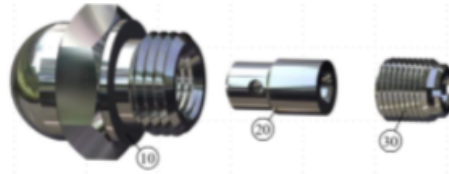


Figure 4.3 – Simplex swirl nozzle utilized on the CHAIRLIFT project.

4.2.1 Operating Conditions

The operating conditions corresponds to the experimental study by [Sedlmaier et al., 2014]. High pressure and high temperature were set-up for the air meanwhile the fuel was not preheated. The operating conditions are reported on Table 4.1.

p_0	ΔP_{nozzle}	T_{air}	T_{fuel}	\dot{m}_{air}	\dot{m}_{fuel}
4bar	3%	573K	323K	32g/s	1.15g/s

Table 4.1 – Sedlmaier test case operating conditions

The effective area A_{eff} is equal to 131mm^2 . The pressure drop across the nozzle remains constant equal to $\Delta P = 3\%$. The air mass flow rate is calculated as:

$$\dot{m}_{\text{air}} = A_{\text{eff}} \rho_{\text{air}} U_{\text{air}} \quad (4.22)$$

where U_{air} is the mean velocity of the air calculated by the Bernoulli's equation $U_{\text{air}} = (2\Delta P / \rho_{\text{air}})^{0.5}$.

The air fuel ratio (AFR) is set up to $AFR = 27.8$. Obtaining the fuel mass flow rate is straightforward $\dot{m}_{\text{fuel}} = \dot{m}_{\text{air}} / AFR$. As a fuel, the Jet A-1 is used. The properties for the fuel and the gas are reported on Table 4.2.

Air		Fuel		Shared	
ρ	ν	ρ	ν	$\rho_{\text{fuel}} / \rho_{\text{air}}$	σ
2.42kg/m^3	$1.58e - 06\text{m}^2/\text{s}$	790kg/m^3	$1e - 06\text{m}^2/\text{s}$	326.45	0.0208N/m

Table 4.2 – Fluid properties for the Sedlmaier test case.

4.3 Air flow modelling

The air flow modelling of the combustion chamber has been carried out by the University of Florence. They performed a LES, single-phase non-reactive simulation as a preliminary study [Langone, 2022]. On Figure 4.4 axial velocity contours for two mesh resolution are presented showing a good agreement with experiments.

The full combustion chamber simulation with the highest resolution tested shows high accuracy over the nozzle. Nevertheless, from the point of view of atomization, the data of the velocity needed is placed some millimeters below the nozzle. In spite of the high mesh resolution of this simulation, to capture the turbulent flow inside of the atomizer, more number of elements are required on this zone. Thus, using as a initial boundary condition one axial plane from the study by [Langone, 2022], an in detail study has been performed. Figure 4.5 shows the domain of the in detail single phase simulation inside the nozzle. On the right, a contour of the velocity from the full chamber simulation is represented. From this results, the mean velocity is mapped into the in detail domain.

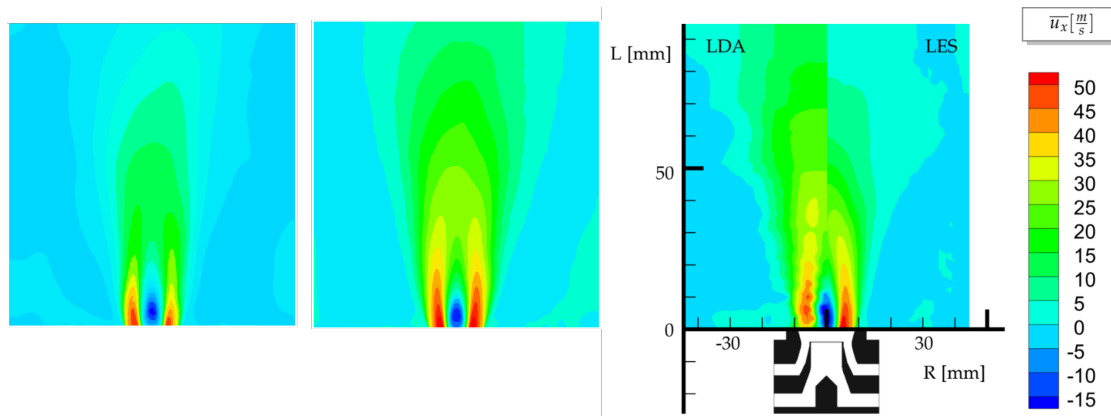


Figure 4.4 – Axial velocity contours from the numerical study by [Langone, 2022] compared to the experimental study by [Sedlmaier, 2016]. On the left: 4 million elements mesh. On the middle: 16 million elements mesh. On the right: Experiment data.

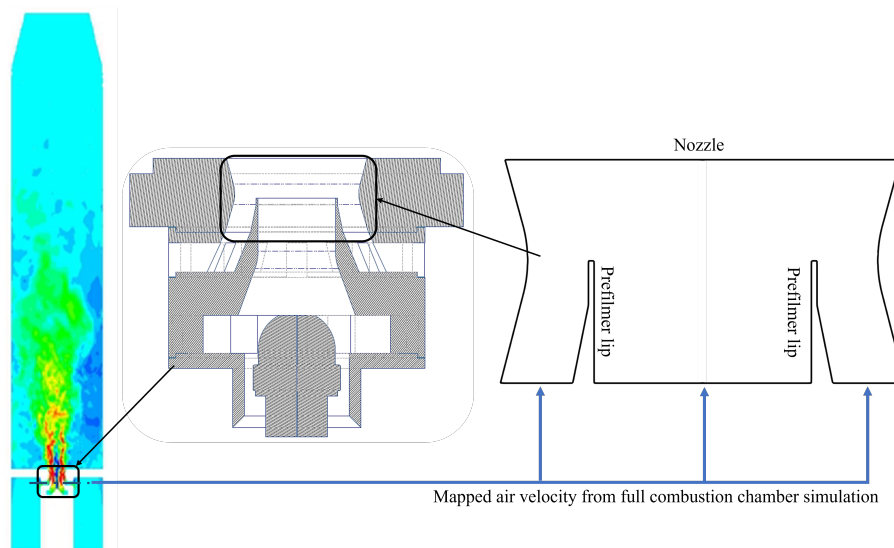


Figure 4.5 – In detail single phase simulation domain.

4.3.1 Computational grid

Due to the simplicity of the geometry domain, a structured mesh is made. The mesh is performed with the `blockMesh` utility. This utility create structure hexahedral meshes in blocks. Figure 4.6 shows a middle cut of the computational grid. It can be observed the special refinement around the walls of the atomizer, specially around the prefilmer. The storage of the data is done $400\mu\text{m}$ before the prefilmer lip, thus, that zone has to be refined enough to capture the velocity perturbation produced by the air flow.

The mesh is fully hexahedral with a total of 8.6 million elements. The smallest spacial length δx of those elements is $5\mu\text{m}$ placed around the prefilmer lip. The simulation has been run for 3ms with a temporal time step of $\Delta t = 0.006\mu\text{s}$ which result in 2880 CPUh.

4.3.2 Numerical set-up

To perform the simulation the `pimpleFoam` solver within the `openFoam V6.0` toolbox was chosen. `pimpleFoam` is a transient solver for incompressible, turbulent flow of Newtonian

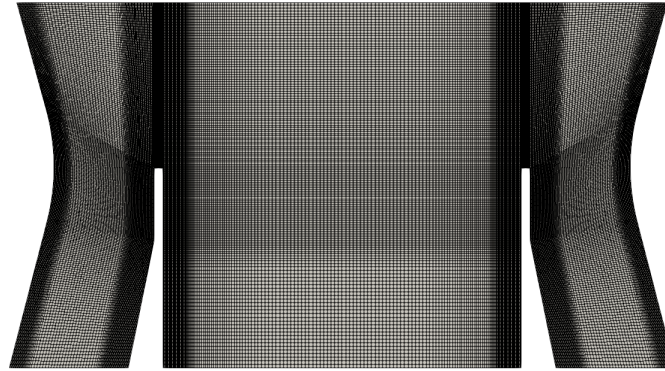


Figure 4.6 – Air flow single phase mesh.

fluids. The turbulence has been modelled with a LES formalism and in particular with sub-grid scale WALE model. For more information check chapter 2. Second order schemes are set up for time and spacial discretization.

The boundary conditions are reported on Table 4.3. The inlet velocity is mapped from the result of the UNIFI single phase simulation [Langone, 2022].

	Inlet	Wall	Outlet
\mathbf{u}	Fixed velocity	$\mathbf{u} = 0$	$\nabla \mathbf{u} = 0$
p	$\nabla p = 0$	$\nabla p = 0$	totalPressure

Table 4.3 – Single-phase in detail simulation of the nozzle: Boundary conditions.

The air properties are collected on Table 4.2 for each operating condition.

4.3.3 Results

Figure 4.7 shows velocity contours on a middle plane. At the left it can be seen instantaneous values in contrast with the time averaged ones on the right.

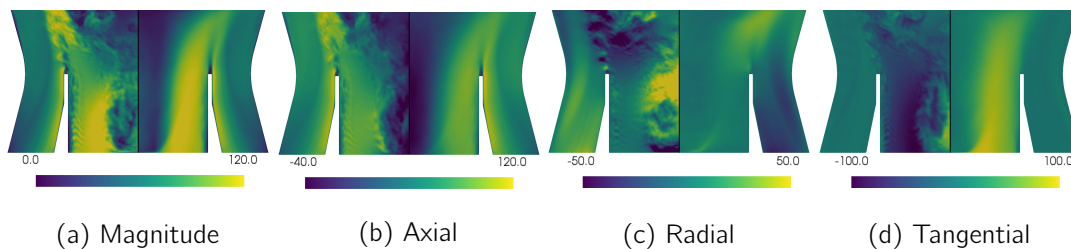


Figure 4.7 – Contours of the velocity at a middle plane. Left side: Instantaneous value. Right side: Mean value

Each $0.5\mu s$ the velocity field is stored on a cross plane before the prefilmer lip. A total of 6400 time steps are stored to afterward map those values into the inlet boundary of the prefilmer simulation. Figure 4.8 shows the transverse plane on the air flow configuration with the magnitude of the mean velocity plotted on it. It can be also appreciated on a black line the outline of the inlet boundary on the sector prefilmer simulation.

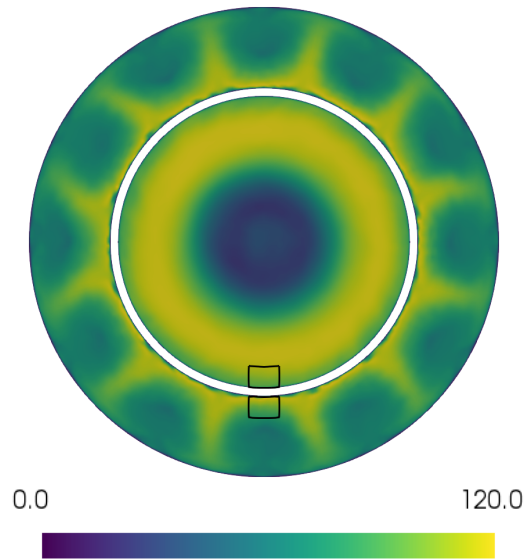


Figure 4.8 – Magnitude velocity contour on a transverse plane with the inlet outline from the prefilmer simulation overimposed.

4.4 Estimation of the liquid film thickness

As we have seen on the state of the art about film thickness correlation, some of the authors claims that the thickness of the liquid film is not linked to the final Sauter mean diameter of the spray. However, some other claims just the contrary. Anyhow, this parameter is required to set up the prefilmer simulation.

Measuring the film thickness from a experimental campaign is not possible due to the complexity of the atomizer geometry. Thus, it has been estimated following a theoretical rough approach, and afterwards, a refined the methodology with numerical simulations.

Theoretical approach

The hypothesis done is that the liquid film developed at the prefilmer lip is thin enough that the velocity profile of the liquid is linear. The liquid velocity at the wall u_{fuel}^w is zero and the liquid velocity at the liquid-gas interface u_{fuel}^s is equal to the velocity of the air at the gas-liquid interface u_{air}^s . Since u_{air}^s is not known, it has been estimated as the mean velocity obtained from Equation 4.22 U_{air} . The liquid mass flow rate is:

$$\dot{m}_{fuel} = 2\pi R_p \rho_{fuel} \int_0^t u_{fuel}(r) dr \quad (4.23)$$

and then, the liquid film thickness is:

$$t = \frac{\dot{m}_{fuel}}{\pi R_p \rho_{fuel} U_{air}} \quad (4.24)$$

where R_p is the prefilmer radius.

Equation 4.24 gives very low values of liquid thickness $t_{testcase} = 3\mu m$. This value is one order of magnitude below from the correlation shown before. Therefore, it is not a physical value, thus, a numerical study was performed to estimate the liquid thickness.

4.4.1 Numerical domain

To estimate the liquid film thickness at the prefilmer lip a multi-phase simulation is carried out. Ideally, a multiphase computation on Figure 4.5 geometry should be performed. However, the length scales involved (film thickness is 2 to 3 order of magnitude below the orifice diameter) in that set-up would increase the computational resources hugely. Therefore, a 2D simulation emulating an "infinite" pipe has carried out instead.

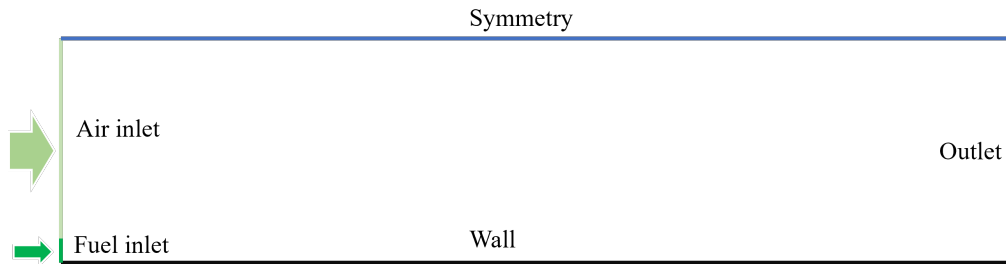


Figure 4.9 – 2D film thickness estimation: Domain and boundary conditions.

Figure 4.9 represents the numerical domain of the 2D simulation. At the left the patch for the air and liquid inlet are set up. The thickness of the liquid inlet patch is the same computed on the previous section $h_l = 3\mu m$ meanwhile the height of the air inlet is 50 times longer than the liquid initial thickness $h_a = 200\mu m$. The domain length is estimated by the length from the droplets expelled from the simplex atomizer reach the wall of the prefilmer up to the prefilmer lip. This length l is shown on Figure 4.10.

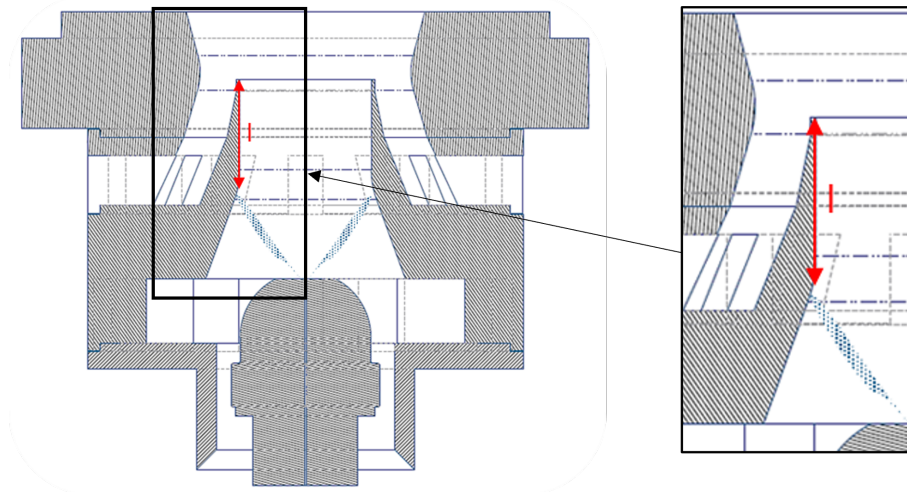


Figure 4.10 – Geometric representation on how to fix l on the 2D simulation to estimate the liquid film thickness

4.4.2 Computational mesh

The computational mesh has been performed with the blockMesh utility to create a 2D structured mesh. The resolution is fixed to $\delta x = 4\mu m$ and $\delta y = 1\mu m$. The mesh is more refined on y direction since the variable of interest, the liquid film thickness t , varies on that direction, and hence, the liquid-gas interface have to be properly captured. On the other hand, on x direction, the mesh resolution is not so important, thus, to speed up the computation a larger cell size has been fixed.

The mesh has $91 \cdot 10^3$ cells. To let the flow develops and afterwards average the liquid volume fraction field, around 0.01s of physical time are required. The computation is performed with 20 CPUs on a total of 14 hours.

4.4.3 Numerical set-up

The interFoam solver is used to capture the surface interface between the liquid sheet and the surrounding gas on the OpenFOAM v6.0 toolbox. Due to the 2D domain, the turbulence model adopted is the $k - \epsilon$ RANS model. The discretization schemes are second order on space and time.

The boundary conditions are reported on Table 4.4. The liquid inlet velocity is calculated from the liquid mass flow rate \dot{m}_{fuel} and the first approach of the liquid film thickness obtained with Equation 4.24. The air inlet velocity is fixed to the averaged air velocity U_{air} calculated by Equation 4.22. Symmetry boundary conditions are set up for the top patch and wall boundary conditions to the bottom patch to replicate the prefilmer behaviour. The pressure at the outlet has been fixed.

	Air Inlet	Liquid Inlet	Outlet	Top - Symmetry	Bottom - Wall
\mathbf{u}	Mapped value	Fixed value	$\nabla \mathbf{u} = 0$	Symmetry	$\mathbf{u} = 0$
p	$\nabla p = 0$	$\nabla p = 0$	totalPressure	Symmetry	$\nabla p = 0$
α	$\alpha = 0$	$\alpha = 1$	$\nabla \alpha = 0$	Symmetry	$\nabla \alpha = 0$

Table 4.4 – Multiphase simulation to estimate the liquid film thickness: boundary conditions

4.4.4 Results

Figure 4.11 shows the liquid volume fraction α . The evolution of the liquid film thickness can be notice from the initial set up value of $t_{testcase}^0 = 3\mu m$ to an averaged value of $t_{testcase}^f = 47\mu m$ which is a more realistic value and in line with the correlation presented on Equation 4.10 $t_{testcase}^{cor} = 20.3\mu m$.

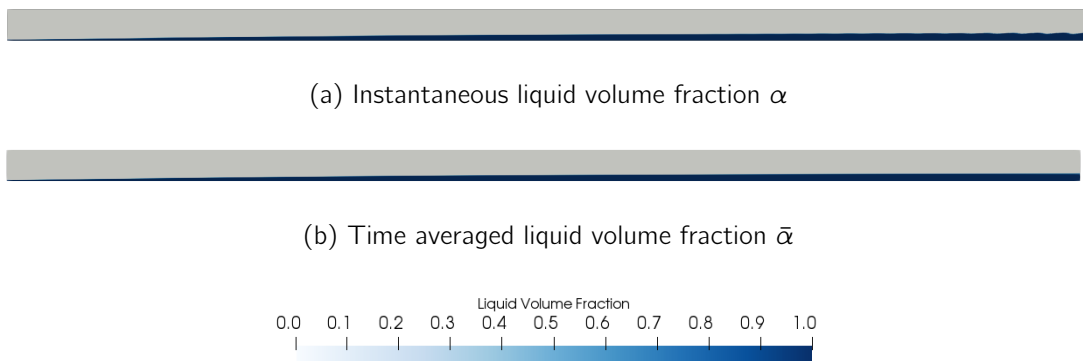


Figure 4.11 – Liquid volume fraction contour to obtain the prefilmer film thickness. Test case operating conditions.

According to [Gepperth et al., 2013, Chaussonnet et al., 2018] the film thickness does not affect to the primary atomization process since at the prefilmer's lip an accumulation process of the liquid is taking place. This effect was also seen by [Inamura et al., 2019] where the conclude that the primary atomization is affected by the air velocity and the prefilmer thickness and not by the liquid film thickness when is an order of magnitude smaller. Thus,

the value from the 2D multiphase simulation $t_{testcase}^f = 47\mu m$ will be used to set up the prefilmer's simulation.

4.5 Airblast prefilming modelling

Once the air flow is modelled and the liquid film thickness is estimated, the prefilmer simulation can be set up. In order to make the computation feasible, only a small sector of the nozzle is studied. A small portion of the full system is enough to collect the required data and perform a statistical study which can be extrapolated to the full system. This procedure is used on the reference works [Sauer et al., 2014, Warncke et al., 2017, Palanti et al., 2022].

To characterize the spray, some data is collected on run time. Afterwards, the data is treated and analysed to achieve a complete description of the spray behaviour.

4.5.1 Numerical domain and computational grid

Following the same approach taken on the air flow modelling, the nozzle geometry has been trimmed and focused around the prefilmer's lip. Therefore, it begins before the prefilmer's lip and it is extended downstream. The dimensions of the numerical domain are parameterized and they are in function of the liquid film thickness as is done on the reference works. The dimensions are shown on Figure 4.12.

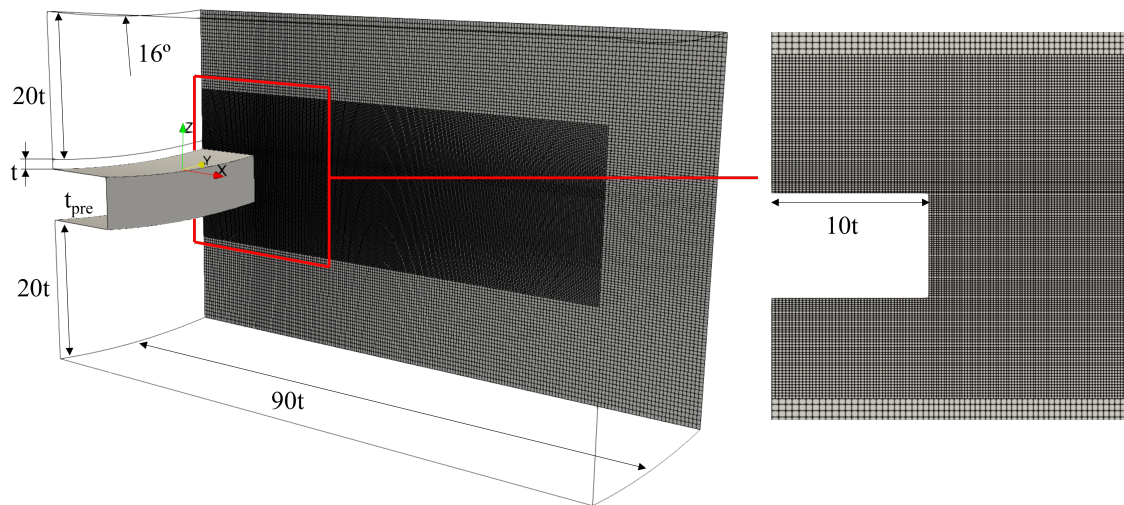


Figure 4.12 – Numerical domain. On the left: geometrical domain on black solid lines with a slice of the mesh. On the right: detail of the numerical mesh.

Taking into account that the coordinates origin is placed at the center of the prefilmer's lip the most important coordinates are the following:

- Inlet: $X = -10t$
- Prefilmer thickness: $Z = 250\mu m$
- Inner boundary: $Z = 20t$
- Outer boundary: $Z = 250\mu m - 20t$
- Outlet: $X = 80t$

where t is the liquid film thickness in each case. The azimuthal coordinate has been fixed by an angle of $\varphi = 16^\circ$.

Every $50\mu m$ a post-processing plane is set up along the streamwise direction which normal is aligned with this direction. Those planes are storing the liquid mass flow rate

($V_l = \iint_S \alpha \mathbf{u} \cdot \mathbf{n} ds$) and the surface interface flow rate ($A_l = \iint_S \Sigma \mathbf{u} \cdot \mathbf{n} ds$) as it is explained on chapter 5.

To store the data that later will be post-processed to compute the surface curvature distribution (SCD), drop size distribution (DSD) and the velocity drop distributions, a cloud of probes is set up at $X = 1.2mm$. On this place the mean curvature κ , the surface interface density flux $\varphi \Sigma$, the liquid volume fraction flux $\varphi \alpha$ and the velocity vector \mathbf{u} are stored to be treated later on.

The number of elements on the computational grid is also parameterized in function of the liquid film thickness to achieve, at least, 12 cells on it. This study is performed to validate the methodology and later repeat it on several operating conditions for the CHAI RLIFT project. Thus, the number of elements and the minimal size of the cells could vary from one operating condition to another but in general every case will have almost the same number of elements and the same cell size. On Figure 4.12 the mesh grid is represented. An hexahedric Cartesian mesh is made with the `blockMesh` utility. One refinement zone is made to double the resolution around the prefilmer's wall and to capture the primary atomization process. The methodology used to characterize the spray relies on the grid resolution since the smaller droplet that can be capture is related to the minimum cell size.

Prefilmer simulation	
Number of elements	12.6e6
Minimal cell size	2.8 μm
Cells liquid film	13
$\Delta t_{physical}$	3.1e-8s
<i>CPUs</i>	288
Δt_{sim}	7.8s
<i>CPUh</i>	60,100

Table 4.5 – Prefilmer simulation: Mesh information

Table 4.5 shows the information about the test case mesh.

4.5.2 Numerical set-up

As it has been explained on chapter 2, the multiphase simulation has been carried out with the `interFoam` solver. As turbulence model the WALE LES sub grid model has been chosen. Regarding the discretization schemes, second order on time and on space have been set up. A global CFL below 0.4 and in particular below 0.25 on the interface is fixed to reach an accurate solution.

The boundary conditions can be grouped on inlet patches, outlet patches, lateral sides and walls. Inside the inlet patches we can find at the left of Figure 4.12 the liquid inlet patch which is the narrow patch we can see up above the prefilmer's lip and the air flow inlet that are the two patches above and below the prefilmer. On the outlet patches we have the right patch and the upper patch. The lateral side patches are both of them periodic patches. Finally, the prefilmer is set up as a wall.

Following this definitions we found the liquid inlet boundary conditions where the liquid volume fraction is fixed to only liquid $\alpha = 1$. The velocity vector is fixed to match the mass flow rate reported on Table 4.1 and the pressure gradient is fixed to zero. The air flow inlet boundary conditions is set up as `timeVaryingMappedFixedValue` already implemented on OpenFOAM V6.0. This boundary conditions interpolates on space and on time a given plane; the data collected from the single phase simulation described previously is used here to set up

the case. The liquid volume fraction is fixed to only gas $\alpha = 0$ and the pressure gradient to zero.

The outlet patches are both set up in the same way. The pressure is fixed as total-Pressure (Equation 2.18) and the velocity and liquid volume fraction gradient are fixed to zero.

Table 4.6 collects the boundary conditions used on the prefilmer simulation.

	Liquid Inlet	Air Inlet	Outlet	Lateral Sides	Prefilmer Wall
\mathbf{u}	Fixed value	Mapped value	$\nabla \mathbf{u} = 0$	Periodic	$\mathbf{u} = 0$
p	$\nabla p = 0$	$\nabla p = 0$	totalPressure	Periodic	$\nabla p = 0$
α	$\alpha = 1$	$\alpha = 0$	$\nabla \alpha = 0$	Periodic	$\nabla \alpha = 0$

Table 4.6 – Prefilmer multiphase simulation: Boundary conditions

4.5.3 Results

Iso-surfaces and contours of the velocity are reported on this section. Due to the lack of experimental data on the spray atomization on the work by [Sedlmaier, 2016], the validation of the workflow is done on the following chapter (chapter 5) where an analysis of the surface interface and curvature is explained. However, some data can be extracted from the prefilmer simulation applying a classical post-processing.

Figure 4.13 shows three different snapshots representing the liquid volume fraction iso-surface for $\alpha = 0.5$. The primary atomization process is well captured and it can be seen that the liquid film is broken up into smaller liquid structures such as ligaments and droplets. The lateral views show some of the fuel is attach to the prefilmer's lip and, eventually, it is detached forming small droplets.

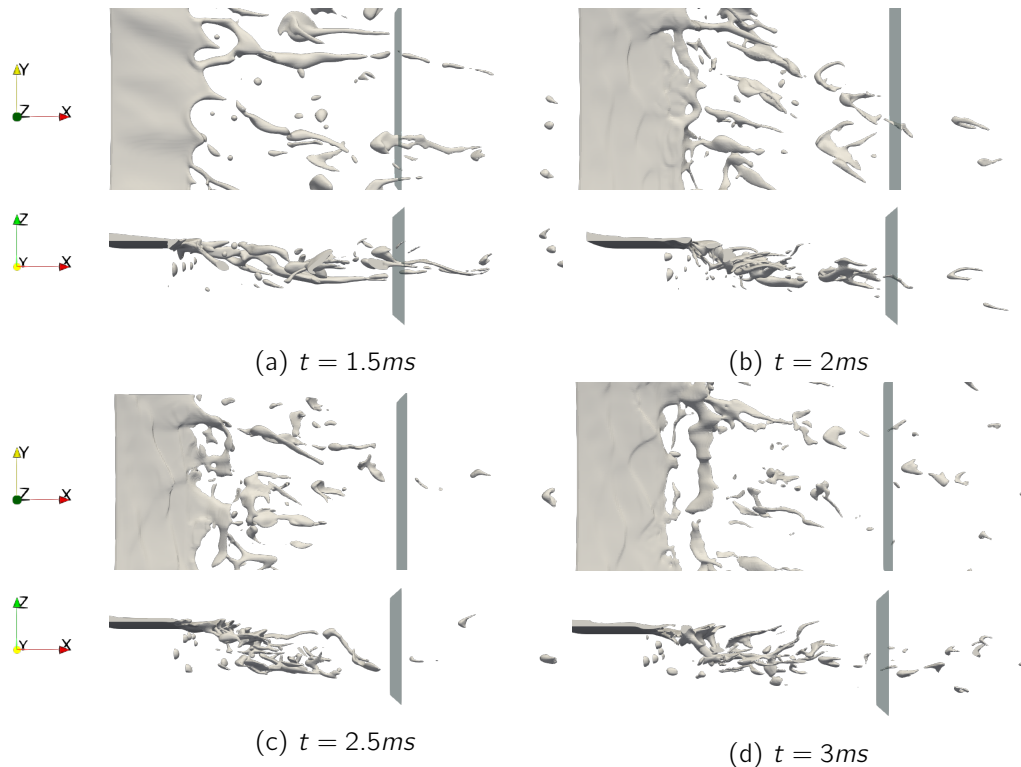


Figure 4.13 – Liquid volume iso-surfaces $\alpha = 0.5$ for three different time steps.

Experimental works such as [Gepperth et al., 2010, Chaussonnet et al., 2018] demonstrated that the fuel is usually attached to the prefilmer's lip creating a reservoir of liquid. On this case the effect is present but less important. Numerical studies such as [Palanti et al., 2022, Sauer et al., 2014] are able to recover this physical effect. The reason why on this simulation the reservoir is attenuated could be due to the high air velocity which prevents the fuel to remain enough time attached to the prefilmer before creating a big reservoir. There is also the fact that on this case we are modelling a real atomizer with swirl flow on the internal swirler. Thus, the tangential velocity transmitted to the fuel could also prevent the reservoir to grow.

Figure 4.14 shows the time averaged liquid volume fraction $\bar{\alpha}$ on a middle plane of the domain. On this picture the formation of a liquid reservoir is clearer viewed agreeing with [Chaussonnet et al., 2018]. The picture also shown the spray angle regarding the center of the prefilmer's edge. An angle of $\varphi = 12.4^\circ$ is recovered. The middle plane shown includes the outer zone without refinement. Meanwhile on the $\bar{\alpha}$ picture it can not be notice, at the right of the figure the time averaged surface interface density $\bar{\Sigma}$ is plotted, and the change of resolution is noticed. Since the surface interface density is computed as $\Sigma = |\nabla\alpha|$ and when the liquid goes to the under-refinement region is diffused and also the interface is, Σ is not conserved among refinement levels. This fact is crucial on the surface-curvature analysis, hence, all the measurements have been performed within the refinement zone.

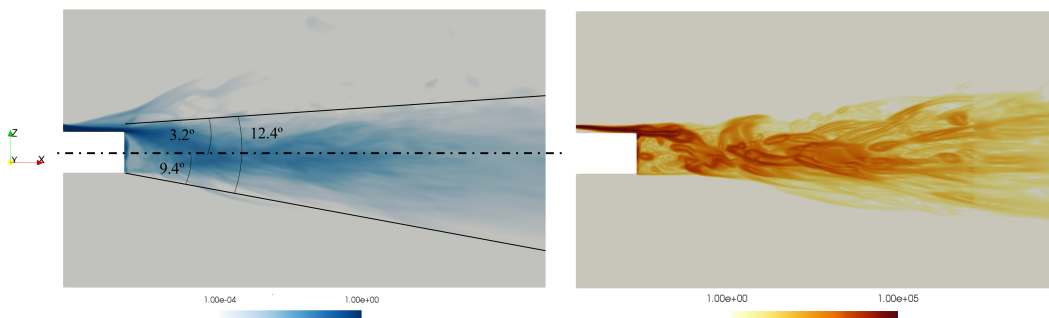


Figure 4.14 – On the left: Time averaged liquid volume fraction $\bar{\alpha}$ on a middle plane. On the right: Time averaged surface interface density $\bar{\Sigma}$. Colour bars are on logarithmic scale. Spray angle is drew on black solid line.

The magnitude of the velocity is plotted on Figure 4.15. It can be compared with the in detail single-phase simulation of the nozzle Figure 4.7 where clearly the time averaged value is recovered on the sectorial multi-phase simulation.

The internal channel of the airblast atomizer is the only one that has a swirling flow. The external channel has mainly axial flow. This is reported on the experimental work by [Sedlmaier, 2016] and the numerical modelling by [Langone et al., 2022]. On Figure 4.16, Figure 4.17 and Figure 4.18 this effect is well modelled.

The radial velocity is mostly nule on the domain but there are some peaks which magnitude is near $U_R^{Peak} = 40m/s$. Those peaks are linked to droplets that before had a high tangential velocity but when they lose the prefilmer's wall, the centripetal forces become zero, hence, the tangential component of the velocity is transformed into radial component of the velocity.

We can see on Figure 4.18 that the maximum tangential velocity within the domain is near to $80m/s$. Therefore, those peaks of radial velocity are inside of the ranges.

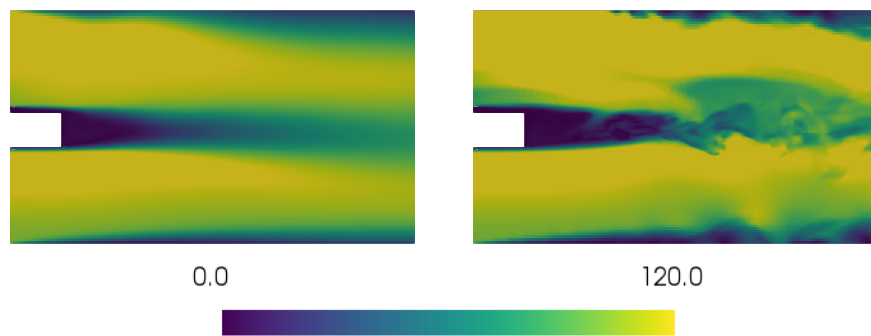


Figure 4.15 – Velocity magnitude contour. On the left: time averaged value. On the right: instantaneous value.

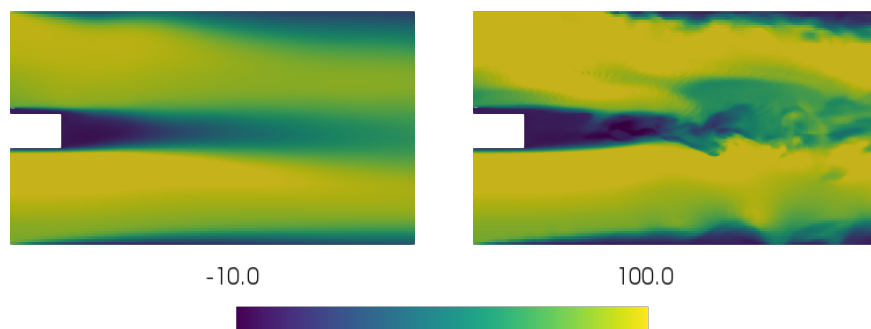


Figure 4.16 – Axial component of the velocity. On the left: time averaged value. On the right: instantaneous value.



Figure 4.18 – Tangential component of the velocity. On the left: time averaged value. On the right: instantaneous value.

4.6 Conclusions

Due to the wide range of length scales within the airblast atomization, modelling this kind of atomizers is a complex process. Instead of trying to handle a single multi-phase simulation and following some articles from the scientific literature, a workflow has been defined to carry out the modelling.

First, the air flow inside of the burner has been computed to afterward perform a single-phase in detail simulation. From it, some data was stored to map on time and on



Figure 4.17 – Radial component of the velocity. On the left: time averaged value. On the right: instantaneous value.

space the main case. Second, a method to estimate the fuel film thickness has been proposed. Accordingly to the literature this value should not be related to the spray formed, but a realistic value is needed to continue the process.

Finally, with those two previous points, the main simulation can be set-up. A 16° domain has been chosen to reduce the computational resources needed. The preliminar results shown a good agreement with the velocity of the air. In other hand, none experimental data on the multi-phase approach is available.

On the next chapter, the characterization of the spray expelled from this atomizer is presented.

5 | Spray Characterization

A new analysis based on the surface interface density and the curvature to extract the drop size distribution from an airblast atomizer was recently proposed by [Palanti et al., 2022]. On this chapter the methodology is explained and further developed to extract the droplet velocity distribution. The process has been applied to the two configuration studied on this work. The simplex swirl atomizer from chapter 3 and the airblast atomizer from chapter 4. Quantitative and qualitative validation are reported with experimental results for both configurations.

Contents

5.1	Drop sizing methods	88
5.1.1	Experimental techniques	88
5.1.2	Numerical methods	89
5.2	Surface interface and curvature analysis	89
5.2.1	Surface interface density	90
5.2.2	Estimation of the curvature	92
5.3	Sauter mean diameter (SMD)	93
5.4	Surface curvature distribution (SCD)	95
5.5	Drop size distribution (DSD)	98
5.6	Velocity joint distribution	101
5.7	Comparison with experiments	103
5.8	Drop size distribution on CRSB injector	105
5.8.1	Ambient temperature case	105
5.8.2	High temperature case	108

A spray is a system of drops immersed in a gaseous continuous phase. Most practical atomizers generate droplets in the size range from a few micrometers up to around $500\mu m$ [Lefebvre and McDonell, 1988]. Since the atomization process of different kinds of injectors is heterogeneous, the ligaments and threads formed by them vary in diameter, the resulting drop diameters vary in size correspondingly. Thus, nozzles are not producing sprays with uniform drop sizes at any given operating condition; instead, the spray is formed as a cloud of different drop sizes distributed about some arbitrarily defined mean value. In addition to the drop mean

value, some mathematical and empirical distribution functions can be used to characterize the drop size distribution of the spray. This very fact can be applied to the drop velocity.

The knowledge of the spray drop size distribution and its velocity distribution is needed to value the performance of the atomizer. Regarding their uses, the spray produced by an atomizer it is considered more or less useful. Concerning the topic of this work, the combustion performed inside an aeronautical gas turbine, the smaller the droplet, the better; smaller droplets evaporates faster, thus, the air-fuel mixing is accelerated and the combustion is better.

There are several methods to measure the spray drop size, experimental and numerical methods. In this chapter some of them are presented and a new methodology to post-process the data from a numerical multiphase simulation is proposed based on the work by [Palanti et al., 2022]. This new methodology allows to predict the early behaviour of the spray near the nozzle. The drop size distribution and the velocity drop size distribution can be computed. On chapter 3 and on chapter 4 this technique is applied to characterize the spray produced by a simplex swirl atomizer and a air-blast prefilming atomizer correspondingly.

The spray characterization can be used as an input for spray reactive flows where the spray is modelled using the lagrangian-eulerian approach. In particular, in the context of the CHAiLIRFT project, the spray has to be sized computationally to, later on, use it as a boundary condition for the reactive flow simulation.

5.1 Drop sizing methods

The characterization of spray has evolved considerably over the last few decades. Though the size of droplets within a spray remains a critical characteristic of a spray, other parameters can be, and are, measured regularly. As instrumentation and simulation methods become more capable, insights into the multitude of behaviors is becoming possible.

In this section the more used techniques are reported of both, experimental and numerical methods. Where experimental techniques are, in general, more accurate, the data accessibility is more difficult than in numerical simulation where the 3D data of the spray is available. In the same way, the numerical simulations are able to extract more data directly from the dense region of the spray meanwhile meanwhile with experimental techniques is more difficult; of course, the experimental campaigns can be performed faster than simulation and it is easier to change parameters as the dimensions of the atomizer or properties of the fluid. To understand better the spray behaviour, these two kind of techniques have to work together since every technique has its advantages and disadvantages.

5.1.1 Experimental techniques

Several techniques in spray measurement technology have emerged on the last few decades. One of the reasons of such a new wave of technologies is the need for more detailed understanding of spray physics in order to develop more spray models. Experimentally, these trends have been enabled largely by advances in lasers, digital cameras, electronics and computers.

In order to measure macroscopic characteristics (cone angle, axial and radial penetration, etc.), optical imaging has been used for centuries and it is still in uses with techniques such as volume illumination [Marchi et al., 2010], back-illumination [Ghandhi and Heim, 2009], shadowgraph and schlieren techniques [Settles, 2001]. Those techniques are performed using digital cameras. Another method to measure macroscopic characteristics are the pulsed laser. Applications such as planar Mie scattering are able to show a 2D planar representation of the spray[Settles, 2001].

Nowadays, high-speed cameras are valuable to obtain many images of transient sprays or to be able to isolate special events. All these pictures have to be treated afterwards and analysed. Numerical post-processing techniques are applied to the pictures to be able to extract the spray from the background, to isolate each ligament and droplet or separate overlapping images. There are many works on going in this topic and some of the algorithms are also used, in some way, into the numerical simulation post-processing.

Phase Doppler interferometry (PDI) measure droplet size and velocity simultaneously [Saffmann et al., 1984]. PDI relies on light scattered from two intersecting, coherent laser beams. The scattered light interferes at three detectors placed at carefully designed locations to generate sinusoidal Doppler burst signals whose frequency is proportional to droplet velocity and whose phase (for spherical scatterers) is related by Mie scattering theory to droplet diameter.

There are many other experimental techniques to measure and characterize the spray behaviour. In this section only the most interesting techniques regarding the purpose of this work are compiled. The reader should read [Bachalo, 2000, McDonell and Samuelsen, 2000, Tropea, 2011, Fansler and Parrish, 2015] for a more complete review of these kind of techniques.

5.1.2 Numerical methods

There are several post-processing techniques to compute the droplet size distribution and the joint velocity distribution depending on the numerical multiphase approach chosen. Regarding the ICM methods, analogous visual techniques can be applied as if a experimental picture were. Connected liquid structures are separated into clusters using Connected Component Labeling (CCL) [Roselfeld and Pfaltz, 1966] algorithm. Afterward the clusters can be analysed individually and the diameter of the droplets, their number and the velocity vector of those can be computed. This technique is used on the works by [Warncke et al., 2017, Braun et al., 2019].

Those techniques are highly accurate but, in the other hand, they require a huge amount of computational storage and a huge computational power to carry out. Consequently, [Palanti et al., 2022] proposed a novel technique to extract the drop sizing data using only global variables from the simulation. The work was performed using the ICM-ELSA model to carry out the multiphase simulation and the variables postprocessed were the liquid volume fraction α , the surface interface density Σ and the general curvature of the surface κ . The post-process technique was carried out on run time and it is able to compute the drop size distribution of the spray.

In this chapter, further work and modifications of this novel technique are proposed and applied to the CRSB simplex swirl atomizer and the CHAiRLIFT air-blast atomizer to valid both, the techniques and the modelling of the injectors.

5.2 Surface interface and curvature analysis

This methodology was firstly proposed by [Palanti et al., 2022] where the planar prefilmer by [Gepperth et al., 2010] is studied numerically to validate the methodology. The technique is based on the ICM-ELSA model and uses the surface interface density Σ and the curvature estimation κ to calculate the drop size distribution of the spray issued by the planar prefilmer resulting in a high accuracy approximation. The data was recover in several control volumes each time step at run time. The statistics were computed also at run time, thus, reducing the amount of data stored hugely regarding classical post-processing techniques.

On the present work, the same methodology is studied to keep developing this new analysis. The modification applied are:

- The ICM-ELSA model is replaced for a VoF based model with an interface capture method. The surface interface density σ is computed from the liquid volume fraction α .
- The data is stored on the faces of the cell on a given plane. This data is store each time step and the statistics are performed afterwards. The data storage increases but also the robustness of the method since it can be use for other purposes.
- The velocity of both, gaseous and liquid phases, is stored. The velocity joint distribution is computed. In addition, the velocity joint distribution by droplet size can be obtained.

The two main variables of this post-processing technique are the surface interface density Σ and the curvature of the liquid elements κ .

5.2.1 Surface interface density

The surface normal vector of a liquid structure within a VoF method with an ICM can be computed as the gradient of the liquid volume fraction:

$$\mathbf{n}_S = \nabla\alpha \quad (5.1)$$

The magnitude of the normal vector \mathbf{n}_S is the surface interface density Σ which represents the surface interface per unit of volume:

$$\Sigma = |\nabla\alpha| \quad (5.2)$$

A small computational test case has been carried out to study the surface interface density Σ and the curvature κ parameters. A droplet of $20\mu m$ of diameter being carried by a gaseous phase. Three different mesh resolutions have been used to see the influence of the mesh refinement on those parameters. The three different cases are called $n8$, $n16$ and $n32$ being n the number of cells along the diameter of the droplet.

On VoF methods, the surface interface between gas and liquid is placed in between $\alpha = 0$ (gas) and $\alpha = 1$ (liquid). Looking at iso-surfaces with different values of α we can appreciate on Figure 5.1 that even with a well resolved interface, there are infinite iso-surfaces in between each of them with an associate surface interface density value. Of course, with the coarsest resolution the location of the interface varies more than on finer resolutions. It can be noticed that the surface interface density normalized by the cell size $\Sigma/(1/\delta x)$ reaches its higher value at the $\alpha = 0.5$ iso-contour. The higher value that it can reach, theoretically, is when the transition between gas and liquid takes place within one cell, hence, $\nabla\alpha = 1/\delta x$. This situation is never taking place on the current VoF based method since the surface interface is always dispersed over two or three elements at maximum when the resolution is high enough. Thus, to recover the total amount of surface over a droplet, the sum of the integrals of Σ has to be calculated over all the iso-surfaces.

Another way to compute the total surface interface on the droplet test is to calculate the flux of surface interface density through a plane every time step and integrating on time, the total surface can be computed as follows:

$$S_{Total} = \int_T \iint_S (\Sigma \mathbf{u} \cdot \mathbf{n} ds) dt \quad (5.3)$$

On Table 5.1 the different mesh resolution results are shown. It can be observed that the simulation volume does not match the theoretical volume in any of the numerical cases due to the initialization process used; when the numerical domain is initialized, the cells within the sphere representing the droplet ($r = 10\mu m$) are set as a liquid, hence, the liquid volume

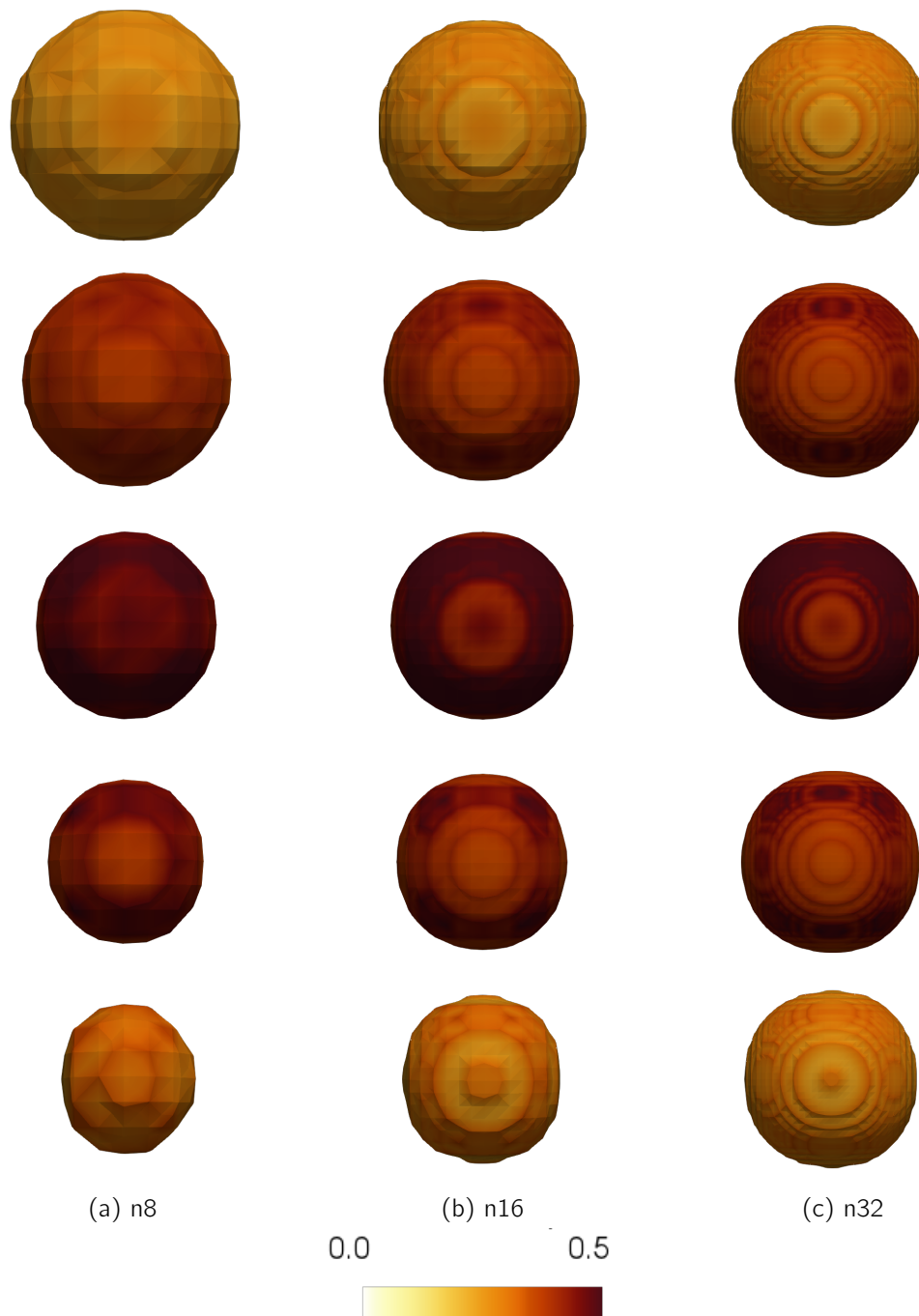


Figure 5.1 – Surface interface density normalized by cell size and plotted over the liquid volume fraction α iso-surface. From top to bottom: $\alpha = 0.1, 0.25, 0.5, 0.75, 0.9$. From left to right: mesh resolution $dx = 2.5\mu m, 1.25\mu m, 0.625\mu m$.

fraction α is equal to 1. Therefore, the initial condition of the droplet is a cube shaped droplet instead of a spherical one. That leads to differences on the volume regarding the theoretical value. Those values are recalculated and represented on the table.

Resolution	Volume	Radius	Surface	Recovered Surf.	Diff.
Theoretical	$4.19 \cdot 10^{-15} m^3$	$1.000 \cdot 10^{-05} m$	$1.2560 \cdot 10^{-09} m^2$	-	-
n8	$4.37 \cdot 10^{-15} m^3$	$1.015 \cdot 10^{-05} m$	$1.2936 \cdot 10^{-09} m^2$	$1.2927 \cdot 10^{-09} m^2$	0.07%
n16	$4.25 \cdot 10^{-15} m^3$	$1.005 \cdot 10^{-05} m$	$1.2696 \cdot 10^{-09} m^2$	$1.2720 \cdot 10^{-09} m^2$	0.25%
n32	$4.19 \cdot 10^{-15} m^3$	$1.001 \cdot 10^{-05} m$	$1.2568 \cdot 10^{-09} m^2$	$1.2600 \cdot 10^{-09} m^2$	0.22%

Table 5.1 – Corrected radius and surfaces of several droplet simulations with different mesh resolution. The recovered surface is computed from Equation 5.3.

We can observe that the finer the mesh, the higher the accuracy on terms of volume and, thus, more reliable is the simulation. The surface calculated is always higher than the theoretical one. Finally, the surface calculated integrating the magnitude of the surface interface density over the volume of the droplet and the surface calculated integrating on time over a transverse plane are reported. It can be observed that on all the resolutions the surface recovered on the plane match accurately with the one computed over the volume. On higher resolutions the error increases slightly; it can be many effects, but a probable one is the apparition of small surface waves that are capture on higher resolution meshes and increases the amount of surface interface.

5.2.2 Estimation of the curvature

The other property used in this technique is the curvature of the liquid structures. There are many methods to estimate the curvature of a surface such a [Kindlmann et al., 2003] where they used a distance function to the interface to compute the two main curvatures κ_1 and κ_2 . This technique is used on Level-set method based solvers, and it can be used also in coupled Level-set Volume of Fluid methods. In the other hand, it can not be applied directly on VoF based methods. The OpenFOAM solver `interFoam` uses another approach to calculate the curvature based on the work by [S.B.Pope, 1988]. The mean curvature $\kappa = (\kappa_1 + \kappa_2)/2$ is calculated as the divergence of the surface unitary normal vector:

$$\kappa = \nabla \cdot \left(\frac{\nabla \alpha}{|\nabla \alpha|} \right) \quad (5.4)$$

As it was done for the surface interface density Σ , the droplet test case was carried out to compute the mean curvature κ over the droplet surface. On Figure 5.2 the mean curvature κ computed with Equation 5.4 is plotted over the iso-surface $\alpha = 0.5$ for the three mesh resolutions.

It can be observed that the lower the resolution the more homogeneous is the curvature distribution provided on Figure 5.3. For the coarsest mesh resolution *n8*, over the surface there are not negative values of the mean curvature, and most of the values are around $\kappa = 2 \cdot 10^5 m^{-1}$ which corresponds to the diameter of the droplet $D = 20 \mu m$ since $D = 4/\kappa$. Moreover, the average curvature $\bar{\kappa}$ is also almost $\kappa = 2 \cdot 10^5 m^{-1}$. On the other hand, the other two resolutions are able to capture negative curvature which corresponds to surface waves. This effect is related and justifying the differences among the recovered surface and the theoretical surface for the cases *n16* and *n32* on Table 5.1. Still, most of the curvature data is placed around the theoretical value so is the mean curvature.

The accuracy of this curvature description has been studied in works such as [Abadie et al., 2015] concluding that accurate transport schemes are required for the advection term.

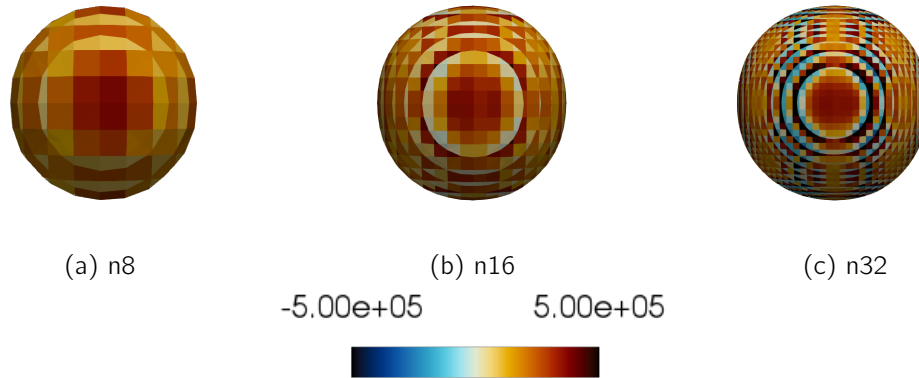


Figure 5.2 – Mean curvature κ plotted over the iso-surface $\alpha = 0.5$. From left to right: mesh resolution $dx = 2.5\mu m, 1.25\mu m, 0.625\mu m$.

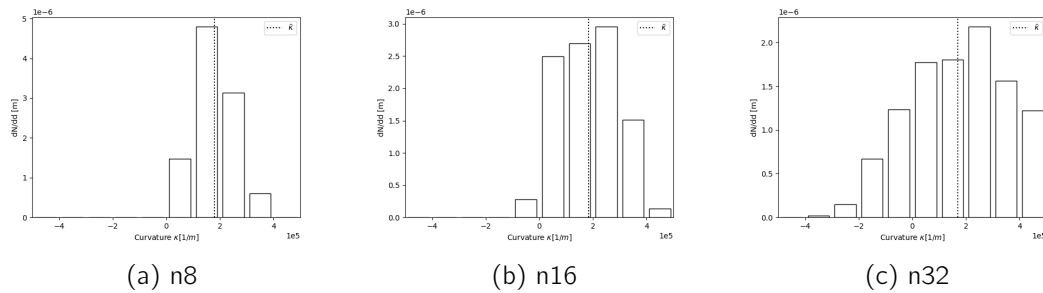


Figure 5.3 – Mean curvature κ distribution on the iso-surface $\alpha = 0.5$. From left to right: mesh resolution $dx = 2.5\mu m, 1.25\mu m, 0.625\mu m$.

Further treatment of the curvature can be done to deal with the not-well resolved curvatures. The work by [Raeni et al., 2012] proposes smoothing of the liquid volume fraction field to have a more accurate calculation of the curvature. Another treatment to smooth the curvature but keep α sharp is reported in [Tretola and Vogiatzaki, 2021].

5.3 Sauter mean diameter (SMD)

A first approach to characterize the spray is to calculate the Sauter mean diameter (SMD) which is a characteristic diameter that measures the ratio between the volume and the surface of the formed droplets. If the singular information of every droplet is known, the Sauter mean diameter is described by the following formula [Lefebvre and McDonell, 1988]:

$$D_{32} = \frac{\sum_i N_i D_i^3}{\sum_i N_i D_i^2} \quad (5.5)$$

where D_{32} is the Sauter mean diameter, N is the number of droplets, D the droplet diameter and the subscript i represent each bin inside of the discrete probability density function. This mean diameter is used mostly to model mass transfers and reaction formulation. It is also used on the well known empirical formulation for spray distribution, Rosin-Rammler [Rosin and Rammler, 1933].

Coming back to methodology proposed by [Palanti et al., 2022], an equivalent equivalent Sauter mean diameter, within the VoF framework is calculated with:

$$l_{32}(S) = 6 \frac{V_l}{A_l} = 6 \frac{\int_T \iint_S (\alpha \mathbf{u} \cdot \mathbf{n} ds) dt}{\int_T \iint_S (\Sigma \mathbf{u} \cdot \mathbf{n} ds) dt} \quad (5.6)$$

where l_{32} is the equivalent Sauter mean diameter length. V_l is the liquid volume and A_l is the liquid-surface interface area. α is the liquid volume fraction, Σ is the surface interface density and \mathbf{u} is the velocity vector. S represents a cross plane where the volume and area of the liquid are measured, and T is the total time.

The equation calculates the equivalent Sauter mean diameter l_{32} as an equivalent length which is equal to D_{32} when all the liquid going through the measurement plane is a full-atomized spray; in other words, every droplet is perfectly spherical. The constant 6 at the left hand of the equation makes analogous this equation to Equation 5.5 when this effect happens:

When the spray is not fully-formed, Equation 5.6 is represented a length scale close to D_{32} . It has been proof by [Palanti et al., 2022] that this parameter has huge importance even when the liquid is not atomized. When l_{32} is measured in function of the axial coordinate, on a injection system such a air-blast prefilming atomization, l_{32} decreases until it reach a plateau. This means that most of the continuous liquid flow has been broken-up into smaller liquid structures, hence, ligaments and droplets have been formed. At this point l_{32} is close to the final D_{32} of the fully atomized-spray.

To apply this approach to the CHAIRLIFT airblast atomizer, several planes measure the liquid volume fraction flux $\varphi\alpha$ and the surface interface flux $\varphi\Sigma$ each time step on run time. Figure 5.4 shows the numerical domain and the planes where the measurements are taken.

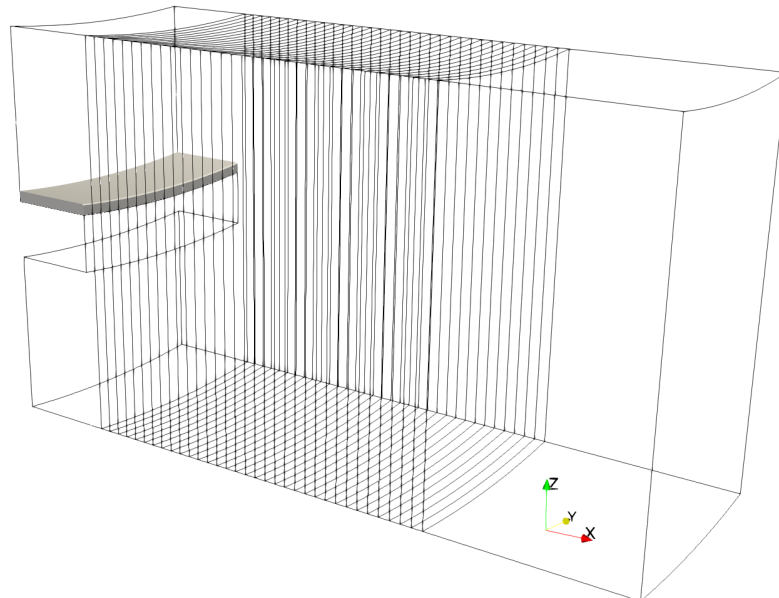


Figure 5.4 – Measurements planes inside of the numerical domain

The planes location starts at the prefilmer's lip ($x = 0mm$) and there is a plane each $0.05mm$ up to the end of the refinement zone. The data collected once the refinement zone is over is not reliable anymore. The liquid volume fraction flux $\varphi\alpha$ is conserved between mesh resolutions but, in the other hand, the surface interface flux $\varphi\Sigma$ is not.

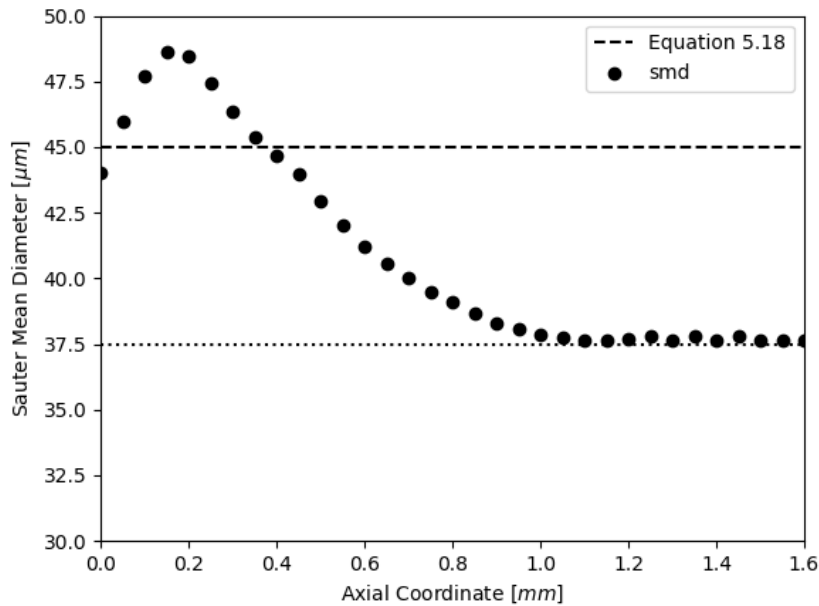


Figure 5.5 – Equivalent Sauter Mean Diameter streamwise evolution.

Figure 5.5 shows the streamwise evolution of the equivalent Sauter Mean Diameter computed with Equation 5.6. It can be appreciated that at the prefilmer’s lip, the value is on the order of the liquid film thickness $l_{32}(0) \approx t$. l_{32} increases up to a maximum value at $x = 0.2\text{mm}$ where the film begins to break-up. Afterwards, the film is broken-up into smaller liquid structures, generating ligaments and droplets. Therefore, the surface interface among liquid and gas starts to increase, decreasing l_{32} . Finally, l_{32} stabilizes and converges around $x = 1\text{mm}$. From this point to the end of the numerical domain, a secondary break-up is not taking place. We can assume that the equivalent Sauter Mean Diameter calculated is almost equal to the final Sauter Mean Diameter $D_{32} \approx l_{32}(x = 1\text{mm})$.

The converged l_{32} is plotted on a dotted line meanwhile on a dashed line the value from the correlation by [Gepperth et al., 2013] (Equation 4.18). The value from the Gepperth correlation is higher $dD_{32}^{\text{Gepperth}} = 45.0\mu\text{m}$ but the computed value $l_{32} = 37.5\mu\text{m}$ is of the same order of magnitude. It is worth nothing that the Gepperth correlation was obtained by a planer prefilmer without any swirl motion. Anyhow, the similarity of both values, is remarkably good.

5.4 Surface curvature distribution (SCD)

Following the work by [Canu et al., 2018] a link between the drop size distribution and the surface curvature distribution can be done. For a given cloud of spherical droplets, it is straightforward to calculate the drop size distribution, and from it, the surface curvature distribution can be calculated following Figure 5.6.

In the inverse way, if we obtain the surface curvature distribution, we can compute the drop size distribution. From the data recovered Σ , κ of both, ligaments and droplets, it is possible to arrange the surface interface (Equation 5.3) to its related curvature and calculate the surface curvature distribution.

To apply this technique into the airblast atomizer a plane fulfilled with probes was

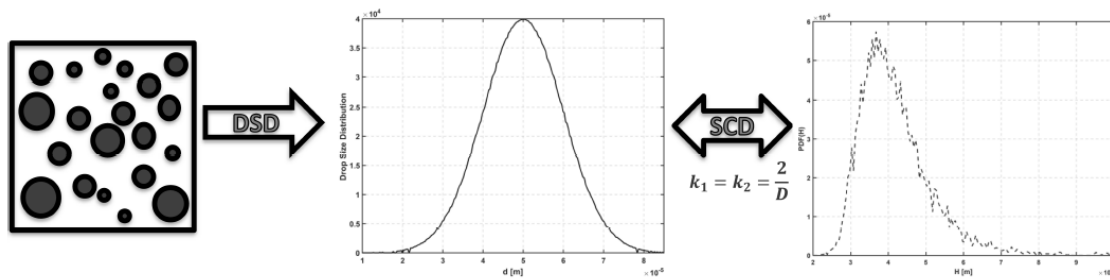


Figure 5.6 – Link between the DSD and the SCD for a known cloud of spherical droplets [Canu et al., 2018].

set-up. A modified version of OpenFOAM probes utility is used. For more information of the implementation of this tool read Appendix B. The location of this plane is not arbitrary. The plane is placed farther from the converged value of l_{32} . As we have seen before on Figure 5.5, at $x = 1.0\text{mm}$ l_{32} stabilized on a constant value. In this case, the plane has set up downstream at $x = 1.2\text{mm}$. Figure 5.7 shows the place where the probes are set up to measure the mean curvature κ , the surface interface flux $\varphi\Sigma$, the velocity vector \mathbf{u} and the liquid volume fraction flux $\varphi\alpha$. Those measurements are taken on the faces of the cells inside of the rectangle shown on the domain which is located within the refinement zone.

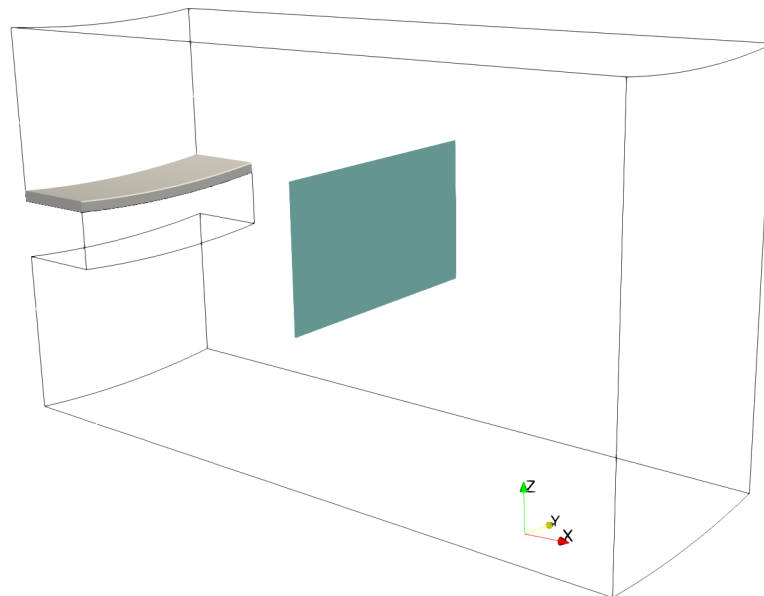


Figure 5.7 – Zone where the measurement probes are set up.

Around 14.000 probes are placed and they store every variable each time step of the simulation on run time. Finally, the raw data after 3ms of simulation is $\approx 1Tb$. This data contain information about the air and liquid fields and many information that is not required for this work. Once treated and removed everything that is not needed the storage is reduced to 90Gb. In this work the statistics are carried out globally, but it could be the case where this technique was used in function of the coordinates.

The SCD can be made arranging the total surface going through each cell face ($A_i^t = \varphi\Sigma_i^t\Delta t$) by its related mean curvature κ . The results of this procedure is shown on

Figure 5.8.

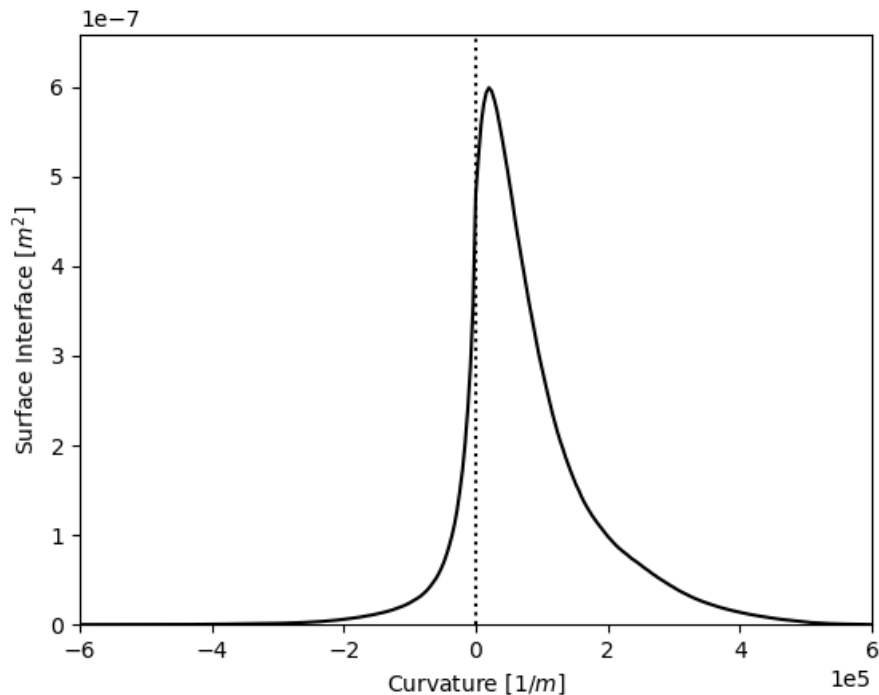


Figure 5.8 – Surface Curvature Distribution at 1.2 mm

It can be seen that some of the surface interface correspond to negative values of the mean curvature. That surface is related to concave liquid structures, thus, bubbles or bent ligaments. This technique takes the assumption that every liquid structure is a perfect spherical droplet, hence, every amount of surface linked to negative values of curvature is discarded. The surface interface related to negative curvature corresponds 11.3% of the total surface interface.

Figure 5.9 shows a liquid volume fraction iso-surface for $\alpha = 0.5$ where the mean curvature κ is plotted on it. On the left side, all the surface is represented and we can see on blue the liquid structures with negative values; those structures are mainly near to the prefilmer's lip and on the not broken up ligaments. On red the liquid structures related to positive values of curvature are plotted which are the droplets or some ligaments. On this case we can observe that those structures appear mainly once the liquid sheet is completely broken-up. Finally, on white the flat or almost flat liquid structures are represented. Again, these structures are mainly placed near the prefilmer's lip.

On the right the picture, the same iso-surface is represented but on this case the negative curvatures are plotted on dark grey color representing the liquid structures that we are discarding from the post-processing technique. A high amount of this surface is located around the prefilmer's lip and where the liquid film has not broken up yet. However, at the measurement plane, there are just few liquid structures with negative curvature values.

Once the negative curvature structures are cleaned up of this analysis, the assumption of having a cloud of perfect spherical droplets is applied to be able to calculate the drop size distribution.

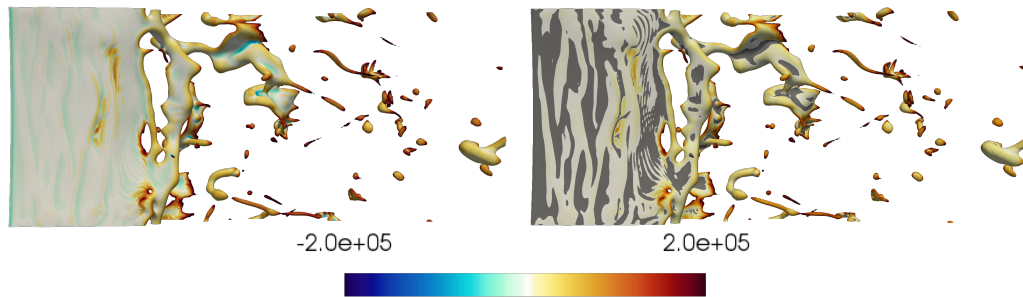


Figure 5.9 – Curvature plotted over a spray iso-surface ($\alpha = 0.5$).

5.5 Drop size distribution (DSD)

From the computed surface curvature distribution, the drop size distribution can be calculated using the following equations:

$$D(\kappa) = \frac{4}{\kappa} \quad (5.7)$$

$$n(\kappa) = \frac{S_T(\kappa)}{\pi D(\kappa)} \quad (5.8)$$

where $D(\kappa)$ is the diameter related to the curvature κ from the SCD and $S_T(\kappa)$ is the total surface related to this value of curvature κ .

Applying this assumption to the surface curvature distribution from Figure 5.8 removing first the surface linked to negative curvatures we obtain the drop size distribution on Figure 5.10.

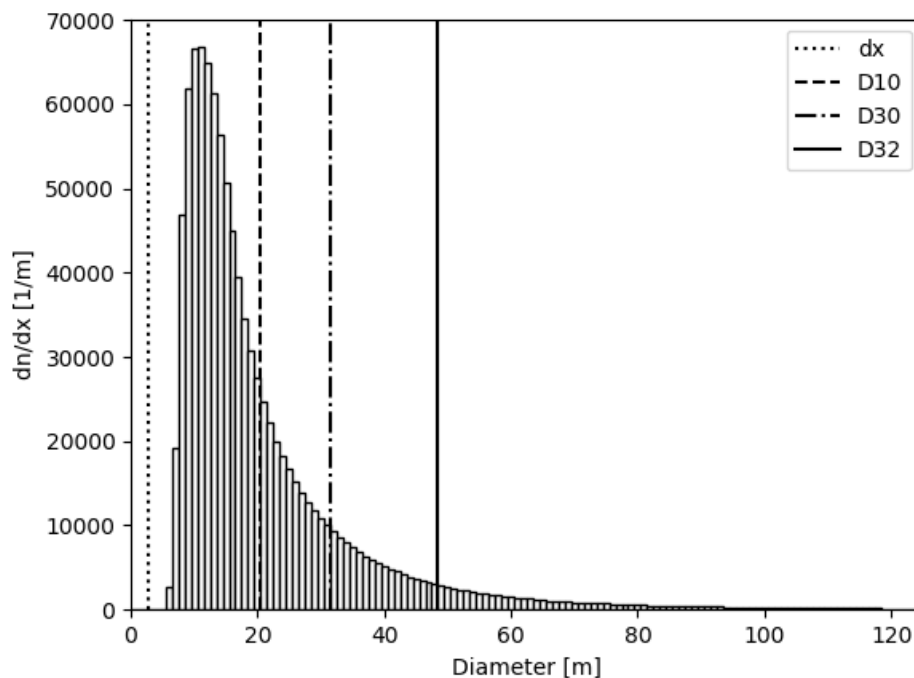


Figure 5.10 – Drop size distribution calculated from the surface curvature distribution on Figure 5.8.

The Sauter mean diameter D_{32} is plotted on solid line. We can observe that the D_{32} calculated with Equation 5.5 directly from the DSD $D_{32}^{DSD} = 48.5\mu m$ is higher than the one obtained with the surface interface-liquid volume fluxes ratio (Equation 5.6) $D_{32}^{flux} = 37.5\mu m$. The discrepancies between the two values are on the rough assumption of considering every liquid structure a spherical droplet. To deal with this matter, [Palanti et al., 2022] proposed to rearrange the DSD and fix the D_{32}^{DSD} to the one obtained by Equation 5.6 D_{32}^{flux} . Thus, the nonphysical large droplets computed by the post-processing technique disappear. The result is shown on Figure 5.11.

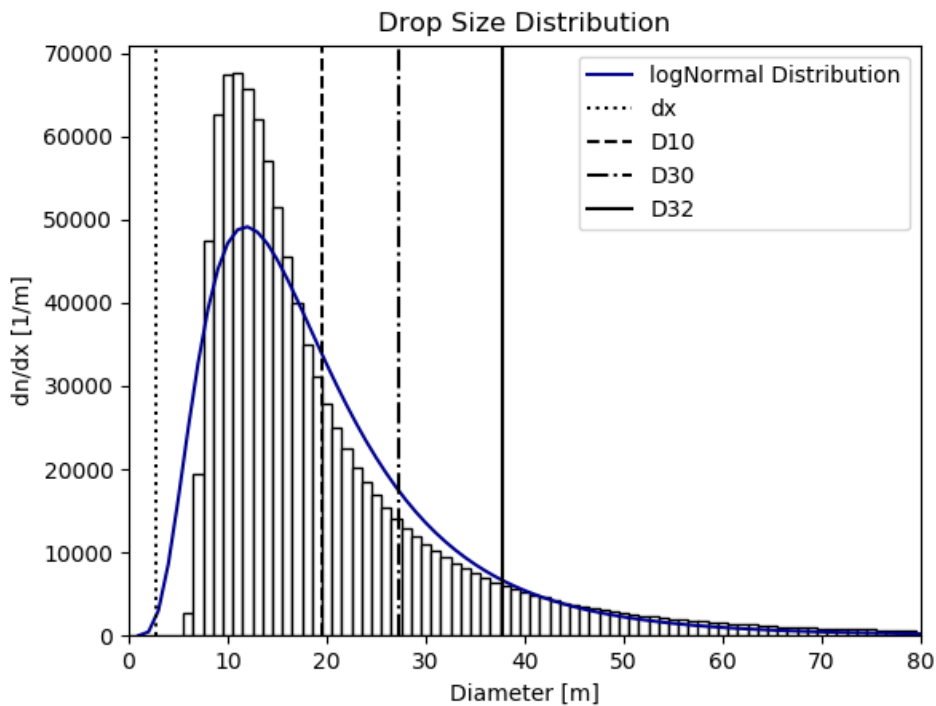


Figure 5.11 – Drop size distribution rearranged to match $D_{32}^{DSD} = D_{32}^{flux}$

The main representative diameters are plotted on Figure 5.11. Also, on dotted line, the smallest cell size is plotted $dx = 3\mu m$. The limitation of this methodology is the mesh resolution since droplets of equal or smaller diameter than the smaller δx can not be captured. In this case, the mesh resolutions is fine enough to capture the smallest droplets. It can be checked looking at the number of droplet of the smallest diameter. The drop size distribution follows a natural tendency where the number of droplets increases up to a maximum ($D_{peak} = 14\mu m$) and then decreases. The distribution is also fitted with a log-normal distribution (blue solid line) which is one of the most common statistical distribution used to characterize spray [Lefebvre and McDonell, 1988].

Removing the larger droplets impacts also on the surface curvature distribution. Figure 5.12 shows the surface curvature distribution at the left. On the top is the already shown SCD. On the middle, the surface related to negative curvatures is highlighted on black lines; the amount of surface of negative curvatures is the 11.3% of the total surface interface captured. On the bottom, the surface related to the large droplets and ligaments is also highlighted on black lines; the sum of the discarded surface is 46.6%. On the middle of the figure, the drop size distribution linked to the SCD are shown; one with the negative curvatures removed, and the other one without the larger droplets. Finally, at the right of the

figure, a liquid volume fraction $\alpha = 0.5$ iso-surface is shown. On top of it, the curvature is plotted: on blue the negative curvatures, on red the positive ones and on white the curvatures near to zero. From top to bottom, the neglected surfaces are plotted on dark grey. Thus, we can see that when we neglect the negative curvature surfaces, most of the ligaments or flat structures are still taken into account on the measurement plane (dashed red line) which are converted into larger droplets later on when the drop size distribution is computed. Meanwhile, when the drop size distribution is rearranged, only the almost spherical droplets or small ligaments are taken into account.

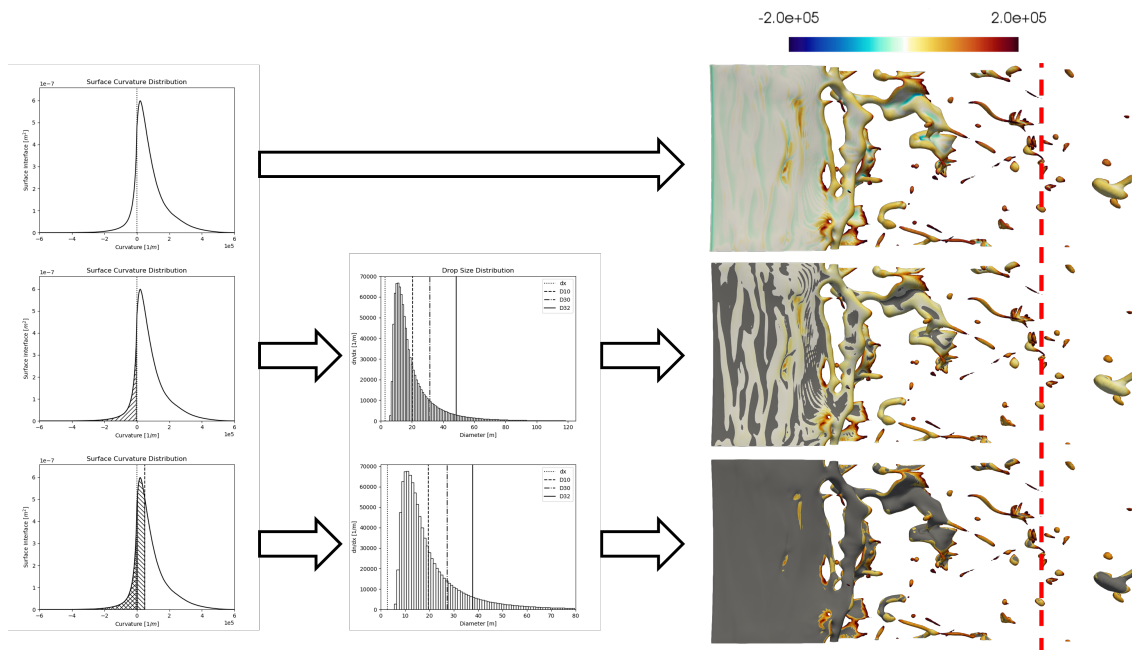


Figure 5.12 – Surface interface kept. From left to right: SCD, DSD and $\alpha = 0.5$ iso-surface with the curvature plotted on it. From top to bottom: all liquid structures, liquid structures with positive curvature $\kappa > 0$ and liquid structures which curvature is less than $\kappa < 4/D_{max}$.

To check the distribution convergence, the evolution over time of the Sauter mean diameter D_{32} , the mean diameter D_{10} and the standard deviation have been plotted on Figures 5.13, 5.14 and 5.15. On dotted lines the convergence values are plotted. It can be seen that around the time $t = 0.5ms$ the convergence is achieved.

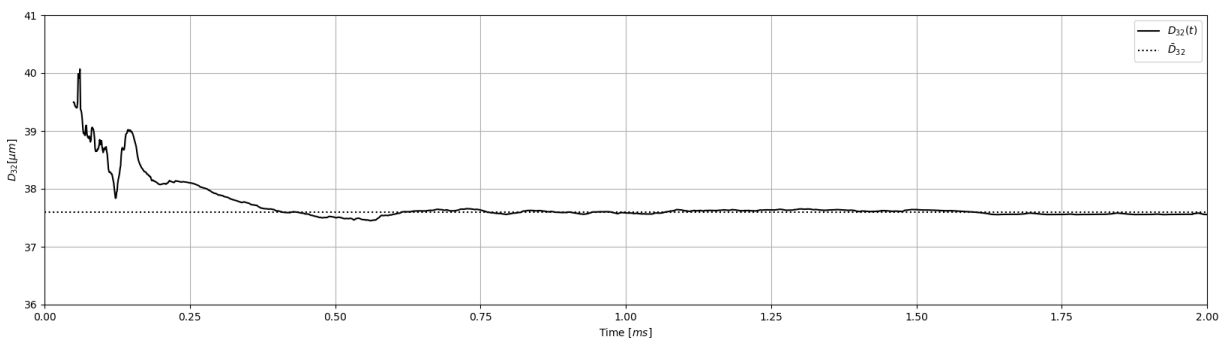
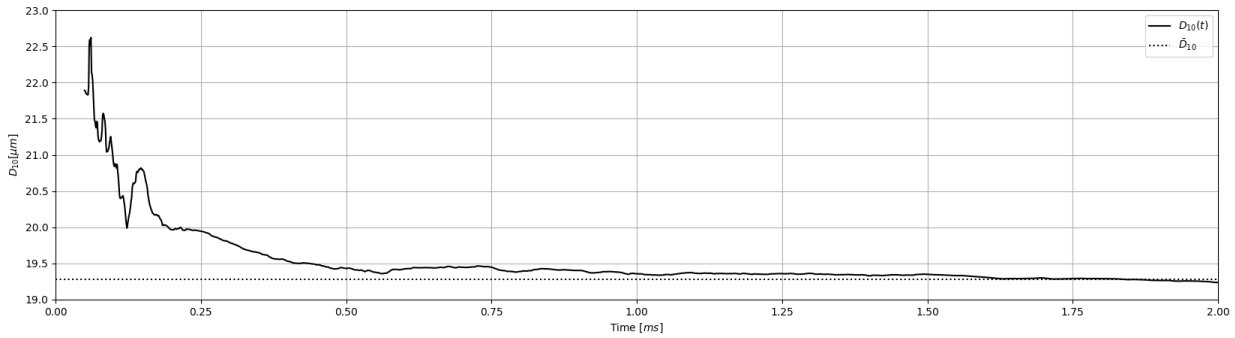
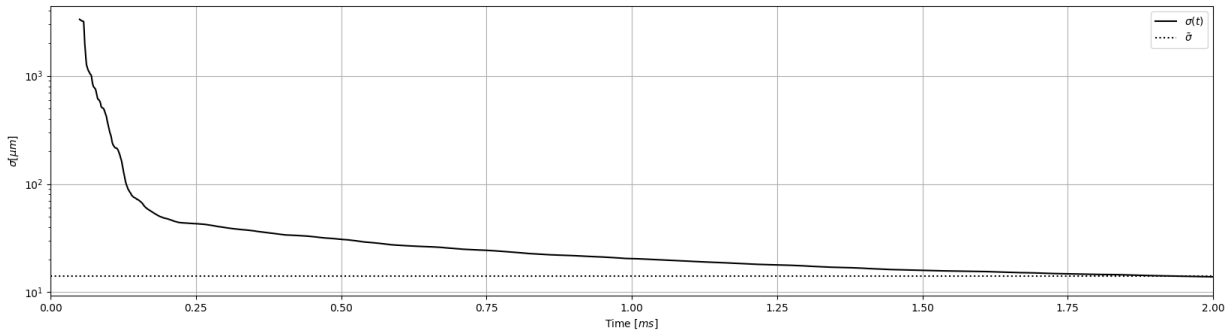


Figure 5.13 – Drop size distribution convergence study: $D_{32}(t)$.

Figure 5.14 – Drop size distribution convergence study: $D_{10}(t)$.Figure 5.15 – Drop size distribution convergence study: $\sigma(t)$.

5.6 Velocity joint distribution

In order to characterize the spray behaviour more in detail, the droplet velocity must be calculated. The most straightforward way to compute the liquid velocity is to average the velocity of the liquid structures weighted by their mass:

$$\dot{m}_l \mathbf{u}_l = \iint_S (\alpha_l \rho_l \mathbf{u}_l \cdot \mathbf{n}) \mathbf{u}_l dS \quad (5.9)$$

where \dot{m}_l and \mathbf{u}_l are the mass flow rate and the velocity of the liquid. α_l and ρ_l are the liquid volume fraction and the density of the liquid. S is the total surface where the measurements are performed, dS corresponds to the surface of each cell where the measurements are taken and \mathbf{n} is the normal vector of these faces.

With this methodology, a global velocity vector for every droplet is computed $\mathbf{u} = (22.6, -3.84, -0.59)m/s$ which correspond to the axial, tangential and radial components of the velocity vector.

This approach would be enough to set up the boundary conditions on a spray flame reactive simulation but, in the other hand, the characterization would not be completed. Due to the turbulent air flow, the velocity of the droplets is not constant, and hence, a velocity distribution is required to achieve a better knowledge of the spray. Following a similar approach explained on the last section, we can compute the velocity distribution of the spray. Since we have the velocity linked to a curvature and a quantity of surface interface $\mathbf{u}_i(\kappa, \varphi \Sigma(\kappa))$ we can calculate the number of droplets with Equation 5.8 and arrange them in a discrete distribution.

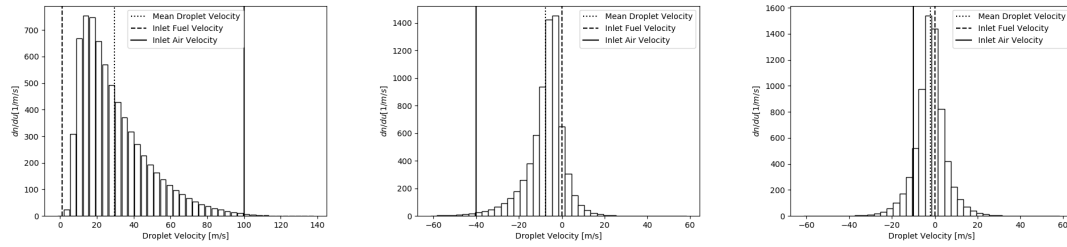


Figure 5.16 – Velocity joint distribution. From left to right: Axial, tangential and radial component of the velocity

Figure 5.16 shows the probability density functions of the three component of the velocity. On dashed line the fuel inlet velocity is plotted meanwhile on solid line the time averaged gas velocity. It can be observed that overall, the droplets are accelerated from the inlet velocity and never overcoming the air velocity. This effect is not taking place on the distribution of the radial component; as [Amini, 2016] says, once the liquid loses the wall, the tangential component of the velocity is converted into radial component, therefore, this behaviour of the droplets is expected.

On dotted line, the mean velocity of the distributions is shown. It can be compared with the velocity obtained weighted by the mass. We can observe that in general terms the velocity obtained by the surface interface and curvature technique is higher than the one obtained by the mass of liquid but always on the same order of magnitude. A comparison of both is reported on Table 5.2.

Method	Axial	Tangential	Radial	Magnitude
$\dot{m}_l \mathbf{u}_l$	22.6m/s	-3.84m/s	-0.59m/s	22.91m/s
$\Sigma - \kappa$	28.7m/s	-7.94m/s	-2.27m/s	29.86m/s

Table 5.2 – Mean velocity by the mass weighted method and the surface-curvature method.

The correlation by [Gepperth et al., 2013] gives a value of $|\mathbf{u}| = 12.76m/s$ which is a value on the order of the ones obtained by the two proposed methods but a bit lower compared to them. This may be explained by the fact that the study by Gepperth was with a planar prefilmer without any swirl motion which may be lead into some discrepancies.

Moreover, the surface-curvature method can be used to calculate the distribution of the velocity for a particular droplet diameter. Figures 5.17, 5.18 and 5.19 show the velocity distribution for a small, medium and a large droplet respectively.

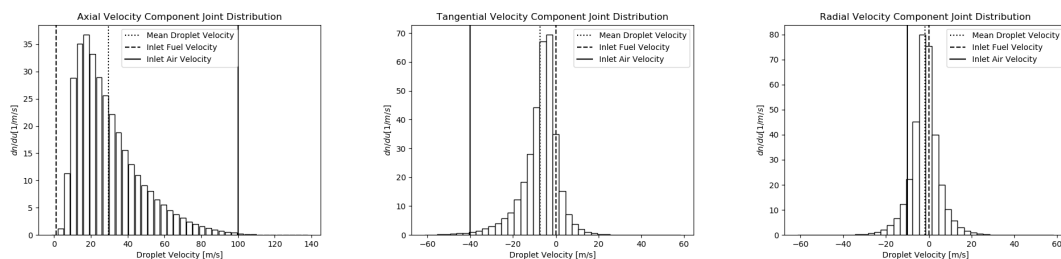


Figure 5.17 – Velocity joint distribution for a droplet of diameter $D = 8.5\mu m$. From left to right: Axial, tangential and radial component of the velocity

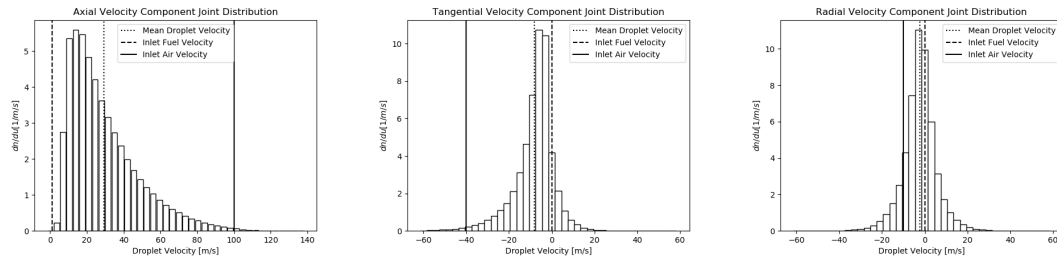


Figure 5.18 – Velocity joint distribution for a droplet of diameter $35.0 < D \leq 36.0 \mu m$. From left to right: Axial, tangential and radial component of the velocity

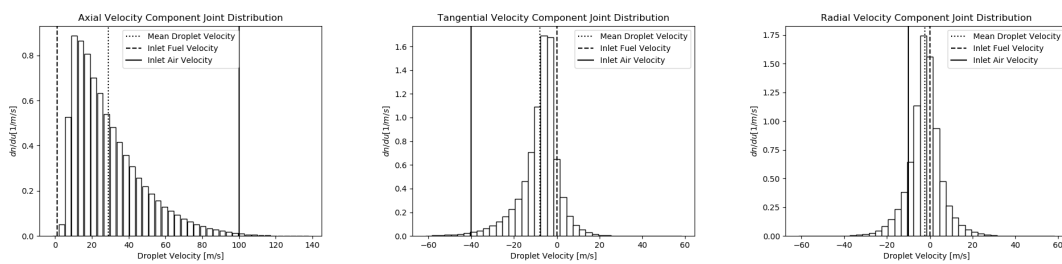


Figure 5.19 – Velocity joint distribution for a droplet of diameter $65.0 < D \leq 66.0 \mu m$. From left to right: Axial, tangential and radial component of the velocity

Not only the shape of the distribution change slightly but also the magnitude of the velocity between diameters. The mean velocity components have been plotted on Figure 5.20 to have a clearer view of this effect.

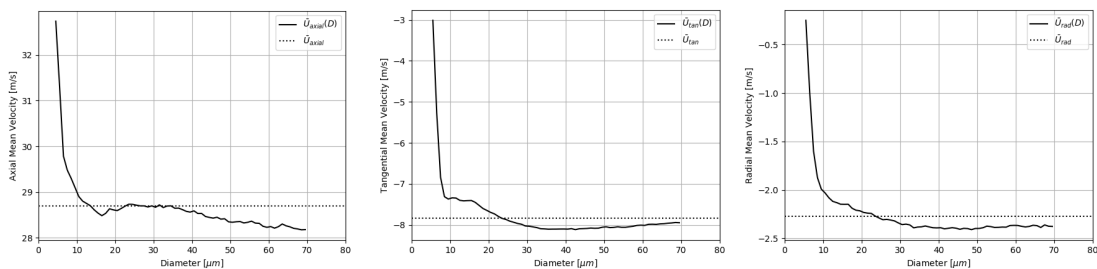


Figure 5.20 – Mean velocity by droplet diameter. From left to right: Axial, tangential and radial component of the velocity.

The air flow tends to accelerate more the smaller droplets than the larger one. This effect is mainly due to the momentum conservation and the lower inertia of the smaller droplets. It can be seen that the smaller droplets are much faster than the larger ones or even the medium ones meanwhile the difference of velocity is negligible between droplets with a diameter bigger than $20 \mu m$.

5.7 Comparison with experiments

There are several methods to use the computed data as a spray inlet boundary condition for a reactive flow. On this work 3 methods have been proposed from the simplest to the one which uses most of the information computed. Usually, to model spray on a reactive simulation, this

is treated as a cloud of lagrangian parcels [Watanabe et al., 2015]. Each parcel is defined in general for a droplet diameter, the velocity vector, the number of droplets and the mass of the parcel.

The simplest spray method proposed is using the Drop Size Distribution on Figure 5.11 and inject each time the same amount of droplets following this distribution. Also, for each droplet diameter the mean velocity vector is computed and given to the parcel. Instead of a random generation of the droplet diameter, we have finally the same parcels with the same velocity each time step.

We can improve this method randomizing the droplet diameter generation using the mass drop size distribution associated to the drop size distribution (Figure 5.21) to obtain a random diameter following the distribution. This method can be done also with the global velocity joint distribution from Figure 5.16. Finally we will have random parcel with the same mass but a different diameter and velocity vector each time step recovering a more natural spray.

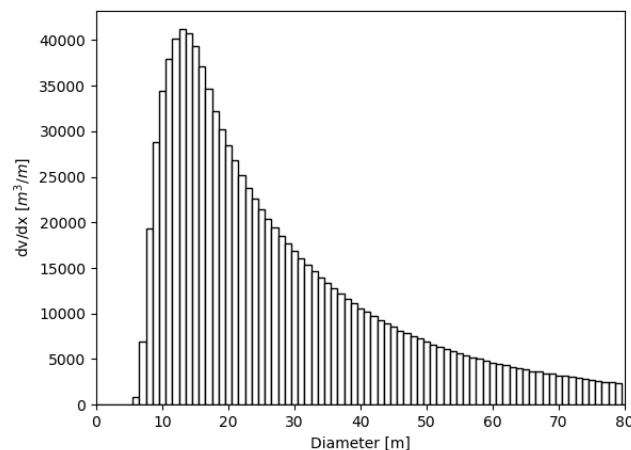


Figure 5.21 – Drop size distribution on mass terms

Finally, the last method is similar to the previous one but instead of using a global velocity joint distribution we use the velocity joint distributions by droplet diameter of Figure 5.17, Figure 5.18, Figure 5.19 for every droplet class we have. On that way we have a more complex description of the spray and we use the most of the data we have.

Before doing the coupling with the reactive simulation a small test was performed. Once the particles were generated a ballistic trajectory (uniform line movement) was applied to each parcel. This process was not done by OpenFOAM or any CFD code. A small Python 3.6 code was developed. The results are shown on Figure 5.22. The time averaged surface interface density $\bar{\Sigma}$ and the time averaged liquid volume fraction $\bar{\alpha}$ are plotted and compared with the experimental results from a MIE Scattering by [Sedlmaier, 2016].

It is true that the variables compared are not the same but the three of those magnitudes give us the idea of how the spray shape looks like. And we can compare without any airflow that the method used to model the spray as a lagrangian particle changes a lot the shape of the final spray. If we take a look to the fist method we can see that as the velocity is constant for each class of droplet diameter the dispersion of the spray is almost null. On the other hand, with the two other methods it is possible to recover a shape that is clearly similar to the experimental picture.

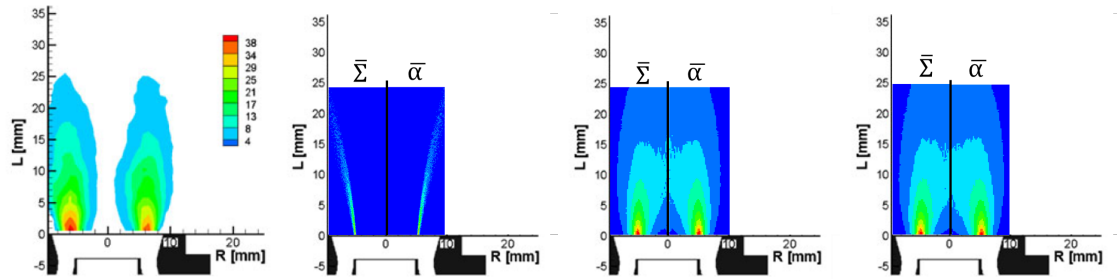


Figure 5.22 – Qualitative validation of the CHAIRLIFT airblast modelling. From left to right MIE-scattering by [Sedlmaier et al., 2014], $\bar{\Sigma}$ and $\bar{\alpha}$ contour for the constant velocity and constant distribution, random particles and global velocity joint distribution and random particles and velocity joint distribution by droplet diameter

5.8 Drop size distribution on CRSB injector

Once surface interface-curvature analysis has been explained with a similar case compared with the original work by [Palanti et al., 2022], it is also applied to the simplex swirl atomizer studied on chapter 3.

5.8.1 Ambient temperature case

In an analogous way, the computation of the equivalent *Sauter Mean Diameter (SMD)* or l_{32} (Equation 5.6) is performed.

Several planes are set-up to measure the liquid volume fraction flux $\varphi\alpha$, which is, indeed, the volumetric flow rate Q , and the surface interface flux $\varphi\Sigma$. A characteristic value of the l_{32} can be computed along the axial axis as it is shown on Figure 5.23.

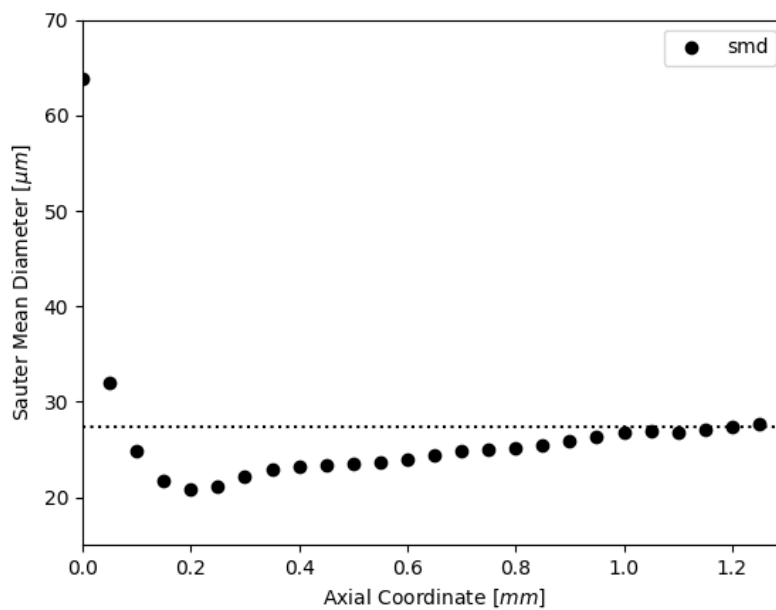


Figure 5.23 – Equivalent Sauter Mean Diameter l_{32} in function of the axial coordinate.

l_{32} has a high value on the nozzle orifice due to the hollow cone shape of the liquid. Of course, at this point $z = 0\text{mm}$, $l_{32}(0)$ does not give any relevant information since there

are not droplets to measure an equivalent SMD. However, we can see that when the fuel goes upstream, l_{32} is going down until it reach a minimum value. This zone is where the primary break-up mechanism is playing a role. The hollow cone liquid sheet begins to break-up into smaller ligaments, hence, the amount of surface interface increases and, since the mass flow rate remains constant, the fuel volume too. On the work by [Palanti et al., 2022] on a planar prefilmer, this value reached a plateau and remained constant. However, in this case we can see that from $z = 0.4mm$ to the end of the refinement zone $z = 1.3mm$ l_{32} is raising slightly. This effect can be due to the fact that the smallest droplets usually are faster on radial direction, and therefore, they leave the spray cone angle leaving, thus, the measurement zone. This effect has been proved on experiments by [Verdier, 2017] and it can be seen on Figure 5.24.

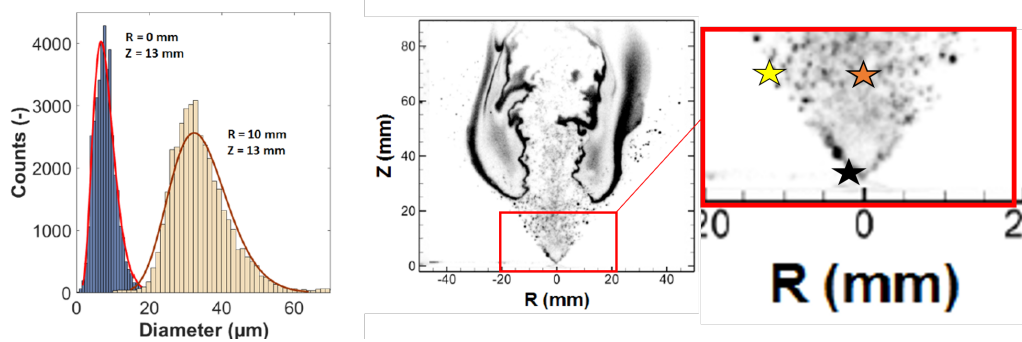


Figure 5.24 – On the left: experimental drop size distribution by [Verdier, 2017]. On the right: measurement point: blue and yellow stars corresponds to the Verdier measurement points meanwhile the black star is the measurement point of this work.

Figure 5.24 shows two drop size distributions from experiments. Both distributions were taken on the same axial coordinate ($z = 10mm$) but one of them on the axis and the other one on the spray cone angle $2\theta = 80^\circ$. The difference among them is clear, on the axis only the smaller droplets are captured meaning that their low inertia keep their radial velocity from inside of the nozzle. On the other hand, on the line aligned with the spray cone angle we can see a wider distribution. If we come back to the Figure 5.23 which is measured from the nozzle $z = 0mm$ to $z = 1.3mm$, we can say we are measuring an early stage of the atomization process, where the smallest droplets have not leaved the spray cone line. Nevertheless, the farther from the nozzle the more droplets leave the line and thus, this could be the reason why the equivalent Sauter mean diameter l_{32} is increasing with the axial position.

Finally, the technique to extract the Drop Size Distribution from the surface interface density Σ and its related curvature κ is applied at $z = 1.2mm$. The result is plotted on Figure 5.25 and it is also compared with the distribution by [Verdier, 2017] of Figure 5.24.

The distribution have been normalized to be able to compare them. It can be noticed that the simulated DSD peak is just in the middle of the experimental distributions. However, since the amount of surface is also linked with the velocity vector is possible to filter the droplets with the trajectory that they will follow. The angle for each amount of surface interface flux stored can be computed as $\theta_i^t(\Sigma_i^t, \kappa_i^t) = \tan^{-1}(u_{ri}^t/u_{ai}^t)$. To compare with the experimental location the stored data has been divided into $\theta = 35^\circ - 45^\circ$ which are the droplets that will follow the experimental spray cone angle measured $\theta_{exp} = 40^\circ \pm 5^\circ$ and the droplets going outside of θ_{exp} which are the rest of them.

The left side of Figure 5.26 shows the filtered distribution which droplets will follow the spray cone angle. Some of the smallest droplets are now removed from the distribution since

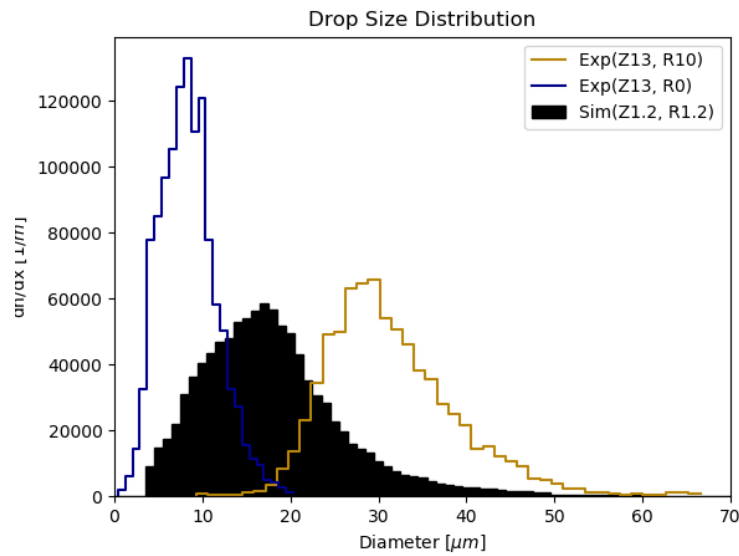


Figure 5.25 – Drop Size Distribution for the ambient temperature case. On black: post-processed DSD from the simulation. On blue and yellow lines: experimental DSD by [Verdier, 2017].

they will go outside of the spray cone angle. The diameter peak $D_{peak}^{sim} = 18\mu m$ is still lower than the experimental distribution $D_{peak}^{exp} = 32\mu m$. The Sauter mean diameter $D_{32}^{sim} = 28\mu m$ is also lower than the experimental one $D_{32}^{exp} = 36\mu m$ but on the same order. The lack of bigger droplets could be due to the modelling itself. Since the simulation performed is at the limit of mesh resolution, the liquid sheet break-up usually takes place due to numerical resolution and not due to a physical process producing smallest droplets. Another reason could be the lack of big fluctuation on the liquid sheet and the absence of coalescence among droplets since the data is measured on a early stage of the atomization process.

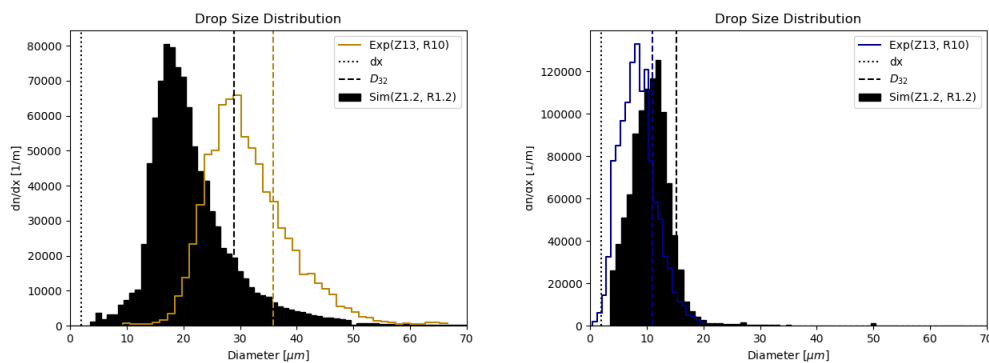


Figure 5.26 – Drop Size Distribution for the ambient temperature case. On the left: Measurements taken on the angle $\theta_{exp} = 40^\circ \pm 5^\circ$; On black: post-processed DSD from the simulation, on yellow line: experimental DSD by [Verdier, 2017]. On the right: Measurements taken on the angle outside of $\theta_{exp} = 40^\circ \pm 5^\circ$; On black: post-processed DSD from the simulation, on blue line: experimental DSD by [Verdier, 2017].

The right side of Figure 5.26 shows the filtered distribution which droplets do not follow

the spray cone angle. On this case both distributions are much more similar. The peak diameter from the simulated data $D_{peak}^{sim} = 12\mu m$ is close to the peak diameter from the experimental data $D_{peak}^{exp} = 8\mu m$. The Sauter mean diameter from the simulation $D_{32}^{sim} = 15\mu m$ is also a bit higher compared with the experimental one $D_{32}^{exp} = 11\mu m$. We can notice that the mesh resolution is playing an important role on the post-processing methodology. The minimum cell size $\delta x = 1\mu m$ is plotted and it can be noticed that the minimum droplet size measured is at least 3 times bigger than this value. The post-processed distribution is abruptly trimmed on the left size of the plot due to the lack of resolution. However, the agreement with experiments is still good to validate the methodology. Finally, it is also possible to notice that some big droplets are going out of the spray cone angle line. This effect could be minimized running more time the simulation and storing more data to post-process. Further experimental analysis would help to validate the methodology if PDA measurements are performed closer to the nozzle.

5.8.2 High temperature case

The same procedure has been applied for the pre-heated case. First, the equivalent Sauter mean diameter l_{32} in function of the axial positions is calculated with Equation 5.6. On this case, on Figure 5.27 we can appreciate a similar behaviour for l_{32} as we have seen on Figure 5.23. At the nozzle, the equivalent Sauter mean diameter, $l_{32}(z = 0) \approx 50\mu m$ is much higher than the experimental one $D_{32}^{exp} \approx 30\mu m$ measured by [Marrero, 2018]. It decreases up to $z = 0.2mm$ where reaches a plateau $l_{32} = 16\mu m$ to afterwards increase upstream. As it has been commented on the previous section, most probable the smallest droplets have higher radial velocity and, hence, some of them leave the spray cone angle θ . Thus, the SMD is calculated with bigger droplets and therefore is higher. The final value obtained is $l_{32} = 23\mu m$ which is again a bit lower compared to the experimental one but on the same order of magnitude.

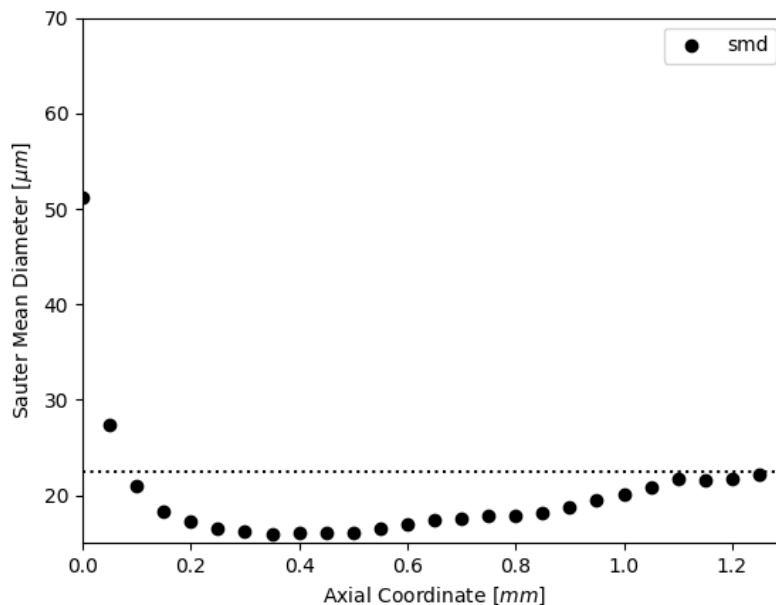


Figure 5.27 – Equivalent Sauter Mean Diameter l_{32} in function of the axial coordinate.

If we compare the l_{32} evolution at ambient and high temperature we can observe that

on the ambient temperature case l_{32}^{amb} has not ever reach a constant value meanwhile on the high temperature case l_{32}^{high} stays constant from $z = 0.2mm$ to $z = 0.6mm$. Taking a look to the iso-surfaces on Figure 3.45 and on Figure 3.49, thicker ligaments are created on the ambient temperature case but also the droplet formation begins earlier, therefore, once the primary break-up is finished, some droplets leave the spray angle path and go outside or inside the spray cone. On the other hand, the ligaments on the high temperature case need some time to atomize into smaller droplets. It can also be observed that on the high temperature case the number of droplets is much higher than on the ambient temperature case.

If we take a look to the drop size distribution we can see that on this case, both, the experimental and the numeric ones looks similar (Figure 5.28). The peak diameter in this case is well captured $D_{peak}^{exp} = D_{peak}^{sim} = 14\mu m$. However, the amount of droplets bigger than $20\mu m$ is less than the experiments.

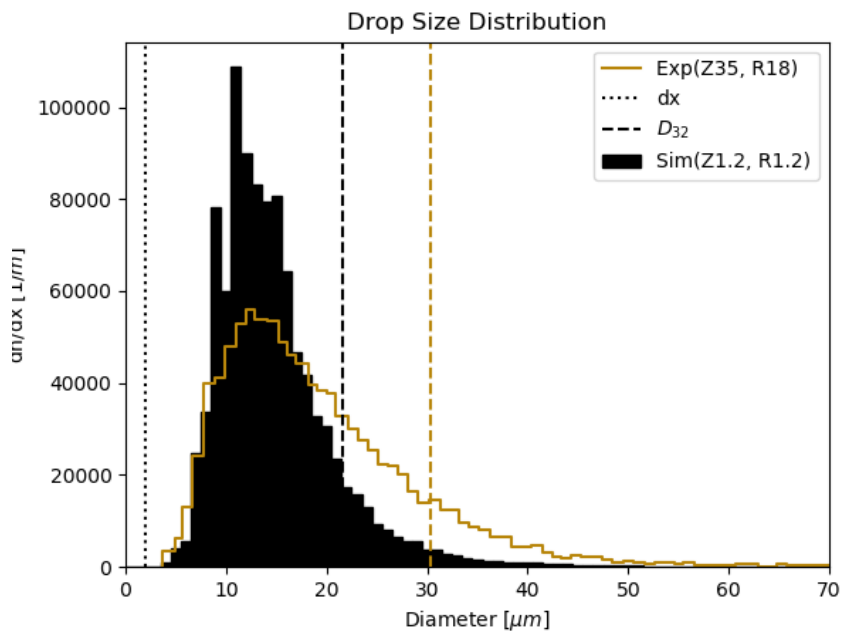


Figure 5.28 – Drop Size Distribution for the high temperature case. On black: post-processed DSD from the simulation. On yellow : experimental DSD by [Marrero, 2018]

We can observe also that the simulated Sauter mean diameter D_{32} is much lower than the experimental one. This fact is due to the lack of big droplets which are the ones that affect more on the SMD calculation.

6 | Conclusions and perspectives

Two configurations of injector systems highly used on the aeronautical field have been numerically modelled and a workflow for each one has been proposed.

The first injector is a simplex swirl atomizer used on the Coria Rouen Spray Burner (CRSB) design for academic studies on spray flame representative of GT combustion even if this injector is not thought for aeronautical proposes but involving similar physical phenomena. On this work, a workflow has been proposed to model a simplex swirl atomizer with a full characterization of the internal flow including its geometry. The first step has been to measure the internal geometry of the injector. This work has been carried out by a collaboration with the Polytechnic University of Valencia where several measurement techniques (silicone molding, optical and electron microscope, CT-scan) that were previously developed and experienced for diesel injectors. Once the geometry was reconstructed the selection of a mesh topology was not clear. On the scientific literature many topologies have been used for this kind of injectors but due to the non-axisymmetric nature of this particular injector, when considering the inlet ports, a hybrid hexahedral-tetrahedral mesh was developed after several tries. This kind of mesh allows to refine in the zones of interest, despite the complexity of the geometry, keeping the numerical stability and controlling numerical error even on the more complex zones. From these simulations, parameters such as the fuel sheet thickness and the spray cone angle could be recovered with respect to available experimental data but the mesh resolution out the orifice nozzle was not fine enough to capture the atomization process. Refining the outer mesh zone up to a level where the atomization could be caught would have increased the computational resources needed preventing to perform the simulation. Thus, to solve this problem, an outer sector domain have been proposed to model only the atomization process. Ideally a full 360° domain would have been set up, but to contain the numerical cost a sector simulation restricted to 45° . To take advantage of the internal simulations, the external atomization simulation has been coupled with data from the internal simulation. These data were mapped into the outer simulation on time and on space. Qualitative validation has been done with two different operating conditions (ambient and high temperature) validating not only the modelling but also the measurements of the geometry and the internal simulation performed initially. The comparison with experimental pictures is good overall but some of the larger structures are not well captured. This effect could be due to the periodic boundary conditions which could cancel some sheet instabilities and the limitation of mesh resolution that triggers a numerical break-up in particular for the liquid sheet perforation. Despite these limitations, results are good if we compare with the current state of the art, accordingly an article has been submitted to the journal of Atomization and Spray (see Appendix C).

The proposed methodology could be applied not only to research purposes but to industrial design of nozzles. The internal flow simulation could be easily replicated with an affordable amount of computational resources. Parametric studies can be done on a reference injector, adding feed inlet ports or modifying the attach angle with the swirl chamber to test the effect on the swirl motion. On the same way, variation of the geometry can be done

to study important properties such as the liquid sheet thickness, the spray cone angle and the swirl number that as we have seen on this work they affect the atomization process. On the other hand, carrying out the spray-atomization simulation requires a huge amount of resources but the methodology could be used for research projects.

Further work can be done to mesh the internal geometry with the same topology as the outer domain to limit numerical error related to the transition between tetrahedral to hexahedral elements. Also it is expected to use Adaptive Mesh Refinement (ARM) techniques. With these improvement it could be possible to carry out a single simulation not increasing too much the computational cost induced by the atomisation process on the outer domain. In parallel, additional experimental campaigns are taking place to study the first stages of the atomization process. The goal would be to combine both techniques, experimental and numerical, to fill the gap on the description of the atomization between the development of the first instability up to the formation of the final dilute spray. To combine the robustness of the numerical simulation which can isolate instantaneous liquid structures and they can provide tridimensional information even from the most difficult places. Combined with the accuracy of the experiments could lead into deeper understanding of this kind of atomization.

The second configuration is a prefilming airblast atomizer used for the CHARiLIRFT project. This kind of atomization involves several length scales; from the diameter of the nozzle to the smallest droplet the range of scale extend over three to four order of magnitudes. Trying to model it with a single simulation would have required a huge amount of computational resources and would take a long time. Therefore, like for the swirl injector, a workflow have been proposed to deal with this kind of complex atomizers using a multi-simulation, multi-scale approach to deal with each phenomena in particular.

The first steps have been to model the air single phase flow going through the nozzle. To capture the turbulent flow an in detail simulation has been carried out feeding it with data from a full simulation performed by the University of Florence. Data at a certain plane has been stored on time to later mapping it on space and on time to the main simulation as it has been done with the simplex swirl atomizer and on the scientific literature.

On parallel, the thickness of the fuel film of the prefilmer has had to be estimated. On the current state of the art this parameter is often neglected assuming it will not influence the final distribution of the spray due to the accumulation effect on the prefilmer. However, it is a parameter needed to set up the simulation. Therefore, a 2D simulation has been proposed and carried out to develop the fuel film through the prefilmer and to extract the film thickness value. The comparison with experimental correlations confirms it providing a thickness of similar order.

Finally, a sector domain of the prefilmer has been simulated following previously published work. On run time, the data necessary to determine the spray size distribution based on the curvature distribution following the work proposed by [Palanti et al., 2022] is stored. This original work has been extended to incorporate the velocity thus allowing for an early prediction of the joint size and velocity distribution of the spray. Thus, the drop size distribution of the CHAiRLIFT burner case has been computed but also the velocity distribution associated to the droplets. Thanks to the joint distribution it has been possible to extract one distribution for each droplet diameter finding out different behaviour of droplets depending on their size: smaller droplets accelerated more than the bigger droplets due to their lower inertia. This information are in principle important for initializing combustion simulation of spray flame. The combination of the drop size distribution with the velocity distribution by droplet class gives a much more complete definition of the spray issued from the injector. The validity of these results has been validated qualitatively against MIE scattering results.

The same analysis has been applied to the simplex swirl atomizer for the two different

operating conditions. On this case, the drop size distribution from experiments was available but measured farther downstream. First, we have checked that the numerical determination of spray characteristic near to the nozzle gives us a different but not incompatible distribution by comparison with experimental results. The remaining difference could be due to two main reasons. The first one has been already mentioned, the numerical resolution can not capture perfectly the largest droplets and, hence, they are not present on spray size distribution. The other one, and most important, is that the methodology does not take into account the dispersion of the spray since it determines the spray characteristics where the droplets are forming at early stage of the atomization process where the dispersion is not acting. This approach is determining droplets before they are dispersed. Anyhow, this methodology could be very useful for lagrangian spray injection on reactive numerical simulations since very often the spray is injected inside of the nozzle. Currently, the spray injected is taken from experimental measurement taken far away from the nozzle. Nevertheless, a first attempt, based on velocity discrimination, filters the droplets by their trajectory has been tried improving the comparison with experimental measurements. This is a perspective of this work to explore more in detail how of the position of injection of the spray influence the spray flame.

To go further, the analysis technique to determine the spray characteristic from surface distribution could be extended in different directions. This approach aims to filter the surface element, to keep for the analysis only those that have reached their final stage of atomization. For this objective the two main curvatures κ_1 and κ_2 to filter every liquid structure that is not spherical. Improving the method to calculate the mean curvature on the Volume of Fluid method would improve also the accuracy of the methodology. Other test are underway with machine learning to create a spray generator that will combine surface curvature distribution, experimental data and known characteristics of sprays. One aspect of the problem concern the number of information stored: each small parts of the surface are stored with their related curvatures, even if these pieces of surface belong to a single droplet, first attempt to recover the the center of the droplet and compress all this information by the definition of a single droplet have been done. Ultimately, a map of every droplet, with its velocity as a function of time could be created and may be combine with machine learning to create a more realistic model of the spray that can be used for instance in further combustion study.

Bibliography

- [Abadie et al., 2015] Abadie, T., Aubin, J., and Legendre, D. (2015). On the combined effects of surface tension force calculation and interface advection on spurious currents within volume of fluid and level set frameworks. *Journal of Computational Physics*, 297:611–636.
- [Ahmed, 2019] Ahmed, A. (2019). *LES of atomization for diesel fuel injectors*. PhD thesis, Université de Rouen Normandie.
- [Aigner, 1986] Aigner, M. (1986). *Charakterisierung der bestimmenden einflussgrossen bei der luftgestutzten zerstaubung: physikalische grundlagen und messtechnische erfassung*. PhD thesis, Institut für Thermische Stromungsmaschinen (ITS), Universität Karlsruhe.
- [Aigner and Wittig, 1988] Aigner, M. and Wittig, S. (1988). Swirl and counterswirl effects in prefilming airblast atomizers. *Journal of Engineering for Gas Turbines and Power*, 110:105–110.
- [Amini, 2016] Amini, G. (2016). Liquid flow in a simplex swirl nozzle. *International Journal of Multiphase Flow*, 79:225–235.
- [Anez et al., 2019] Anez, J., Ahmed, A., Hecht, N., Duret, B., Reveillon, J., and Demoulin, F. (2019). Eulerian–lagrangian spray atomization model coupled with interface capturing method for diesel injectors. *International Journal of Multiphase flow*, 113:325–342.
- [Ariatabar et al., 2017] Ariatabar, B., Koch, R., and Bauer, H.-J. (2017). Short helical combustor: Dynamic flow analysis in a combustion system with angular air supply. *Journal of Engineering for Gas Turbines and Power*, 139:041505–1.
- [Ariatabar et al., 2018] Ariatabar, B., Koch, R., and Bauer, H.-J. (2018). Short helical combustor: Flow control in a combustion system with angular air supply. *Journal of Engineering for Gas Turbines and Power*, 139:041505–1.
- [Ariatabar et al., 2016] Ariatabar, B., Koch, R., Bauer, H.-J., and Negulescu, D.-A. (2016). Short helical combustor: Concept study of an innovative gas turbine combustor with angular air supply. *Journal of Engineering for Gas Turbines and Power*, 138:031503.
- [Ashgriz, 2011] Ashgriz, N. (2011). *Handbook of Atomization and Sprays*. Springer US.
- [Añez, 2019] Añez, J. (2019). *Modeling an oil injector for a FCC reactor*. PhD thesis, Université de Rouen Normandie.
- [Bachalo, 2000] Bachalo, W. D. (2000). Spray diagnostics for the twenty-first century. *Atomization Sprays*, 10:439–474.
- [Billiant et al., 1998] Billiant, P., Chomaz, J.-M., and Huerre, P. (1998). Experimental study of vortex breakdown in swirling jets. *Journal of Fluid Mechanics*, 376:183–219.

- [Binnie and Harris, 1950] Binnie, A. M. and Harris, D. P. (1950). The application of boundary-layer theory to swirling liquid flow through a nozzle. *The Quarterly Journal of Mechanics and Applied Mathematics*, 3(1):80–106.
- [Boris and Book, 1968] Boris, J. and Book, D. (1968). Flux-corrected transport. i. shasta, a fluid transport algorithm that works. *Journal of Computational Physics*, 11(1):38–69.
- [Brackbill et al., 1992] Brackbill, J. U., Douglas, B. K., and Charles, Z. (1992). A continuum method for modeling surface tension. *Journal of computational physics*, 100.2:335–354.
- [Braun et al., 2019] Braun, S., Wieth, L., Holz, S., Dauch, T. F., Keller, M. C., Chaussonnet, G., Gepperth, S., Koch, R., and Bauer, H.-J. (2019). Numerical prediction of air-assisted primary atomization using smoothed particle hydrodynamics. *International Journal of Multiphase flow*, 114:303–315.
- [Brennen, 2005] Brennen, C. E. (2005). *Fundamentals of multiphase flow*. Cambridge university press.
- [Burluka and Borghi, 2001] Burluka, A. and Borghi, R. (2001). Development of a eulerian model for the “atomization” of a liquid jet. *Atomization and sprays*, 11(6):–.
- [Canu, 2019] Canu, R. (2019). *Développement d’une méthode compressible avec évaporation pour la simulation d’interface résolue dans le cadre de l’atomisation*. PhD thesis, Université de Rouen Normandie.
- [Canu et al., 2019] Canu, R., Duret, B., Reveillon, J., and Demoulin, F.-X. (2019). A surface resolution criterion for two-phase flows dns. In *ILASS–Europe 2019, 29th Conference on Liquid Atomization and Spray Systems*.
- [Canu et al., 2018] Canu, R., Puggelli, S., Essadki, M., Duret, B., Menard, T., Massot, M., Reveillon, J., and Demoulin, F. (2018). Where does the droplet size distribution come from? *International Journal of Multiphase Flow*, 107:230–245.
- [Chaussonnet et al., 2020] Chaussonnet, G., Gepperth, S., Holz, S., R.Koch, and H.J.Bauer (2020). Influence of the ambient pressure on the liquid accumulation and on the primary spray in prefilming airblast atomization. *International Journal of Multiphase Flow*, 125.
- [Chaussonnet et al., 2018] Chaussonnet, G., Laroche, T., Lieber, C., Holz, S., Koch, R., and Bauer, H.-J. (2018). Investigation of the liquid accumulation characteristics in planar prefilming airblast atomization. In *International Conference on Liquid Atomization and Spray Systems*.
- [Chaussonnet et al., 2013] Chaussonnet, G., Riber, E., Vermorel, O., Cuenot, B., Gepperth, S., and Koch, R. (2013). Large eddy simulation of a prefilming airblast atomizer. In *International Conference on Liquid Atomization and Spray Systems*.
- [Chaussonnet et al., 2016] Chaussonnet, G., Vermorel, O., and amjnd B. Cuenot, E. (2016). A new phenomenological model to predict drop size distribution in large-eddy simulations of airblast atomizers. *International Journal of Multiphase Flow*, 80:29–42.
- [Chen and Tang, 2020] Chen, C. and Tang, Z. (2020). Investigation of the spray formation and breakup process in an open-end swirl injector. *Science Progress*, 103(3):1–19.

- [Chen et al., 1992] Chen, S. K., Lefebvre, A. H., and Rollbuhler, J. (1992). Factors influencing the effective spray cone angle of pressure-swirl atomizers. *Journal of Engineering for Gas Turbines and Power*, 114(1):97–103.
- [Chesnel et al., 2011] Chesnel, J., Reveillon, J., Menard, T., and Demoulin, F.-X. (2011). Large eddy simulation of liquid jet atomization. *Atomization and sprays*, 21(9):711–736.
- [Chigier and Beér, 1964] Chigier, N. A. and Beér, J. M. (1964). Velocity and static-pressure distributions in swirling air jets issuing from annular and divergent nozzles. *Journal of Basic Engineering*, 86(4):788–796.
- [Chinn, 2009a] Chinn, J. J. (2009a). An appraisal of swirl atomizer inviscid flow analysis, part 1: The principle of maximum flow for a swirl atomizer and its use in the exposition of early flow analyses. *Atomization Sprays*, 19:263–282.
- [Chinn, 2009b] Chinn, J. J. (2009b). An appraisal of swirl atomizer inviscid flow analysis, part 2: Inviscid spray cone angle analysis and comparison of inviscid methods with experimental results for discharge coefficient, air core radius, and spray cone angle. *Atomization Sprays*, 19:283–308.
- [Chorin, 1968] Chorin, A. (1968). Numerical solution of the navier-stokes equations. *Mathematics of computation*, 22(104):745–762.
- [Christensen and Deigaard, 2001] Christensen, E. and Deigaard, R. (2001). Large eddy simulation of breaking waves. *Coastal engineering*, 42(1):53–86.
- [CleanAviation, 2022] CleanAviation (2022). Programme overview and structure. <https://www.clean-aviation.eu/programme-overview-and-structure>. Accessed: 2022-03-15.
- [Cordier et al., 2013] Cordier, M., Vandel, A., Cabot, G., Renou, B., and Boukhalfa, A. M. (2013). Laser-induced spark ignition of premixed confined swirled flames. *Combustion Science and Technology*, 185(3):379–407.
- [Craig et al., 2012] Craig, L., Barlow, N., Patel, S. N., Kanya, B., and Lin, S. P. (2012). Optimal and non optimal flows in a swirl atomizer. *Atomization and Sprays*, 19(12):1113–1124.
- [Crank and Nicolson, 1947] Crank, J. and Nicolson, P. (1947). A practical method for numerical evaluation of solutions of partial differential equations of the heat-conduction type. *Mathematical Proceedings of the Cambridge Philosophical Society*, 43(1):50–67.
- [Crowe, 2005] Crowe, C. T. (2005). *Multiphase flow handbook*. CRC press.
- [Danfoss, 2020] Danfoss (2020). Oil nozzles: Practical tips. <https://assets.danfoss.com/documents/100691/AG045286446960en-010101.pdf>. Accessed: 2021-07-27.
- [De-Giorgi et al., 2021] De-Giorgi, M. G., Bonuso, S., Mehdi, G., Shamma, M., Harth, S. R., Zarzalis, N., and Trimis, D. (2021). Enhancement of blowout limits in lifted swirled flames in methane-air combustor by the use of sinusoidally driven plasma discharges. In *Active Flow and Combustion Control Conference*.
- [DeBar, 1974] DeBar, R. (1974). Fundamentals of the kraken code. [eulerian hydrodynamics code for compressible nonviscous flow of several fluids in two-dimensional (axially symmetric) region]. Technical report, Technical Report UCID-17366.

- [Demoulin et al., 2001] Demoulin, F.-X., Beau, P.-A., Blokkeel, G., Mura, A., and Borghi, R. (2001). A new model for turbulent flows with large density fluctuations: Application to liquid atomization. *Atomization and sprays*, 17(4):–.
- [Deshpande et al., 2012] Deshpande, S., Anumolu, L., and Trujillo, M. (2012). Evaluating the performance of the two-phase flow solver interFoam. *Computational science & discovery*, 5(1):014016.
- [Ding et al., 2016] Ding, J.-W., Li, G.-X., Yu, Y.-S., and Li, H.-M. (2016). Numerical investigation on primary atomization mechanism of hollow cone swirling sprays. *International Journal of Rotating Machinery*, 2016:11.
- [Dombrowski and Hasson, 1969] Dombrowski, N. and Hasson, D. (1969). The flow characteristics of swirl centrifugal spray pressure nozzles with low viscosity liquids. *American Institute of Chemical Engineers Journal*, 15(4):604–611.
- [Ducros et al., 1998] Ducros, F., Nicoud, F., and Poinso, T. (1998). Wall-adapting local eddy-viscosity models for simulations in complex geometries. *Numerical Methods for Fluid Dynamics*, VI:–.
- [El-Shanawany and Lefebvre, 1980] El-Shanawany, M. and Lefebvre, A. (1980). Airblast atomization: The effect of linear scale on mean drop size. *Journal of Energy*, 4(4):184–189.
- [Fansler and Parrish, 2015] Fansler, T. and Parrish, S. E. (2015). Spray measurement technology: A review. *Measurement Science and Technology*, 26:1–35.
- [Ferrando et al., 2021a] Ferrando, D., Belmar-Gil, M., Palanti, L., Carreres, M., Demoulin, F.-X., Renou, B., Duret, B., and Reveillon, J. (2021a). Internal numerical simulation of a swirl simplex atomizer to predict atomization outputs. In *International Conference on Liquid Atomization and Spray Systems*.
- [Ferrando et al., 2021b] Ferrando, D., Carreres, M., Belmar-Gil, M., Cervelló-Sanz, D., Duret, B., reveillon, J., Salvador, F., and Demoulin, F.-X. (2021b). Modelling internal flow and primary atomization in a simplex pressure-swirl atomizer. *Atomization and Sprays*.
- [Ferrando et al., 2021c] Ferrando, D., Palanti, L., Demoulin, F.-X., Duret, B., and Reveillon, J. (2021c). Spray drop size distribution and velocity distribution issued from a prefilming airblast atomizer. In *International Conference on Liquid Atomization and Spray Systems*.
- [Ferziger and Peric, 1996] Ferziger, J. and Peric, M. (1996). *Computational Method for Fluid Dynamics*. Springer.
- [Fokaides et al., 2007] Fokaides, P. A., Kasabov, P., and Zarzalis, N. (2007). Experimental investigation of the stability mechanism and emissions of a lifted swirl non-premixed flame. In *ASME Turbo Expo 2007: Power for Land, Sea and Air*.
- [Frohlich et al., 2005] Frohlich, J., Mellen, C., Rodi, W., Temmerman, L., and Leschziner, M. (2005). Highly resolved large-eddy simulation of separated flow in a channel with streamwise periodic constrictions. *Journal of Fluid Mechanics*, 526:19–66.
- [Galbiati et al., 2016] Galbiati, C., Tonini, S., Weigand, B., and Cossali, G. E. (2016). Direct numerical simulation of primary break-up in swirling liquid jets. In *International Conference on Multiphase Flow*.

- [Gepperth et al., 2010] Gepperth, S., Guildenbecher, D., Koch, R., and Bauer, H.-J. (2010). Pre-filming primary atomization: Experiments and modeling. In *23rd Annual Conference on Liquid Atomization and Spray Systems*.
- [Gepperth et al., 2013] Gepperth, S., Koch, R., and Bauer, H.-J. (2013). Analysis and comparison of primary droplet characteristics in the near field of a prefilming airblast atomizer. In *Proceedings of ASME Turbo Expo 2013: Turbine Technical Conference and Exposition*.
- [Gepperth et al., 2012] Gepperth, S., Müller, A., Koch, R., and Bauer, H.-J. (2012). Ligament and droplet characteristics in prefilming airblast atomization. In *Triennial International Conference on Liquid Atomization and Spray System*.
- [Ghandhi and Heim, 2009] Ghandhi, J. B. and Heim, D. M. (2009). An optimized optical system for backlit imaging. *Review of Scientific Instruments*, 80(5).
- [Giffen and Muraszew, 1953] Giffen, E. and Muraszew, A. (1953). Atomization of liquid fuels. *Journal of the royal aeronautic society*, 58:146.
- [Greenshields, 2019] Greenshields, C. J. (2019). *OpenFOAM: User Guide version 6*. The OpenFoam Foundation.
- [Gueyffier et al., 1999] Gueyffier, D., Li, J., Nadim, A., Scardovelli, R., , and Zaleski, S. (1999). Volume-of-fluid interface tracking with smoothed surface stress methods for three-dimensional flows. *Journal of computational physics*, 152(2):423–456.
- [Guo et al., 2014] Guo, Y., Wei, L., Liang, G., and Shen, S. (2014). Simulation of droplet impact on liquid film with clsvof. *International Communications in Heat and Mass Transfer*, 56:26–33.
- [Hansen et al., 2002] Hansen, K. G., Madsen, J., Trinh, C. M., Ibsen, C. H., Solberg, T., and Hjertager, B. H. (2002). A computational and experimental study of the internal flow in a scaled pressure-swirl atomizer. In *ILASS-Europe*.
- [Hewitt and Hall-Taylor, 1970] Hewitt, G. and Hall-Taylor, N. (1970). *Annular two-phase flow*. Oxford ; New York : Pergamon Press.
- [Hirt and Nichols, 1981] Hirt, C. W. and Nichols, B. D. (1981). Volume of fluid (vof) method for dynamics of free boundaries. *Journal of computational physics*, 39:201–225.
- [Hoffmann et al., 2021] Hoffmann, S., Koch, R., and Bauer, H.-J. (2021). Numerical investigation of the low-swirl flow in an aeronautical combustor with angular air supply. In *Proceedings of ASME Turbo Expo 2021 Turbomachinery Technical Conference and Exposition*.
- [Holz et al., 2016] Holz, S., Chaussonnet, G., Gepperth, S., Koch, R., and Bauer, H.-J. (2016). Comparison of the primary atomization model pamela with drop size distributions of an industrial prefilming airblast nozzle. In *Europe 2016, 27th Annual Conference on Liquid Atomization and Spray Systems*.
- [Holzmann, 2020] Holzmann, T. (2020). *Mathematics, Numerics, Derivations And Open-FOAM*. Tobias Holzmann.

- [Ibrahim and Jog, 2007] Ibrahim, A. A. and Jog, M. A. (2007). Nonlinear breakup model for a liquid sheet emanating from a pressure-swirl atomizer. *Journal of Engineering for Gas Turbines and Power*, 129(4):945–953.
- [Inamura et al., 2019] Inamura, T., Katagata, N., Nishikawa, H., Okabe, T., and Fumoto, K. (2019). Effects of prefilmer edge thickness on spray characteristics in prefilming airblast atomization. *International Journal of Multiphase Flow*, 121.
- [Issa et al., 1986] Issa, R., Gosman, A., and Watkins, A. (1986). The computation of compressible and incompressible recirculating flows by a non-iterative implicit scheme. *Journal of computational physics*, 62(1):66–82.
- [Juric and Tryggvason, 1998] Juric, D. and Tryggvason, G. (1998). Computations of boiling flows. *International Journal of Multiphase Flow*, 24(3):387–410.
- [Kasabov, 2014] Kasabov, P. (2014). *Experimentelle Untersuchungen an abgehobenen Flammen unter Druck*. PhD thesis, Karlsruher Instituts für Technologie.
- [Kasabov et al., 2013] Kasabov, P., Zarzalis, N., and Habisreuther, P. (2013). Experimental study on lifted flames operated with liquid kerosene at elevated pressure and stabilized by outer recirculation. *Flow Turbulence Combust*, 90:605–619.
- [Kindlmann et al., 2003] Kindlmann, G., Whitaker, R., Tasdizen, T., and Moller, T. (2003). Curvature-based transfer functions for direct volume rendering: Methods and applications. *IEEE Visualization*, 2003:513–520.
- [Kutty et al., 1978] Kutty, P. S., Narasimhan, M. V., and Narayanaswamy, K. (1978). Design and prediction of discharge rate, cone angle, and air core diameter of swirl chamber atomizers. In *Proceedings of the 1st International Conference on Liquid Atomization and Spray Systems*.
- [Langone, 2022] Langone, L. (2022). *Numerical Modelling of Partially Premixed Low-Swirl Flames for Aero-Engine Applications*. PhD thesis, Universita degli Studi di Firenze, Italy.
- [Langone et al., 2022] Langone, L., Amerighi, M., and Andreini, A. (2022). Large eddy simulations of a low-swirl gaseous partially premixed lifted flame in presence of wall heat losses. *Energies*, 15:788.
- [Lebas et al., 2005] Lebas, R., Blokkeel, G., Beau, P., and Demoulin, F. (2005). Coupling vaporization model with the eulerian-lagrangian spray atomization (elsa) model in diesel engine conditions. In *SAE 2005 World Congress & Exhibition*.
- [Lebas et al., 2009] Lebas, R., Ménard, T., Beau, P.-A., Berlemont, A., and Demoulin, F.-X. (2009). Numerical simulation of primary break-up and atomization: Dns and modelling study. *International Journal of Multiphase Flow*, 35(3):247–260.
- [Lee et al., 2021] Lee, D., Fahey, D., Skowron, A., Allen, M., Burkhardt, U., Chen, Q., Doherty, S., Freeman, S., Forster, P., Fuglestvedt, J., Gettelman, A., Leon, R. D., Lim, L., Lund, M., Millar, R., Owen, B., Penner, J., Pitari, G., Prather, M., Sausen, R., and Wilcox, L. (2021). The contribution of global aviation to anthropogenic climate forcing for 2000 to 2018. *Atmospheric Environment*, 224:117834.
- [Lefebvre, 1989] Lefebvre, A. (1989). Properties of sprays. *Particle and Particle Systems Characterization*, 6:176–186.

- [Lefebvre, 1992] Lefebvre, A. (1992). Twin-fluid atomization: Factors influencing mean drop size. *Atomization and Sprays*, 2(2):101–119.
- [Lefebvre and Miller, 1966] Lefebvre, A. and Miller, D. (1966). The development of an air blast atomizer for gas turbine application. In *CoA-Report- AERO-193, College of Aeronautics*.
- [Lefebvre, 1983] Lefebvre, A. H. (1983). *Gas Turbine Combustion*. Hemisphere Pub. Corp, Washington.
- [Lefebvre and McDonell, 1988] Lefebvre, A. H. and McDonell, V. G. (1988). *Atomization and Sprays*. CRC Press Taylor & Francis Group, 6000 Broken Sound Parkway NW.
- [LeVeque, 1992] LeVeque, R. (1992). *Numerical methods for conservation laws*. Springer, Washington.
- [LeVeque, 2002] LeVeque, R. (2002). *Finite volume methods for hyperbolic problems*. Cambridge university press, -.
- [Lin et al., 2019] Lin, Y., Liu, G. R., and Wang, G. (2019). A particle-based free surface detection method and its application to the surface tension effects simulation in smoothed particle hydrodynamics (sph). *Journal of Computational Physics*, 383:196–206.
- [Lubin et al., 2006] Lubin, P., Vincent, S., Abadie, S., and Caltagirone., J.-P. (2006). Three-dimensional large eddy simulation of air entrainment under plunging breaking waves. *Coastal engineering*, 53(8):631–655.
- [Macian et al., 2003] Macian, V., Bermúdez, V., Payri, R., and Gimeno, J. (2003). New technique for determination of internal geometry of a diesel nozzle with the use of silicone methodology. *Experimental Techniques*, 27(2):39–43.
- [Madsen et al., 2004] Madsen, J., Hjertager, B. H., and Solberg, T. (2004). Numerical simulation of internal flow in a large-scale pressure-swirl atomizer. In *ILASS-Europe*.
- [Maly et al., 2018] Maly, M., Sapik, M., Jedelsky, J., Janackova, L., Jicha, M., Slama, J., and Wigley, G. (2018). Internal flow characteristics in scaled pressure-swirl atomizer. In *Experimental Fluid Mechanics*.
- [Marchi et al., 2010] Marchi, A., Nouri, J., Yan, Y., Arcoumanis, C., and Arcoumanis, D. (2010). Spray stability of outwards opening pintle injectors for stratified direct injection spark ignition engine operation. *International Journal of Engine Research*, 11 (6):413–437.
- [Marrero, 2018] Marrero, J. (2018). *Experimental study of lean aeronautical ignition : impact of critical parameters on the mechanisms acting along the different ignition phases*. PhD thesis, Université de Rouen Normandie, France.
- [Mazareanu, 2021] Mazareanu, E. (2021). Global air traffic - number of flights 2004–2022. <https://www.statista.com/statistics/564769/airline-industry-number-of-flights/>. Accessed: 2022-01-25.
- [McDonell and Samuelsen, 2000] McDonell, V. G. and Samuelsen, G. S. (2000). Measurement of fuel mixing and transport processes in gas turbine combustion. *Measurement Science and Technology*, 11:870–886.

- [Miglierina, 2021] Miglierina, L. (2021). Liquid injection for gas turbine. Master's thesis, Université de Rouen Normandie, France.
- [Mirjalili et al., 2017] Mirjalili, S., Jain, S. S., and Dodd, M. S. (2017). Interface-capturing methods for two-phase flows: An overview and recent developments. *Annual Research Briefs 2017*.
- [Monroy and Seng, 2017] Monroy, C. and Seng, S. (2017). Time-stepping schemes for seakeeping in openfoam. In *10th International Workshop on Ship and Marine Hydrodynamics*.
- [Mughal, 2016] Mughal, M. O. (2016). *Wind Prediction Modelling and Validation using Coherent Doppler LIDAR Data*. PhD thesis, Singapore ETH Center.
- [Mukundan et al., 2019] Mukundan, A. A., Ménard, T., Berlemont, A., and de Motta, J. C. B. (2019). A comparative study of dns of airblast atomization using clsmof and clsvof methods. In *ILASS-Europe. Conference on Liquid Atomization and Spray Systems*.
- [Ménard et al., 2007] Ménard, T., Tanguy, S., and Berlemont, A. (2007). Coupling level set vof ghost fluid methods: Validation and application to 3d simulation of the primary break-up of a liquid jet. *International Journal of Multiphase Flow*, 33(5):510–524.
- [Nicoud and Ducros, 1999] Nicoud, F. and Ducros, F. (1999). Subgrid-scale stress modelling based on the square of the velocity gradient tensor. *Flow of Turbulent Combustion*, 62(3):183–200.
- [Noh and Woodward, 1976] Noh, W. and Woodward, P. (1976). Slic (simple line interface calculation). In *Proceedings of the fifth international conference on numerical methods in fluid dynamics*.
- [Noh and Woodward, 2005] Noh, W. F. and Woodward, P. (2005). Slic (simple line interface calculation). In *Proceedings of the Fifth International Conference on Numerical Methods in Fluid Dynamics*.
- [Osher and Sethian, 1988] Osher, S. and Sethian, J. A. (1988). Fronts propagating with curvature-dependent speed: Algorithms based on hamilton-jacobi formulations. *Journal of Computational Physics*, 79(1):12–49.
- [Palanti et al., 2022] Palanti, L., Puggelli, S., Langone, L., Andreini, A., Reveillon, J., Duret, B., and Demoulin, F.-X. (2022). An attempt to predict spray characteristics at early stage of the atomization process by using surfacedensity and curvature distribution. *International Journal of Multiphase Flow*, 147:103879.
- [Payri et al., 2021] Payri, R., Salvador, F., Carreres, M., and Moreno-Montagud, C. (2021). A novel inlet boundary condition for vof-dns simulations of the primary breakup of prefilming airblast atomizers. In *International Conference on Liquid Atomization and Spray Systems*.
- [Piscaglia et al., 2019] Piscaglia, F., Giussani, F., Montorfano, A., Hélie, J., and Aithal, S. (2019). A multiphase dynamic-vof solver to model primary jet atomization and cavitation inside high-pressure fuel injectors in openfoam. *Acta Astronautica*, 158:375–387.
- [Pope, 1985] Pope, S. B. (1985). Pdf methods for turbulent reactive flows. *Progress in energy and combustion science*, 11(2):119–192.
- [Puggelli, 2018] Puggelli, S. (2018). *Towards a unified approach for Large Eddy Simulation of turbulent spray flames*. PhD thesis, Université de Rouen Normandie.

- [Radcliffe, 1955] Radcliffe, A. (1955). The performance of a type of swirl atomizer. *Proceedings of the Institution of Mechanical Engineers*, 169(1):93–106.
- [Raeini et al., 2012] Raeini, A. Q., Blunt, M. J., and Bijeljic, B. (2012). Modelling two-phase flow in porous media at the pore scale using the volume-of-fluid method. *Journal of Computational Physics*, 231(17):5653–5668.
- [Ramsey and Villarraga-Gómez, 2017] Ramsey, A. and Villarraga-Gómez, H. (2017). The inspection and quality control of metal am parts with x-ray computed tomography (micro ct). *Metal Additive Manufacturing*, 3(2):1–8.
- [Razeghi and Özgür Ertunç, 2018] Razeghi, A. and Özgür Ertunç (2018). Numerical simulation of multiphase flow inside a pressure swirl atomizer at the initial stage of injection. *Atomization and Sprays*, 28(5):417–441.
- [Remigi, 2021] Remigi, A. (2021). *Numerical modeling of an aeronautical injector : from the internal flow to the dispersed spray*. PhD thesis, Université de Rouen Normandie, France.
- [Ritchie, 2020] Ritchie, H. (2020). Climate change and flying: what share of global co2 emissions come from aviation? <https://ourworldindata.org/co2-emissions-from-aviation>. Accessed: 2022-01-25.
- [Rizk and Lefebvre, 1980] Rizk, N. and Lefebvre, A. (1980). The influence of liquid film thickness on airblast atomization. *Journal of Engineering for Gas Turbines and Power*, 102(3):706–710.
- [Rizk and Lefebvre, 1985a] Rizk, N. and Lefebvre, A. (1985a). Internal flow characteristics of simplex swirl atomizers. *Journal of Propulsion Power*, 1(3):193–199.
- [Rizk and Lefebvre, 1985b] Rizk, N. K. and Lefebvre, A. H. (1985b). Prediction of velocity coefficient and spray cone angle for simplex swirl atomizers. In *Proceedings of the 3rd International Conference on Liquid Atomization and Spray Systems*.
- [Rizkalla and Lefebvre, 1975] Rizkalla, A. and Lefebvre, A. (1975). The influence of air and liquid properties on airblast atomization. *Journal of Fluids Engineering*, 97:316–320.
- [Roselfeld and Pfaltz, 1966] Roselfeld, A. and Pfaltz, J. L. (1966). Sequential operations in digital picture processing. *Journal of the Association for Computing Machinery*, 13(4):471–494.
- [Rosin and Rammler, 1933] Rosin, P. and Rammler, E. (1933). The laws governing the fineness of powdered coal. *Journal of the Institute of Fuel*, 7:29–36.
- [Rusche, 2002] Rusche, H. (2002). *Computational Fluid Dynamics of Dispersed Two-Phase Flows at High Phase Fractions*. PhD thesis, London: Imperial College.
- [Saffmann et al., 1984] Saffmann, M., Buchave, P., and Tanger, H. (1984). Simultaneous measurement of size, concentration and velocity of spherical particles by a laser doppler method. In *Proceedings 2nd International Symposium of Laser Anemometry and Fluid Mechanics*.
- [Sagaut, 2006] Sagaut, P. (2006). *Large Eddy Simulation for Incompressible Flows: An Introduction*. Springer Science & Business Media, -.

- [Salvador et al., 2018] Salvador, F. J., Gimeno, J., Morena, J. D. L., and Carreres, M. (2018). Comparison of different techniques for characterizing the diesel injector internal dimensions. *Experimental Techniques*, 42:467–472.
- [Sanchez, 2021] Sanchez, S. (2021). -. Master's thesis, Universitat Politècnica de València, Spain.
- [Sattelmayer and Wittig, 1986] Sattelmayer, T. and Wittig, S. (1986). Internal flow effects in prefilming airblast atomizers: Mechanisms of atomization and droplet spectra. *Journal of Engineering for Gas Turbines and Power*, 108(86-GT-150):465–472.
- [Sauer et al., 2014] Sauer, B., Sadiki, A., and Janicka, J. (2014). Numerical analysis of the primary breakup applying the embedded dns approach to a generic prefilming airblast atomizer. *The Journal of Computational Multiphase Flows*, 6(3):179–192.
- [Saurel and Pantano, 2018] Saurel, R. and Pantano, C. (2018). Diffuse-interface capturing methods for compressible two-phase flows. *Annual Review of Fluid Mechanics*, 50.1:105–107.
- [S.B.Pope, 1988] S.B.Pope (1988). The evolution of surfaces in turbulence. *International Journal of Engineering Science*, 26(5):445–469.
- [Scardovelli and Zaleski, 1999] Scardovelli, R. and Zaleski, S. (1999). Direct numerical simulation of free-surface and interfacial flow. *Annual Review of Fluid Mechanics*, 31(1):567–603.
- [Schlick, 2020] Schlick (2020). Schlick series 121-123. <https://www.myschlick.com>. Accessed: 2021-11-23.
- [Sedlmaier, 2016] Sedlmaier, J. (2016). *Numerische und experimentelle Untersuchung einer abgehobenen Flamme unter Druck*. PhD thesis, Karlsruher Institut für Technologie (KIT).
- [Sedlmaier et al., 2014] Sedlmaier, J., Habisreuther, P., and Zarzalis, N. (2014). Influence of liquid and gaseous fuel on lifted flames at elevated pressure stabilized by outer recirculation. In *Proceedings of ASME Turbo Expo 2014: Turbine Technical Conference and Exposition*.
- [Sethian, 1999] Sethian, J. A. (1999). *Level Set Methods and Fast Marching Methods*. Cambridge Monographs on Applied and Computational Mathematics, University of California, Berkeley.
- [Settles, 2001] Settles, G. (2001). *Schlieren and Shadowgraph Techniques*. Springer US.
- [Shamma et al., 2021] Shamma, M., Harth, S.-R., Zarzalis, N., Trimis, D., Hoffmann, S., Koch, R., Bauer, H.-J., Langone, L., Galeotti, S., and Andreini, A. (2021). Investigation of adjacent lifted flames interaction in an inline and inclined multi-burner arrangement. In *Proceedings of ASME Turbo Expo 2021 Turbomachinery Technical Conference and Exposition*.
- [Shao et al., 2017] Shao, C., Luo, K., Yang, Y., and Fan, J. (2017). Detailed numerical simulation of swirling primary atomization using a mass conservative level set method. *International Journal of Multiphase Flow*, 89:57–68.
- [Sheen et al., 1996] Sheen, H. J., Chen, W. J., Jeng, S. Y., and Huang, T. L. (1996). Correlation of swirl number for a radial-type swirl generator. *Experimental Thermal and Fluid Science*, 12(4):444–451.

- [Simmons and Harding, 1981] Simmons, H. C. and Harding, C. F. (1981). Some effects of using water as a test fluid in fuel nozzle spray analysis. *Journal of Engineering for Gas Turbines and Power*, 103(1):118–123.
- [Simonin et al., 1993] Simonin, O., Deutsch, E., , and Minier, J. (1993). Eulerian prediction of the fluid/particle correlated motion in turbulent two-phase flows. *Applied Scientific Research*, 51(1-2):275–283.
- [Skarysz et al., 2000] Skarysz, M., Garmory, A., and Dianat, M. (2000). A coupled level set and volume-of-fluid method for computing 3d and axisymmetric incompressible two-phase flows. *Journal of Computational Physics*, 162(2):301–337.
- [Skarysz et al., 2018] Skarysz, M., Garmory, A., and Dianat, M. (2018). An iterative interface reconstruction method for plic in general convex grids as part of a coupled level set volume of fluid solver. *Journal of Computational Physics*, 368:254–276.
- [Smagorinsky, 1963] Smagorinsky, J. (1963). General circulation experiments with the primitive equations. *Monthly Weather Review*, 91(3):99–164.
- [Sumer et al., 2012] Sumer, B., Erkan, N., Uzol, O., and I.H.Tuncer (2012). Experimental and numerical investigation of a pressure swirl atomizer. In *International Conference on Liquid Atomization and Spray Systems*.
- [Sussman et al., 1994] Sussman, M., Smereka, P., , and Osher, S. (1994). A level set approach for computing solutions to incompressible two-phase flow. *Journal of computational physics*, 144(1):146–159.
- [Suyari and Lefebvre, 1986] Suyari, M. and Lefebvre, A. (1986). Film thickness measurements in a simplex swirl atomizer. *Journal of Propulsion Power*, 2(6):528–533.
- [Tavares et al., 2015] Tavares, M., Vincent, S., Ould-Rouiss, M., and Estivalezes, J.-L. (2015). A priori study for the modeling of les subgrid scale terms in resolved scale multiphase flows. *Turbulence and Interactions*, -:249–254.
- [Taylor, 1948] Taylor, G. I. (1948). The mechanics of swirl atomizers. In *Seventh International Congress of Applied Mechanics*.
- [Taylor, 1950] Taylor, G. I. (1950). The boundary layer in the converging nozzle of a swirl atomizer. *The Quarterly Journal of Mechanics and Applied Mathematics*, 3 (2):129–139.
- [Thomson, 1871] Thomson, W. (1871). Xlvi. hydrokinetic solutions and observations. *The London, Edinburgh, and Dublin Philosophical Magazine and Journal of Science*, 42.281:362–377.
- [Tretola and Vogiatzaki, 2021] Tretola, G. and Vogiatzaki, K. (2021). Numerical treatment of the interface in two phase flows using a compressible framework in openfoam: Demonstration on a high velocity droplet impact case. *Fluids*, 6:78.
- [Tropea, 2011] Tropea, C. (2011). Optical particle characterization in flows. *Annual revision of fluid mechanics*, 43:399–426.
- [Tryggvason et al., 2001] Tryggvason, G., Bunner, B., Esmarelli, A., Juric, D., Al-Rawahi, N., Tauber, W., Han, J., Nas, S., and Jan, Y. J. (2001). A front-tracking method for the computations of multiphase flow. *Journal of Computational Physics*, 169(2):708–759.

- [Tryggvason and Lu, 2015] Tryggvason, G. and Lu, J. (2015). Direct numerical simulations of flows with phase change. *Procedia IUTAM*, 15:2–13.
- [Unverdi and Tryggvason, 1992] Unverdi, S. O. and Tryggvason, G. (1992). A front-tracking method for viscous, incompressible, multi-fluid flows. *Journal of computational physics*, 100(1):25–37.
- [Vallet and Borghi, 1999] Vallet, A. and Borghi, R. (1999). Modélisation eulerienne de l'atomisation d'un jet liquide. *Comptes Rendus de l'Académie des Sciences*, 327(10):1015–1020.
- [van Leer., 1974] van Leer., B. (1974). Towards the ultimate conservative difference scheme. ii. monotonicity and conservation combined in a second-order scheme. *Journal of computational physics*, 14(4):361–370.
- [Verdier, 2017] Verdier, A. (2017). *Experimental study of dilute spray combustion*. PhD thesis, Université de Rouen Normandie, France.
- [Vincent et al., 2018] Vincent, S., Tavares, M., Fleau, S., Mimouni, S., Ould-Rouiss, M., and Estivalezes., J.-L. (2018). A priori filtering and les modeling of turbulent two-phase flows application to phase separation. *Computers and Fluids*, -:245–259.
- [Wardle and Weller, 2013] Wardle, K. and Weller, H. (2013). Hybrid multiphase cfd solver for coupled dispersed/ segregated flows in liquid-liquid extraction. *International Journal of Chemical Engineering*, 2013:–.
- [Warncke et al., 2017] Warncke, K., Gepperth, S., B.Sauer, Sadiki, A., Janicka, J., Koch, R., and Bauer, H.-J. (2017). Experimental and numerical investigation of the primary breakup of an airblasted liquid sheet. *International Journal of Multiphase flow*, 91:208–224.
- [Watanabe et al., 2015] Watanabe, T., Sakai, Y., Nagata, K., Ito, Y., and Hayase, T. (2015). Les–lagrangian particle method for turbulent reactive flows based on the approximate deconvolution model and mixing model. *Journal of Computational Physics*, 294:127–148.
- [White, 1991] White, F. (1991). *Viscous fluid flow*. McGraw-Hill, New-York.
- [Youngs, 1984] Youngs, D. L. (1984). An interface tracking method for a 3d eulerian hydrodynamics code. Technical report, Atomic Weapons Research Establishment (AWRE) Technical Report 44(92).
- [Zalesak, 1979] Zalesak, S. (1979). Fully multidimensional flux-corrected transport algorithms for fluids. *Journal of computational physics*, 31(3):335–362.

Appendices

A | CHAiRLIFT airblast atomizer: Test rig operating conditions

The process presented on chapter 4 is repeated for the CHAiRLIFT test rig operating conditions. During the process, the behaviour of the liquid film is different regarding the test case at high pressure. Thus, a preliminar study with a non steady liquid film thickness has been carried out. The analysis reported on chapter 5 is applied for the steady and non-steady liquid film thickness.

Contents

A.1	Air flow modelling	130
A.2	Estimation of the liquid film thickness	130
A.2.1	3D film thickness modelling	130
A.3	Prefilmer simulation	132
A.3.1	Steady fuel film thickness	133
A.3.2	Unsteady fuel film thickness	133
A.4	Spray post-processing	134
A.4.1	Steady fuel film thickness	134
A.4.2	Unsteady fuel film thickness	134

On this appendix the work performed to model the airblast atomizer based on the work by [Kasabov, 2014] and studied on the CHAiRLIFT experimental test rig is shown. Since at the moment of the writing of this thesis the experimental results on the spray have not been yet carried out, the numerical results are just reported and not validated.

The main differences with the test case studied on chapter 4 are the operating conditions, on this case atmospheric pressure and ambient temperature are set up and the nozzle is bigger on scale keeping the same shape with an effective area of $A_{eff}^{kasabov} = 319mm^2$. The operating conditions are reported on Table A.1.

p_0	ΔP_{nozzle}	T_{air}	T_{fuel}	\dot{m}_{air}	\dot{m}_{fuel}
1bar	3%	273K	273K	19g/s	1.15g/s

Table A.1 – CHAiRLIFT test rig ambient operating conditions

The properties of the fluids are reported on Table A.1.

Air		Fuel		Shared	
ρ	ν	ρ	ν	ρ_{fuel}/ρ_{air}	σ
$1.184\text{kg}/\text{m}^3$	$1.562\text{e} - 05\text{m}^2/\text{s}$	$810\text{kg}/\text{m}^3$	$1.5\text{e} - 06\text{m}^2/\text{s}$	684.12	$0.023\text{N}/\text{m}$

Table A.2 – Fluid properties for the CHAIRLIFT test rig case.

A.1 Air flow modelling

On this case the data extracted from section 4.3 is scaled on space and on magnitude to match the bigger geometry from Kasabov and to keep the air mass flow rate equal to the value reported on Table A.1. This procedure allow us to reduce computational resources keeping a good accuracy.

A.2 Estimation of the liquid film thickness

On this section the same approach proposed on section 4.4 is followed. Thus, the same computational domain and grid are used. First, a rough estimation is done with Equation 4.24 obtaining a value of $t_{CHAIRLIFT} = 1\mu\text{m}$ which is a small value. Later a 2D simulation has been performed.

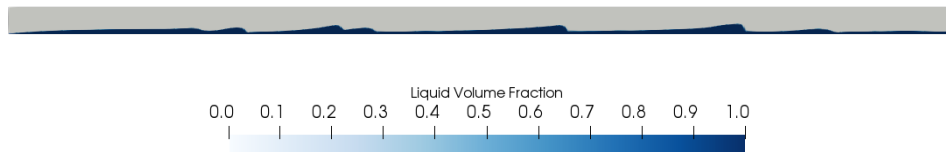


Figure A.1 – Liquid volume fraction contour to obtain the prefilmer film thickness. CHAIRLIFT test rig operating conditions.

The results are shown on Figure A.1 where a contour of the liquid volume fraction α is plotted. We can observe that the liquid film has a wavy behaviour and its thickness is $t = 27 \pm 18\mu\text{m}$. On the scientific literature is probed that the liquid film thickness does not play any role on the atomization process [Gepperth et al., 2013, Chaussonnet et al., 2016], but on this case another study has been carried out to implement a varying thickness on the prefilming atomization modelling to afterward compare both studies.

A.2.1 3D film thickness modelling

The study by [Payri et al., 2021] implements a non-constant liquid film thickness boundary condition to study a planar prefilmer. Using this work as a reference, the same process has been implemented on OpenFOAM V6.0 and on the airblast CHAIRLIFT configuration.

Numerical domain

To adapt the reference channel to the requirement of this work, a small curvature has been applied to the channel to match the diameter of the prefilmer. Figure A.2 shows the domain geometry (black solid lines) and two cut views of the numerical mesh. The length of the domain it is the same than the 2D cases so is the height of it. Then, the 2D is revolved an angle of $\phi = 14^\circ$, wider than the one used on the prefilmer simulation to avoid any problem.

In agreement with the 2D multiphase simulation, the boundary conditions are analogous with the addition of the periodic boundary conditions on the sides. The air inlet velocity it is mapped from the single phase simulation explained on chapter 4, varying on space and on time with a linear interpolation. The initial thickness of the liquid film is set up to

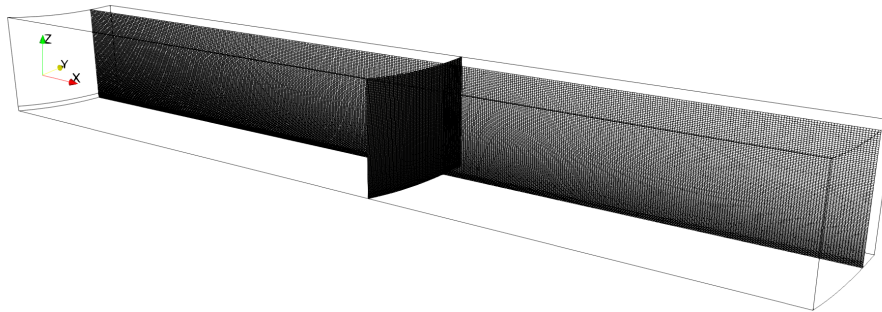


Figure A.2 – Geometrical domain and two slices representing the numerical grid

$t_{3D}^0 = t_{2D}^f = 27\mu m$; in this study the final thickness is not searched but the storage of the liquid volume fraction field at the end of the domain to map it into the prefilmer simulation. Therefore, as initial value the final value from the 2D simulation is set up. The velocity of the fuel is calculated to match the mass flow rate. The top boundary is still a symmetry boundary condition meanwhile the bottom one is still a wall boundary condition. Finally, at the outlet, a pressure fixed boundary condition. A summary of the boundary conditions can be found on Table A.3.

	Air Inlet	Liquid Inlet	Outlet
u	Mapped value	Fixed value	$\nabla \mathbf{u} = 0$
p	$\nabla p = 0$	$\nabla p = 0$	totalPressure
α	$\alpha = 0$	$\alpha = 1$	$\nabla \alpha = 0$

	Top-Symmetry	Bottom-Wall	Sides-Periodic
u	symmetry	$\nabla \mathbf{u} = 0$	periodic
p	symmetry	$\nabla p = 0$	periodic
α	symmetry	$\nabla \alpha = 0$	periodic

Table A.3 – 3D channel boundary conditions

The numerical mesh has $5.7 \cdot 10^6$ cells. The minimal resolution of the mesh cells is $\delta x_{min} = 4\mu m$ located around the prefilmer's wall. The simulation has been carried out with 140 CPUs over less than 4 days spending a total of $11 \cdot 10^3$ CPU· hours.

In the same manner that the 2D simulation, the solver used was `interFoam` from OpenFOAM v6.0 toolbox. The turbulence has been modelled with a LES approach, using the WALE sub-grid model. The discretization schemes are second order on space and on time.

An instantaneous result is shown on Figure A.3 where the iso-surface of the liquid volume fraction α is represented. The wavy motion is remarkable in both, axial and transverse directions.

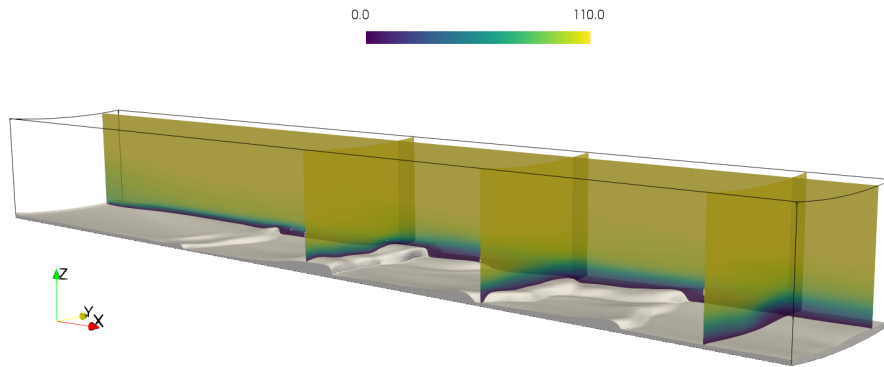


Figure A.3 – Instantaneous snapshot showing the liquid volume fraction iso-surface ($\alpha = 0.5$) and some slices of the velocity magnitude

The liquid volume fraction and the velocity of the liquid is stored on transverse planes at the end of the domain each $0.5\mu s$. Some of the stored planes are shown on Figure A.4.

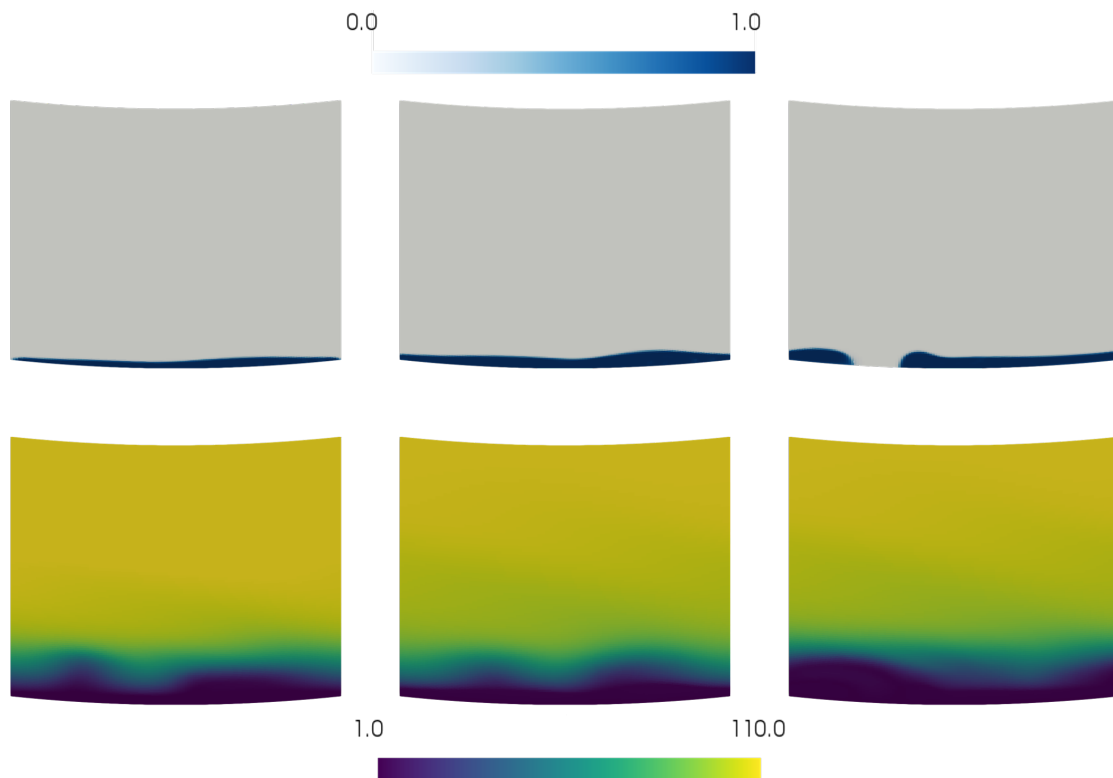


Figure A.4 – Planes stored on run time to map the prefilmer simulation. On the top: liquid volume fraction α . On the bottom: velocity magnitude $|\mathbf{u}|$.

A.3 Prefilmer simulation

Following the methodology shown on section 4.5 the constant fuel film thickness case has been set up. For the varying fuel film thickness case a similar methodology has been adopted.

On this case, the instantaneous liquid volume fraction $\alpha(t)$ planes have been mapped on time and space as the air velocity has been done previously.

A.3.1 Steady fuel film thickness

We can observe on Figure A.5 that the accumulation effect is bigger with this operating conditions in comparison with the test case shown on Figure 4.13. Another thing that can be remarked is the fact that the primary break-up is not completely over and we have more ligaments than droplets. Moreover, the droplets seems larger than the ones at high pressure.

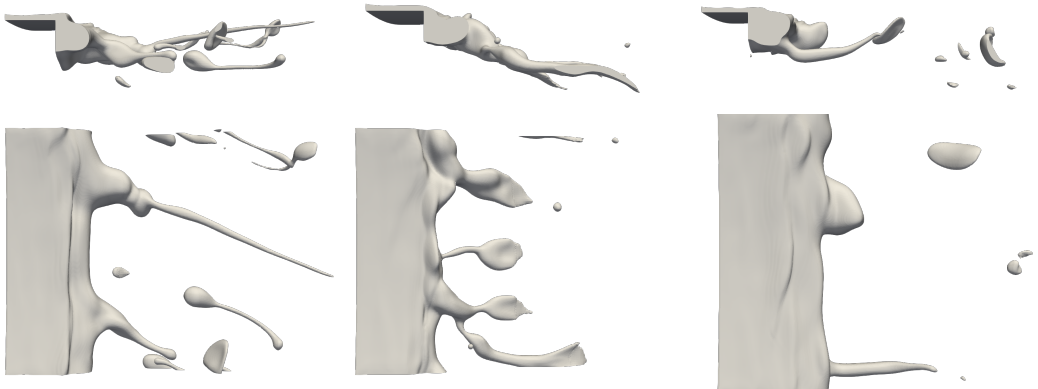


Figure A.5 – Instantaneous iso-surfaces ($\alpha = 0.5$) for the steady fuel film thickness, airblast case.

A.3.2 Unsteady fuel film thickness

On this case, we can see on Figure A.6 that the thickness of the inlet is varying on time. However, on this case the accumulation effect that creates a reservoir is not as pronounced as it is on Figure A.5. Thus, when the fuel film reach its maximum peak, it creates larger droplets. It is also remarkable the fact that more droplets are generated regarding the previous case, even smaller droplets.

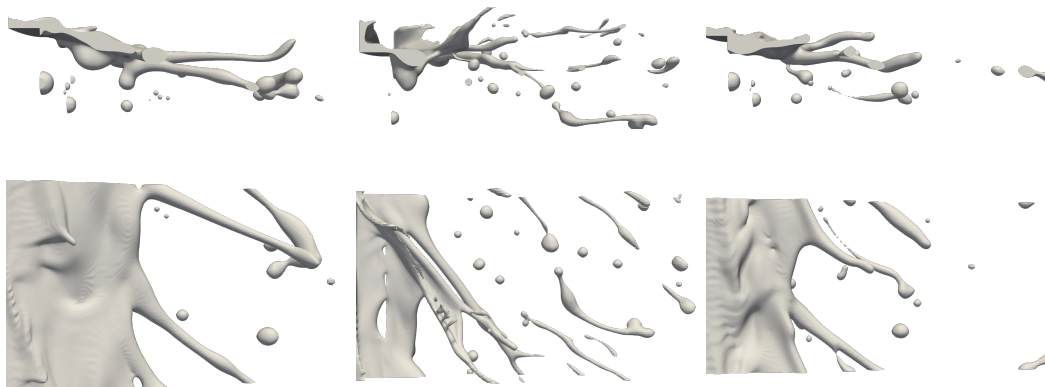


Figure A.6 – Instantaneous iso-surfaces ($\alpha = 0.5$) for the unsteady fuel film thickness, airblast case.

This case should be investigated more because it contradicts the experimental studies cited before. Moreover, the work by [Payri et al., 2021] concludes on the nule effect of

the waves of this kind of atomizers even with numerical simulation. However, on that work the amplitude of the waves was smaller meanwhile on this case the differences among the minimum and maximum liquid film thickness is almost the double which could affect on the accumulation effect on the prefilmer's lip.

A.4 Spray post-processing

A.4.1 Steady fuel film thickness

Figure A.7 shows the drop size distribution computed with the methodology shown on chapter 5. We can see that the Sauter Mean Diameter $D_{32} = 37\mu m$ is almost the same that we have obtained on the test case from Figure 5.11. On the other hand, the mean diameter $D_{10} = 18\mu m$ is a bit smaller than the one from the test case.

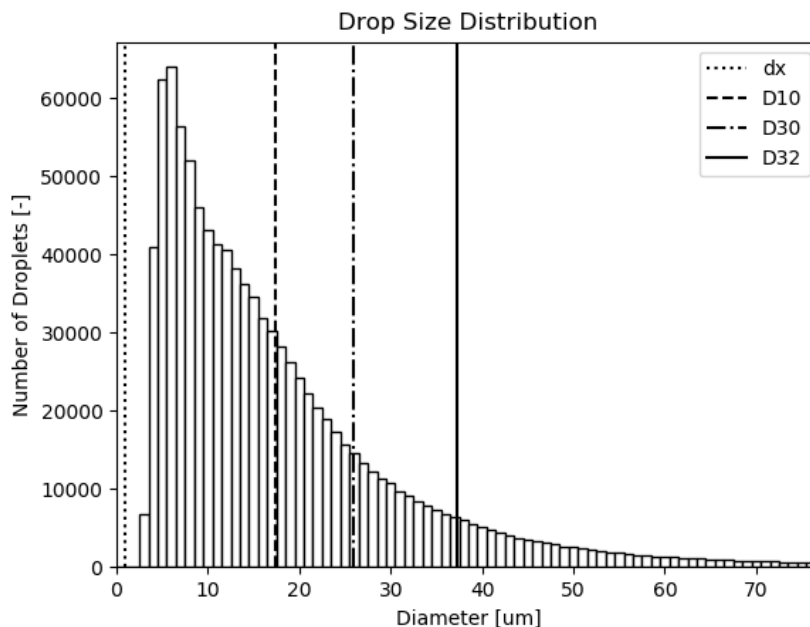


Figure A.7 – Drop size distribution of the steady fuel film thickness case.

The peak diameter is $D_{peak} = 6\mu m$ which is two time smaller than the one from chapter 4. At atmospheric pressure and ambient temperature the droplets expelled by the airblast atomizer are in general smaller. However, on the test case, most of the droplets are concentrated around diameters from $10\mu m$ to $20\mu m$; just a few medium droplets ($D = 20 - 50\mu m$) and almost none large droplets ($D = 50 - 80\mu m$) are expelled at those operating conditions. On the other hand, we can observed that at atmospheric pressure the number of smaller droplets is higher but also the distribution is thicker meaning that the amount of medium droplets represents still a high number of the total. The comparison with the correlation from Equation 4.18 gives us a value of $D_{32}^{Geppert} = 67\mu m$ that is twice the value obtained from the simulation.

A.4.2 Unsteady fuel film thickness

On this case, we can see directly the differences among both drop size distribution. On Figure A.8 the distribution obtained from the unsteady fuel film thickness simulation is plotted. First, the Sauter Mean Diameter recovered match better the one from the Geppert correlation

$D_{32} = 62\mu m$. Larger droplets are captured in contrast with Figure A.7. Moreover the peak diameter is also a bit larger $D_{peak} = 11\mu m$.

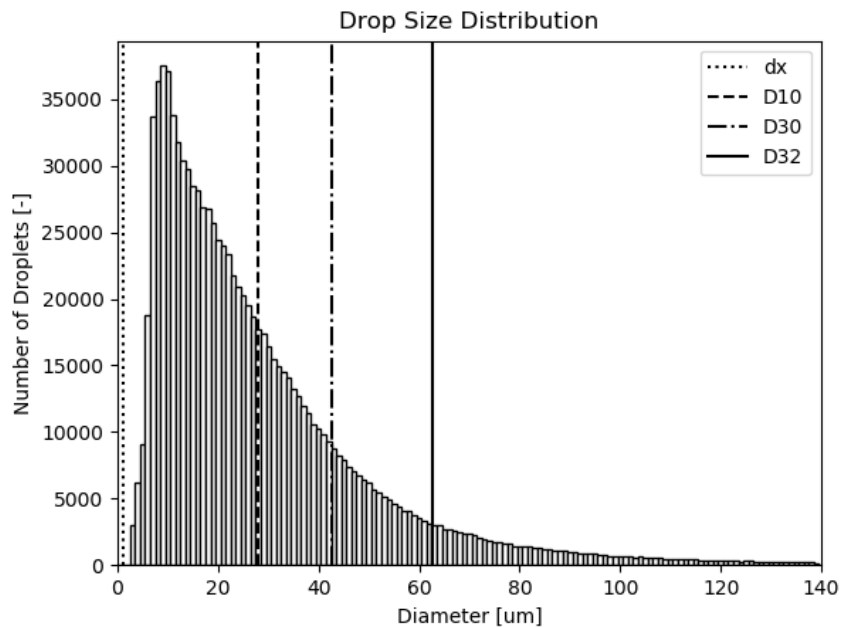


Figure A.8 – Drop size distribution of the unsteady fuel film thickness case.

As it has been reported before, this contradicts the experimental y numerical studies from the scientific literature. It is also true that the waves of those studies had smaller amplitudes. Anyhow, the results presented about the unsteady film thickness are just preliminary results and further investigations are required to determine if those results are physical. Comparison with experimental results would help to understand the effect of the waves on the fuel film.

B | Data measurement utility

This appendix shows the implementation of a new OpenFOAM utility to extract data on run time at the face of the computational cells. It is based on the default OpenFOAM utility probes.

Contents

B.1	Implementation	137
B.2	Utility performance	139

B.1 Implementation

On this appendix the tool to store data shown on chapter 5 is explained. To perform the postprocessing method proposed, the local storage of data on the face of the some computational cells is required. Therefore, the default probes utility in OpenFoam v6.0 was considered. A cartesian coordinate is given to the utility $p_i(x_i, y_i, z_i)$ and the field of interest. If the variable of the field is stored on the cell center, the utility will directly store it. Otherwise, if it is stored on the face center, the utility will look for the closet face to the cell center and it will store only the value of this particular face. The description of an OpenFoam cell and the behaviour of the probes utility is shown Figure B.1

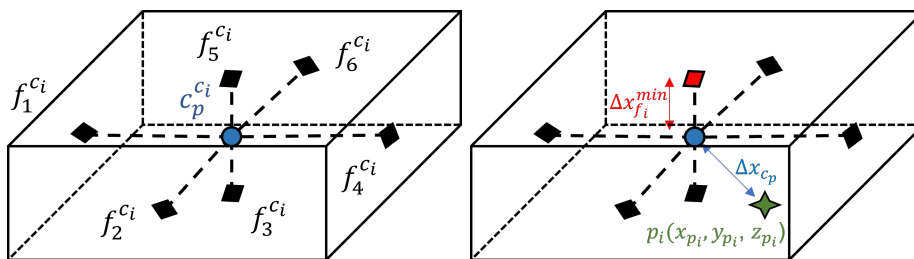


Figure B.1 – On the right: description of the one computational cell. On the left: behaviour of the default probes utility . c_i is the cell i on the computational grid, c_p is the center of the cell, f_i is the i face of the cell, p_i is the probe i , Δx_{f_i} is the distance among the face center and the cell center and Δx_{c_p} is the distance among the cell center and the probe.

Nevertheless, the post-processing technique required to choose the face aligned with the flux and since on both configurations the numerical grid is almost structured and isotropic,

the election of the face where the data will be stored would be arbitrary with the default utility. Thus, a modification has been developed and implemented on OpenFoam v6.0 called `faceProbes`. The modification includes the possibility to choose a directional vector reflecting the flux to choose the face more aligned with it. The following C++ code shows the modification to the default utility:

```

1  forAll(*this, faceProbei)
2      {
3          const vector& location = operator[] (faceProbei);
4          vector& fluxDir = fluxVector_;
5
6          const label celli = mesh.findCell(location);
7          labelList fluxFaces;
8          fluxFaces.setSize(2);
9          elementList_[faceProbei] = celli;
10
11         if (celli != -1)
12             {
13                 const labelList& cellFaces = mesh.cells()[celli];
14                 const vectorField& faceCentres = mesh.faceCentres();
15                 const surfaceVectorField& surfaces = mesh.Sf();
16                 label choosenFaceID = cellFaces[0];
17                 double minDotProduct1 = 1.0, minDotProduct2 = 1.0;
18
19                 forAll(cellFaces, i)
20                     {
21                         label facei = cellFaces[i];
22                         vector surface = surfaces[facei]/mag(surfaces[facei]);
23                         double dotProduct = fluxDir & surface;
24                         double diffDotProduct = mag(mag(dotProduct) - 1.0);
25
26                         if (diffDotProduct < minDotProduct1)
27                             {
28                                 minDotProduct1 = diffDotProduct;
29                                 fluxFaces[0] = facei;
30                             }
31
32                         else if (diffDotProduct < minDotProduct2)
33                             {
34                                 minDotProduct2 = diffDotProduct;
35                                 fluxFaces[1] = facei;
36                             }
37
38                     }
39
40                 if (
41                     (fluxDir & faceCentres[fluxFaces[0]]) <
42                     (fluxDir & faceCentres[fluxFaces[1]])
43                     and mesh.isInternalFace(fluxFaces[0])
44                 )
45                     {
46                         choosenFaceID = fluxFaces[0];
47                     }
48                 else if(mesh.isInternalFace(fluxFaces[1]))
49                     {
50                         choosenFaceID = fluxFaces[1];
51                     }
52                 else
53                     {
54                         choosenFaceID = fluxFaces[0];

```

```

55     }
56     faceList_[faceProbei] = chosenFaceID;
57     }
58 }

```

The "for" loop swept all coordinates p_i that we have given to the utility and for each of them it creates a location vector and it read the flux direction vector. It searches for the closest cell (by default) and create a list of labels for the faces $f_i^{c_i}$ from the chosen cell c_i . It calculates the center of these faces and the surface vector of each face. For each face inside of the cell, it calculates the unit normal vector to the face and it calculates the dot product among the normal vector and the flux vector. Finally, it chooses the face which dot product among its normal vector and the flux vector is closet to 0.

This methodology worked well for computation with a single core. When the case is decompose and run in parallel, if the face chosen is on a boundary face among processor, the value there is not well calculated by the utility. Thus, the last part of the development changes the face for the second face which dot product among its normal vector and the flux vector is closet to 0 that on these configurations is always the opposite face to the first face. It has to be further developed and tested since with another kind of mesh topology it can be generate some problems.

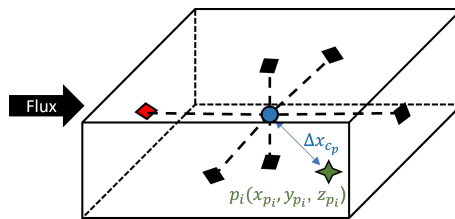


Figure B.2

Figure B.2 shows the final implementation of the faceProbes utility.

B.2 Utility performance

To see the viability of using this tool on run time, two small test were performed. The first one checks the computational time step Δt in function of the number of probes n_p . Figure B.3 shows the results of this study where the normalized time step $\Delta t(n_p)/\Delta t(0)$ is plotted.

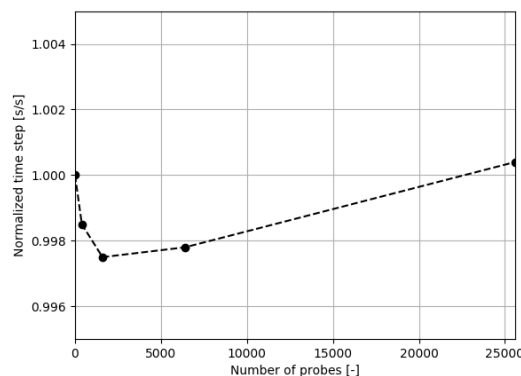


Figure B.3 – Normalized time step by number of probes

We can see that the time step is independent on the number of probes and the small variation among the different tests ($\approx 0.002\%$) are due to the general performance of the computer. This Independence of the number of probes is essential for the methodology since regarding the computational domain the number of probes could be elevated.

The second study performed is the amount of storage required in function of the number of probes used. Figure B.4 reflect the result of this study showing a linear evolution with the number of probes.

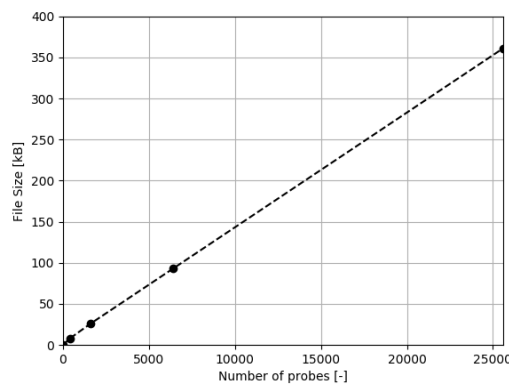


Figure B.4 – Probes file size by number of probes

According to this study, the required storage is $\approx 13 \frac{\text{byte}}{\text{probe}\Delta t}$.

C | Publications

On this appendix the published works are reported. The first publication is a journal paper about the work done on the CRSB injector reported on chapter 3 that at the time of writing this thesis is under-review on the Atomization and Sprays journal (Bell House) . Another publication was done on the same topic and presented on the International Conference on Liquid Atomization & Spray Systems (ICLASS) 2021 in Edinburgh (Scotland). A second publication was submitted and presented at the same conference about the modelling of the CHAiRLIFT airblast atomizer and the surface-curvature analysis to obtain the distribution of the droplets.

Ferrando, D., Belmar-Gil, M., Palanti, L., Carreres, M., Demoulin, F.-X., Renou, B., Duret, B., and Reveillon, J. (2022). Modelling Internal Flow and Primary Atomization in a Simplex Pressure-Swirl atomizer. *Atomization and Sprays* Ferrando,

D., Belmar-Gil, M., Palanti, L., Carreres, M., Demoulin, F.-X., Renou, B., Duret, B., and Reveillon, J. (2021). Internal numerical simulation of a swirl simplex atomizer to predict atomization outputs. *In International Conference on Liquid Atomization and Spray Systems* Ferrando, D., Palanti, L., Demoulin, F.-X., Duret, B., and Reveillon,

J. (2021). Spray drop size distribution and velocity distribution issued from a prefilming airblast atomizer. *In International Conference on Liquid Atomization and Spray Systems*

MODELLING INTERNAL FLOW AND PRIMARY ATOMIZATION IN A SIMPLEX PRESSURE-SWIRL ATOMIZER

D. Ferrando,^{1,*} M. Carreres,² M. Belmar-Gil,²
D. Cervelló-Sanz,² B. Duret,¹ J. Reveillon,¹ F.J. Salvador,² &
F.X. Demoulin¹

¹CNRS CORIA UMR 6614, Université de Rouen Normandie,
CNRS-University and INSA of Rouen, Saint Etienne du Rouvray 76800,
France

²CMT-Motores Térmicos, Universitat Politècnica de València, Camino de Vera
s/n, Valencia, E-46022, Spain

*Address all correspondence to: D. Ferrando, CNRS CORIA UMR 6614, Université de
Rouen Normandie, CNRS-University and INSA of Rouen, Saint Etienne du Rouvray
76800, France, E-mail: diego.ferrando@coria.fr

Original Manuscript Submitted: 02/dd/2022; Final Draft Received: mm/dd/yyyy

Numerical simulations of simplex pressure-swirl atomizers can aid their design process towards better atomization. This work aims at studying the two-phase flow at both the internal geometry and the first millimeters of the external domain of such atomizers where primary breakup takes place. In particular, the atomizer under study has been used for the CORIA Rouen Spray Burner (CRSB) that aims to study lean premixed turbulent flame. Ultimately, our goal is to complete spray characterization in the vicinity of the injector. Such data will potentially enforce the validity of numerical simulations for this burner. Injection characteristics are analyzed through the Volume of Fluid (VOF) method in a Large-Eddy Simulation (LES) framework. We focus our attention on the internal flow inside the injector and how it impact the atomization process. In the present investigation, an experimental methodology combining different techniques is applied to obtain and parametrize the actual internal geometry of the atomizer. The numerical workflow is separated in two simulations to separately study the internal flow formation and the external spray development, given the difficulty to mesh the whole computational domain that handles all length scales still preserving the required accuracy. Several mesh refinements are studied for each simulation, as well as the coupling between internal and external simulations. The methodology is validated against experimental data for two CRSB operating condition. The investigation then proves it is possible to couple the internal and external flow in order to describe the actual air core formation, liquid film behavior and breakup mechanism of these atomizers, extracting relevant atomization outputs in the near-field region where experimental data are scarce.

KEY WORDS: two-phase flow; internal flow; primary atomization; simplex atomizer; pressure-swirl atomizer; geometry measurement; numerical simulation; pre-processing; Large-Eddy Simulation; Volume of Fluid

1. INTRODUCTION

Simplex pressure-swirl atomizers have engineering applications in several fields, such as agricultural spraying (De Luca and Vallet, 2009), fire suppression (Amini, 2016), spray painting, spray cooling, spray drying for food or pharmaceutical processing and different combustion applications (Amedorme and Apodi, 2018; Park and Heister, 2010). Focusing on thermal engines, spray characteristics strongly influence their performance, fuel consumption and emissions generation (Lefebvre and Ballal, 2010). Even though the industry and transportation sectors are progressively being decarbonized, air transport will still need to rely on fossil fuels for some time due to the large power requirements (European Commission, 2020). In this regard, the state of the art of aero engines (such as the lean-burn GE-TAPS) tend to use airblast atomizers together with simplex pressure-swirl atomizers that generate the pilot flame for the startup and low-power regimes (Mongia, 2003).

In simplex pressure-swirl atomizers, fuel is fed to a spin chamber through several tangential ports before being injected through the atomizer outlet (Lefebvre and McDonell, 2017). This situation is depicted in Figure 1. If the Reynolds number (Re) is above a given threshold, the swirling motion generated in the spin chamber induces a depression that pulls external air inside the atomizer, shaping the so-called air core (Som, 2012). Hence, the fuel is forced to stick to the walls in the shape of a film, being injected into the environment as a hollow cone. Chinn (2009) reviewed some earlier works and developed an inviscid flow analysis to justify the discharge coefficient, air core radius and spray cone angle observed for this kind of atomizer as a function of the so-called *atomizer constant*, which embeds the relevant atomizer dimensions. Park et al. (2007) found the liquid temperature can influence the air core stability through Re , defining an unstable and a transitional regime. The initial liquid film thickness at the atomizer outlet can be derived from these estimations.

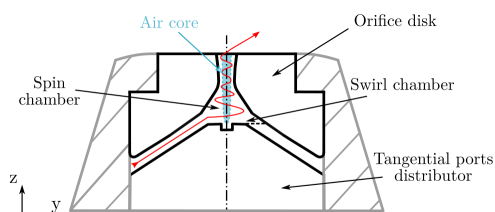


FIG. 1: Cross-section sketch of the upper part of a simplex Danfoss pressure-swirl atomizer and paths for the liquid (red) and air (light blue).

Leaving the internal flow and focusing on the atomizing features, simplex pressure-swirl atomizers have drawn the attention of both experimentalist and modelling researchers. From the experimental side, the techniques employed include Mie-scattering (Liu et al., 2019), Phase Doppler Anemometry (PDA) (Dafsari et al., 2019; Leask et al., 2019; Maly et al., 2019), Laser Doppler Anemometry (LDA) (Laurila et al., 2020) or Particle Induced Velocimetry (PIV) (Durdina et al., 2014; Jedelsky et al., 2018). These investigations qualitatively show that primary breakup is produced by the growth of a Kelvin-Helmholtz instability on the liquid sheet as soon as the fuel leaves the atomizer and interacts with the surrounding gas. However, the quantitative analysis by experimental means is restricted to the secondary breakup region, since the dense

spray in the near-nozzle region is difficult to visualize by the current optical techniques. Numerical simulation can then bridge the gap among the near and the far-field by offering a level of detail that experiments cannot offer.

In this way, from the computational point of view, most investigations make use of diverse Volume of Fluid (VOF) methods that deal with the two-phase flow in a fully Eulerian framework. All turbulence modelling approaches have been used, including the laminar assumption (Amini, 2016; Razeghi and Ertu, 2018), Reynolds-Averaged Navier-Stokes (RANS) (Alajbegovic et al., 2002) and Large-Eddy Simulation (LES) (Laurila et al., 2019). Even though these works cover both the internal and the external flow simultaneously, they do not seem to reproduce the liquid sheet instabilities that have been observed to produce breakup, and thus predict atomization mechanisms that may differ from the actual one. Except for Laurila et al. (2019) (with an atomizer configuration fairly different from those used for combustion applications), only investigations using computationally expensive Direct Numerical Simulation (DNS) either through VOF (Fuster et al., 2009; Galbiati et al., 2016) or Level Set (Shao et al., 2017) do capture liquid film instabilities triggering atomization. Shao et al. (2017) realized they needed to prescribe a turbulent inflow condition in order to reproduce these fluctuations, highlighting the role of turbulence on the process.

The objective of the present investigation is to present a methodology to numerically analyze primary atomization in simplex pressure-swirl atomizers. The atomizer mounted in the CORIA Rouen Spray Burner (CRSB) is particularly investigated, considering this configuration was studied as a reference for gas turbine applications in the last Turbulent Combustion of Sprays workshops (TCS: <http://www.tcs-workshop.org>). Hence, some spray features in the spray secondary breakup region (Shum-Kivan et al., 2017; Verdier et al., 2017) and combustion outcomes (Mulla et al., 2019a,b; Mulla and Renou, 2019) have already been determined experimentally. The present investigation thus aims at filling the gap between this far-field region and the atomizer outlet, where experimental data can scarcely be obtained, as stated. The proposed methodology includes three pre-processing stages, namely the experimental determination of the atomizer internal geometry, the mesh generation and the definition of a numerical setup able to handle this multi-scale problem. The study discusses the addressing of these steps towards the accurate obtaining of atomization outputs.

2. EXPERIMENTAL GEOMETRY CHARACTERIZATION

The first pre-processing step towards numerically modelling the internal flow and atomization process is to determine the computational domain. The pressure-swirl atomizer mounted in the CRSB is a commercial Danfoss OD-H 030H8103 oil nozzle. This is a hollow-cone atomizer manufactured in accordance with European standard EN 293 with a nominal opening angle of 80° and a nominal mass flow rate of 1.35 kg/h.

As shown in Figure 1, two of the injector pieces (namely the tangential ports distributor and the orifice disk) shape the internal geometry of the atomizer. This includes three inlet fuel ports, the swirl and spin chambers and the orifice itself. The atomizer internal geometry has then been characterized through a combination of experimental techniques applied to the aforementioned pieces:

- Computed Tomography scan (CT-Scan).
- Optical microscope visualization.

- Scanning Electron Microscope (SEM) visualization.

Additionally, a caliper was used to measure the global dimensions of the atomizer pieces. The techniques, described in the following subsections, have been applied either to:

- The disassembled metallic pieces, or
- Silicon molds of the atomizer pieces, obtained as introduced by Macian et al. (2003) for diesel injector nozzles.

This methodology has been described by Salvador et al. (2018), who validated its use when determining the internal features of a Diesel injector. The reader is referred to this work for a detailed description of the techniques and a comparison of their advantages and limitations.

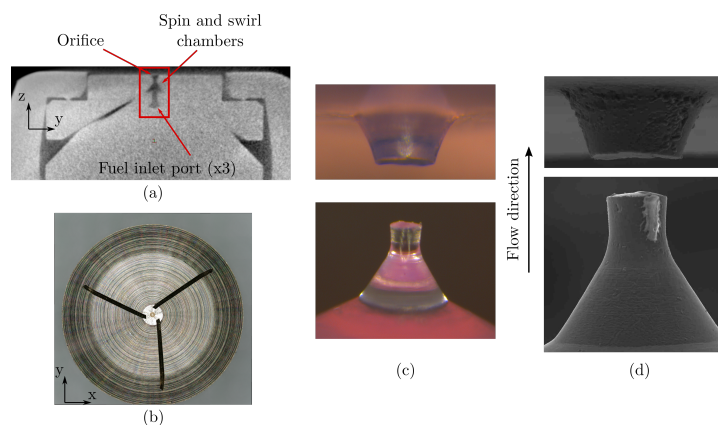


FIG. 2: Sample pictures of the internal geometry of the CRSB atomizer: (a) CT-Scan visualization of the upper part of the atomizer assembly; (b) Optical microscope visualization of the tangential ports distributor piece, top view; (c) Optical microscope visualization of the silicon molds of the spin and swirl chambers, side view; (d) SEM visualization of the silicon molds of the spin chamber, side view.

2.1 Computed Tomography scan (CT-Scan)

The Computed Tomography allows obtaining tomography cuts of the atomizer pieces in non-transversal planes. These images are then used to reconstruct the full 3D geometry. A Nikon XT H-160 CT-Scan machine able to produce x-ray beams with a power up to 60 W at a maximum voltage of 60 kV was used.

The resolution achieved by this technique depends on the particular geometry and the material that the beams have to travel through. The produced images in this application have a maximum magnification of 150x and a pixel size in the order of 10 μm . This resolution is poorer than the one reached with the other techniques, but it is the only one that allows visualizing the full atomizer assembly, as shown in Figure 2(a). Hence, in this investigation it has only been used to validate the other two techniques and to help determining the orifice contour.

2.2 Optical microscope visualization

A Leica MZ APO system with up to 80x magnification has been used. It mounts a PLANAPO 1.0X objective and a KL1500 optic fiber illuminator.

Figure 2(b) and Figure 2(c) show samples of visualization corresponding to a disassembled metallic piece and the silicon molds of the CRSB atomizer, respectively.

2.3 Scanning Electron Microscope (SEM) visualization

A Jeol JSM6300 Scanning Electron Microscope (SEM) has been employed. It operates at 30 kV and offers a magnification up to 1000x.

The SEM requires the observed sample to be conductor. Hence, the silicon molds need to be covered by a thin layer (in the order of nm) of gold dust. The accuracy of the technique was reported to be around 2% (2-3 μm) in the determination of injector nozzle orifices outlet diameter.

Figure 2(d) shows an example of SEM visualization of the CRSB atomizer silicon molds of the spin chamber.

2.4 Geometry parametrization

From visualization through the aforementioned techniques it is possible to parametrize the atomizer geometry, as shown in Figure 3. This parametrization allows generating CAD volumes for CFD modelling purposes and enables sensitivity studies on the geometry through the variation of the parameter values.

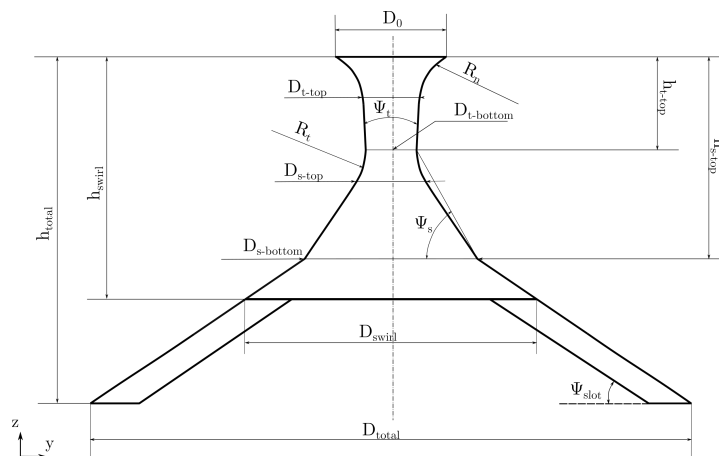


FIG. 3: Abstraction of the Danfoss OD-H nozzle with the defined geometrical parametrization (over-constrained).

Collecting images through optical microscope and SEM visualization allowed determining the values of the geometrical parameters of the actual CRSB atomizer unit. A given parameter

can be obtained through several images with different techniques or different magnification rates. A mean value and standard deviation can then be determined for each parameter.

Results from the application of the techniques are summarized in Table 1 together with the values finally accepted to build the computational domain.

Parameter	Unit	Dimensions				
		Optical micr. (molds)	SEM (molds)	SEM (direct visualization)	CT	Accepted
D_0	μm	313 ± 2	300 ± 2	298 ± 1	301 ± 3	300
D_{t-top}	μm	179 ± 4	180 ± 5	-	-	180
$D_{t-bottom}$	μm	164 ± 2	160 ± 1	160 ± 1	169 ± 3	165
D_{s-top}	μm	209 ± 3	213 ± 2	-	-	210
$D_{s-bottom}$	μm	491 ± 5	480 ± 5	496 ± 2	500 ± 1	500
D_{swirl}	μm	774 ± 6	781 ± 6	776 ± 2	773 ± 4	780
D_{total}	μm	-	-	3492 ± 1	3375 ± 1	3375
h_{t-top}	μm	233 ± 4	238 ± 3	-	-	240
h_{s-top}	μm	532 ± 6	546 ± 3	-	540 ± 2	540
h_{swirl}	μm	600 ± 5	605 ± 4	-	600 ± 2	620
h_{total}	μm	-	-	-	2400 ± 1	2400
R_n	μm	303 ± 5	300 ± 4	-	-	308
R_t	μm	171 ± 6	191 ± 5	-	-	190
ψ_t	$^\circ$	6 ± 4	6 ± 2	-	-	6
ψ_s	$^\circ$	57 ± 6	58 ± 4	-	-	61
ψ_{slot}	$^\circ$	27 ± 6	28 ± 3	-	-	30

TABLE 1: Summary of the results obtained from each metrology technique and *accepted* values to construct the inner computational domain.

3. NUMERICAL STRATEGY

Due to the large range of length scales to be considered, about several millimeters for injector scale down to few microns for the liquid film and drop size, the present work proposes a two steps coupling methodology: first, the internal flow of the injector is modelled; afterwards, an external simulation is set up to predict the early stage of the atomization process. Both numerical simulations are carried out using the same numerical methods to keep consistency among them.

3.1 Numerical methods

The numerical simulation is based on the well known *OpenFoam 6.0* library that already contains many features needed for liquid-gas flows simulation on complex geometries, with a built-in parallel computing ability to handle intensive simulation (The OpenFoam Foundation, 2018). The solver used is the *interFoam* multiphase solver which uses the Volume of Fluid (VoF) method with an Interface Capturing Method (ICM) to capture the interface among liquid and gas. The

Modelling internal flow and primary atomization in a simplex pressure-swirl atomizer

7

equations are the mass and momentum conservation:

$$\frac{\partial u_j}{\partial x_j} = 0 \quad (1)$$

$$\frac{\partial \rho u_i}{\partial t} + \frac{\partial}{\partial x_i} (\rho u_j u_i) = -\frac{\partial P}{\partial x_i} + \frac{\partial}{\partial x_j} (\tau_{ij} + \tau_{tij}) + \rho g_i + f_{\sigma i} \quad (2)$$

where u represents the velocity vector, P the pressure, ρ the density of the cell mixture defined as $\rho = \alpha \rho_l + (1 - \alpha) \rho_g$, τ_{ij} and τ_{tij} the viscous and turbulent stresses, g_i the gravitational acceleration and f_{σ} the surface tension forces, calculated as:

$$f_{\sigma} = \sigma \kappa \frac{\partial \alpha}{\partial x_j} \quad (3)$$

where σ is the surface tension among the liquid and the gas, α is the liquid volume fraction and κ is the curvature of the liquid, computed as:

$$\kappa = -\frac{\partial}{\partial x_j} \left(\frac{\partial \alpha / \partial x_j}{|\partial \alpha / \partial x_j|} \right) \quad (4)$$

In order to determine the interface position, an equation for the liquid volume fraction α is solved:

$$\frac{\partial \alpha}{\partial t} + \frac{\partial (\alpha u_j)}{\partial x_j} + \frac{U_j^r \partial (\alpha (1 - \alpha))}{\partial x_j} = 0 \quad (5)$$

where U^r is a suitable velocity field selected to compress the interface region defined as a relative velocity between the two phases.

The interface is implicitly captured through the liquid volume fraction (α) equation. Thus, the interface is localized at the transition between the gas ($\alpha = 0$) and the liquid ($\alpha = 1$). To keep an accurate description of the interface, the transition should remain sharp with a size in the order of few Δx . On regular VOF approaches, the interface position is reconstructed (Scardovelli and Zaleski, 1999) and the liquid volume flux are based on the geometrical advection of this surface. This geometrical approach brings difficulties for the generic polygons used in OpenFoam as numerical cells to handle complex geometries. Thus, liquid advection is based on standard numerical schemes bringing numerical diffusion that potentially enlarges the transition zone. A sharpening term is introduced to counter this effect (Rusche, 2002; Wardle and Weller, 2013).

Regarding turbulence, a LES approach has been used. Some tests were performed in order to choose a LES sub-grid scale (SGS) model. Finally, the work is performed with the WALE model by Nicoud and Ducros (1999), which led to more reasonable results in the internal region of the atomizer.

The *OpenFOAM* toolbox includes low order methods since it is thought as an industrial toolbox to perform CFD simulations. In time, the *backward* second order scheme and the hybrid first-second order *CrankNicolson* are set, the latter with a factor of 0.9 closely resembling second order. The convection schemes are either *limited linear* or *van Leer*, both corresponding to second order accuracy.

Volume x, Issue x, 2022

3.2 Operating conditions

The operating conditions studied on this work are the ones experimentally studied by Verdier et al. (2017), corresponding to atmospheric pressure and temperature (no fuel pre-heating). Given that the *interFoam* solver is an incompressible isothermal solver, the density ρ and the kinematic viscosity ν for both the fuel (n-heptane) and air have to be defined. Also, the surface tension σ between the two fluids is needed. The values of the parameters used in the simulation at the studied temperature are reported in Table 2.

	$T[K]$	$\rho[kg/m^3]$	$\nu[m^2/s]$	$\sigma[mN/m^2]$
Fuel	298	678.9	$5.67e-07$	20.0
Air	298	1.117	$1.57e-05$	

TABLE 2: Fuel and air properties used in the simulations.

4. INTERNAL FLOW MODELLING

4.1 Numerical domain, mesh and boundary conditions

The choice of the computational mesh topology is an important step in a multiphase simulation. The minimal resolution has to be enough to be able to capture the interface between the liquid and the gas. Therefore, studies such as Hansen et al. (2002); Sumer et al. (2012) used full hexahedral structured meshes because it is straightforward to modify the length of the cells of interest.

Nevertheless, for the present injector, the inlet ports are placed with a certain tilting angle with respect to the swirl chamber, thus, preventing the geometry from being fully axisymmetric. Hence, induce a high number of hexahedral cells had high values of skewness, aspect ratio and non-orthogonality, producing a poor quality mesh. Several attempts were performed to improve the mesh quality keeping the structured approach, but none of them was successful.

To overcome this problem, the approach used by Madsen et al. (2004) or Ding et al. (2016) was utilized, adopting a strategy based on a hybrid tetrahedral-hexahedral mesh. The main idea of this approach is to keep as much hexahedral elements as possible everywhere in the domain but in the conflicting zone. Accordingly, a ring of tetrahedral elements is placed around the axial center, where the tangential ports intersect the swirl chamber. The rest of the domain (i.e. the three tangential ports, the body of the injector and also the external zone of the domain) is made of hexahedral elements following a structured mesh.

A representation of the final mesh strategy is shown in Figure 4, where the different cell topologies are represented.

Three boundary zones are defined to set up the boundary conditions: the tangential ports inlet, the wall corresponding to the metallic pieces of the injector and the outlet boundary surface corresponding to the atmosphere. Those zones are represented in Figure 5: green for the inlet patches (number 1), grey for the wall patches (number 2) and blue for the outlet patches (number 3).

At the inlet, the fuel mass flow rate $\dot{m}_{fuel} = 0.28g/s$ (corresponding to the CRSB operating condition) is equally splitted among the three tangential ports. This imposes the boundary condition for the velocity as a fixed mass flow rate in each tangential port. Also at these patches, a zero gradient condition is imposed for the pressure and a fixed value is used for the liquid volume fraction, with $\alpha = 1$ (only liquid entering the domain through the inlet).

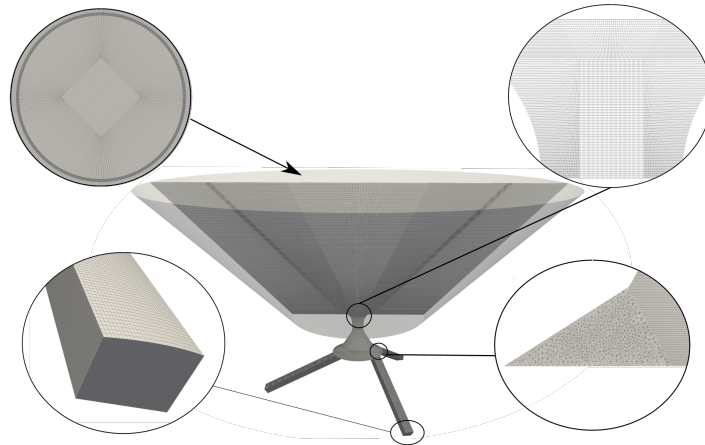


FIG. 4: Computational grid sketch. Hybrid mesh made of hexahedral and tetrahedral elements.

The walls are set up with usual boundary conditions. Therefore, the *no slip* boundary condition is set for the velocity. The pressure and liquid volume fraction are set as zero gradient boundary conditions.

Finally, for the *outlet* patch, the zero gradient condition is imposed for the velocity as it is for the liquid volume fraction α . The *totalPressure* boundary condition is used and fixed to atmospheric pressure. This boundary condition sets the value of the patch pressure as follows:

$$p_p = p_0 - \frac{1}{2}|\mathbf{u}|^2 \quad (6)$$

where p_p is the patch pressure, p_0 is the total pressure given to the boundary, and the last term $\frac{1}{2}|\mathbf{u}|^2$ represents the dynamic pressure.

A summary of the boundary conditions is reported in Table 3:

	1. Inlet	2. Wall	3. Outlet
\mathbf{u}	Dirichlet: imposed flux	Dirichlet: $\mathbf{u} = 0$	Neumann: zero-gradient
p	Neumann: zero-gradient	Neumann: zero-gradient	Dirichlet: totalPressure
α	Dirichlet: $\alpha = 1$	Neumann: zero-gradient	Neumann: zero-gradient

TABLE 3: Boundary conditions for the relevant magnitudes at the different domain patches.

The computation has been run with several mesh resolutions to carry out a mesh convergence study. The characteristics of the computational grids are shown in Table 4. At least 85% of the cells are hexahedral shaped cells. From the coarsest to the finest mesh, the main goal is to increase the number hexahedral elements trying to keep the number of tetrahedral elements as low as possible. On the bottom of the table, the y^+ maximum and averaged values are shown at different zones of the geometry. It is important to have a good y^+ value around the spin chamber since at this location the swirl motion is developed (Amini, 2016).

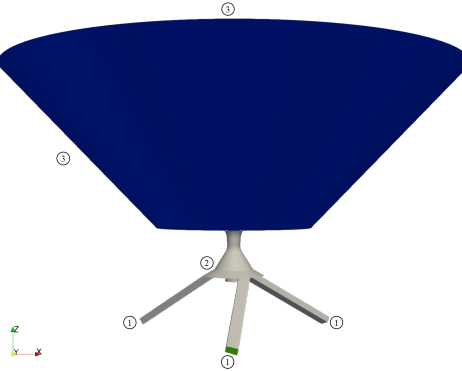


FIG. 5: Boundary conditions patches of the CRSB internal flow simulation.

	Coarse Mesh		Medium Mesh		Fine Mesh	
Number of elements	2.7e6		13.2e6		32.8e6	
Tetrahedra	0.13e6		1.6e6		3.2e6	
Hexahedra	2.6e6		11.6e6		29.6e6	
Pyramids	4.3e3		11.7e3		24.9e3	
Y^+	Max	Avg	Max	Avg	Max	Avg
Full geometry	66.1	12.1	21.8	2.6	3.4	1e-2
Inlet ports	66.1	9.2	21.8	2.8	1.7	0.78
Swirl Chamber	28.5	12.8	11.3	3.7	3.4	0.96
Spin Chamber	13.7	3.2	2.9	1.3	2.7	1.8
Throat	24.6	13.8	3.3	2.4	2.3	1.8
Nozzle	33.4	21.5	3.5	2.6	2.8	2.2

TABLE 4: Features of the meshes used for the internal flow simulations.

As a first step, the initialization is performed with the coarse mesh until the flow reaches a steady regime to reduce the computational resources. The CPU-hours are collected on Table 5. Afterwards, the computed fields are mapped into the more refined meshes to continue the calculations, reducing computational resources in the transient stages.

4.2 Initialization: Time evolution of hollow cone generation

Having a clear understanding of the liquid flow emanating from orifice section could be important for some engine regimes. Considering the boundary and initial conditions, a certain amount of time is required by the fluid to establish the cone-shaped flow (Razeghi and Ertunç, 2018).

Figure 6 shows the time evolution of the air core generation and the hollow cone shape of the spray. Figure 6a represents the initial conditions of the simulation where the fuel fills the whole injector. From Figure 6b to Figure 6d the fuel is expelled in a distorted pencil shape.

From Figure 6f the jet begins to break-up and in Figure 6i it starts being comparable with the onion stage shape. From Figure 6k the hollow cone spray is established, meaning the cone angle

Modelling internal flow and primary atomization in a simplex pressure-swirl atomizer

11

	Coarse Mesh	Medium Mesh	Fine Mesh
Δt	5e-9 s	2.5e-9 s	5e-10
CPU_s	112	420	672
Δt_{real}	0.26 s	0.6 s	2.9 s
$CPUh/ms$	1.6e3	28e3	1e6

TABLE 5: Computational resources for the internal flow computations.

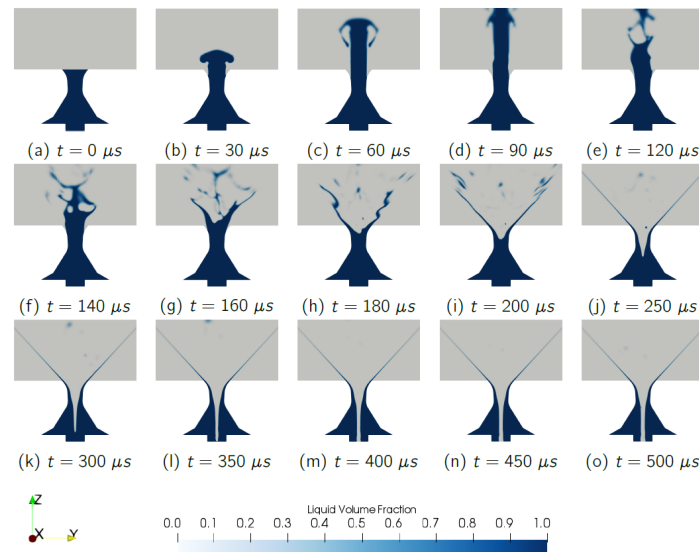


FIG. 6: Hollow cone transient evolution depicted through liquid volume fraction contours at the domain mid-plane.

and the liquid film thickness can be measured. Nevertheless, the air core is not fully developed and it was necessary to compute additional $250\mu s$ for this to happen. With the air core developed, it reaches the bottom wall of the injector and it widens.

In conclusion, the total time to initialize the simulation (i.e. the transient period of the injector from rest to nominal conditions) is in the order of $0.5ms$.

4.3 Liquid volume fraction

As stated in Section 4.1, the initialized results from the coarser mesh (velocity, liquid volume fraction and pressure fields) are mapped into the medium and fine resolution meshes. Figure 7 depicts a mid-plane contour of the liquid volume fraction α for each mesh resolution. It can be observed that the coarser mesh is not able to capture as much instabilities on the bottom zone of the air core as the other two meshes. Computations with the more refined meshes do show

Volume x, Issue x, 2022

instabilities at the air core. This phenomenon has already been reported on other studies about simplex swirling injectors such as Sumer et al. (2012) or Maly et al. (2018). Regarding these instabilities, no remarkable differences are seen among the medium and fine meshes.

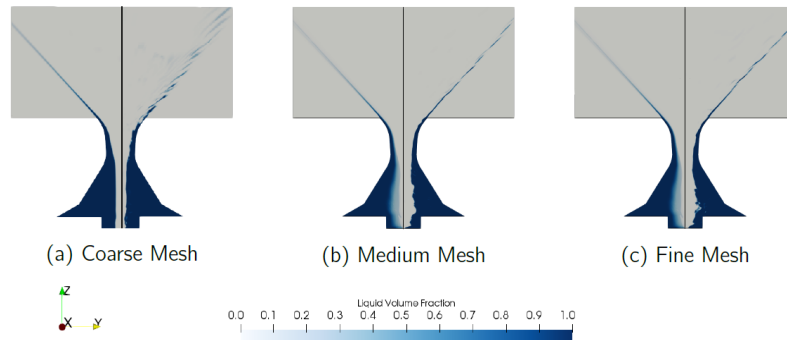


FIG. 7: Liquid volume fraction contours at the domain mid-plane for the three mesh resolutions presented. In each case, the left-hand side represents time-averaged data, whereas the right-hand side depicts instantaneous data.

Figure 8 shows iso-contours of liquid volume fraction $\alpha = 0.5$ representing the liquid-gas interface for each of the three meshes. The air core thickening is again observed in the medium and fine meshes, but no substantial differences are found at the external part of the domain.

Figure 9 shows some experimental pictures reported by Verdier et al. (2017) for illustrating purposes. The comparison among Figure 8 and Figure 9 indicates a poor agreement of the numerical computation due to a lack of resolution at the external zone downstream the nozzle orifice outlet. With the nearly structured mesh approach adopted for this simulation, increasing the cell resolution at the external part would also imply the need for more cells at the internal part of the domain, where they are not needed anymore. This fact drove the authors to divide the problem in two steps, analyzing the external domain by means of a specific simulation with a different mesh strategy, as presented in Section 5.

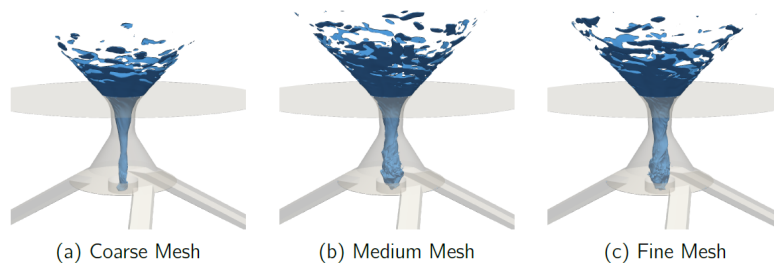


FIG. 8: Liquid volume fraction iso-contour for $\alpha = 0.5$.

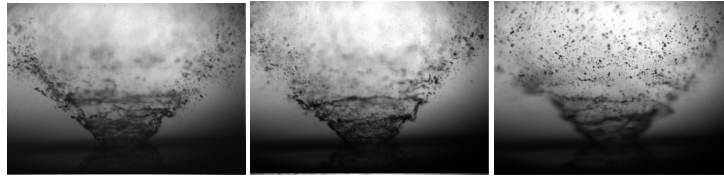


FIG. 9: Sample experimental pictures by Verdier et al. (2017) for three different instants.

4.4 Liquid film thickness

The liquid film thickness is retrieved at the nozzle orifice for the three cases. These values are compared with some empirical equations to validate the computations. Equation 7 is nowadays used to characterize the film thickness (t_l) in the design of pressure-swirl atomizers (Lefebvre and McDonnell, 2017):

$$t_l = 2.7 \left[\frac{d_o FN \mu_{fuel}}{(\rho_{fuel} \cdot \Delta P)^{0.5}} \right] \quad (7)$$

where d_o is the orifice diameter, ΔP is the pressure drop along the nozzle, $FN = \dot{m}_{fuel}/(\Delta P \rho_{fuel})^{0.5}$ is the flow number, μ_{fuel} and ρ_{fuel} are the dynamic viscosity and the density of the fuel, respectively.

Since Equation 7 is based on the geometry of a simple injector, its accuracy for complex geometries is not assured. However, it is also possible to reach an expression for the film thickness through the discharge coefficient C_d , as follows:

$$C_d = \frac{\dot{m}_{fuel}}{\dot{m}_{th}} = \frac{\dot{m}_{fuel}}{A_o \sqrt{2 \Delta P \rho_{fuel}}} \quad (8)$$

The ratio among the air core area (A_a) and the orifice area (A_o) is expressed as:

$$X = \frac{A_a}{A_o} = \frac{\pi(d_o - 2t_l)^2/4}{\pi d_o^2/4} \quad (9)$$

from the ratio X it is possible to calculate the fuel sheet thickness:

$$t_l = \frac{d_o(1 - \sqrt{X})}{2} \quad (10)$$

Equation 11, proposed by Giffen and Muraszew (1953), relates the discharge coefficient to the ratio of areas X :

$$C_d = 1.17 \left[\frac{(1 - X)^3}{1 + X} \right]^{0.5} \quad (11)$$

The procedure to estimate the liquid film thickness with this method is as follows. First the discharge coefficient is calculated from the mass flow rate of the operating condition studied through Equation 8. X is then obtained iteratively from Equation 11. It is then straightforward to obtain t_l from Equation 10.

Figure 10 plots the radial evolution of the liquid volume fraction along the nozzle outlet for the coarse, medium and fine meshes. The vertical lines represent the thickness obtained from

empirical equations. It can be observed that the computational prediction is far from the film thickness derived from Equation 7, but in very good agreement with the value predicted by Equation 10. In any case, Equation 7 is reported to overestimate mean liquid film thickness for atomizers whose inlet ports have a relatively small cross-sectional area Lefebvre and McDonell (2017). Hence, the results on liquid film thickness enhance the confidence on the simulation outcomes.

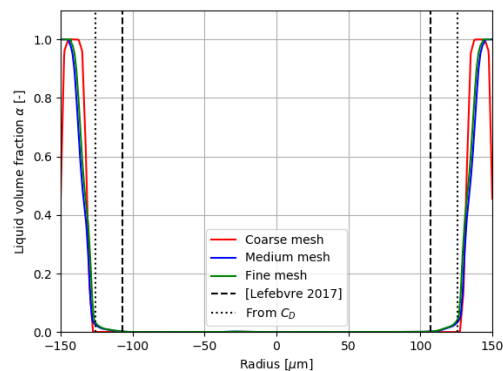


FIG. 10: Liquid volume fraction α plot along the radial axis on the nozzle outlet. Red: coarse mesh; blue: medium mesh; green: fine mesh; black: empirical equations.

Both the medium and fine meshes show similar results, where the film fluctuations inside the nozzle are captured. Finally, identifying the film from iso-liquid volume fraction contours of $\alpha = 0.5$, the film thickness on the coarsest mesh has a value of $t_l^{coarse} = 24 \pm 4 \mu m$ whereas both the medium and fine meshes yield a value $t_l^{fine} = 22 \pm 15 \mu m$.

4.5 Spray cone angle

The spray cone angle is another characteristic parameter in simplex swirl atomizers. For the numerical study it can be determined from Figure 7. The value of this angle 2θ is equal to 82° , matching the value obtained from experiments of 80° (Verdier et al., 2017).

4.6 First-second order discretization effects

Once the mapping described in Section 4.1 from the coarsest mesh into each subsequent finer mesh is done, some time is needed for the simulation outcomes to reach nominal values. To avoid numerical instabilities during this process, first order spatial schemes are initially set-up. After running on the finer mesh for some time, they are fully replaced by second order schemes.

Figure 11 shows a comparison concerning the liquid film thickness appearance at the atomizer outlet cross-section for these two numerical schemes. It can be observed how first order schemes are more dissipative, not being able to capture instabilities on the fuel liquid sheet.

Second order schemes, in turn, allow capturing those instabilities that could be responsible for triggering atomization.

In order to further investigate the role of these Rayleigh–Taylor instabilities on primary breakup, results from both approaches (i.e. first order -constant fuel sheet thickness- and second order -varying fuel sheet thickness) were stored to be later mapped to the inlet of the specific external flow simulation discussed in Section 5.

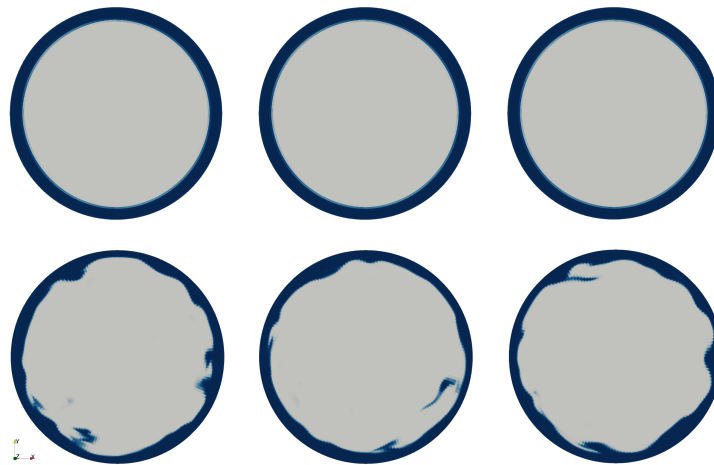


FIG. 11: Liquid volume fraction α contour at the atomizer outlet cross-section. Top: three snapshots using the *upwind* scheme for the spatial divergence. Bottom: three snapshots using the *limitedLinear* scheme for the spatial divergence. The time step between pictures is $\Delta t = 5\mu s$

5. EXTERNAL FLOW MODELLING: ZOOM ON ATOMIZATION PROCESS

In order to overcome the resolution problem on the external zone above the nozzle orifice shown in the simulations from Section 4, a specific high resolution simulation for the outer part of the domain is performed. Focusing only on this part of the problem should allow reliably modelling the primary breakup mechanism of the pressure-swirl atomizer.

5.1 Numerical domain, mesh and boundary conditions

Figure 12 shows a sketch of the numerical domain and the boundary conditions considered for the external flow simulation. The angle of the sector is $\varphi = 45^\circ$. The domain radius and height are 12.5 times the orifice diameter d_o : $r_{dom} = h_{dom} \approx 4mm$. These dimensions follow the work by Galbiati et al. (2016).

Number 1 is the inlet patch of the domain. It is an arc whose radius is equal to the orifice radius. The boundary conditions for the velocity \mathbf{u} and the liquid volume fraction α are dynamically provided (time-varying) with the results from the previous internal flow simulation presented in Section 4. The pressure p is set with a *zeroGradient* boundary condition.

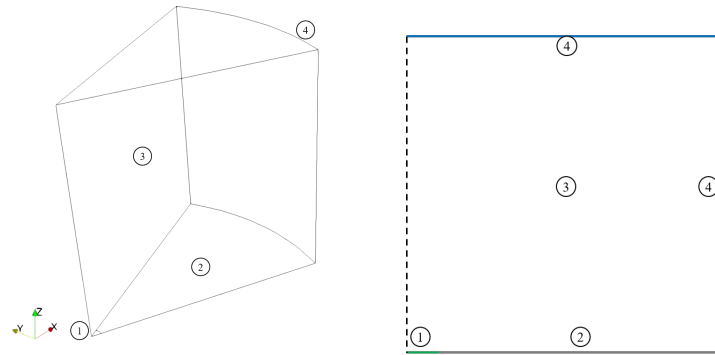


FIG. 12: Geometry domain and boundary condition of the external flow simulation. Left: 3D view; right: view normal to a cyclic patch. 1: Inlet; 2: Wall; 3: Cyclic patches; 4: Outlet.

Number 2 is treated as a wall boundary condition: the velocity \mathbf{u} is then set as *noSlip*. The pressure p and the liquid volume fraction α are in turn set as *zeroGradient*.

Number 3 are two periodic patches. In *OpenFOAM*, such boundary conditions are called *cyclic*; specifically, in this case, as the two patches are not equally created, the specific *CyclicArbitraryMeshInterface* version of this boundary condition is used.

Finally, number 4 is the outlet of this simulation. As it was done in the previous simulation, the velocity \mathbf{u} and the liquid volume fraction α are set as *zeroGradient*, whereas the pressure p is set as *totalPressure* as already explained in Equation 6.

A summary of the boundary conditions is reported in Table 6:

	1. Inlet	2. Wall	3. Periodic	4. Outlet
\mathbf{u}	D: time varying fixed value	D: $\mathbf{u} = 0$	Cyclic	N: zero-gradient
p	N: zero-gradient	N: zero-gradient	Cyclic	D: totalPressure
α	D: time varying fixed value	N: zero-gradient	Cyclic	N: zero-gradient

TABLE 6: Boundary conditions. **D:** Dirichlet. **N:** Neumann

As far as the mesh strategy is concerned, following the same approach of hexahedral structured meshes to model the external breakup process leads to additional issues. While this approach would allow freely refining the cells in the radial and axial directions, the further away from the nozzle orifice (in the axial direction) the larger the tangential dimension of the cells. Since the spray cone angle is wide, following this strategy leads to high aspect ratio cells that lower their resolution in terms of interface capturing.

Numerical studies such as those performed by Galbiati et al. (2016) or Laurila et al. (2020, 2019) propose Cartesian isotropic meshes to model the atomization process of swirling injectors. Due to the aforementioned issues, the same approach is adopted in this work.

In order to find the proper mesh resolution before running the actual 3D simulation, a small 2D axisymmetric study was performed beforehand. In this study, a 2D structured mesh with no tangential dimension is used, thus accurately replicating the Cartesian mesh approach. Table 7

reports mesh information for three different meshes used in the 2D grid convergence study. Since these simulations are 2D, the number of cells increase by a factor of two every time the resolution is doubled. Given that the Courant number remains the same for the three cases, the time step Δt is reduced by half for each refinement level and also the physical time invested per iteration Δt_{real} increases by a factor of two.

	$2\mu m$	$1\mu m$	$0.5\mu m$
Number of elements	0.27e6	1.1e6	4.4e6
Cells at liquid sheet	4	8	16
Δt	$1.7e-8$ s	$0.8e-8$ s	$0.4e-8$ s
CPU_s	72	72	72
Δt_{real}	0.92 s	1.8 s	3.7 s
$CPUh/ms$	≈ 1000	≈ 4500	≈ 18500

TABLE 7: 2D grid convergence study: mesh information.

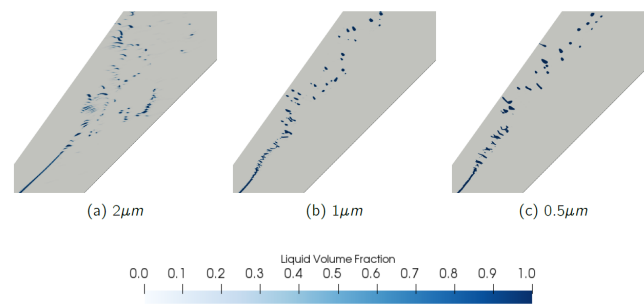


FIG. 13: Liquid volume fraction contours for different cell size cases in the 2D mesh convergence study for the external simulation. From left to right: $2\mu m$, $1\mu m$, $0.5\mu m$

Figure 13 shows the contour of liquid volume fraction α for the three different mesh cell sizes. All mesh resolutions tested are able to capture the interface between the liquid and the gas, not only on the liquid sheet but also on the "droplets" that break-up from it. The main difference among the lowest resolution and the highest one is the lack of instabilities of the liquid sheet in the former. Even though the mesh resolution in the $2\mu m$ cell size case is greater than the one showed in Section 4 at the external zone, this resolution is not enough to capture the fluctuations triggered on the liquid sheet by the air motion. However, the cell size of $1\mu m$ allows capturing those fluctuations. Moreover, as expected, it provides a better interface capturing of the liquid sheet and the predicted shape of the 2D "droplets" is more realistic. Finally, the finest resolution also sharpens the interface capturing but it does not increase the amount of instabilities triggered on the sheet. For this reason, a cell size of $1\mu m$ is chosen as a reference for the 3D study.

Once the cell size is chosen from the previous study, the 3D sector Cartesian mesh is set. Figure 14 shows a mid-plane cut on the mesh. The refinement zone following the spray cone angle can be appreciated, reaching up to 1.3 mm along the axial coordinate. The mesh has around 88e6 elements where most of them correspond to $\Delta x = 1\mu m$.

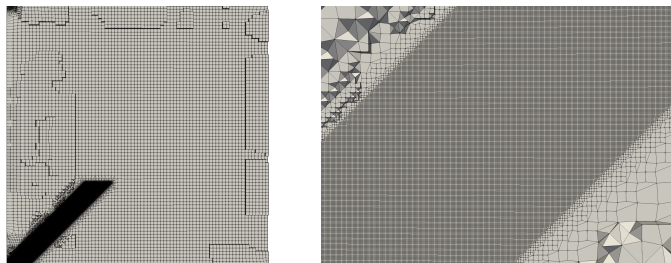


FIG. 14: Slice on the external mesh. Left: full mesh slice; right: refinement zone detail.

5.2 Coupling methodology

The coupling between simulations is done storing the data from the velocity \mathbf{u} and the liquid volume fraction α from the internal flow simulation (Section 4) and setting up the inlet boundary condition of the external flow simulation as the *timeVaryingMappedFixedValue* boundary condition already implemented in *OpenFOAM*. This boundary condition takes the data from one field and interpolates linearly in time and space, if needed. Data from the internal simulation have been stored every $0.05\mu\text{s}$, which has been checked to be way below the air core rotation period.

No major variation is noticed from one mesh to another. Thus, since the medium and fine meshes produce similar results and due to the lower computational resources requirements of the medium mesh, the mapping data for the external simulation is recovered only on this mesh.

To validate the efficiency of the boundary condition acting as a link among simulations, the conservation of the swirl number and the turbulent kinetic energy has been checked. This study is done with the medium internal mesh, ambient operating conditions and the WALE LES SGS model, as stated in Section 4.

5.2.1 Swirl number

The swirl number relates the swirling momentum to the axial motion. It was originally proposed by Chigier and Beér (1964) and simplified by Sheen et al. (1996) as follows:

$$SN = \frac{G_{tg}}{R G_{ax}} = \frac{\int_0^R w u r^2 dr}{R \int_0^R u^2 r dr} \quad (12)$$

where SN is the swirl number, G_{tg} is the axial flux of the tangential momentum, G_{ax} is the axial flux of the axial momentum, R is the outer radius, w and u are the tangential and axial velocity at corresponding radial position r , respectively.

Figure 15 shows the swirl number evolution along the axial axis (Z) for both the internal and external simulations. It can be appreciated that the output from the internal flow simulation matches the input for the external flow simulation, validating the data exchange among simulations after the interpolation process.

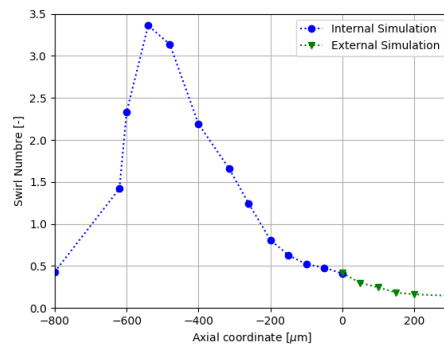


FIG. 15: Swirl number evolution along the axial axis for both the internal flow and external flow simulations.

5.2.2 Turbulent kinetic energy

The preservation of turbulent kinetic energy (*TKE*) is fundamental in the mapping process. Since not every time step is stored and mapped into the external flow simulation, some turbulence-related energy may be lost. The sub-grid modeled turbulence can also be missed in the process. In order to assess the behavior of the method, the turbulent kinetic energy is plotted in Figure 16.

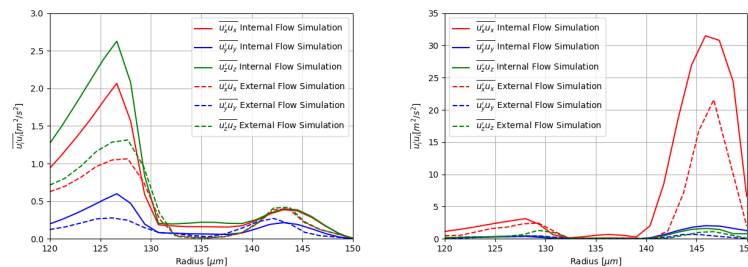


FIG. 16: Turbulent kinetic energy. Left: resolved scales; right: sub-grid energy.

It can be observed that, in general, the turbulent kinetic energy is underestimated in the external flow simulation. This means that some data of the turbulent flow are lost during the mapping process. Nevertheless, main trends are well recovered through the coupling procedure, ensuring proper effects on the external flow simulations. It is remarkable that, despite no mapping or injecting sub-grid turbulence to the domain, the sub-grid turbulent kinetic energy computed in the external simulation has good agreement with the internal one. Still, the level of turbulent kinetic energy is underestimated. To improve this point full simulation covering the whole flow are required but this is beyond the scope of the present work.

5.3 Steady and unsteady fuel film thickness

In Section 4.6, we noticed fuel sheet thickness fluctuation at the atomizer outlet that depend on the numerical scheme. With first order spatial schemes in the internal flow simulation, no fluctuations were recovered, but second order schemes provided fuel sheet instabilities. Two external flow simulations have been carried out mapping data at inlet with and without these instabilities. Both simulations are performed with second order discretization schemes in space and time, so as to isolate the role of the liquid film instabilities on primary breakup. Figure 17 shows the results from these two cases. The iso-surface for $\alpha = 0.5$ is plotted for both cases and qualitatively compared with an experimental picture by Miglierina (2021).

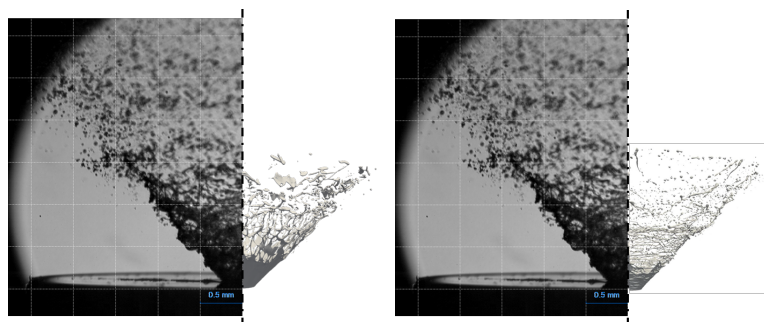


FIG. 17: Left: Comparison among the iso-surface ($\alpha = 0.5$) from the constant fuel sheet thickness case and the experimental picture by Miglierina (2021); right: Comparison among the iso-surface ($\alpha = 0.5$) from the varying fuel sheet thickness and the experimental picture by Miglierina (2021).

It can be observed that with the constant sheet thickness case (first order scheme used in the internal simulation to compute the mapped data) the liquid sheet contour, along the main flow direction, remains straight until it breaks up, whereas the experiments show a wrinkling or fluctuations of the film sheet starting from the nozzle orifice. Another difference is observed concerning the arrangement of the ligaments that represent the intermediate state between liquid sheet perforation and the production of final droplet: in the experiments, the ligaments are arranged in a transversal direction (horizontal on the presented figure); but, in the simulation, ligaments are aligned to the streamwise direction. Finally, the droplet formation seems not fully developed with most of the liquid composed by flat liquid structured.

On the other hand, the results obtained by mapping the fuel injection with fluctuating liquid film thickness (second order scheme used in the internal simulation to gather the mapped data) provide a better match with the experimental results. In this case, the liquid sheet starts fluctuating from the beginning of the external domain. Moreover, the ligaments are arranged in the same direction than in the experiment and the droplets are obtained with sizes that seem to be in the same order than the experimental ones.

This study points out that the liquid film thickness instability plays a driving role on the primary breakup mechanism of simplex pressure-swirl atomizers. Properly capturing these fluctuations, which was achieved in the current investigation thanks to a proper resolution of the internal flow. Thus, it is essential to carry out an accurate modelling of the interior flow justifying all the work devoted to the careful measurement of the internal geometry, since the whole

process of atomization that takes place outside of the injector can be completely changed with slight modification of the injection characteristic.

5.4 Further analysis

Figure 18 represents the liquid volume fraction α iso-contour ($\alpha = 0.5$). To have a closer view to the experimental results, the sector iso-surface has been copied and rotated to cover the 360° of the total cone, considering the use of a periodic boundary condition.

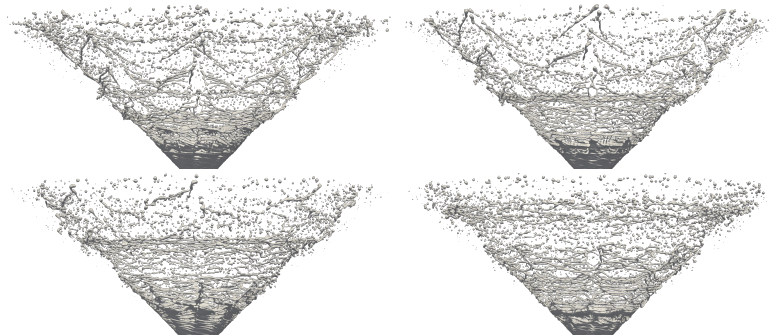


FIG. 18: Liquid volume fraction α contour ($\alpha = 0.5$) 360° render. From left to right, snapshots at: $t = 60\mu\text{s}$, $t = 65\mu\text{s}$, $t = 70\mu\text{s}$ and $t = 80\mu\text{s}$

A closer experimental view of the spray is compared to an instantaneous snapshot of the 3D rendering. Two comparisons with different experimental pictures can be observed in Figure 19. On the left, the liquid volume fraction iso-surface is compared with the experiments by Verdier et al. (2017). The arrangement of the ligaments is similar and it can be seen that the simulation yields drop sizes in the order of those from the experiments. On the right, numerical results are compared with more recent experimental pictures by Miglierina (2021) where a rearrangement of the experiment allow a better view of the injector exit. In this picture it can be seen that there are small fluctuations on the fuel sheet breaking it up near the nozzle orifice. This early break-up is captured by the numerical simulation. These comparison show that there is a need for more refined experimental data to characterise the early stage of the liquid sheet instability to go further on this comparisons, this would be the topic of further work. An additional feature of such injector that are commonly measured is the drop size distribution. However, most off the experimental techniques required a dispersed spray composed by spherical droplet (PDA, Diffraction, ...). Thus, such measurements are conducted downstream where such conditions are achieved.

Applying the post-processing technique based on the surface interface Σ and the mean curvature κ proposed by Palanti et al. (2022), the drop size distribution can be determined. A comparison between the drop size distribution extracted from the numerical modeling and those experimentally by PDA is shown on Figure 20.

The experimental distributions are taken at $Z = 13\text{mm}$ (first downstream location where experimental PDA data was reported to be reliable by Verdier et al. (2017)) and in two different radial positions: at the axis $R = 0\text{mm}$ and at an angle around 40° ($R = 10\text{mm}$). It can be seen

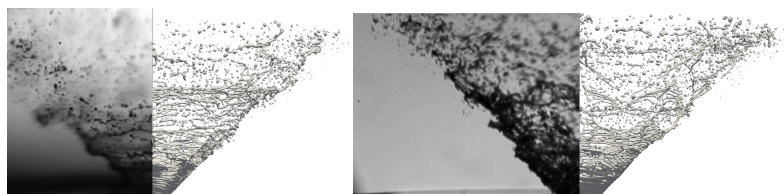


FIG. 19: Qualitative validation. Left: comparison with experiments by Verdier et al. (2017); right: comparison with experiments by Miglierina (2021).

that near the axis the distribution (Exp(Z13,R0)) is mostly formed by small droplets from $D = 1\mu m$ to $D = 20\mu m$. Meanwhile, the distribution taken at the spray cone angle (Exp(Z13,R10)) is wider and is formed by medium and big droplets on the range $D = [10, 67]\mu m$. This means that the smallest droplets tend to disperse into the hollow cone though the largest ones remain on the streamwise direction thanks to their inertia. The distribution obtained through the simulations is obtained much more upstream at of the early stage of the atomization process. To reconstruct the drop size distribution, first, the curvature distribution is measured per unite of liquid surface. Then the negative curvature (droplet curvature are positive in our definition) are filtered because they do not correspond to droplets and represent elements of surface that have not achieve yet the atomization process. Then diameter distribution is obtained from the definition of the curvature assuming both main principal curvature to be the same. This reconstruction finally required then one free parameter that is set by enforcing the Sauter mean diameter that is obtained as the ration of the liquid volume fraction to the liquid surface density. For more detail, please refer to Palanti et al. (2022). For the present analysis it is important to note that the numerical drop size distribution is determined at early stage of the atomization process ($Z=1.2mm$) though the PDA experiment are achieve further downstream ($Z=13mm$). However, the numerical drop size distribution shows that it falls between two the experimental distributions. This is reasonable since the degregation between the smallest droplets and the largest droplet though the convection and dispersion process have not been done yet. Thus all the droplet are still collected by the post-processing technique applied on the numerical simulation.

6. CONCLUSION AND PERSPECTIVES

A complete analysis of a swirl injector representative of gas turbine injection and of interest for combustion research has been conducted. A workflow to replicate the process with any commercial injector has been defined starting from the measurement of the internal geometry. Several measurement techniques such as computed tomography scan, optical microscope visualization and scanning electron microscope have been used to achieve an accurate description of the geometry. Both the actual metallic pieces and their silicon molds have been measured. The internal geometry has then been reconstructed and parametrized.

A two step coupling between numerical simulation has been proposed to separately study the internal flow of the injector and the external flow focused on the atomization process. A hybrid tetrahedral-hexahedral mesh is used on the internal flow simulation to avoid numerical instabilities due to the complexity of the geometry. From this simulation, main characteristics of the injection are recovered such as the spray cone angle and the fuel sheet thickness. The liquid volume fraction and velocity fields on the nozzle orifice have been stored to feed the external flow

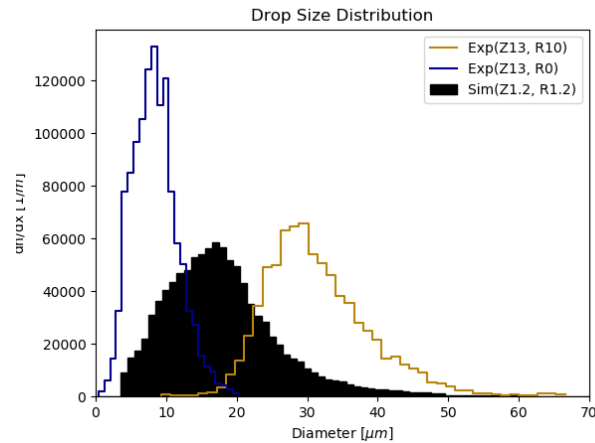


FIG. 20: Drop size distribution. Black Sim(Z1.2, R1.2): numerical results taken at $Z = 1.2\text{mm}$ and $R = 1.2\text{mm}$; blue line Exp(Z13, R0): experimental distribution placed at $Z = 13\text{mm}$ and $R = 0\text{mm}$; yellow line Exp(Z13, R10): experimental distribution placed at $Z = 13\text{mm}$ and $R = 10\text{mm}$.

simulation. In the latter, a full Cartesian mesh has been built to model the atomization process where a high resolution zone to properly capture liquid structures and break up process. The conservation of the swirl motion and the turbulence between simulations have been checked. By comparing liquid gas surface with a experimental image a good qualitative agreement between the simulation and experiments has been found.

Finally, the post-processing based on the surface and curvature analysis proposed by Palanti et al. (2022) was applied to the external flow simulation, allowing the drop size distribution to be reconstructed. Further investigations are needed both experimentally and numerically to achieve this final comparison, but the result obtained for the drop size distribution is compatible with reported experimental data.

The perspectives of this work are the combination of experimental and numerical studies to achieve synergies among them. Most of the experimental studies are focused on the spray disperse phase where the distribution and velocity of the droplets can be measured. However, the difficult access to certain zones, such as the internal part of the injector or even the first steps of the atomization process, can be resolved applying numerical simulations providing instantaneous data on the areas where the experiments can not reach. The symbiosis of both methodologies could lead into improvements on both methodologies.

ACKNOWLEDGMENTS

Authors from Université de Rouen Normandie thankfully acknowledge the computer resources at IDRID, TGCC and CINES under the allocation A0112B06153 and A0092B06153 made by GENCI (Grand Equipement National de Calcul Intensif) and also for the computing time at

CRIANN (Centre Régional Informatique et d'Applications Numériques de Normandie) under the scientific project No. 2006011. This work has been possible thanks to the CHAIRLIFT European project 831881 - CHAIRLIFT - H2020-CS2-CFP08-2018-01.

Authors from Universitat Politècnica de València thankfully acknowledge the computer resources at Altamira (RES-IM-2020-1-0018) and MareNostrum (RES-IM-2020-412-0009) in the frame of the Spanish Supercomputing Network. Additionally, the support given to Dr. Marcos Carreres by "Ministerio de Educación, Cultura y Deporte" through the "Estancias de movilidad en el extranjero José Castillejo para jóvenes doctores" grant (ref. CAS18/00289) within the "Programa Estatal de Promoción del Talento y su Empleabilidad en I+D+i, Subprograma Estatal de Movilidad, del Plan Estatal de I+D+I" is gratefully acknowledged.

We would also like to thank Said Idlahcen, José Enrique del Rey and Ignacio Sevilla for their assistance with the experimental measurements of the atomizer geometry.

REFERENCES

- Alajbegovic, A., Meister, G., Greif, D., and Basara, B., Three phase cavitating flows in high-pressure swirl injectors, *Experimental Thermal and Fluid Science*, vol. **26**, pp. 677–681, 2002.
- Amedorme, S.K. and Apodi, J., Computational study of two phase flow in pressure swirl atomizer using entirely Eulerian model, *AIP Conference Proceedings*, p. 020026, 2018.
URL <http://aip.scitation.org/doi/abs/10.1063/1.5055428>
- Amini, G., Liquid flow in a simplex swirl nozzle, *International Journal of Multiphase Flow*, vol. **79**, pp. 225–235, 2016.
- Chigier, N.A. and Beér, J.M., Velocity and static-pressure distributions in swirling air jets issuing from annular and divergent nozzles, *Journal of Basic Engineering*, vol. **86(4)**, pp. 788–796, 1964.
- Chinn, J.J., An appraisal of swirl atomizer inviscid flow analysis, Part 2: Inviscid spray cone angle analysis and comparison of inviscid methods with experimental results for discharge coefficient, air core radius, and spray cone angle, *Atomization and Sprays*, vol. **19**, no. 3, pp. 283–308, 2009.
- Dafsari, R.A., Lee, H.J., Han, J., Park, D.C., and Lee, J., Viscosity effect on the pressure swirl atomization of an alternative aviation fuel, *Fuel*, vol. **240**, pp. 179–191, 2019.
URL <https://doi.org/10.1016/j.fuel.2018.11.132>
- De Luca, M. and Vallet, A., Pesticide atomization modeling for hollow-cone nozzle, *Atomization and Sprays*, vol. **19**, no. 8, pp. 741–753, 2009.
- Ding, J.W., Li, G.X., Yu, Y.S., and Li, H.M., Numerical investigation on primary atomization mechanism of hollow cone swirling sprays, *International Journal of Rotating Machinery*, vol. **2016**, p. 11, 2016.
- Durdina, L., Jedelsky, J., and Jicha, M., Investigation and comparison of spray characteristics of pressure-swirl atomizers for a small-sized aircraft turbine engine, *International Journal of Heat and Mass Transfer*, vol. **78**, pp. 892–900, 2014.
URL <http://dx.doi.org/10.1016/j.ijheatmasstransfer.2014.07.066>
- European Commission, E., Communication from the Commission to the European Parliament, the Council, the European Economic and Social Committee and the Committee of the Regions: Sustainable and Smart Mobility Strategy - putting European transport on track for the future, Tech. rep., European Commission, Brussels, 2020.
- Fuster, D., Bagué, A., Boeck, T., Le Moyne, L., Leboissetier, A., Popinet, S., Ray, P., Scardovelli, R., and Zaleski, S., Simulation of primary atomization with an octree adaptive mesh refinement and VOF method, *International Journal of Multiphase Flow*, vol. **35**, no. 6, pp. 550–565, 2009.
URL <https://linkinghub.elsevier.com/retrieve/pii/S0301932209000305>

- Galbiati, C., Tonini, S., Weigand, B., and Cossali, G.E., Direct numerical simulation of primary break-up in swirling liquid jets, *9th International Conference on Multiphase Flow*, Firenze, Italy, 2016.
- Giffen, E. and Muraszew, A., *The Atomisation of Liquid Fuels*, Chapman Hall, 1953.
- Hansen, K., Madsen, J., Trinh, C., Ibsen, C., Solberg, T., and Hjertager, B., A computational and experimental study of the internal flow in a scaled pressure-swirl atomizer, *ILASS-Europe 2002*, Zaragoza, Spain, 2002.
- Jedelsky, J., Maly, M., Pinto del Corral, N., Wigley, G., Janackova, L., and Jicha, M., Air-liquid interactions in a pressure-swirl spray, *International Journal of Heat and Mass Transfer*, vol. **121**, pp. 788–804, 2018.
URL <https://doi.org/10.1016/j.ijheatmasstransfer.2018.01.003>
- Laurila, E., Koivisto, S., Kankkunen, A., Saari, K., Maakala, V., Järvinen, M., and Vuorinen, V., Computational and experimental investigation of a swirl nozzle for viscous fluids, *International Journal of Multiphase Flow*, vol. **128**, 2020.
- Laurila, E., Roenby, J., Maakala, V., Peltonen, P., Kahila, H., and Vuorinen, V., Analysis of viscous fluid flow in a pressure-swirl atomizer using large-eddy simulation, *International Journal of Multiphase Flow*, vol. **113**, pp. 371–388, 2019.
URL <https://doi.org/10.1016/j.ijmultiphaseflow.2018.10.008>
- Leask, S.B., Li, A.K., McDonell, V.G., and Samuelsen, S., Preliminary Development of a Measurement Reference Using a Research Simplex Atomizer, *Journal of Fluids Engineering, Transactions of the ASME*, vol. **141**, no. 12, pp. 1–11, 2019.
- Lefebvre, A.H. and Ballal, D.R., *Gas Turbine Combustion: Alternative Fuels and Emissions*, 3rd Edition, CRC Press, Boca Raton, FL, 2010.
- Lefebvre, A.H. and McDonell, V.G., *Atomization and Sprays*, 2nd Edition, CRC Press, Boca Raton, FL, 2017.
- Liu, C., Liu, F., Yang, J., Mu, Y., Hu, C., and Xu, G., Experimental investigations of spray generated by a pressure swirl atomizer, *Journal of the Energy Institute*, vol. **92**, no. 2, pp. 210–221, 2019.
URL <https://doi.org/10.1016/j.joei.2018.01.014>
- Macian, V., Bermúdez, V., Payri, R., and Gimeno, J., New technique for determination of internal geometry of a Diesel nozzle with the use of silicone methodology, *Experimental Techniques*, vol. **27**, no. 2, pp. 39–43, 2003.
URL <http://doi.wiley.com/10.1111/j.1747-1567.2003.tb00107.x>
- Madsen, J., Hjertager, B., and Solberg, T., Numerical simulation of internal flow in a large-scale pressure-swirl atomizer, *ILASS-Europe 2004*, Nottingham, UK, pp. 183–188, 2004.
URL <http://citeseerx.ist.psu.edu/viewdoc/download?doi=10.1.1.131.9942&rep=rep1&type=pdf>
- Maly, M., Jedelsky, J., Slama, J., Janackova, L., Sapik, M., Wigley, G., and Jicha, M., Internal flow and air core dynamics in Simplex and Spill-return pressure-swirl atomizers, *International Journal of Heat and Mass Transfer*, vol. **123**, pp. 805–814, 2018.
URL <https://doi.org/10.1016/j.ijheatmasstransfer.2018.02.090>
- Maly, M., Sapik, M., Cejpek, O., Wigley, G., Katolicky, J., and Jedelsky, J., Effect of spill orifice geometry on spray and control characteristics of spill-return pressure-swirl atomizers, *Experimental Thermal and Fluid Science*, vol. **106**, no. April, pp. 159–170, 2019.
URL <https://doi.org/10.1016/j.expthermflusci.2019.04.014>
- Miglierina, L., 2021. Liquid injection for gas turbine. Master's thesis, Université de Rouen Normandie, France.
- Mongia, H., TAPS: A Fourth Generation Propulsion Combustor Technology for Low Emissions, *AIAA International Air and Space Symposium and Exposition: The Next 100 Years*, no. July, American Institute of Aeronautics and Astronautics, Reston, Virginia, pp. 1–11, 2003.

- URL <https://arc.aiaa.org/doi/10.2514/6.2003-2657>
- Mulla, I.A., Godard, G., Cabot, G., Grisch, F., and Renou, B., Quantitative imaging of nitric oxide concentration in a turbulent n-heptane spray flame, *Combustion and Flame*, vol. **203**, pp. 217–229, 2019a.
URL <https://doi.org/10.1016/j.combustflame.2019.02.005>
- Mulla, I.A., Godard, G., and Renou, B., Instantaneous planar measurements of nitric oxide concentration in a turbulent n-heptane spray flame, *Combustion and Flame*, vol. **208**, pp. 451–471, 2019b.
- Mulla, I.A. and Renou, B., Simultaneous imaging of soot volume fraction, PAH, and OH in a turbulent n-heptane spray flame, *Combustion and Flame*, vol. **209**, pp. 452–466, 2019.
URL <https://doi.org/10.1016/j.combustflame.2019.08.012>
- Nicoud, F. and Ducros, F., Subgrid-Scale Stress Modelling Based on the Square of the Velocity Gradient Tensor, *Flow, Turbulence and Combustion*, vol. **62**, no. 3, pp. 183–200, 1999.
URL <https://doi.org/10.1023/A:1009995426001>
- Palanti, L., Puggelli, S., Langone, L., Andreini, A., Reveillon, J., Duret, B., and Demoulin, F.X., An attempt to predict spray characteristics at early stage of the atomization process by using surface density and curvature distribution, *International Journal of Multiphase Flow*, vol. **147**, p. 103879, 2022.
- Park, B.S., Kim, H.Y., and Yoon, S.S., Transitional instability of a pressure-swirl atomizer due to air-core eruption at low temperature, *Atomization and Sprays*, vol. **17**, no. 6, pp. 551–568, 2007.
- Park, K.S. and Heister, S.D., Nonlinear modeling of drop size distributions produced by pressure-swirl atomizers, *International Journal of Multiphase Flow*, vol. **36**, no. 1, pp. 1–12, 2010.
URL <http://dx.doi.org/10.1016/j.ijmultiphaseflow.2009.09.004>
- Razeghi, A. and Ertuğ, Ö., Numerical investigation of multiphase flow inside a pressure swirl atomizer at the initial stage of injection, *Atomization and Sprays*, vol. **28**, no. 5, pp. 417–441, 2018.
- Rusche, H., Computational fluid dynamics of dispersed two-phase flows at high phase fractions, 2002.
- Salvador, F.J., Gimeno, J., De la Morena, J., and Carreres, M., Comparison of Different Techniques for Characterizing the Diesel Injector Internal Dimensions, *Experimental Techniques*, vol. **42**, no. 5, pp. 467–472, 2018.
URL <http://link.springer.com/10.1007/s40799-018-0246-1>
- Scardovelli, R. and Zaleski, S., Direct numerical simulation of free-surface and interfacial flow, *Annual Review of Fluid Mechanics*, vol. **31**, pp. 567–603, 1999.
- Shao, C., Luo, K., Yang, Y., and Fan, J., Detailed numerical simulation of swirling primary atomization using a mass conservative level set method, *International Journal of Multiphase Flow*, vol. **89**, pp. 57–68, 2017.
- Sheen, H.J., Chen, W.J., Jeng, S.Y., and Huang, T.L., Correlation of swirl number for a radial-type swirl generator, *Experimental Thermal and Fluid Science*, vol. **12(4)**, pp. 444–451, 1996.
- Shum-Kivan, F., Marrero Santiago, J., Verdier, A., Riber, E., Renou, B., Cabot, G., and Cuenot, B., Experimental and numerical analysis of a turbulent spray flame structure, *Proceedings of the Combustion Institute*, vol. **36**, no. 2, pp. 2567–2575, 2017.
URL <http://dx.doi.org/10.1016/j.proci.2016.06.039>
- Som, S.K., Air core in pressure swirl atomizing nozzles, *Atomization and Sprays*, vol. **22**, no. 4, pp. 283–303, 2012.
- Sumer, B., Erkan, N., Uzol, O., and Tuncer, I.H., Experimental and Numerical Investigation of a Pressure Swirl Atomizer, *ICLASS 2012, 12th Triennial International Conference on Liquid Atomization and Spray Systems*, Heidelberg, Germany, 2012.
- The OpenFoam Foundation, OpenFOAM 6, , 2018.
URL <https://openfoam.org/version/6/>

Modelling internal flow and primary atomization in a simplex pressure-swirl atomizer 27

Verdier, A., Marrero Santiago, J., Vandel, A., Saengkaew, S., Cabot, G., Grehan, G., and Renou, B., Experimental study of local flame structures and fuel droplet properties of a spray jet flame, *Proceedings of the Combustion Institute*, vol. **36**, no. 2, pp. 2595–2602, 2017.

Wardle, K.E. and Weller, H.G., Hybrid multiphase cfd solver for coupled dispersed/segreated flows in liquid-liquid extraction, *International Journal of Chemical Engineering*, vol. **2013**, p. 11, 2013.

Volume x, Issue x, 2022

Internal Numerical Simulation of a Swirl Simplex Atomizer to Predict Atomization Outputs

D. Ferrando^{*1}, M. Belmar-Gil², L. Palanti³, M. Carreres², D. Cervelló-Sanz², F.X. Demoulin¹, B. Renou¹, B. Duret¹, J. Reveillon¹

¹CNRS CORIA UMR 6614, University of Rouen Normandie, France

²CMT-Motores Térmicos, Universitat Politècnica de València, Spain

³Department of Industrial Engineering (DIEF), University of Florence, Italy

*Corresponding author email: diego.ferrando@coria.fr

Abstract

Numerical simulation of injectors could help improving their designs. In particular, a two-phase flow simulation of a swirl simplex atomizer allows computing the main characteristic parameters such as the spray cone angle, the fuel sheet thickness and the air core diameter. This work describes an attempt to go a step further to characterize atomization and spray characteristics with the ultimate goal to predict the spray distribution in terms of size and velocity.

A commercial injector has been used in the CORIA Rouen Spray Burner (CRSB) set up to study turbulent spray combustion. This experiment has produced a well-documented database for the last two TCS workshops (see TCS 6 and 7 at <http://www.tcs-workshop.org/>). Even though spray measurements are used to define the fuel injection in combustion numerical simulations, the spray injection characteristics remain the main cause of uncertainties. The present work aims at answering this question: Is it possible to complete our knowledge of spray injection by numerical simulation of the full atomization process?

The first challenge is to measure the inner geometry. Standards techniques such as X-ray tomography and microscopy have been applied. In order to accurately reproduce the internal throat and swirl chamber, additional measurements have been performed by silicon molding, leading to the definition of a nominal geometry that can be used for further CFD simulation. The second challenge is to produce a mesh regular enough to be compatible with the interface capturing method. Several mesh strategies have been tested starting from the swirl chamber with very thin mesh layers to capture the liquid film at the injector wall and to describe the external liquid sheet. Then, a third challenge concerns the numerical simulation itself, since it must handle the multi-scale nature of such flows until the formation of the spray. A non-reactive condition has been tested with the interFoam solver (OpenFOAM library) in a Large Eddy Simulation (LES) framework.

Eventually, the last challenge is to build an analysis to connect the numerical simulation that is limited to the close vicinity of the injector and the experimental measurements that are rejected farther downstream on the dispersed spray. This last step is based on the analysis of the surface curvature distribution that is described with more detail on another presentation at this ICLASS conference.

Keywords

swirl-simplex-atomizer, two-phase flow, numerical simulation, atomization

Introduction

In pressure-swirl (simplex) atomizers, fuel is fed to an internal chamber through several tangential ports. The chamber outlet constitutes the atomizer orifice. Hence, the swirling motion in the chamber generates an air core so that the fuel is atomized to the exterior as a hollow cone. The swirling motion allows the liquid sheet to spread out achieving wider cone angles than those obtained with plain-orifice atomizers [1]. The applications of these atomizers are

ICLASS 2021, 15th Triennial International Conference on Liquid Atomization and Spray Systems, Edinburgh, UK, 29 Aug. - 2 Sept. 2021

diverse, including agricultural spraying processes, paint spraying, spray drying of wet solids, food processing and several combustion applications [2, 3].

Focusing on combustion applications, these include internal combustion engines, gas turbine engines and others [4], where the spray characteristics are of key relevance to the engine performance, fuel consumption and generation of emissions. While fossil fuels are being progressively replaced in land transportation, aircraft engines will still rely on their combustion for some decades. Last-generation lean-burn engines such as the GE-TAPS start making use of airblast atomizers together with simplex atomizers, the latter generating the pilot flame for engine startup and low-power operations [5].

Due to its importance in the industry, research studies on the atomization features of this kind of atomizer are varied. Experiments include high-speed imaging and the application of optical techniques such as Phase Doppler Anemometry (PDA) [6, 7], Laser Doppler Anemometry (LDA) [8] or Mie-scattering [9]. These works reveal that the primary breakup takes place by the growth of disturbances on the liquid sheet that are generated by the external surrounding air as soon as the fuel leaves the atomizer. Nevertheless, quantitative studies are limited to the secondary atomization regime, as observation of ligament and droplet formation in the near-nozzle region is precluded by limitations of the optical techniques and experimental arrangements. These limitations can be overcome through computational techniques.

Many numerical studies are based on the transport equation of the liquid volume fraction method to treat the two-phase flow in a Eulerian framework. These approaches are often referred as Volume of Fluid (VOF) methods even if this appellation hides a wide range of treatment of the liquid volume flux. Turbulence modelling approaches include laminar assumption [10, 11], RANS [12] and LES [13, 14]. The computational domain generally includes the internal and the external flow, but none of these works seems to reproduce the instabilities in the liquid sheet experimentally reported to produce breakup, thus predicting different atomization mechanisms. Except for Laurila et al. [14], whose atomizer configuration differs from those of combustion applications, only works making use of costly DNS through VOF [15, 16] or Level Set [17] are able to capture the film instabilities triggering atomization.

The main objective of the present work is then to present a methodology that allows studying the primary atomization in pressure-swirl (simplex) atomizers. Three main stages are here reported to this end: on the measurement of the geometry, on the production of the mesh and on the development of a numerical strategy to handle the multi-scale nature of the problem.

The particular atomizer under study belongs to the CORIA Rouen Spray Burner (CRSB) setup that has been used to create a well-documented database of relevance for gas turbine applications and used for the two last TCS (Turbulent Combustion of Sprays) workshops [18]. Thus, some of the features of the generated spray have been experimentally investigated in the secondary breakup region [19, 20]. The present investigation will then help filling the gap between this region and the atomizer outlet, thus allowing to generate realistic boundary conditions for standard Eulerian-Lagrangian simulations of the full burner geometry in a wide range of operating conditions.

Experimental characterization of the geometry

The simplex atomizer used in the CRSB burner is a Danfoss commercial nozzle. Its three main pieces shape the three fuel inlet tangential ports, the swirl chamber and the orifice duct, as shown in Figure 1(b). The geometrical details of the interior of the atomizer have been experimentally obtained via silicone molding of the outer piece, labelled as (1) in Figure 1(b). This technique was first applied to determine the internal geometry of Diesel nozzles by Macian et al. [21]. Metrology on the obtained molds and atomizer pieces is performed through a combination of three visualization techniques (see Figure 1), namely optical microscope visualization, Scanning Electron Microscope (SEM) visualization and Computed Tomography (CT) scan. Please note that a gold coating (in the order of nm) must be applied to the molds before visual-

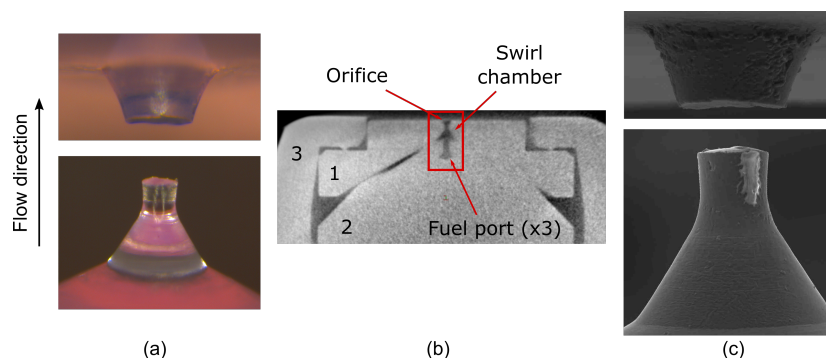


Figure 1. Sample pictures of the CRSB atomizer: (a) optical microscope visualization of the silicone molds, (b) CT scan of the atomizer assembly, (c) SEM visualization of the silicone molds.

izing them in the SEM so that they become conductor. The accuracy of the methodology has been reported to be around 2% in the determination of diesel injector nozzle outlet diameters [22].

As a result from the experimental metrology, the internal geometry of the atomizer is reconstructed as sketched in Figure 2. The main dimensions obtained are summarized in Table 1.

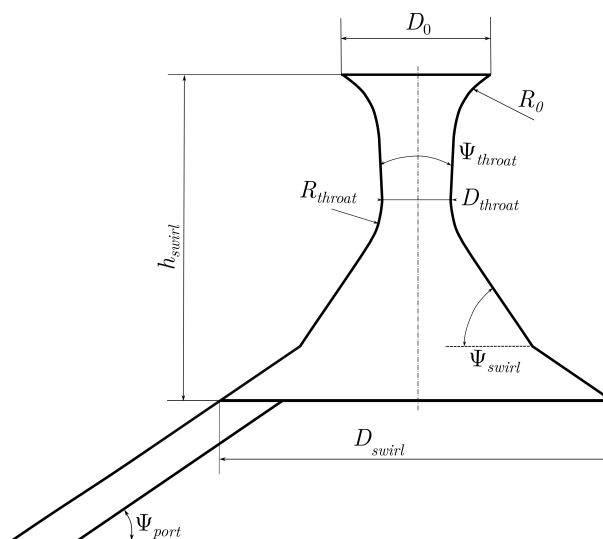


Figure 2. Sketch of the CRSB atomizer reconstructed internal geometry.

Numerical methodology

The numerical simulation is based on the well known OpenFoam library that already contains many features needed for liquid-gas flows simulation on complex geometries, with a built-in parallel computing ability to handle intensive simulation. Two important flow characteristics have to be considered: turbulence and the liquid-gas interface. Regarding turbulence, a LES approach has been used with the Smagorinsky model [23] and the WALE model [24]. The interface is implicitly captured through the liquid volume fraction (α) equation. Thus, the interface is localized at the transition between the gas ($\alpha = 0$) and the liquid ($\alpha = 1$). To keep an

Table 1. Summary of the CRSB atomizer internal dimensions.

	D_0	D_{throat}	D_{swirl}	h_{swirl}	R_0	R_t
Value [μm]	340	165	780	620	310	190
	Ψ_{throat}		Ψ_{swirl}		Ψ_{port}	
Value [$^\circ$]	6		60		30	

accurate description of the interface the transition should remain sharp with a size of the order of few Δx . On regular VOF approaches the interface position is reconstructed [26][27] and the liquid volume flux are based on the geometrical advection of this surface. This geometrical approach brings difficulties for the general polygons used in OpenFoam as numerical cells used to handle complex geometries. Thus, liquid advection is based on standard numerical schemes bringing numerical diffusion that potentially enlarges the transition zone. To counter this effect a sharpening term is introduced [28][29].

The numerical simulation has to deal with a wide length scale range. Hence, the mesh resolution needs to be fine enough at particular locations to accurately capture the smallest length scales. Starting in the internal zone of the injector, the mesh resolution has been refined in the normal direction to the wall in order to compute the boundary layer. The liquid film thickness inside the nozzle also needs to be accurately meshed. On the other hand, downstream of the nozzle, the liquid sheet is developed, becoming thinner and thinner, requiring additional mesh resolution. Finally, once the liquid sheet breaks up, the droplets are atomized. The mesh resolution has to be fine enough to capture the smallest droplets. As a conclusion, the computational meshing process is not straightforward and, thus, a workflow to handle the simulation has been proposed. The workflow of the simulations is shown in Figure 3.

First, the inner flow has to be modelled. A full 3D simulation of the atomizer internal flow (swirl chamber and the three fuel ports) and 2 mm of the external region is carried out to this end. Data on the velocity coordinates and the liquid volume fraction are sampled at an orifice cross-section slightly upstream of the atomizer outlet. As the second step, these data are then fed to a more refined sector simulation (25°) of the external domain where the spray is captured. These simulations have been run in a preliminary manner with the ultimate goal to perform a single full domain simulation which could handle the multi-scale nature of the simplex atomizer. The operating condition tested has been chosen from the guidelines of TCS7 [18], from where some experimental data and reference images taken in the CRSB are available. The main parameters used to define the boundary conditions of the simulations are shown in Table 2.

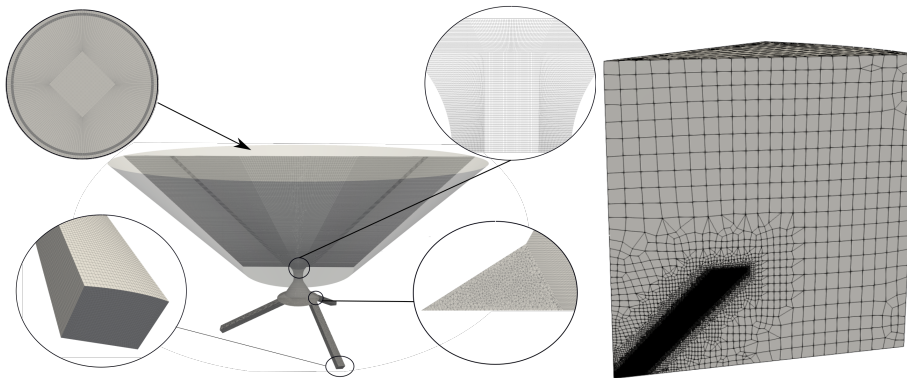
**Figure 3.** Simulation workflow: internal flow simulation (left) and external flow simulation (right).

Table 2. Summary of the operating condition tested.

	Fuel	\dot{m}_f [g/s]	T	p [MPa]
Value	n-Heptane	0.28	298	0.1

Internal flow simulation

As depicted in Figure 3, the mesh for the internal flow simulation is hybrid: a structured mesh is adopted at the fuel ports and for most of the atomizer interior. A transition region between the fuel ports and the structured region of the swirl chamber is filled with polyhedra to overcome the limitations posed by the asymmetry of the channels. Special refinement is adopted near the walls, both to keep the y^+ below 5 at the walls anywhere in the domain (no wall functions are then used) and to represent the liquid film inside the atomizer with at least 10 cells in the radial direction. A mesh sensitivity study (not shown for the sake of brevity) has been carried out considering the purpose of this simulation is to feed the sector simulation. A compromise between accuracy and cost provided a mesh with a total of 13 M cells.

The WALE (Wall-Adapting Local Eddy-viscosity) sub-grid scale model introduced by Nicoud and Ducros [24] has been used as it theoretically replicates the proper near-wall scaling for the subgrid scale eddy-viscosity at the wall. Please note that the situation is even more complex since it concerns a two-phase flow boundary layer for which no model has been proposed up to now. As boundary conditions, the fuel mass flow rate from Table 2 prescribes the velocity at the three inlet ports. Atmospheric pressure is set at the outlet. A no-slip condition has been used at the physical walls, whereas a zero gradient condition is used at the outer external boundaries. Concerning the numerical setup, a PIMPLE algorithm is employed. 2nd order accurate schemes are chosen both in space and time. Variable time-stepping is used, the maximum CFL number being limited to 0.4. This results in time steps in the order of 2.5×10^{-9} s. The simulation is run for a physical time of 0.4 ms, with a cost of 32,000 CPU·h. Data for the external flow simulation were sampled every 5×10^{-8} s for 0.1 ms.

The main flow features obtained at the atomizer mid-plane are shown in Figure 4. From the liquid volume fraction representation, a spray angle of 82° is recovered in good agreement with the manufacturer's nominal opening angle (80°). A liquid film thickness of $15 \mu\text{m}$ is obtained at the outlet, in agreement with Lefebvre's correlation [1]. However, the diffuse behavior of the interface at the external part highlights the need for additional refinement. Despite the air core fluctuating motion at the bottom of the chamber, the instantaneous and averaged fields downstream of the throat resemble each other. The important radial velocities lead to a computed swirl number $S_w \approx 1.5$ at the chamber inlet plane, $S_w \approx 2.5$ in the chamber and $S_w \approx 0.5$ at the orifice outlet. The axial velocity contour shows a shear layer around the liquid-gas interface, with an important acceleration of the liquid film from the throat to the outlet and an accused air entrainment at the orifice axis.

External flow: sector simulation

The instability of the liquid sheet is what triggers the primary break-up, thus, it must be captured in the numerical simulation. This physical phenomena happens due to the combination of the streamwise shear and the centrifugal instability due to the azimuthal motion within the liquid sheet [25]. Capturing the liquid sheet instabilities requires a well refined computational mesh and an extended domain in axial and radial directions as reported in [14] [16].

In order to define the domain length and the mesh resolution, several 2D asymmetric simulations have been carried out. The aim of this work is to be able to catch these instabilities and the atomization process in a sector 3D simulation and later on in a single simulation of the complete injector.

Three different mesh resolutions have been used to study the mesh sensitivity. The most refined cell sizes located around the liquid sheet are $2 \mu\text{m}$, $1 \mu\text{m}$ and $0.5 \mu\text{m}$. The domain begins

ICLASS 2021, 15th Triennial International Conference on Liquid Atomization and Spray Systems, Edinburgh, UK, 29 Aug. - 2 Sept. 2021

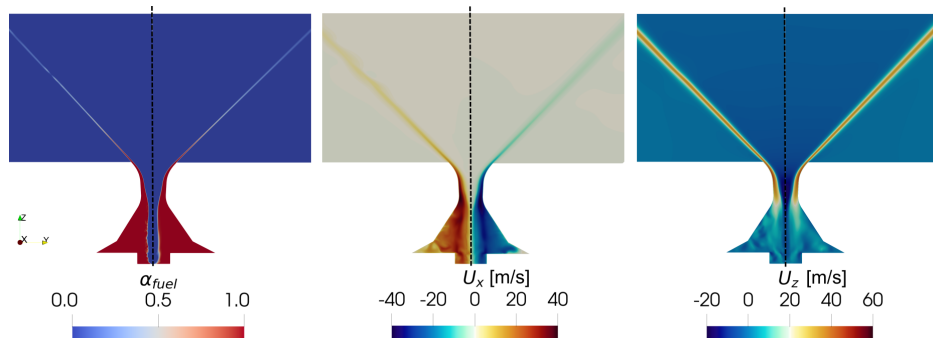


Figure 4. Mid-plane contours of liquid volume fraction (left), radial velocity (center) and axial velocity (right). In each case the left-hand side represents instantaneous data and the right-hand side shows averaged data.

at the throat of the atomizer (where the sampling surface has been recorded) and is extended up to 15 times the nozzle diameter in both axial and radial directions.

As it has been reported for the internal flow simulation, the WALE sub-grid scale model has been retained. As boundary conditions, Dirichlet time-varying boundary conditions have been used both for the velocity and the liquid volume fraction. This boundary condition has been mapped from the sampling of the internal simulation. Atmospheric pressure is set at the outlet and no-slip boundary condition has been set at the wall.

The liquid sheet destabilisation is captured only for mesh resolution with less than $1\ \mu\text{m}$. On the other hand, with a cell size of $2\ \mu\text{m}$ the liquid sheet remains straight up to a point where the break-up occurs by lack of resolution (Figure 5).

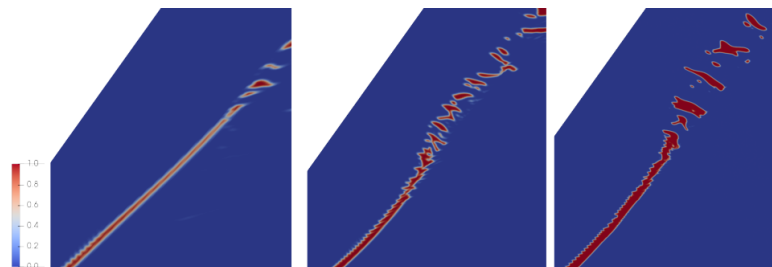


Figure 5. Liquid sheet instabilities on different 2D asymmetric resolution meshes: $2\ \mu\text{m}$ (left), $1\ \mu\text{m}$ (center), $0.5\ \mu\text{m}$ (right)

Further work is going on following the same methodology but with a sector domain using a periodic boundary condition. As Figure 6 shows (the sector simulation has been replicated and rotated to fulfill 360°), the liquid sheet seems more stable than in the 2D test cases despite the fine mesh resolution that has been preserved. However, the liquid-gas interface defined as the iso-contour of the liquid volume fraction ($\alpha = 0.5$) looks qualitatively in agreement with the experimental pictures. The angle of the spray is correctly reproduced and the size of the liquid droplet seems of the same order of magnitude. However, the liquid sheet instability on the experimental side seems to produce a more wavy behaviour than in the simulation. We are presently using the sector simulation extensively in order to understand what could trigger this wavy behaviour on the liquid sheet. It is also possible that the interpolation induced by the connection between the internal and external sector simulations damped the transmission of the internal fluctuations. This preparatory simulation has set the characteristics of the full single simulation (around 200 M elements and 500,000 CPU-h) that will be tested and presented at the

ICLASS meeting.



Figure 6. Comparison among experiments and sector simulation

Conclusions

In this paper, we have presented a methodology to model a commercial simplex-injector. The measurements of the internal geometry of the injector have been obtained by metrology techniques such as optical microscope visualization, SEM visualization and CT scan. From this internal geometry, several computational meshes have been designed to fulfill the mesh refinement requirement necessary to handle the small scale features of this atomization process. A hybrid mesh has been used to handle the non-asymmetric internal geometry prescribed by the fuel inlet ports. In order to optimize the computational cost, a methodology has been proposed to be able to capture the liquid sheet and the droplets with an interface capturing method based on the OpenFoam library. The process has been divided in an internal simulation where the air core is developed reaching the bottom wall of the injector. The angle of the spray is well captured and in a good agreement with the experimental measurements. The second part of this methodology is to simulate the primary break-up itself, which takes place outside of the injector. Several 2D asymmetric simulations have been carried out to determine the minimal mesh resolution required to catch the liquid sheet instabilities. A first work based on the 3D sector simulation has been performed leading to a good agreement with experimental pictures, but missing the wavy behaviour of the instabilities occurring on the liquid sheet. Additional works are ongoing to simulate the full injector flow in one single simulation and to capture the full interaction between the internal flow and the external atomization process.

Acknowledgements

This work was granted access to the HPC resources of IDRID, TGCC and CINES under the allocation A0072B06153 and A0092B06153 made by GENCI (Grand Equipement National de Calcul Intensit) and also for the computing time at CRIANN (Centre Régional Informatique et d'Applications Numériques de Normandie) under the scientific project No. 2006011. Dr. Carreres received a "José Castillejo" aid (ref. CAS18/00289) from "Ministerio de Educación, Cultura y Deporte" in the frame of "Programa Estatal de Promoción del Talento y su Empleabilidad en I+D+i, Subprograma Estatal de Movilidad, del Plan Estatal de I+D+i". Support given to Mr. Mario Belmar by Universitat Politècnica de València through the "FPI-Subprograma 2" grant within the "Programa de Apoyo para la Investigación y Desarrollo (PAID-01-18)" is also gratefully acknowledged. Additionally, the authors would like to thank José Enrique del Rey and Ignacio Sevilla for their technical help with the silicone molding and image processing.

Nomenclature

D	Diameter [μm]	R	Rounding radius [μm]
h	Internal chamber height [μm]	S_w	Swirl number [-]

ICLASS 2021, 15th Triennial International Conference on Liquid Atomization and Spray Systems, Edinburgh, UK, 29 Aug. - 2 Sept. 2021

\dot{m}_f Fuel mass flow rate [g s⁻¹] T Temperature [K]
 p Pressure [MPa]

References

- [1] Lefebvre, A. H., McDonell, V. G., 2017, "Atomization and Sprays". CRC Press.
- [2] Park, K. S., and Heister, S. D., 2010, *International Journal of Multiphase Flow*, 36, pp. 1-12.
- [3] Amedorme, S. K., and Apodi, J. A., 2018, *AIP Conference Proceedings*, pp. 020026.
- [4] Rezaei, S., Vashahi, F., Ryu, G., Lee, J., 2019, *Fuel*, 258, pp. 116094.
- [5] Mongia, H. C., Jul. 14-17. 2003, AIAA/ICAS International Air and Space Symposium and Exposition.
- [6] Leask, S. B., Li, A. K., McDonell, V. G., and Samuelsen, G. S., 2019, *Journal of Fluids Engineering*, 141, pp. 121407.
- [7] Dafsari, R. A., Lee, H. J., Han, J., et al., 2019, *Fuel*, 240, pp. 179-191.
- [8] Maly, M., Sapik, M., Jedelsky, J., et al., 2018, *EPJ Web of Conferences*, 180, pp. 02059.
- [9] Liu, C., Liu, F., Yang, J., et al., 2019, *Journal of the Energy Institute*, 92, pp. 210-221.
- [10] Sumer, B., Erkan, N., Uzol, O., Tuncer, I. H., Sept. 2-6. 2012, ICLASS 2012, 12th Triennial International Conference on Liquid Atomization and Spray Systems.
- [11] Amini, G., 2016, *International Journal of Multiphase Flow*, 79, pp. 225-235.
- [12] Alajbegovic, A., Meister, G., Greif, D., Basara, B., 2002, *Experimental Thermal and Fluid Science*, 26, pp. 677-681.
- [13] Madsen, J., Hjertager, B. H., Solberg, T., Sept. 6-8. 2004, ILASS-Europe 2004.
- [14] Laurila, E., Roenby, J., Maakala, V., et al., 2019, *International Journal of Multiphase Flow*, 113, pp. 371-378.
- [15] Fuster, D., Bague, A., Boeck, T., et al., 2009, *International Journal of Multiphase Flow*, 35, pp. 550-565.
- [16] Galbiati, C., Tonini, S., Weigand, B., Cossa, G. E., May 22-27. 2016, ICMF-2016 9th International Conference on Multiphase Flow.
- [17] Shao, C., Luo, K., Yang, Y., Fan, J., 2017, *International Journal of Multiphase Flow*, 89, pp. 57-68.
- [18] Workshop on Turbulent Combustion of Sprays (TCS), <http://www.tcs-workshop.org/>.
- [19] Shum-Kivan, F., Marrero, J., Verdier, A., et al., 2017, *Proceedings of the Combustion Institute*, 36, pp. 2567-2575.
- [20] Verdier, A., Marrero, J., Vandel, A., et al., 2017, *Proceedings of the Combustion Institute*, 36, pp. 2595-2602.
- [21] Macian, V., Bermúdez, V., Payri, R., Gimeno, J., 2003, *Experimental Techniques*, 27(2), pp. 39-43.
- [22] Salvador, F. J., Gimeno, J., De la Morena, J., Carreres, M., 2018, *Experimental Techniques*, 42(5), pp. 467-472.
- [23] Smagorinsky, J., 1963, *Monthly Weather Review*, 91(3), pp. 99-164.
- [24] Nicoud, F., and Ducros, F., 1999, *Flow, Turbulence and Combustion*, 62(3), pp. 183-200.
- [25] Billiant, P., Chomaz, J. M., Huerre, P., 1998, *Journal of Fluid Mechanics*, 376, pp. 183-219.
- [26] Scardovelli, R. and Zaleski, S., 1999, *Annual review of fluid mechanics*, 31(1), pp. 567-603.
- [27] Li, J., 1995, *Comptes rendus de l'Académie des sciences. Série II, Mécanique, physique, chimie, astronomie*, 320(8), pp. 391-396;
- [28] Rusche, H., 2002-2012.
- [29] Wardle, K.E., Weller, H.G., 2013, *International Journal of Chemical Engineering*, 2013.

Spray Drop Size Distribution and Velocity Distribution issued from a Prefilming Airblast Atomizer

Diego Ferrando*¹, Lorenzo Palanti², François-Xavier Demoulin¹, Benjamin Duret¹, Julien Reveillon¹

¹CNRS CORIA UMR 6614, University of Rouen Normandie, France

²Department of Industrial Engineering (DIEF), University of Florence, Italy

*Corresponding author email: diego.ferrando@coria.fr

Abstract

This work explores the possibility to determine the spray characteristics at early stage of the atomization process. This approach has been firstly proposed in [7] propose to characterize the liquid-gas surface in term of surface curvature distribution allowing the determination of which part of the surface is already representative of the final spray. This innovative approach is based on numerical simulation but could be extended in principle on experimental imagery techniques for instance. In this work, the methodology is extended to include surface velocity measurements to provide the joint distribution of the spray in term of diameter and velocity. The configuration is representative of an aeronautic injector used in the European project CHAIR-LIFT and focus on the prefilming airblast atomization. Such an atomization process involves a wide range of length scales. The diameter of the aeronautic atomizer could be three orders of magnitude higher than the diameter of the smallest droplet. Therefore, performing a CFD simulation is neither a straightforward nor a cheap process computationally speaking. Thus, a workflow, which divides the atomizer in less complex processes, is presented in this work to make the simulation affordable in an industrial perspective. The objective is to compute the properties that determine the spray behavior for the following combustion process. The OpenFOAM library is used to perform the simulation. In addition to the numerical strategy to capture first steps of the atomization process the focus of our presentation will be on the post processing of the simulation to extract the main features of the spray. The results presented concern the drop size distribution of the spray and the joint velocity distributions of the droplets. The post processing methodology is based on an analysis of the surface density joint distribution for curvatures and velocity. We believe this methodology can be used to enrich the spray injection models for further reactive spray flame simulations.

Keywords

Airblast Atomization, Spray, Volume of Fluid, Drop Size Distribution, Curvature.

Introduction

Prefilming airblast nozzles are suited for atomizing liquid fuels in continuous-flow combustion systems, such as gas turbines, where high velocity air flows are available. In this kind of atomizers, the fuel is first spread out in a thin liquid sheet and then subject to the atomization provoked by the shear stress at the liquid gas surface due to the high-velocity air flows [1]. Prefilming airblast atomizers are widely used in the aeronautic field since they allow an excellent atomization of the liquid fuel. Unlike other kind of atomizers, prefilming airblast atomizers creates smaller droplets which evaporates faster than large droplets. Thus, they preserve well balanced fuel vapor - air mixing before reaching the flame front, allowing for a better controlled combustion[2].

The goal of this work is to perform a numerical simulation of the prefilming airblast atomizer able to characterize the spray. Then, these characteristics are used as spray injection data for large scale turbulent combustion simulation. This approach is an attempt to complete the

ICLASS 2021, 15th Triennial International Conference on Liquid Atomization and Spray Systems, Edinburgh, UK, 29 Aug. - 2 Sept. 2021

experimental measurement of the spray that is usually done to get this kind of information : Spray size distribution and spray angles. Numerically, the ultimate goal is to compute the Drop Size Distribution (DSD) and the droplet velocity joint distribution. The challenge is to connect the experimental spray data generally obtained far away downstream of the injector with the numerical characterisation of the spray that is limited to the close vicinity of the injector due to the cost of such simulation. The main concept is to analyse the spray formation at an early stage of the atomization by characterizing the spray surface and to determine which part of this surface carry relevant spray information [7].

The present work is part of the CHAIRLIFT European project 831881 - CHAIRLIFT - H2020-CS2-CFP08-2018-01 which study compact helical arranged combustors with lifted flames which is suited for small aeronautical gas turbines. The Figure 1 shown the CHAIRLIFT atomizer which is the same studied in [3].

The whole injection system is fed by a simplex atomizer which creates a spray with a hollow cone shape. Most of the droplets reach the wall of the prefilmer where a thin fuel film is developed. In this atomizer, the inner air flow has a swirl component meanwhile the outer air flow has no swirl. The fuel film is carried by the air flow and is atomized to produce small droplets.

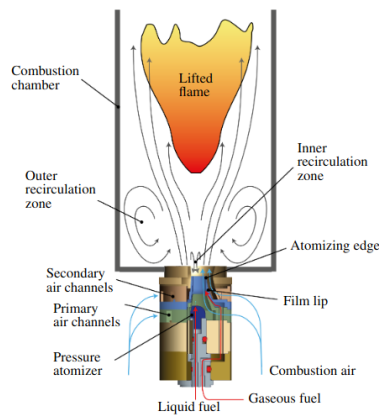


Figure 1. Schematic view of the CHAIRLIFT combustor [3]

Carrying out a single simulation to model the full airblast atomizer is still very time consuming and expensive computationally speaking. Due to the wide range of scale involved it cannot be achieved yet despite the CPU resources to our disposal . Indeed, the smallest droplet diameter could be three or four orders of magnitude smaller than the airblast nozzle diameter. Since the size of the computational cell have to be smaller than the smallest droplet to capture accurately the surface interface between the liquid and the air [11], performing a full domain simulation requires a large computational mesh [10]. Therefore, a modelling workflow has been defined to handle every part of the prefilming airblast atomizer separately. Then the last simulation concerning the liquid film atomization is analysed in details to provide spray characteristics. Nowadays, numerical post-processing techniques to determine the droplet characteristics are based on interface capturing techniques then the droplets are identified and characterized one by one [4][5][6]. These approaches are able to compute the droplet and velocity distribution accurately, but they demand an important computational resources; they require to simulate the spray formation until the end of the atomization process. On the other hand, the post-processing technique proposed in [7] use only surface based information to compute the drop size distribution at early stage of the atomization process. In the present work, this approach is developed a step further to compute simultaneously the joint distribution of diameter and velocity of the spray.

Prefilming airblast modelling workflow

The workflow proposed is shown in the Figure 2. The point 1 is the modelling of the pressure swirl atomizer. The spray angle is obtained from this simulation. The liquid film thickness is unknown, therefore it has to be estimated (point 2). Hence, a 2D simulation is carried out for this purpose and the length of this computational domain is calculated with the spray angle computed in the previous step.

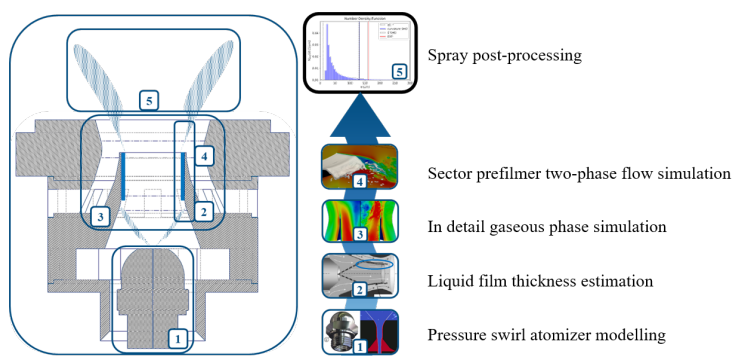


Figure 2. Prefilmer airblast atomizer modelling workflow

Following the work done by [7][9] in the planar prefilmer test case [12] a reduce angular sector numerical domain is simulated. To characterise the inlet velocity boundary condition for the gaseous phase, a single phase simulation is carried out to sample the velocity field (point 3) at different time steps to, afterwards, map it as transient Dirichlet boundary condition for the prefilmer simulation. Then the prefilmer has been simulated on a restricted angular sector of 8 degrees. At run time, the necessary variables for post processing analysis are stored on transverse measurement planes (point 5).

Numerical methodology

The OpenFOAM library is used to perform the simulation, specifically, the well known *interFoam* solver. It offers an interface capturing method mostly based on the simulation of the liquid volume fraction by preserving a sharp transition between liquid and gas phase with a special sharpening numerical method used to limit the numerical diffusion. Time varying velocity is set up for the gaseous inlet velocity from an external simulation to reproduce accurate turbulent boundary condition. Meanwhile, a constant value velocity is set up for the fuel preserving the actual mass flow rate. A no-slip boundary condition has been used for the prefilmer walls and atmospheric pressure has been set up for the external boundaries. Finally, the two patches limiting the domains are related through periodic boundary conditions. The computational mesh is shown in the Figure 3. It has 8M cells and the zone where data are sampled for the post processing is particularly refined. The Smagorinsky turbulence LES sub-model has been used in this study. Concerning the numerical setup, a PIMPLE algorithm is employed and coupled with the liquid volume fraction equation. Second-order schemes are used both in space and time. Variable time-stepping is used, the maximum CFL number is limited to 0.4. The computation has ran for 10 days using 240 CPU having a total of 60K of computational hours.

Sampling and Post-processing methodology

This technique is based on the measurement of the interface between the liquid and the gas to extract its characteristics in term of velocity and curvature. These information are then analyse to characterize the droplets. In other words, every variable sampled is weighted by the amount of surface (area). The sampled variables are the surface interface density flux ($\phi\Sigma = \mathbf{u} \cdot \mathbf{n} |\nabla\alpha|$),

ICLASS 2021, 15th Triennial International Conference on Liquid Atomization and Spray Systems, Edinburgh, UK, 29 Aug. - 2 Sept. 2021

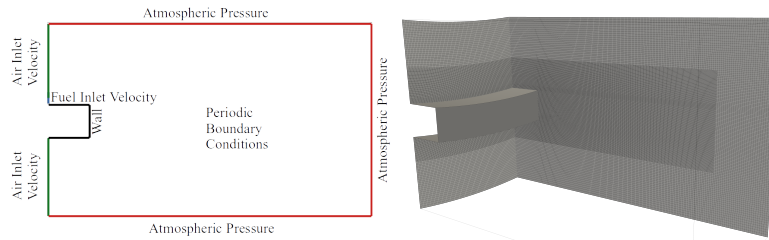


Figure 3. Simulation set-up and computational mesh

the curvature ($\kappa = \nabla \cdot (\nabla\alpha/|\nabla\alpha|)$), the velocity vector (\mathbf{u}) and liquid volume fraction flux ($\phi\alpha = \mathbf{u} \cdot \mathbf{n}\alpha$). These variables are stored at determined coordinates and at every time step. To sample the data a measurement zone is set characterized by its surface with its normal directed to stream-wise direction. All fluxes going through the surface have to be recorded but keeping the local information. Thus, this surface is filled by a set of probes, having one probe on every face of the numerical cell composing the surface.

Sauter Mean Diameter results

The Sauter mean diameter (SMD) represents the ratio of the volume to the surface of a spray but this notion can be extended even for a general liquid-gas flows composed of liquid structured of any shape: (Equation 1).

$$D_{32} = \frac{\sum_i D_{p,i}^3}{\sum_i D_{p,i}^2} = 6 \frac{V_l}{A_l} [1] \quad (1)$$

Thus, the SMD can be computed for a liquid-gas flow crossing a surface and averaged in time following the Equation 2 that is computed using the stored variables over the measurement surface.

$$D_{32}(S) = 6 \frac{\int_T \iint_S (\alpha \mathbf{u} \cdot \mathbf{n} ds) dt}{\int_T \iint_S (\Sigma \mathbf{u} \cdot \mathbf{n} ds) dt} [7] \quad (2)$$

The Figure 4 shows the evolution of the SMD along the axial axis starting from the edge of the prefilmer. The value calculated at the lip of the atomizer is not a representation of any characteristic diameter but a characteristic length. The SMD first increases up to a maximum value where some liquid is accumulated increasing the thickness of the liquid sheet just before being atomized. Then, the SMD strongly decreases due to an active primary break-up that generates smaller liquid elements. Finally, this value remains constant, which is an indication that most of the primary break-up has been taken place even if there are some ligaments or other liquid parcel with complex surface morphology that are not yet fully atomized.

Surface Curvature Distribution (SCD)

From a known cloud of droplets (drop size distribution) is it possible to obtain the surface curvature distribution[8] since the two distribution are linked by the relationship between the diameter and the curvature. In the reverse way, it is possible to compute the drop size distribution from the surface curvature distribution. From the sampled data, the total amount of surface interface is stored in different types of curvature obtaining the surface curvature distribution.

Not all the curvature samplings are representatives of the final droplet, thus, the distribution has to be cleaned up to distinguish which surface elements has to be preserved. In the Figure 5 it can be observed that there are different kinds of structures. Starting from the left side of distribution, it can be seen that there is surface area which is related to a negative curvature.

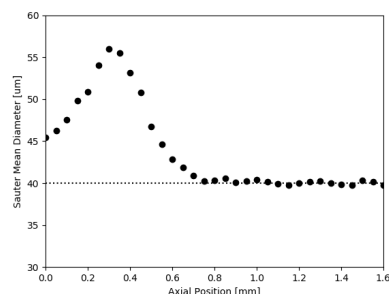


Figure 4. Sauter Mean Diameter computed along the axial axis

This liquid structures correspond to concave elements such a bubbles, ligaments or surface waves (capillary waves for instance). As a preliminary post-process, all the surface related to a negative value is removed since that structures are definitely not droplets. The not considered surfaces (negative curvatures) are shown in black and it correspond to 11.3 % of the total surface sampled.

Drop Size Distribution (DSD)

Once the surface curvature distribution is cleaned up, the drop size distribution is computed by the relation between the curvature and the diameter ($d_{\kappa} = 4/\kappa$) and the relation between the surface interface and the number of droplets ($n(d_{\kappa}) = A_{\kappa}/\pi d_{\kappa}$). These relations are based on the most simple assumption that the retained surface correspond to shell piece of the final droplets. Many other possibilities could be considered but for the time being we have kept this simple approach corresponding also to the approach developed in [7].

The Figure 6 shows the drop size distribution computed from the surface curvature distribution. We can observe that there are a small number of large droplets. They are non-physical droplets since they correspond to a bigger liquid structures such as ligaments or almost flat structures. To discard this very large diameters, the distribution is clipped to match the SMD estimated through the global relation Equation 2. This procedure proposed in [7] enforced the linked between local surface curvature measurement and the global characteristic of the spray that are also computed within the numerical simulation keep a self-consistent approach.

The result of this methodology can be observed on Figure 5. The last figure shows the SCD where the negative curvatures and the party corresponding to non-physical large droplets have been discarded. On the right hand side, the iso-surface of the liquid volume fraction is drawn colored by the curvature where the surface have been retained. All the discarded structures corresponding to the surface element still under atomization process before, i.e. that have not yet reach there final state where they can be considered has representative of the final spray, are represented in black. As expected close to the injector lip most of the surface is blacked since the atomization has not started yet, but farther downstream more and more colour surface element appear as the primary break up and the full atomization process takes places. At the transverse plane location, where the global SMD is stable and the curvature distribution used to estimate the SMD is measured, the surface kept to compute the DSD is 54% of the total surface.

Velocity joint distributions

In a similar way, the velocity joint distributions can be computed. The number of droplets is associate with their velocity vector. In the Figure 7 the three velocity component distributions are shown. The dotted line is the inlet fuel velocity meanwhile the straight line is the inlet air

ICLASS 2021, 15th Triennial International Conference on Liquid Atomization and Spray Systems, Edinburgh, UK, 29 Aug. - 2 Sept. 2021

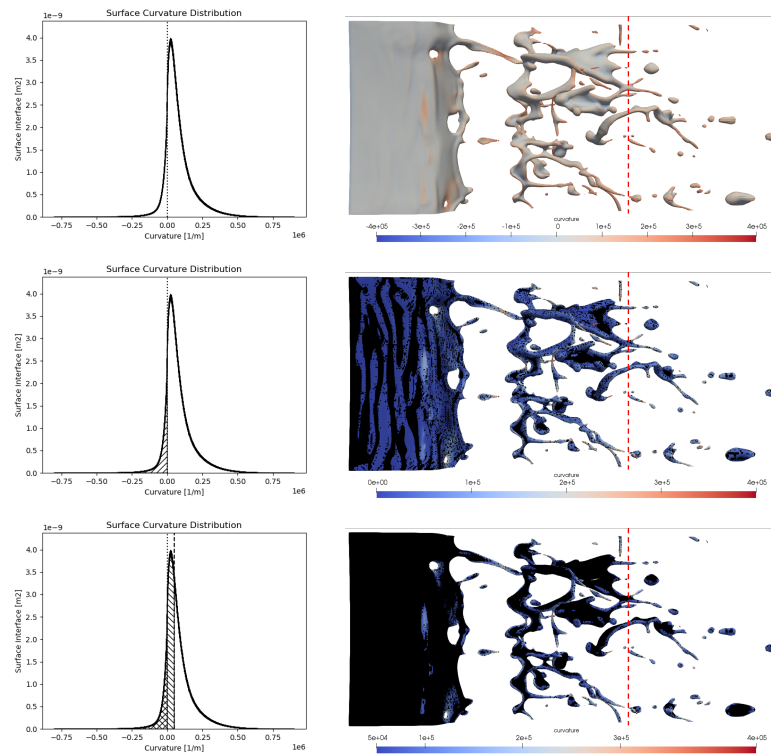


Figure 5. Surface Curvature Distribution (Left) and α contours (right) displaying the removed surface each step of the post-processing. From top to bottom: None surface removed, negative curvature surfaces removed and small curvature surfaces removed. Red dotted line represents the post-processing measurement plane.

velocity averaged on time and space. As expected, the estimated droplets are accelerated from their initial velocity but not overcoming the air velocity. This fact does not happen in the radial component distribution but still the result is physical since once the fuel have left the prefilmer wall, the tangential component of the liquid structures is converted into the radial component. It is also possible to compute the drop velocity distribution for each kind of droplet diameter. It can be noticed in Figure 8 that the smaller droplets ($D = [10 - 11]\mu m$) are more accelerated by the air flow than the medium droplets ($D = [40 - 41]\mu m$) and the bigger droplets ($D = [70 - 71]\mu m$). This effect is expected due to the lower inertia of the smaller droplets compared to the bigger ones and also to the momentum conservation.

Conclusions

A workflow to carry out the modelling of an industrial prefilming airblast atomizer has been proposed. The computational resources has been greatly reduced in contrast to perform one single simulation that encompasses all the physical phenomena taking place and dividing them in different length scales.

The innovative post-processing technique proposed by [7] has been further developed using a CFD simulation based on OpenFoam that include an interface capturing method. It has been reported that it is possible to extract from the prefilmer sector simulation the surface curvature distribution. Then, a self-consistent analysis allows to estimate the final drop size distribution at early stage of the atomization process. The new contribution to this post-processing methodology concerns the calculation of the joint distribution for the three velocity components and

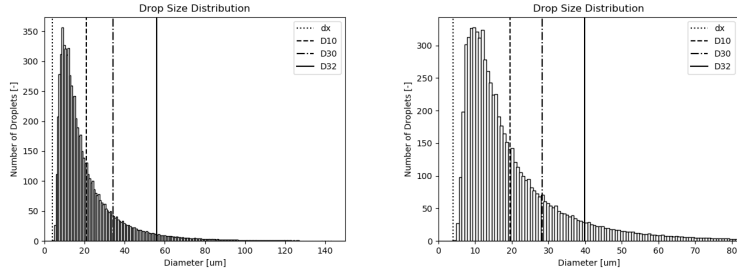


Figure 6. Drop Size Distribution: before clean up (left) and cleaned up(right)

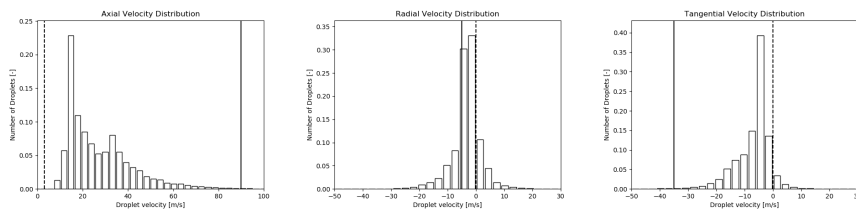


Figure 7. Velocity joint Distribution. Left to right: axial, radial and tangential component

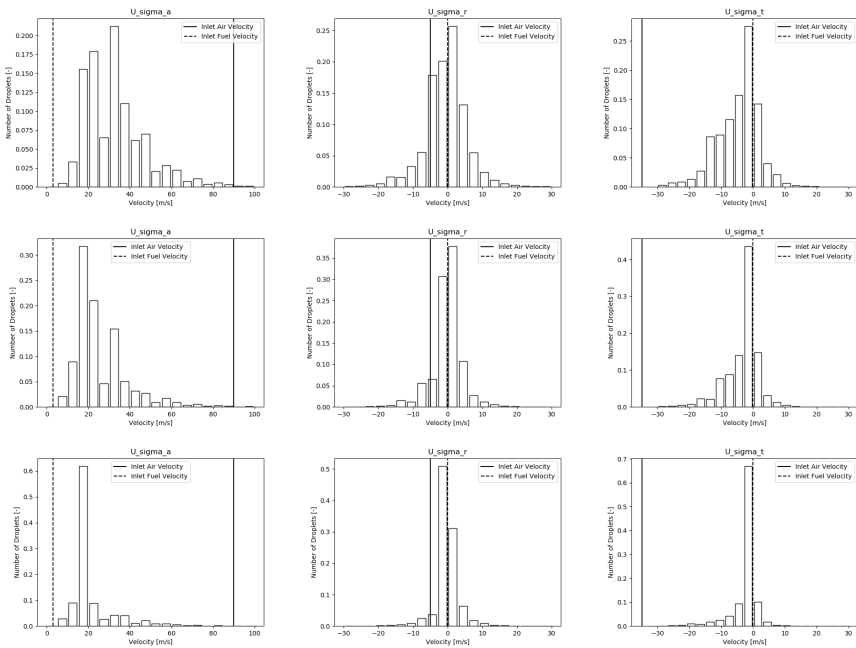


Figure 8. Velocity joint Distribution by droplet diameter. Left to right, axial, radial and tangential component. Top to bottom: small, medium and big droplets

ICLASS 2021, 15th Triennial International Conference on Liquid Atomization and Spray Systems, Edinburgh, UK, 29 Aug. - 2 Sept. 2021

the droplet diameter. Hence, the spray injection characteristics can be determined giving the opportunity to use these data to set-up the injection model for further reacting flow simulation which is the purpose of this work inside the CHAIRLIFT project.

Acknowledgements

This work was granted access to the HPC resources of IDRID, TGCC and CINES under the allocation A0072B06153 and A0092B06153 made by GENCI (Grand Equipement National de Calcul Intensif) and also for the computing time at CRIANN (Centre Régional Informatique et d'Applications Numériques de Normandie) under the scientific project No. 2006011. This work has been also founded by the CHAIRLIFT European project 831881 - CHAIRLIFT - H2020-CS2-CFP08-2018-01.

Nomenclature

α	Liquid Volume Fraction [-]
Σ	Surface Interface Density [m^{-1}]
ϕ	Flux [$m^3 s^{-1}$]
κ	Curvature [m^{-1}]
D_{32}	Sauter Mean Diameter [m]
\mathbf{u}	Velocity vector [ms^{-1}]
d_k	Diameter related to a curvature [m]
$n(d_k)$	Number of droplets related to a curvature [-]
A_k	Surface area related to a curvature [m^2]

References

- [1] Lefebvre, A. H., McDonell, V. G., 2017, "Atomization and Sprays". CRC Press.
- [2] Chaussonnet, G., Riber, E., Vermorel, O., Cuenot, B., Gepperth, S., Koch, R., 2013, ICLASS 2013, 13th Triennial International Conference on Liquid Atomization and Spray Systems.
- [3] Sedlmaier, J., Habisreuther, P., Zarzalis, N., Jansohn, P., 2014, Proceedings of ASME Turbo Expo 2014: Turbine Technical Conference and Exposition.
- [4] Braun, S., Wieth, L., Holz, S., Dauch, T.F., Keller, M.C., Chaussonnet, G., Gepperth, S., Koch, R., Bauer, H.-J., 2019, *International Journal of Multiphase Flows*, 114 , pp. 303-315.
- [5] Warncke, K., Gepperth, S., Sauer, B., Sadiki, A., Janicka, J., Koch, R., Bauher, H.-J., 2017, *International Journal of Multiphase Flows*, 91 , pp. 208-224.
- [6] Mukundan, A.A., Ménard, T., Berlemont, A., Brändle de Motta, J. C., 2019, ICLASS 2019, 29th Triennial International Conference on Liquid Atomization and Spray Systems.
- [7] Palanti, L., Puggelli, S., Langone, L., Andreini, A., Reveillon, J., Duret, B., Demoulin, F.X., 2021, *International Journal of Multiphase Flows*, xx (x), pp. xxxxxxx.
- [8] Canu, R., Puggelli, S., Essadki, M., Duret, B., Menard, T., Massot, M., Reveillon, J., Demoulin, F.X., 2018, *International Journal of Multiphase Flows*, 107 , pp. 230-245.
- [9] Sauer, B., Sadiki, A., Janicka, J., 2014, *The Journal of Computational Multiphase Flows*, 6(3), pp.179-192.
- [10] Li, X., Soteriou, M. C., Kim, W., Cohen, J. M., 2014, *Journal of Engineering for Gas Turbines and Power*, 136, 36(7): 071503 (10 pages).
- [11] Anez, J., Ahmed, A., Hecht, N., Duret, B., Reveillon, J., Demoulin, F.X., 2019 *International Journal of Multiphase Flows*, 113, pp. 325-342.
- [12] Gepperth, S., Guildenbecher, D., Koch, R., Bauer, H.-J., 2010, ICLASS 2010, 10th Triennial International Conference on Liquid Atomization and Spray Systems.

